

---

# The Development of New Techniques for Integral Field Spectroscopy in Astronomy

Matthew Alexander Kenworthy



Institute of Astronomy  
and  
Clare College, Cambridge

November 1998

A thesis submitted to the University of Cambridge  
in accordance with the regulations for  
admittance to the degree of Doctor of Philosophy.

---

---

---

---

# Declaration

The research described in this thesis was carried out under the supervision of Dr. Ian Parry at the Institute of Astronomy, University of Cambridge. No part of this thesis has already been, or is being currently, submitted for a degree, diploma, or any similar qualification at any other University.

The thesis is the outcome of my own work, except when explicit reference has been made to the work of others.

Some of the work presented in this thesis has appeared in the following publications:

I. Parry, M.A. Kenworthy, K. Taylor. "SPIRAL Phase A: A Prototype Integral Field Spectrograph for the AAT" *Proc. SPIE* **2871**, 1325 - 1331 (1997).

M.A. Kenworthy, I.R. Parry, K.A. Ennico. "COHSI: a lens array and fibre feed for the near infra-red", in *Fiber Optics in Astronomy III* (1998), in press.

M.A. Kenworthy, I.R. Parry, K. Taylor. "Integral Field Units for SPIRAL and COHSI" *Proc. SPIE* **3355**, 926 - 931 (1998).

This dissertation text does not exceed the limit of 60,000 words.

In accordance with the Law of Copyright, no information derived from this dissertation, nor any quotation from it, may be published without full acknowledgment of the source being made, and no substantial extract from this dissertation may be published without the author's written consent.

Matthew Alexander Kenworthy  
Cambridge  
November 17, 1998

---

---

---

---

*For my parents  
and especially my sister Eve  
for all the times she took me to the movies*

---

---

---

# Acknowledgements

---

The biggest thanks go to my supervisor **Ian Parry**, who has kept me on the right path over the past three and a half years. Without his help and advice I would have rapidly veered off course and never have been seen or heard by any living soul again. Ian proof-read most of this thesis whilst working on COHSI in Hawaii, and I am extremely grateful that he took the time out of his schedule to talk to me. As well as being a great supervisor he is always willing to talk about ideas over a beer or two in the pub, which can't be a bad thing in my books!

Thanks too to **Keith Taylor**, the Australian end of the SPIRAL connection, for his guidance on the second SPIRAL run. Without his help, I would have been in very deep water. On the subject of help, major thanks and kudos go to **Karl Glazebrook**, for the massive amount of help he gave in the first SPIRAL run - without it, the observing would've been very difficult indeed. Thanks too to **Dave Lee** for his help with SPIRAL. Equally at home running all over the AAT looking for a spare ratchet or bravely throwing caution to the wind by eating a badly cooked meat pastie, Dave is an all round top bloke. My stay at the AAT on both occasions was fantastic and I received help, interest and encouragement from **all the staff** at the Coona site.

Back in Britain, **Kimberley Ennico** deserves respect as the other half of the graduate Instrumentation Group at the IoA, providing the most fantastic chocolate chip cookies and a sympathetic ear when I moaned about problems with the optical fibres. I also thank **Martin Beckett** for introducing me to the world of **Dilbert** and providing me with a monumental amount of computing power with which to play Quake and Doom! Many an hour was wasted with fire fights in the deeper dungeons...

The memories of **Jim and Steve** will inevitably revolve around the attempted Hawaiian midnight walk across brittle lava with only two small torches to showing the way - how any of us didn't kill ourselves scrambling over that stuff, I still don't know! The rest of the Instrumentation Group (**Craig, Richard, Ram**) have made working in Cambridge a great experience, one which I will remember fondly.

A big mention has to be made for the co-creator of the World of Fun™, **Jon Willis**, who made the Royal Astronomical Meetings something to actually look forward to... other astronomers worthy of a chocolate gold medal are **Jarle, Sara, Meghan, Marcus, Andy, Aylwyn, Vern, Ian B,**

---

---

the honourably late **Kester, Melvyn** and host of others including the **secretaries and staff in the IoA**.

**Clare college** people also get a big mention, including **Dan and Joanne, Richard and Zuzanna**, the glorious **Evan Jones, Aimee** and **Jeremy** (also for being top flat mates) and the fantastic form of **Erik Somelar**, who always did more boat house circuits than the rest of the boat crew combined!

Beyond the realm of Cambridge people include **Doctor Mark Garlick**, who inspired me to start all this PhD business, along with **John Stockton**, who kept me guessing and working at all those maths problems. Two astronomers who are worthy of special mention are **Richard ‘Lemon’ Ogley** and **Nick ‘Yoghurt’ Tothill** with whom I have enjoyed the most bizarre nights out on the town. May there be many more in our post-doctorate years!

And finally, a massive massive massive set of hugs to **Vicky**, who has made the greatest difference to my life in Cambridge and has shown me that there is more to it than just fibres and lenses!

Matt

17<sup>th</sup> November 1998

---

# Contents

---

1. Introduction .....	1
1.1 Introduction .....	1
1.2 What is Integral Field Spectroscopy? .....	1
1.3 A review of IFS techniques .....	2
1.3.1 Scanning long slit spectrograph .....	2
1.3.2 Scanning Fabry Perot .....	3
1.3.3 Fourier Transform Spectrographs .....	4
1.3.4 Multi-pupil spectroscopy .....	6
1.3.5 Micro mirror IFU's .....	7
1.3.6 Bare fibre IFU's .....	8
1.3.7 Lens arrays and optical fibres .....	10
1.4 Conclusions and format of the thesis .....	10
2. Properties of optical fibres .....	13
2.1 Introduction .....	13
2.2 Physical properties of optical fibres .....	13
2.2.1 Physical composition of a fibre .....	13
2.2.2 The propagation of light through a step-index fibre .....	14
2.3 Optical properties of step-index fibres .....	15
2.3.1 Radial image and azimuthal scrambling .....	15
2.3.2 Focal Ratio Degradation .....	17
2.3.3 Internal transmission of fibres .....	18
2.4 Polishing the fibres .....	20
2.4.1 Mounting single fibres for polishing .....	20
2.4.2 Mounting many fibres into fibre slits for polishing .....	23
2.4.3 First time use: Conditioning the polishing jig and polishing plate .....	24
2.4.4 The polishing itself .....	25
2.5 Optical testing .....	28

2.5.1 Examining the surfaces of the fibres .....	28
2.5.2 Tests for FRD and throughput .....	29
2.6 Results of optical tests on the fibres .....	31
2.6.1 Optical properties of focal ratio degradation .....	32
2.6.2 The SPIRAL fibre feed.....	32
2.6.3 The COHSI fibre feeds .....	34
2.6.4 Comparison of CeramOptec and Polymicro fibres .....	35
2.6.5 Measuring FRD in an unmounted fibre.....	35
2.6.6 FRD as a function of temperature .....	37
3.The Design of Fibre-fed I.F.S. ....	39
3.1 Introduction .....	39
3.2 Optimising designs for use with optical fibres .....	40
3.2.1 Layout of a fibre-fed spectrograph.....	40
3.2.2 The optimum focal ratio for working with fibres .....	41
3.2.3 The angular extent of a fibre on the sky .....	42
3.2.4 The A- $\Omega$ product .....	43
3.3 The focal plane unit (FPU).....	44
3.3.1 From one fibre to many fibres: the packing fraction problem.....	44
3.3.2 Microlens arrays.....	45
3.3.3 Fore-optics and macrolens arrays.....	47
3.4 Fibre-fed spectrographs.....	48
3.4.1 The problems with a slit-based spectrograph.....	48
3.4.2 The advantages of a fibre-fed spectrograph.....	50
3.4.3 Optimal matching to the detector pixels.....	51
4.SPIRAL Phase A .....	55
4.1 Introduction .....	55
4.2 Overview of the design .....	56
4.2.1 Physical layout of the fibre feed .....	56
4.3 The observational modes.....	58
4.3.1 Integral Field Spectroscopy .....	58
4.3.2 Single Object Spectroscopy (Pupil imaging).....	59
4.4 Design parameters.....	61
4.4.1 The choice of fibre diameter, lens array and fore-optics .....	62

4.4.2 Conduit and strain relief boxes .....	65
4.4.3 The fibre slit.....	66
4.4.4 The spectrograph.....	67
4.5 Construction of the fibre feed.....	68
4.5.1 Conduit and strain relief boxes .....	68
4.5.2 Lens array unit and fore-optics .....	71
4.5.3 The fibre slit.....	75
4.6 Laboratory testing.....	76
4.6.1 The fibre slit.....	77
4.6.2 The lens array.....	77
4.7 Alignment of SPIRAL on the telescope.....	80
4.7.1 Alignment of IFS mode.....	81
4.7.2 Alignment of the PS mode .....	84
4.7.3 Calibration of the SPIRAL spectrograph.....	85
4.7.4 Flexure of the fore-optics table .....	86
4.8 Conclusions .....	87
4.8.1 The construction of the fibre feed .....	87
4.8.2 Alignment on the telescope .....	88
5.The COHSI fibre-feeds .....	89
5.1 Introduction .....	89
5.2 The scientific case for COHSI.....	89
5.2.1 The infra-red night sky .....	90
5.2.2 OH Suppression techniques .....	91
5.3 The design parameters for COHSI on UKIRT .....	92
5.3.1 Protecting the fibre bundle.....	96
5.3.2 The lens array.....	96
5.3.3 The curved double slit .....	97
5.3.4 The cold fibre slit .....	99
5.4 Building the fibre feed .....	100
5.4.1 The fibre conduits .....	100
5.4.2 Lens array .....	101
5.4.3 The curved double slit .....	105
5.4.4 The cold fibre slit .....	108
5.5 Measured performance of the fibre feeds.....	111

5.5.1 The lens array.....	111
5.5.2 The curved fibre slit .....	113
5.5.3 The cold fibre slit .....	113
5.6 Conclusions .....	114
6.Reduction of COHSI and SPIRAL data.....	117
6.1 Introduction .....	117
6.2 The MIT/Lincoln Lab 2kx4k CCD (SPIRAL) .....	118
6.2.1 Physical description the CCDs .....	118
6.2.2 The CCD controller and computer .....	120
6.2.3 The black level and dark current of the MIT/LL CCD .....	121
6.2.4 Flat fields .....	121
6.2.5 CRE removal and hot pixels .....	122
6.2.6 Summary of data reduction for SPIRAL .....	123
6.3 The PICNIC Infra-Red Array (COHSI).....	123
6.3.1 Physical description.....	124
6.3.2 The PICNIC controller and computer .....	125
6.3.3 Black level and dark current .....	125
6.3.4 Flat fielding.....	126
6.3.5 Hot pixels in IR arrays.....	127
6.3.6 Non-destructive reads and CRE removal .....	128
6.3.7 Summary of data reduction for IR array.....	129
6.4 Beam switching and other techniques.....	130
6.5 Extraction of fibre spectra for COHSI and SPIRAL .....	133
6.5.1 Scattered light subtraction (SPIRAL).....	133
6.5.2 Tracing and extraction .....	134
6.5.3 Fibre throughput and flat fielding .....	136
6.5.4 Wavelength and flux calibration .....	137
6.6 Tracing the fibre spectra in COHSI data.....	139
6.6.1 Tracing using a lens array mask.....	139
6.6.2 Interpolation of fibre tracks .....	140
6.7 Simulations of fibre cross-talk.....	141
6.7.1 Simulation of data and measurement of cross-talk .....	142
6.7.2 Minimising the cross-talk with a spatial filter .....	144
6.7.3 Tolerance of extraction to errors in tramline determination .....	145

## TABLE OF CONTENTS

---

6.7.4 Conclusions of the simulations .....	146
6.8 Displaying IFS data with LDISPLAY .....	147
6.8.1 Introduction and use .....	148
6.8.2 The ‘multispec’ mode.....	150
6.8.3 The ‘quicklook’ mode .....	151
6.8.4 The hexagonal array routine .....	152
6.8.5 Current status and conclusions.....	152
6.9 Summary of data reduction .....	153
6.9.1 SPIRAL integral field spectroscopy mode .....	154
6.9.2 SPIRAL pupil imaging mode .....	155
6.9.3 COHSI integral field spectroscopy mode .....	157
7.The Performance of SPIRAL Phase A.....	159
7.1 Introduction .....	159
7.2 The astronomical performance of the SPIRAL spectrograph.....	160
7.2.1 Spectral resolution and PSF across the detector .....	161
7.2.2 Scattered light .....	162
7.2.3 Relative throughputs of the fibres .....	162
7.2.4 Total transmission as a function of wavelength.....	164
7.2.5 Testing the dome flat fielding.....	166
7.3 Science with the SPIRAL fibre feed.....	168
7.3.1 Introduction: big explosions and cool embers .....	168
7.3.2 The pupil imaging mode: brown dwarf candidates.....	168
7.3.3 The brown dwarf LP 944-20.....	169
7.3.4 Results and conclusions.....	169
7.3.5 Observations of SN 1987A.....	171
7.4 SPIRAL and the pupil imaging mode.....	175
7.4.1 Rationale.....	175
7.4.2 The sky background in the pupil imaging mode.....	175
7.4.3 The usability of the pupil imaging mode.....	177
7.4.4 The future of the pupil imaging mode.....	177
8.SPIRAL Phase B - a design study .....	179
8.1 Introduction .....	179
8.1.1 The fibre feed.....	179

## TABLE OF CONTENTS

---

8.1.2 The fibre slit.....	180
8.1.3 The lens array.....	181
8.1.4 The fore-optics.....	184
8.1.5 The final design.....	185
8.2 Conclusions.....	188
9. Conclusions.....	191
9.1 SPIRAL Phase A and the COHSI fibre feeds.....	191
9.2 Data reduction techniques.....	192
9.3 To the future.....	193
10. References.....	195

# List of Figures

Figure 1-1 An imaging Michelson interferometer.....	5
Figure 1-2 The multi-pupil spectrograph.....	6
Figure 1-3 Image slicing as used in the 3D spectrometer.....	8
Figure 1-4 Summary of imaging spectroscopy techniques.....	11
Figure 2-1 Structure of a step-index optical fibre.....	13
Figure 2-2 Ray of light entering a fibre. ....	14
Figure 2-3 Azimuthal scrambling.....	16
Figure 2-4 Radial image scrambling.....	16
Figure 2-5 Focal Ratio Degradation. ....	17
Figure 2-6 Schematic graph comparing a circular aperture to a fibre with FRD. ....	18
Figure 2-7 Data taken from measurements of different types of step-index.....	19
Figure 2-8 Diagram showing arrangement of ferrules for the SPIRAL lens array.....	22
Figure 2-9. Putting ferrules into the metal polishing block. ....	23
Figure 2-10 Detail of the SPIRAL fibre slit.....	24
Figure 2-11 The polishing jig.....	25
Figure 2-12 The polishing jig sitting on top of the polishing plate.....	26
Figure 2-13 The microscope and camera used for examining the fibre faces.....	28
Figure 2-14 Examining the fibre faces.....	29
Figure 2-15 A typical FRD plot.. ....	30
Figure 2-16 Testing the fastest input aperture beam .....	32
Figure 2-17 Varying the wavelength and position of the input spot. ....	32
Figure 2-18 Layout of the SPIRAL FRD test apparatus.....	33
Figure 2-19 FRD test results for seven SPIRAL fibres. ....	33
Figure 2-20 FRD measurements for the two COHSI fibre feeds.. ....	34
Figure 2-21 FRD plots of CeramOptec and Polymicro test fibres. ....	35
Figure 2-22 Images of the Polymicro and CeramOptec test fibres in steel ferrules.....	36
Figure 2-23 FRD plot for an unmounted CeramOptec fibre.....	36
Figure 2-24 Variation of FRD with temperature.....	37
Figure 2-25 Layout of the FRD test bench. ....	38
Figure 3-1 Schematic layout of a fibre-fed spectrograph with one fibre. ....	40
Figure 3-2 The loss of flux in a beam due to FRD.....	41

Figure 3-3 Diagram of telescope and fibre.....	42
Figure 3-4 The area/solid-angle product.....	43
Figure 3-5 The packing fraction for fibres.....	44
Figure 3-6 Comparing the different polygons.....	45
Figure 3-7 Cross section of a microlens array feeding optical fibres.....	46
Figure 3-8 Using fore-optics to increase the plate scale of the telescope.....	47
Figure 3-9 Detail of the macrolens array.....	47
Figure 3-10 The input and output of a slit based spectrograph.....	49
Figure 3-11 The input and output of a fibre-fed spectrograph with square lens array.....	50
Figure 4-1 Diagram of the SPIRAL Phase A and Phase B lens arrays.....	56
Figure 4-2 Layout of the fibre feed on the Anglo-Australian Telescope.....	57
Figure 4-3 Layout of the fore-optics for the integral field mode.....	58
Figure 4-4 Pupil imaging mode.....	59
Figure 4-5 Matching the fibres to the seeing in the pupil imaging mode.....	60
Figure 4-6 Face-on view of a SPIRAL fibre ferrule.....	61
Figure 4-7 Layout of the SPIRAL lens array and fibre ferrules.....	63
Figure 4-8 Cross-section of a SPIRAL fibre ferrule.....	63
Figure 4-9 Schematic of the IFS fore-optics.....	64
Figure 4-10 Schematic of the PS fore-optics.....	65
Figure 4-11 Schematic layout of the SPIRAL fibre slit.....	66
Figure 4-12 Layout of the SPIRAL spectrograph.....	68
Figure 4-13 The chromatic focal shift for the SPIRAL Littrow spectrograph.....	69
Figure 4-14 The fibre feed.....	69
Figure 4-15 The strain relief box at the lens array end of the conduit.....	70
Figure 4-16 Diagram of the SPIRAL fibre ferrule.....	71
Figure 4-17 Photograph of aluminium former used for SPIRAL array.....	72
Figure 4-18 Aligning the SPIRAL fibre ferrules on the lens array.....	73
Figure 4-19 The order of fibre placement on the lens array.....	74
Figure 4-20 End-on view of the SPIRAL fibre slit during assembly.....	75
Figure 4-21 Graph of measured fibre pitch on the SPIRAL fibre slit.....	77
Figure 4-22 The measured fibre position errors on the SPIRAL lens array.....	78
Figure 4-23 Fibre decentering errors in the SPIRAL lens array.....	79
Figure 4-24 Layout of auto-guider unit and TV slit viewing camera for the AAT.....	80
Figure 4-25 Technical drawings of the two pick-off mirrors used with SPIRAL.....	81

Figure 4-26 Fore-optics and lens array mounted on the optical table in the Cassegrain cage ..... 82

Figure 4-27 Layout of the IFS mode optics on the telescope. .... 83

Figure 4-28 Schematic of the pick-off mirror arrangement. .... 84

Figure 4-29 Aligning the pupil imaging mode on the telescope. .... 85

Figure 4-30 Arrangement of micrometers for adjustment on the SPIRAL Littrow Spectrograph... 86

Figure 5-1 The COHSI IFU lens array. .... 90

Figure 5-2 The infra-red sky above Mauna Kea..... 91

Figure 5-3 Principle of OH hardware suppression.. .... 92

Figure 5-4 Layout of COHSI. .... 93

Figure 5-5 Layout of the COHSI lens array..... 93

Figure 5-6 Framework holding the COHSI fore-optics on UKIRT. .... 94

Figure 5-7 Layout of the COHSI OH suppressor..... 95

Figure 5-8 Inside the cryogenic dewar..... 96

Figure 5-9 Wire frame of the COHSI fore-optics..... 97

Figure 5-10 A single fibre in the OH suppressor. .... 98

Figure 5-11 Spot diagrams for the OH suppressor. .... 98

Figure 5-12 Inter fibre spacing reduced by a staggered fibre slit ..... 99

Figure 5-13 Dimensions of the COHSI fibre feeds..... 100

Figure 5-14 The COHSI lens array IFU. .... 101

Figure 5-15 Aluminium formers for the COHSI and SPIRAL lens arrays..... 102

Figure 5-16 Close-up of the COHSI lens array with two fibres in place..... 102

Figure 5-17 The custom ferrule for the COHSI fibres..... 103

Figure 5-18 The complete set of ferrules for the COHSI lens array fibres..... 103

Figure 5-19 Layout of the COHSI fibre alignment apparatus..... 104

Figure 5-20 The curved fibre slit assembly..... 106

Figure 5-21 The order of the fibres in the curved fibre slit..... 106

Figure 5-22 The curved fibre slit on the spherical polishing plate..... 107

Figure 5-23 The curved fibre slit mounted in the middle of the OH suppressor. .... 108

Figure 5-24 The finished curved fibre slit. .... 108

Figure 5-25 Cryogenic fibre feed inside COHSI dewar. .... 109

Figure 5-26 Schematic drawing of the cold fibre slit.. .... 110

Figure 5-27 The positioning error of fibres on the back of the COHSI array..... 111

Figure 5-28 Histogram of fibre positioning errors on the COHSI lens array. .... 112

Figure 5-29 COHSI curved fibre slit positioning errors..... 112

Figure 5-30 Variation of the length of the fibre slit vector with position on the fibre slit ..... 113

Figure 5-31 COHSI on UKIRT. .... 114

Figure 5-32 The completed COHSI fibre feed. .... 115

Figure 6-1 A raw IFS data frame..... 117

Figure 6-2 Schematic of a CCD. .... 119

Figure 6-3 A single metal-oxide-semiconductor (MOS) storage well..... 120

Figure 6-4 Quantum efficiency curves for the MIT/LL CCD, the Tek 1K<sup>2</sup> and a HAWAII array. 122

Figure 6-5 Layout of the IR array..... 124

Figure 6-6 What defines a hot pixel in a PICNIC array. .... 127

Figure 6-7 The different NDR methods for an exposure..... 128

Figure 6-8 Detection of CRE in pixels using NDRs.. .... 129

Figure 6-9 Beam-switching with COHSI. .... 131

Figure 6-10 Comparison of beam-switching..... 132

Figure 6-11 Alternate fibre subtraction..... 132

Figure 6-12 A stylised version of an IFS frame. .... 133

Figure 6-13 A scattered light image.. .... 134

Figure 6-14 A cut across the spatial axis of a SPIRAL twilight image..... 135

Figure 6-15 Fitted apertures in APEDIT. .... 135

Figure 6-16 A plot of residuals to a tramline fit on a SPIRAL fibre spectrum..... 136

Figure 6-17 An arc spectrum in the program IDENTIFY..... 138

Figure 6-18 Fitting the dispersion function. .... 138

Figure 6-19 Flat field in H band from COHSI..... 139

Figure 6-20 The mask for the COHSI lens array. .... 140

Figure 6-21 Illuminating alternate fibres in the H band to help define the tramlines. .... 140

Figure 6-22 A graph showing the interpolation technique.. .... 141

Figure 6-23 The effect of fibre cross-talk.. .... 142

Figure 6-24 The reference spectrum and simulated emission line galaxy spectrum..... 143

Figure 6-25 The cross-talk in COHSI data.. .... 143

Figure 6-26 Frame showing reference spectrum and simulated galaxy spectrum..... 144

Figure 6-27 Ripple with variation of extraction aperture width..... 144

Figure 6-28 Using a spatial filter to minimise the cross-talk..... 145

Figure 6-29 The results of the cross-talk simulations..... 145

Figure 6-30 The variation in cross-talk for fibre separation and error in tramline determination.. 146

Figure 6-31 LDISPLAY running in an X server..... 148

Figure 6-32 The parameters of ‘quicklook’ for a raw data frame. ....	151
Figure 6-33 The SPIRAL and COHSI fibre slit maps used in LDISPLAY. ....	152
Figure 6-34 A pupil imaging data frame.....	155
Figure 6-35 The effect of a tilted fibre slit on pupil imaging extraction. ....	156
Figure 6-36 The COHSI flat fields. ....	157
Figure 7-1 Vignetting and scattered light in the spectrograph. ....	160
Figure 7-2 Point spread function of arc emission lines across the MIT/LL CCD.....	161
Figure 7-3 Normalised SPIRAL aperture throughputs and fibre throughputs. ....	163
Figure 7-4 Histograms of the aperture throughputs/fibre throughputs of the SPIRAL lens array. ....	164
Figure 7-5 Transmission versus wavelength for SPIRAL. ....	165
Figure 7-6 The effect of misalignment on throughput.....	166
Figure 7-7 Pixel to pixel flat fielding with SPIRAL. ....	167
Figure 7-8 The spectrum of BRI 0337-3535.....	170
Figure 7-9 HST WFPC image of 1987A. ....	172
Figure 7-10 SPIRAL maps of hydrogen in SN 1987A.....	172
Figure 7-11 Sky background spectra for SN 1987A. ....	173
Figure 7-12 The combined fibre spectra of SN 1987A.....	173
Figure 7-13 The SN 1987A spectrum.....	174
Figure 7-14 Maps of [OII]6364 and its ratio with Ha.....	174
Figure 8-1 Angular size of fibres for the AAT and Gemini telescopes. ....	180
Figure 8-2 A set of cylindrical lenses. ....	182
Figure 8-3 Simple hexagonal array.....	182
Figure 8-4 Drawings of possible hexagonal lens arrays for SPIRAL B. ....	183
Figure 8-5 Schematic of the SPIRAL Phase B fore-optics.....	185
Figure 8-6 Spot diagrams for a fibre at the edge of the array. ....	186
Figure 8-7 Spot diagrams for a lenslet in the middle of the array.....	186
Figure 8-8 The transmission curves for the field lens. ....	186
Figure 8-9 The layout of the SPIRAL Phase B fore-optics. ....	187
Figure 9-1 Image reconstruction using the LDISPLAY software.....	193



# List of Tables

Table 2-1 Conversion table for focal ratios.....	15
Table 2-2 Optical fibres used in COHSI and SPIRAL.....	20
Table 2-3 Polishing pastes used for the optical fibres. ....	26
Table 2-4 Microscope images at the different stages of polishing.....	27
Table 2-5 Physical details of the two COHSI fibre feeds.....	34
Table 4-1 Examples of different pupil imaging modes .....	60
Table 4-2 Parameters of the Anglo-Australian Telescope .....	62
Table 4-3 Ideal and real lenses for the IFS mode.....	64
Table 4-4 Parameters for the SPIRAL Pupil Spectrograph (SPS) .....	67
Table 6-1 Physical parameters of detectors used for SPIRAL and COHSI.....	118
Table 6-2 The RESET-READ-READ mode of the PICNIC arrays.....	126
Table 6-3 Parameter file for LDISPLAY.....	149
Table 6-4 Table of IFS data reduction steps. ....	153
Table 7-1 The dates and CCD's used on the SPIRAL observation runs.....	159
Table 7-2 Measured dispersions and resolutions of the SPIRAL spectrograph.....	162
Table 7-3 Scattered light levels for different gratings. ....	162
Table 7-4 Comparison of LP 944-20 properties.....	170
Table 7-5 Magnitudes and colours of LP 944-20.....	170
Table 8-1 Combinations of fibre diameter and number of fibres in the fibre slit .....	181
Table 8-2 Different possible hexagonal lens arrays for SPIRAL Phase B. ....	184
Table 8-3 Different possible crossed lens arrays for SPIRAL Phase B.....	184
Table 8-4 Results of SPIRAL Phase B study.....	187
Table 8-5 Estimated cost of the SPIRAL B project .....	188

Finally Cutangle spoke, very slowly and carefully.

“I look at it like this,” he said. “Before I heard him talk, I was like everyone else. You know what I mean? I was confused and uncertain about the little details of life. But now,” he brightened up, “while I’m still confused and uncertain it’s on a much higher plane, d’you see, and at least I know I’m bewildered about the really fundamental and important facts of the universe.”

Treatle nodded. “I hadn’t really looked at it like that,” he said, “but you’re absolutely right, He’s really pushed back the boundaries of ignorance. There’s so much about the universe we don’t know.”

--- *Equal Rites, Terry Pratchett*

# 1. Introduction

---

## 1.1 Introduction

Integral field spectroscopy is a rapidly expanding field in astronomical instrumentation. This powerful technique allows astronomers to gain new insights into the structures and dynamics of astronomical objects on all scales, from the atmospheres of Jovian moons, through the stellar dynamics of globular clusters to analysing the gravitationally distorted images of distant galaxies. The explanation of integral field spectroscopy is given in §1.2, showing how it improves over more classical methods of observing. A brief review of the different IFS techniques is given in §1.3 and the individual advantages and disadvantages for each technique are discussed.

This thesis explores the techniques needed to build an integral field spectrograph and reduce the data taken with it. The layout of the thesis is given in §1.4.

## 1.2 What is Integral Field Spectroscopy?

Integral field spectroscopy (IFS) is the recording of spectral information for every imaged pixel over a given area of sky, where ideally the size of a pixel is limited by the seeing conditions or the diffraction limit of the telescope. The two most common observational techniques (imaging and long slit spectroscopy) record data on two dimensional detectors, such as a charge coupled device (CCD).

Astronomical imaging records the spatial distribution of an object for a given wavelength range, and is used for photometry and morphology studies where detailed spectral information is not required. Multiple exposures using different colour filters then allow simple spectral properties of the object to be determined, but for greater spectral resolution a long slit spectrograph is used. Long slit spectroscopy is ideal for point-like sources or for looking at a specific cut across an extended object, but it cannot simultaneously record both spectral and two-dimensional spatial information.

IFS differs from imaging and long slit spectroscopy in that it requires recording of three dimensions of data ( $x$ ,  $y$  and  $\lambda$ ), otherwise known as a 'data cube'. This data cube needs to be reformatted before it can be recorded on a detector, and the various techniques used to generate a data cube are reviewed in the next section.

### 1.3 A review of IFS techniques

The growth of IFS instruments over the past few years has been prodigious. Astronomers are fully aware of the new research that data cubes can bring - the internal dynamics of galaxies, velocity maps showing the distribution and motion of gas within star clusters and jets from galactic cores, and the reconstruction of gravitationally lensed star forming galaxies are just a few of the research areas that have benefited.

Broadly speaking, there are two different methods used to form a data cube. The first is a scanning technique, where two of the three dimensions (one spatial and one spectral, or both spatial) are recorded in one exposure and the third dimension of the data cube is filled in by taking subsequent exposures. The other technique is integral field spectroscopy, where all three dimensions are recorded simultaneously with a single exposure. Both techniques are known as ‘imaging spectroscopy’, ‘bidimensional spectroscopy’ or sometimes ‘spectral imaging’.

The methods which need successive exposures to make up a data cube are susceptible to systematic errors. Sources of error include variability in atmospheric transmission, variation in image quality between successive exposures and flexure in the telescope instrumentation, these require extra flat fielding and calibration frames. Even temporal variability in the object being observed can cause extra data reduction difficulties. IFS techniques do not suffer from these errors as all three dimensions are recorded simultaneously.

The three most common scanning methods are the scanning long slit spectrograph, the scanning Fabry-Perot and the Fourier transform spectrograph. The most common IFS techniques can be separated into those which use mirrors as image slicers (micro mirrors) and those which use lens arrays or optical fibres to segment the image plane. In some IFS instruments, optical fibres and lens arrays are used in combination. A brief review of all these methods and their advantages and disadvantages are given below.

#### 1.3.1 Scanning long slit spectrograph

The data cube is built up by scanning the long slit in a direction perpendicular to its length, and taking an exposure for each position such that the step size between exposures is equal to the width of the slit. This is the simplest method of generating a data cube with existing long slit spectrographs. One example of a scanning long slit spectrograph is the ASPECT mode (Clark & Wallace 1984) for the Anglo Australian Telescope’s RGO spectrograph and Integrated Photon Counting System (IPCS). The field of view was  $\sim 3$  arcminutes long per exposure, with a typical spatial resolution of 2.4 arcseconds. The size of the area scanned was limited by the number of separate exposures needed to cover the area with the slit, and the spectral range was typically 3500-7500Å for the low dispersion grating.

The core of NGC 5128 was imaged with 71 exposures and a 2.4 arcsecond slit, forming an observed area of 120 by 200 arcseconds (Wilkinson et al. 1986) but this technique has not been developed since.

The major limitations to this method is due to various seeing losses with the spectrograph and the non-uniformity of the slit jaw, resulting in lost flux and variable photometry from one exposure to the next. A degradation in seeing also results in variable image quality throughout the data cube.

### 1.3.2 Scanning Fabry Perot

The Fabry Perot etalon consists of two plane parallel pieces of glass with a thin partially reflective coating on the inside faces. Light passing through the etalon undergoes multiple reflections between the two surfaces and interference takes place in the emerging beam. If an extended monochromatic source is viewed through an etalon a series of circular fringes can be seen superimposed on the light from the source, and the radius of these fringes varies with the optical distance between the two plates and the wavelength of the incident light.

Astronomical etalons offer medium to high spectral resolution capabilities ( $R \sim 5000-20000$ ) with an imaging field of view of 1-10 arcminutes, depending on what telescope the etalon is on and how big the etalon is. The spectral resolution and free spectral range (the distance between two adjacent spectral orders measured in Angstroms) are defined by the spacing  $t$  and reflectivity  $R$  of the plane surfaces. The derivation of the Fabry Perot formulae are given in many standard optics books (for example, Pain 1993) but the relevant expressions for spectral resolution are:

$$\frac{\lambda}{\delta\lambda} = \frac{2nt}{\lambda} \cdot N_e \quad (1-1)$$

and the free spectral range is

$$FSR = \frac{\lambda^2}{2nt} \quad (1-2)$$

where  $nt$  is the optical distance between the etalon plates and  $N_e$  is defined as:

$$N_e = \frac{\pi \cdot \sqrt{R}}{(1-R)} \quad (1-3)$$

with  $R$  being the reflectivity of the plates.

The free spectral range shows the range of wavelengths that the etalon can scan without the orders of successive interference fringes being confused with each other. The transmission profile of an etalon is called the Airy function, and the free spectral range divided by the FWHM of this function gives the finesse of the etalon. The quantity  $N_e$  is the finesse of the etalon, and it shows how many scanning steps can be taken with the etalon to cover the free spectral range. The finesse for astronomical etalons is approximately 20-30, but due to non-parallelism of the plates and other

aberrations in the optics this value is degraded. The finesse also gives the minimum number of exposures needed to be taken with the etalon to sample the free spectral range.

The etalon sits in a collimated beam between the camera and telescope, and the spacing of the etalon plates is controlled with closed loop electronic equipment. For each of the data exposures the etalon gap is adjusted so that the free spectral range is eventually covered. Each image represents a complicated cut through the  $(x,y,\lambda)$  data cube, with each pixel on the image being a function of  $x$ ,  $y$  and  $\lambda$ . Variations in seeing and atmospheric transmission mean that many flat fields are needed for the accurate reconstruction of the data cubes.

The advantages of etalons are the high spectral resolution and large fields of view that they can offer. Their limited free spectral range means that only a few Angstroms can be observed for a given band pass, and narrow band filters are needed to avoid confusion with overlapping orders. Etalons are mainly used for mapping out emission lines in cores of galaxies and stellar clusters. Their instrumental profile is known as an Airy function, with a narrow transmission peak at the central wavelength with faint extended wings over the rest of the spectral range. This makes the mapping of absorption lines difficult and so etalons are not often used for this type of mapping.

The accuracy of the coatings and control of the etalon spacing limited their astronomical use for many years, but due to advances in electronic control and new coating deposition techniques, scanning Fabry Perot etalons are now in regular use, such as Taurus-II (Taylor & Atherton 1980, Atherton 1982) at the AAT and CIGALE (Boulesteix 1984) and HIFI (Bland 1990) both at the CFHT.

### 1.3.3 Fourier Transform Spectrographs

Fourier transform spectrographs (FTS) have been used in laboratories for many years to obtain high ( $R > 10^6$ ) spectral resolutions. The only FTS in common astronomical use today is the CHFT FTS (Maillard 1995), which uses a Michelson interferometer (see Figure 1-1). The telescope beam from the focus is passed through a collimator lens to form a plane parallel beam. A beam splitter takes the collimated light and sends it down two different paths. One path has a fixed mirror, and the other has a mirror that can alter its distance from the beam splitter. The beams are sent back to the beam splitter and form interference fringes. The beams are then imaged onto the detector with a camera lens.

By varying the path length of the movable mirror, each pixel on the detector records an interferogram for each point on the sky. The movable mirror is held stationary whilst an exposure is taken, then the mirror moves to the next position and the next integration begins. Eventually, a data cube of interferograms is generated and by taking the Fourier transform of the data cube the spectral information can be recovered.

The Michelson interferometer loses 50% of the incoming light due to the beamsplitter, but due to a careful design (Maillard 1982) the interferometer is built such that beams from both sides of the splitter are imaged and a very high efficiency can be attained.

The resolution of the interferometer is a function of the maximum path difference introduced between the two mirrors, the wavelength of the incident light and the field of view of the interferometer on the sky. In the case of the CFHT instrument, the maximum spectral resolution is  $\sim 30,000$  for a field of view of 20 arcseconds and a maximum path difference of 30cm. The spectral coverage of the FTS is determined by a bandpass filter placed in the collimated beam, and the amount of time needed to perform all the exposures needed to construct the interferograms. The number of steps in the interferogram also set the number of points in the resultant spectral image.

The positional accuracy and required flatness of the mirrors needed is dependent on the wavelengths being observed. For optical wavelengths the tolerances are very high and difficult to achieve, so FTS is better suited to the infra-red region, from  $1.0\mu\text{m} - 2.5\mu\text{m}$ .

The main limitation of the FTS is the signal-to-noise requirements on the detector. Each mirror position needs to have an integration such that the dominant source of noise is the photon shot noise. Unfortunately, infra-red detectors have high read-out noises and this implies long integration

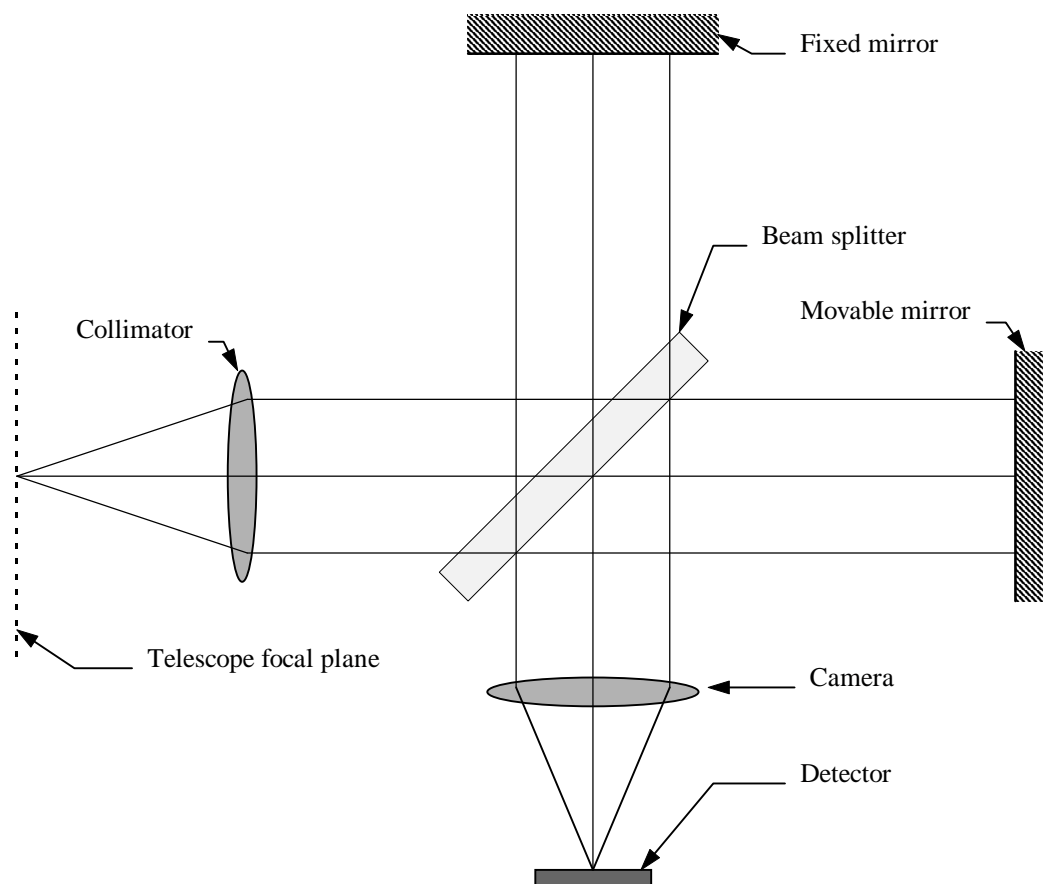


**Figure 1-1** An imaging Michelson interferometer.

times, but on the other hand most targets are brighter in the infra-red. Since each pixel is receiving light from the whole night spectrum, there is a contribution from the OH night sky emission lines on top of which are the fringes of interest. These are usually limited by using a narrow bandwidth filter.

### 1.3.4 Multi-pupil spectroscopy

A method proposed by Courtes (1982) uses a focal enlarger to project an image of the telescope focal plane onto a microlens array. This microlens then segments the enlarged focal plane and produces a pupil image on the back of the lens array. A spectrograph then takes the array of pupil images, disperses them with a grating and images the resultant spectra onto a detector (see Figure 1-2).

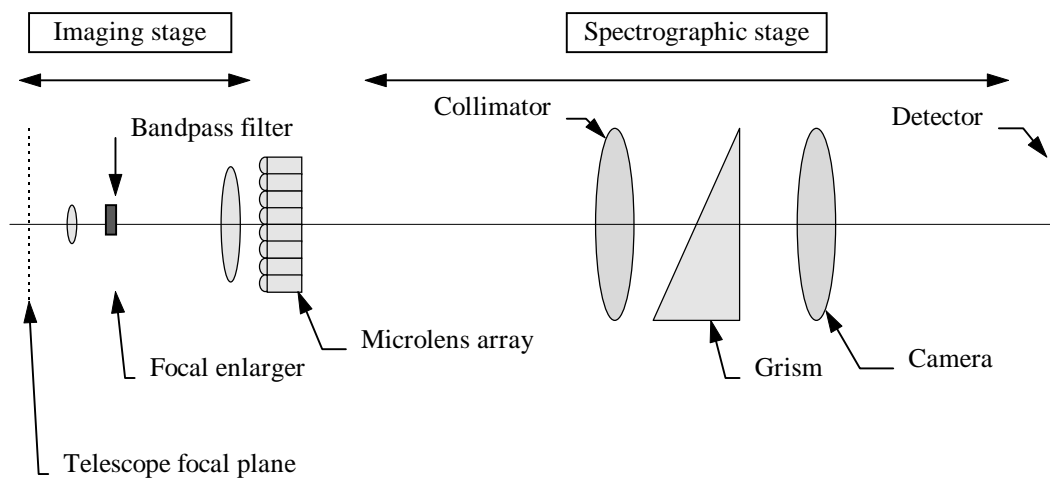


**Figure 1-2** *The multi-pupil spectrograph.*

This method is used in the prototype TIGER spectrograph (Bacon 1995a and Bacon 1995b). The lenslet array is made up of 564 circular lenses arranged in a 24 by 21 hexagonal matrix, each 1.3mm diameter lens producing a 45 $\mu$ m diameter image of the exit pupil of the CFHT. The spectrograph is unusual in that it disperses the pupil images of the telescope, with the advantage that the point spread function on the detector is now independent of the spatial information within the image.

With no dispersing element in place, the collimator and camera optics form a regular hexagonal array of pupil images on the 1024<sup>2</sup> 15 $\mu$ m pixel CCD. When these pupils are dispersed, the ends of the spectra overlap each other on the detector. A slight rotation between the dispersion axis and the micro-lens array, combined with a broad band interference filter inserted in the focal reducer, avoids overlapping between spectra and limits the spectral range possible with this type of spectrograph. The only disadvantages are the truncation of spectra at the edge of the detector and the limited number of pixels used per spectrum. For a spectral resolution of 1800 at 6850 $\text{\AA}$ , the wavelength range is 540 $\text{\AA}$ .

The success of the original prototype system has produced many similar integral field spectrographs, along with an improved and enlarged version of TIGER incorporated as part of a larger multi-mode spectrograph known as OASIS. This common user instrument has a greater variety of wavelength ranges and dispersions available, building on the original TIGER design.

One design that allows higher spectral resolutions is PYTHEAS (Le Coarer 1995 and Georgelin 1995) which uses a similar layout to Tiger but inserts a Fabry Perot etalon in front of the microlens array. With the etalon in a collimated beam, the etalon acts as a tuneable periodic narrow-band filter - the spectra produced in the TIGER spectrograph are now modulated by the Airy fringes to produce a series of evenly separated Fabry 'spots' along the path of each spectrum.

The etalon is then scanned in steps across its free spectral range and the detector read out at every step. In this way, spectral resolutions of over 19,000 have been achieved. In this mode, PYTHEAS is no longer an integral field spectrograph, with the detector now being used as a spectrometer and the scanning time dependent component is re-introduced. Nevertheless, the advantages of higher resolution and large field of view make this a powerful investigative method for astronomers.

### 1.3.5 Micro mirror IFU's

In this IFS design the focal plane of the telescope is re-formatted into a long slit by the use of mirrors. Two sets of mirrors are used, the first set sends horizontal strips of the field off to a second set of distributed mirrors that image the strips at a common focus to form a pseudo slit configuration suitable for entry into a spectrograph (see Figure 1-3). This design has been used in a near infra-red spectrograph called 3D, built by the MPE group at Garching (Krabbe 1996, Krabbe 1995, Weitzel 1996).

Because the image slicer uses only reflecting surfaces, it is suitable for cryogenic cooling - by building the image slicer in a dewar with a spectrograph the whole apparatus can be cooled to liquid nitrogen temperatures and hence reduce the infra-red thermal background from room temperature objects. The metal construction is more resistant to the thermal cycling process and is less susceptible to misalignment, something that has to be considered with cryogenic refractive optics.

The detector used is a  $256^2$  IR array, allowing 16 by 16 spatial pixels on the sky and 256 spectral elements per spatial pixel, with two interleaved exposures ensuring that the spectra are adequately sampled. Another advantage to using an all reflecting system is that it is completely achromatic.

In order to match to the plate scale of the telescope, the height of each slicing mirror in the first module is just 0.4mm high, demonstrating the success of computer aided machining. The mechanical tolerances specified for the mirror surface and pointing is high, and the individual mirrors have to be aligned with great accuracy to ensure the correct optical path through the slicer.

Increasing the number of spatial pixels presents a difficult technical challenge - the mirrors will have an even smaller pitch and the total reformatted slit length increases, enlarging the second set of correcting mirrors. It is interesting to note that the next IFS that the Garching group is intending to build will be using optical fibres and a lens array to perform the reformating of the field of view (Tecza 1998).

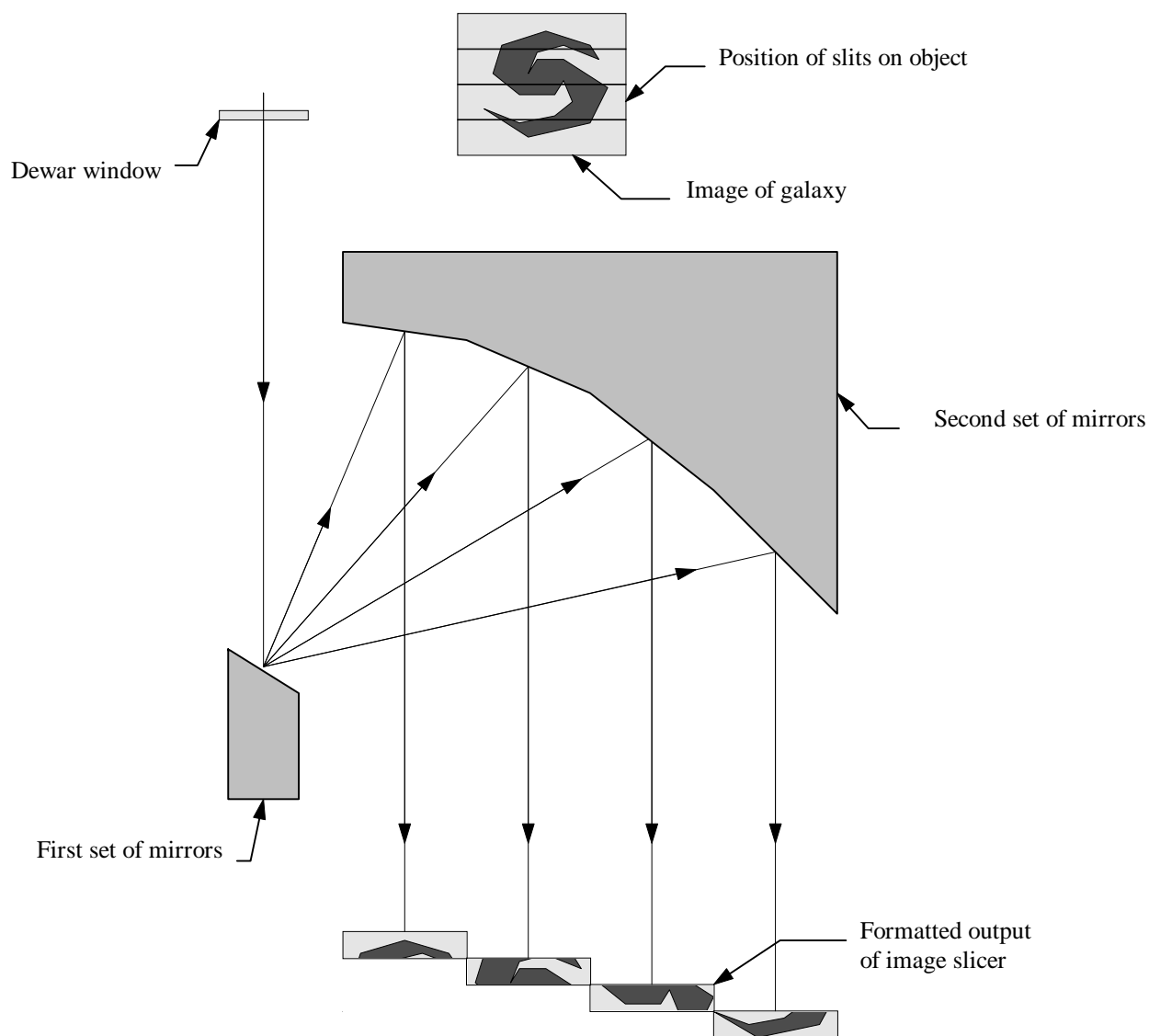


**Figure 1-3** Image slicing as used in the 3D spectrometer.

### 1.3.6 Bare fibre IFU's

Some of the first image reformatters used on telescopes were made with optical fibres (see Chapter 2 for a description of optical fibres). The ability of optical fibres to conveniently reformat light has been known for many years to astronomers, and the versatility of optical fibre and its possible applications to astronomy has been noted from an early time (for example Angel 1980).

The principle of the optical fibre reformatter is simple. A bundle of optical fibres is placed in the focal plane of a telescope and the other ends of the fibres are rearranged into a straight line suitable for dispersion in a spectrograph. This arrangement of fibres is sometimes known as a 'fibre slit'. By knowing the relationship between the fibre in the bundle and the fibre on the slit, an image of the sky can be reconstructed from the spectra on the detector.

Many of these bare fibre feeds have been built, partially due to their simplicity of construction and immediate multiplex gain. There are two main disadvantages to the bare fibre feeds - the first is that the fibres do not completely cover the focal plane of the telescope, resulting in loss of light in the inter-fibre spaces. The second disadvantage is that the input focal ratio of the telescope is not optimal for efficient transmission of light through the fibres (see Chapter 2 and Chapter 3 for details). These systems are listed with the salient points in rough chronological order below:

- One of the first bare fibre reformatters was a 53 fibre system tested on the AAT (Gray 1981), with 200 $\mu$ m diameter fibres arranged in the Cassegrain  $f/8$  focal plane. The length of the fibre feed was 2.5 metres, feeding the RGO spectrograph with a 50mm long fibre slit. Each fibre had a diameter of 1.3 arcseconds on the sky, with the bundle forming a field of view of 17 by 22 arcseconds.
- **DensePak I** (Barden and Scott 1986) was composed of 49 QSF AS fibres arranged in a 7 by 7 array with each fibre having a 100 $\mu$ m core diameter. The packing fraction losses were large, with 96% of the light lost from the focal plane due to the large buffer diameter of 480 $\mu$ m for the fibres. A dithering method was used to fill in the missing focal plane area.
- **DensePak II** (Barden and Wade 1988) was a development of DensePak I and used Polymicro Technologies optical fibres with 320 $\mu$ m core diameter and 415 $\mu$ m buffer diameter, resulting in a significantly improved packing fraction of 54%. Used on the KPNO 4 meter telescope, it gave a view of 16 by 19 arcseconds with each fibre subtending 2.1 arcseconds.
- **HEXAFLEX** (Arribas 1991, Arribas 1993 and Rasilla 1990) consisted of two fibre bundles which both have 61 fibres in them, but the spatial distribution of the fibres was different. The fibre slits were arranged so that the fibre bundles could be easily interchanged according to the observing programme and telescope conditions. The bundles were used on the WHT 4.2m telescope, with an input focal ratio of  $f/11$ . The spatial coverage and sampling for the first bundle was 13 arcseconds and 1.5 arcseconds respectively. The second bundle was 60 arcseconds and 1.7 arcseconds respectively. Both arrangements had low packing fractions but their large scale was considered useful for various types of science.
- **SILFID** (Vanderriest 1988 and Vanderriest 1993) is a hexagonal close-packed array of 100 $\mu$ m diameter fibres with 4 $\mu$ m cladding arranged in a compact hexagonal array. The field of view is 16 arcseconds at the  $f/8$  Cassegrain focus of the CFH telescope, with each fibre sampling 0.7 arcseconds. The length of the fibre slit is 53mm. This is one of the only fibre feeds with over a hundred fibres in it.

There are other systems which use bare fibres that have not been mentioned in this text, but all have the similar problems of packing fraction losses and poor matching of the focal ratio with the fibre.

### 1.3.7 Lens arrays and optical fibres

With the poor packing fraction of optical fibres it seems that the losses are inevitable. However, by using a lens array to feed the optical fibres a nearly perfect filling factor can be achieved. One of the first lens array IFS was built at the Special Astrophysical Observatory for the 6 metre telescope (Afanasiev 1990).

A focal enlarger converts the  $f/4$  telescope focal ratio into  $f/124$ , converting the telescope scale from 8.6 arcseconds/mm into 0.278 arcseconds/mm. The lens array consists of square lenslets each 4.5mm to a side and forming a matrix of 15 by 15 lenslets. 200 $\mu$ m core fibres behind each lenslet take the collected light to a spectrograph slit and the resultant spectra are analysed by an integrated photon counting system.

An alternative is to use a microlens array to feed the fibres, and this approach has been taken by the Durham Instrumentation Group. Here, no focal enlarger is used to change the plate scale of the telescope. Instead, an array of microlenses directly samples the focal plane of the telescope and feeds the light into optical fibres. The Durham unit is called the SMIRFS IFU (Haynes 1998) and is used as a fibre feed for the infra-red spectrograph CGS4 on the United Kingdom Infra-Red Telescope (UKIRT).

Both methods combine the high filling factor achievable with lens arrays with the optical reformatting capabilities of optical fibres. This is the method used and developed in the rest of this thesis, and the relative merits of macrolens arrays versus microlens arrays are discussed in Chapter 3.

The different techniques for acquiring data cubes are summarised in Figure 1-4.

## 1.4 Conclusions and format of the thesis

This thesis is about the techniques developed for building an integral field spectrograph. The design is based around the use of optical fibres as versatile spatial reformatters that allow easy segmentation of the focal plane of a telescopes into a fibre slit suitable for feeding into a spectrograph.

Chapter 2 covers the physical properties of optical fibres relevant to their astronomical use and efficiency. Test apparatus is explained and the results of tests on various fibres are presented.

Chapter 3 deals with the design aspects of fibres coupled to lens arrays and the relative merits of macro lens arrays and microlens arrays are compared. It is found that macro lens arrays in combination with a dedicated fibre-fed spectrograph makes for the best design.

Chapter 4 details the construction of the prototype fibre feed ‘SPIRAL Phase A’ using macrolenses and a fibre feed with a dedicated spectrograph. The techniques and methods used in constructing the lens array and fibre feed are discussed, along with tests that investigate their success and merit.

Chapter 5 presents the construction of two fibre feeds for the Cambridge OH Suppression Instrument (COHSI). The techniques learnt in Chapter 4 are built on and improved, leading to a

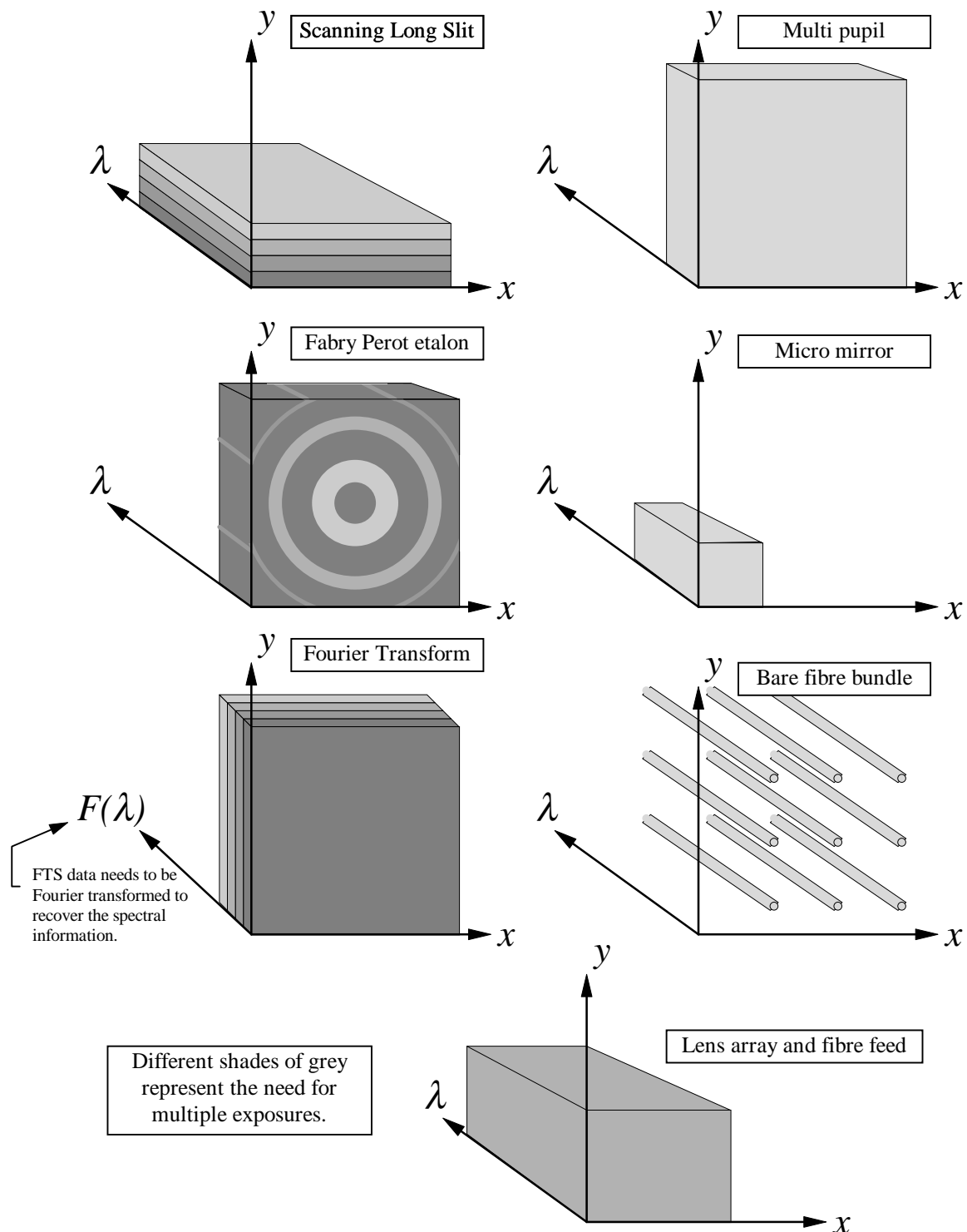


**Figure 1-4** Summary of imaging spectroscopy techniques

successful assembly of four hundred fibre ends into different configurations. Tests performed on the COHSI fibre feeds show that the techniques developed with SPIRAL are successful and produce results within the stated error budgets.

Chapter 6 covers the different aspects of data reduction and processing needed to extract IFS information from the raw data frames, dealing with two different extremes of IFS data in the form of well separated fibre spectra and the other with overlapping spectra. Simulations of cross talk indicate potential problems for future IFS devices that rely on optimal fibre extraction, and the data reduction methods are detailed.

Chapter 7 records the performance of the SPIRAL lens array and fibre feed, showing the efficiency of the system. Science taken with SPIRAL 'A' is also presented, along with an evaluation of a novel single object spectrographic mode (the pupil imaging mode) which was being tested.

Chapter 8 presents a design study for SPIRAL Phase B, a large lens array and fibre feed, showing the adaptability of the macrolens array with focal reducer. A simple exchange of fore-optics allows SPIRAL 'B' to be transferred to other telescopes, demonstrating the versatility of the chosen focal enlarger system.

Chapter 9 gives the conclusions of this thesis, the current status of other IFS projects and the future prospects for integral field spectroscopy in astronomy.

# 2. Properties of optical fibres

---

## 2.1 Introduction

In this chapter the relevant properties of optical fibres in relation to their astronomical use are presented. The physical composition of an optical fibre (§2.2) leads to an understanding of its optical properties (§2.3) along with some defining parameters for the fibre, such as the presence of focal ratio degradation (§2.3.2) and internal transmission (§2.3.3). These turn out to be important considerations for the optical design of spectrographs involving optical fibres (see Chapter 3).

The methods used for polishing the fibres (§2.4) also determine the efficiency of the fibres, and optical methods for examining the surface of the fibre and determining the focal ratio degradation are shown (§2.5). Results of the optical tests on different makes of fibres are then presented (§2.6).

## 2.2 Physical properties of optical fibres

### 2.2.1 Physical composition of a fibre

The property of total internal reflection has been known and demonstrated in water fountains (Tyndall 1854) but the practical form of using thin glass strands with an outer transparent layer was suggested much later (Heel 1954). A fibre consisting solely of a single light transmitting core (see Figure 2-1) is prone to severe attenuation and scattering, as any imperfection (dirt, scratches, moisture,

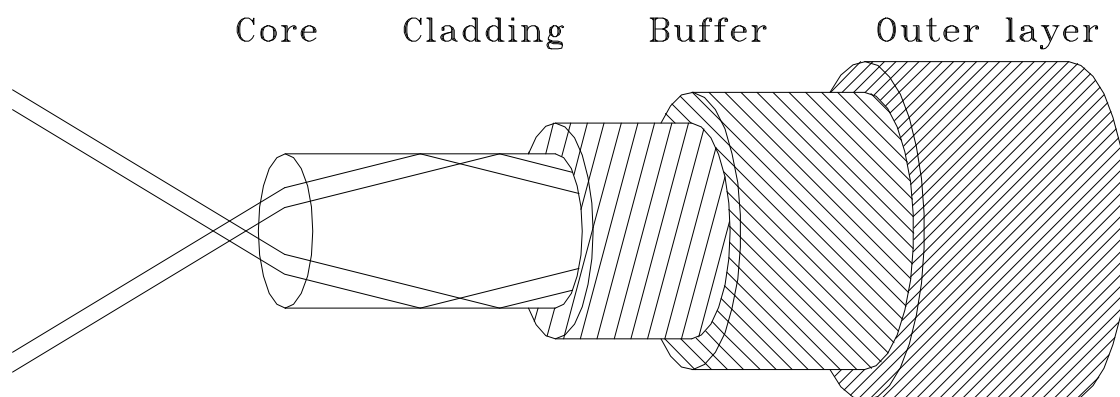


**Figure 2-1** Structure of a step-index optical fibre. The light transmitting core is surrounded by a lower refractive index cladding. A buffer and outer layer provide environmental protection.

contact with other fibres, etc.) on its outer surface causes loss of total internal reflection and light consequently passes out of the fibre. The addition of an extra layer of lower refractive index material (called 'cladding') around the core of the fibre keeps the core boundary free from imperfections. For the fibres best suited for astronomy a 'buffer' is added (usually polyamide) during the fibre drawing process for extra protection of the cladding and a final outer jacket of soft polythene keeps the fibre free from damage during handling. This type of fibre is called a **step-index** fibre, the name referring to the sharp radial change in refractive index between the core and cladding.

The other type of fibre in common commercial use is the **GRaded INdex** (GRIN) fibre. Instead of using two separate optical components to form an internal reflecting surface, the GRIN fibre consists of a single core with an impurity diffused into it. The introduction of impurity into the core increases the effective refractive index of the glass, and this diffusion process creates a gradual reduction of refractive index with distance from the fibre-axis. Instead of total internal reflection, the propagating light paths in the fibre describe sine-like waves. As a consequence of this, GRIN fibres have optical properties that make them unsuitable for astronomical use - most notably, GRIN fibres have large amounts of focal ratio degradation and poor radial scrambling (see §2.3).

### 2.2.2 The propagation of light through a step-index fibre

Optical fibres are waveguides for electromagnetic radiation at optical frequencies and can be fully described by electromagnetic wave propagation theory. However, their properties can be approximated and considerably simplified with geometrical optic theory when the core diameter of the fibre is much larger than the wavelength of incident light.

A straight fibre with a core refractive index  $n_1$  is clad with a medium of refractive index  $n_2$ , where  $n_1 > n_2$  (see Figure 2-2). A ray of light passes through the fibre axis from a medium of refractive index  $n_0$  onto the perpendicular face end at an angle  $\alpha_c$ . The ray is refracted at the face end and will be

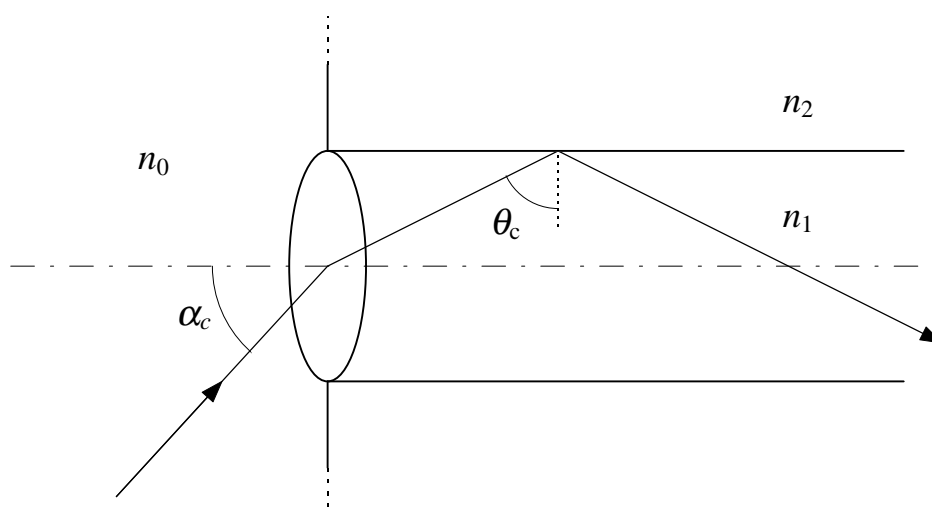


**Figure 2-2** Ray of light entering a fibre. A ray entering at the largest possible angle of acceptance into the fibre,  $\alpha_c$ .

totally reflected at the fibre wall if its angle of incidence is greater than the critical angle  $\theta_c$ . By geometry and application of Snell's law, the critical exterior angle  $\alpha_c$  can be written as:

$$N.A. = n_0 \cdot \sin \alpha_c = \sqrt{n_1^2 - n_2^2} \quad (2-1)$$

N.A. is known as the **numerical aperture** of the fibre and is a measure of the largest acceptable cone of light which the fibre will accept. For real fibres there is not a sharp cut-off angle due to the limits of geometrical theory, so the working N.A. is usually defined as the angle at which the light input or output falls to 50% of its maximum (radial) value.

The fastest input focal ratio is then given by:

$$f \approx \frac{1}{2 \times N.A.} \quad (2-2)$$

However, the effects of diffraction and surface irregularities tend to reduce the effective N.A. for a given fibre. A comparison of N.A. with focal ratio and half angle is given in Table 2-1.

N.A.	f/number	Acceptance cone half angle $\alpha_c$
0.10	5.00	5.7°
0.20	2.45	11.5°
0.30	1.58	17.5°
0.40	1.14	23.4°
0.50	0.87	30.0°

**Table 2-1** Conversion table for focal ratios.

## 2.3 Optical properties of step-index fibres

### 2.3.1 Radial image and azimuthal scrambling

Ideally, a ray transmitted by the fibre in the same azimuthal plane as the axis of the fibre (a meridional ray) will remain in the same azimuthal plane throughout its passage, emerging at the same angle  $\alpha$  from the fibre as it entered (see Figure 2-3). However, in reality a small but finite diameter bundle of rays entering at an angle  $\alpha$  will gradually disperse in azimuth as the bundle is multiply reflected by the curved surface of the core/cladding boundary. When combined with the large number of internal reflections a typical beam makes in a fibre this means that the beam emerges as a hollow cone with half-angle  $\alpha$ , seen projected in the far field of the fibre as a ring of light. This is azimuthal scrambling.

This effect leads to radial image scrambling in the near field of the fibre. For long pieces of fibre (>10cm) the input image on the fibre forms a radially scrambled image at the output. When this image is dispersed in a spectrograph the resultant point spread function is symmetrical (see Figure 2-4). This

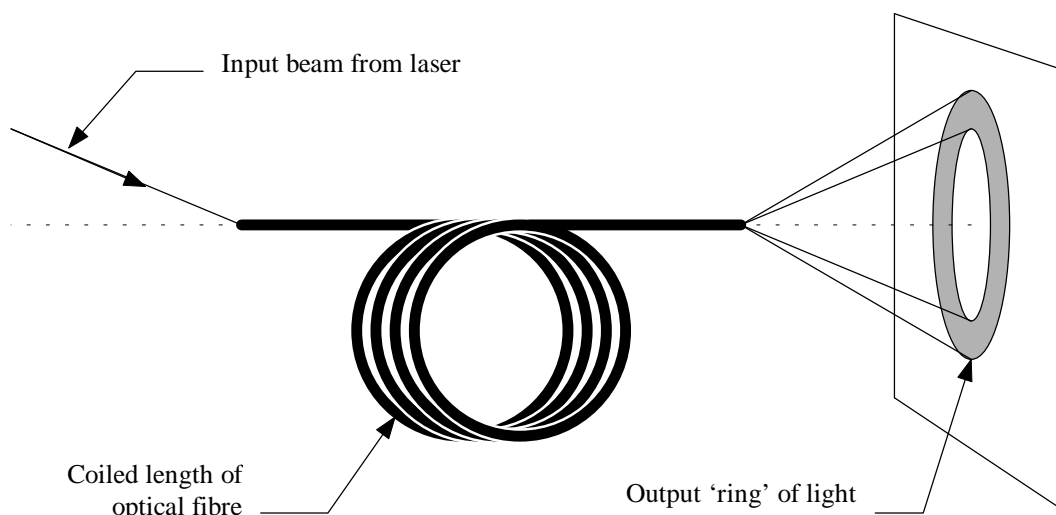


**Figure 2-3** *Azimuthal scrambling.* An input beam will undergo azimuthal dispersion and to a lesser extent radial dispersion. This radial dispersion is due to FRD.

makes them excellent image scramblers, suitable for high resolution stellar velocity science where seeing effects and uneven input illumination in slit-based spectrographs can lead to systematic errors.

The both types of scrambling can be understood in terms of how many reflections a typical ray makes. If  $f$  is the input f-ratio in air,  $d$  is the diameter of the fibre and  $L$  is the length of the fibre, a ray will undergo  $k$  reflections in traversing a straight fibre, (Heacox 1983) where:

$$k \approx \frac{L}{2.9 \times d \cdot n_1 \cdot f} \quad (2-3)$$

An expression for the fraction of rays that undergo less than one rotation about the optical axis of the fibre (and to a rough approximation do not undergo radial scrambling) is:

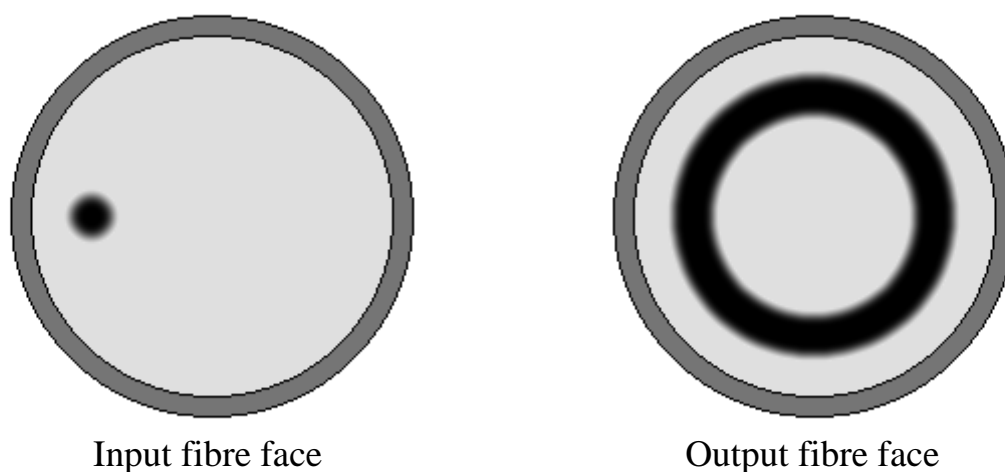


**Figure 2-4** *Radial image scrambling.* The left hand diagram shows an off-axis spot of light on the input face of the fibre. For a long piece of fibre the output face (shown on the right) shows that the light is radially scrambled with respect to the optical axis of the fibre.

$$\left( \frac{d \cdot n_1 \cdot f}{2L} \right)^2 \quad (2-4)$$

which for the shortest fibre feed in COHSI means that less than one in  $10^6$  rays pass through the fibre unscrambled.

### 2.3.2 Focal Ratio Degradation

Focal ratio degradation (FRD) is caused by imperfections on the core/cladding boundary that deviate the shape of the fibre from that of a perfect cylindrical waveguide, causing light to be scattered into a larger N.A. (see Figure 2-5). These imperfections (called microbends) can be caused by a badly fitting cladding, inhomogeneities in the core material and changes in core diameter due to the fibre drawing process. Typical microbend defect sizes are on the order of  $1\mu\text{m}$  and in the case of fused silica fibres, they can also be caused by stress on the fibre core from the surrounding cladding and jacket.

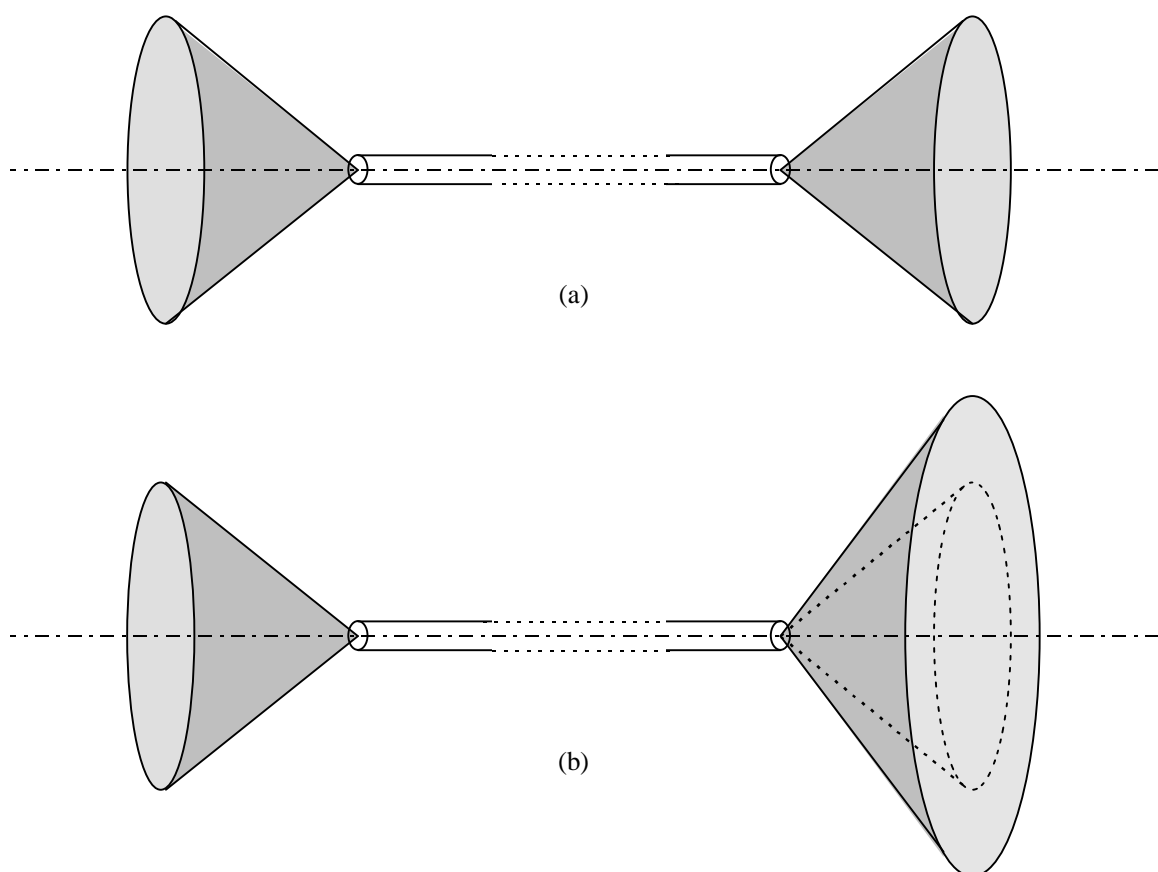


**Figure 2-5** *Focal Ratio Degradation.* In (a) an ideal fibre with no FRD preserves the input focal ratio at its output. In (b) the effect of FRD causes the output beam to fill a wider cone than its associated input beam.

Other losses can be induced by macrobending, where the fibre is bent into curves with radii of 5cm or less (Clayton 1989). The jacket exerts extra stress on the core and in extreme cases the macrobending can cause the N.A. of the fibre to be exceeded, and light to be lost.

FRD always causes a loss in efficiency in an astronomical instrument, as can be seen from Figure 2-6. Here the throughput of a fibre is compared with the throughput of a circular aperture with the same diameter as the fibre core. For a given input f-ratio the graph shows what output f-ratio is needed to collect all the emerging light. The circular aperture obeys geometric optics with the output f-ratio equal to the input f-ratio, but this is not the case for the fibre with FRD. For fast (low numerical value) input beams the output f-ratio is closely matched at first. Beyond  $f/5$  however the f-ratios quickly differ, with slower output beams being produced by the fibre, as in Figure 2-5.

The optimal design for slit based spectrographs is when the focal ratio of the collimator optics match the focal ratio of the telescope. These designs are typically matched to the Cassegrain focus where the f-ratio is typically  $f/8 - f/15$ . Building an optical fibre feed for such a spectrograph then results in light-loss due to FRD and a decrease in the spectrograph's efficiency which cannot be avoided. By designing the spectrograph to accommodate the FRD this loss can be avoided and this method is discussed in Chapter 3.

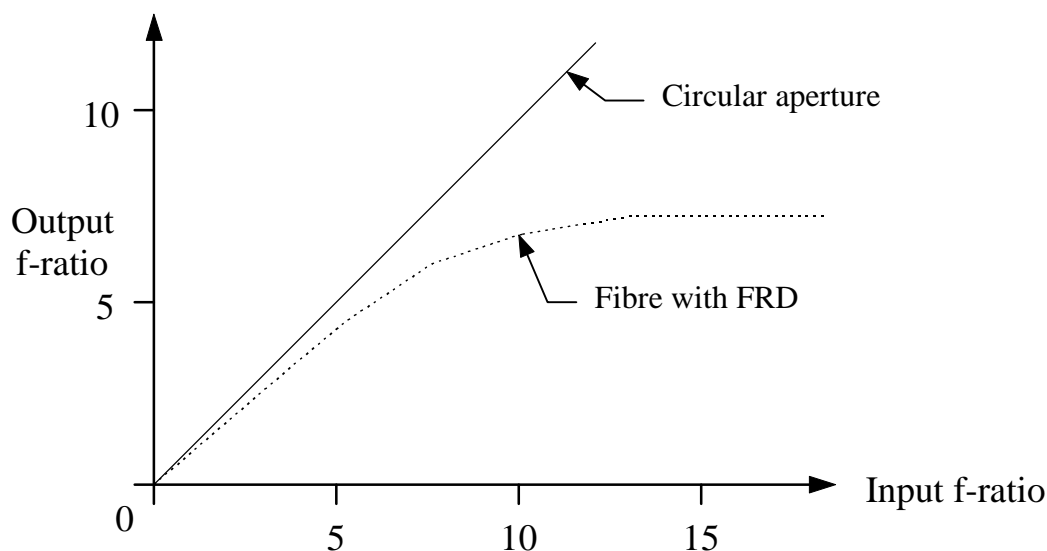


**Figure 2-6** Schematic graph comparing a circular aperture to a fibre with FRD.

### 2.3.3 Internal transmission of fibres

Attenuation in optical fibres is due to absorption within the core material, scattering from defects and imperfect reflections from the core/cladding boundary. The transmission for a given wavelength  $\lambda$  is characterised by an **attenuation coefficient**  $\beta$  measured in decibels per kilometre (dB/km) - the unusual unit comes from the use of fibre optics in telecommunications. The flux a distance  $x$  along the fibre is:

$$T_x = T_0 \cdot 10^{-\frac{\beta \cdot x}{10}} \quad (2-5)$$

where  $T_0$  is the flux at  $x = 0$  and  $T_x$  is the flux at distance  $x$  in kilometres. The attenuation can be also expressed as:

$$T_x = T_0 \cdot e^{-Bx}$$

where  $x$  is in metres, and the conversion from  $B$  to  $\beta$  is:

$$B = \frac{\beta}{10000} \cdot \ln 10 \cong 2.3 \times 10^{-4} \cdot \beta$$

The attenuation coefficient is also a function of wavelength (Figure 2-7). These wavelength

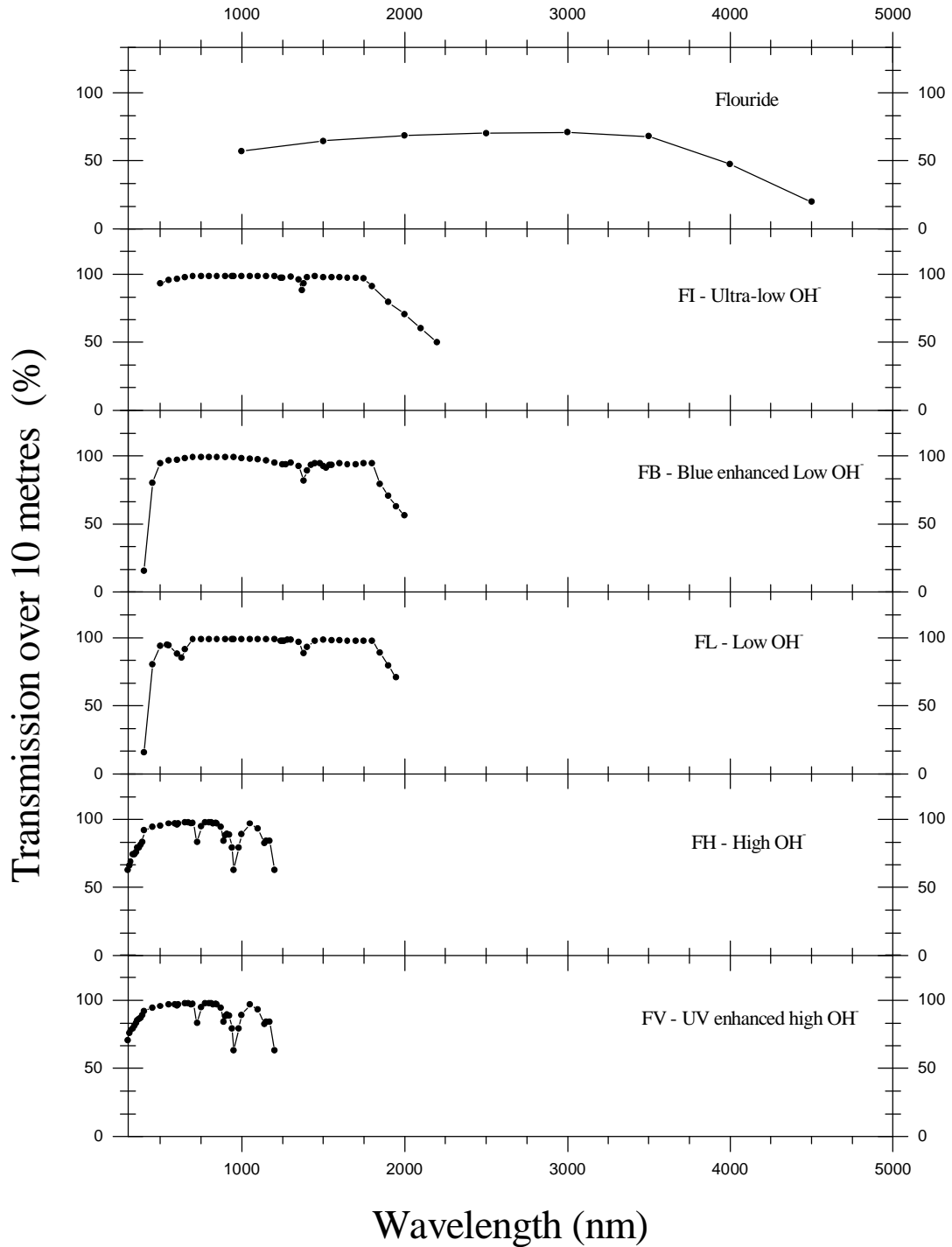


**Figure 2-7** Data taken from measurements of different types of step-index fibre. The titles on the right are the trade names for the fibre from CeramOptec.

dependent losses are predominantly in the form of intrinsic absorption (leading to the short wavelength cut-off in the ultraviolet) and impurity absorption (seen as the absorption dips in Figure 2-7). Intrinsic absorption is due to charge transfer bands at ultraviolet photon energies and multiphonon bands in the near infra-red energy range.

Impurity absorption bands are in the form of transition metal ions in the blue/UV bands and 2.73 $\mu\text{m}$  hydroxyl ion bands with overtones appearing at 1.37, 0.95 and 0.72 $\mu\text{m}$ .

## 2.4 Polishing the fibres

It is very important to have high quality end faces for the optical fibres, since that is where light enters and exits the fibre. Any scratches, chips or imperfections in these two surfaces cause light to be scattered out of the optical beam, resulting in loss of efficiency. The best way to produce a consistent, high quality surface finish is by polishing the fibres. The optical fibres used in COHSI and SPIRAL are listed in Table 2-2.

Instrument	Made by	Core diameter ( $\mu\text{m}$ )	Cladding diameter ( $\mu\text{m}$ )	Buffer diameter ( $\mu\text{m}$ )	Outer layer
SPIRAL phase A	Polymicro	50	70	90	110
COHSI IFS mode IFU - suppressor	CeramOptec Optran WF	110	135	155	240
COHSI IFS mode Suppressor - spectrograph	CeramOptec Optran WF	200	244	262	360
COHSI MOS mode MOS plate - suppressor	CeramOptec Optran WF	150	180	200	300
COHSI MOS mode Suppressor - spectrograph	CeramOptec Optran WF	250	275	295	400

**Table 2-2** Optical fibres used in COHSI and SPIRAL.

Polishing is the process of abrading the fibre with a suspension of small, evenly sized hard particles known as a polishing paste. The paste is applied between the fibre and a moving flat metal surface (known as a polishing plate), resulting in a evenly ground finish to the fibre end. Each paste is specified by the size of particles it contains, and by using successively finer polishing pastes the desired surface finish can be produced.

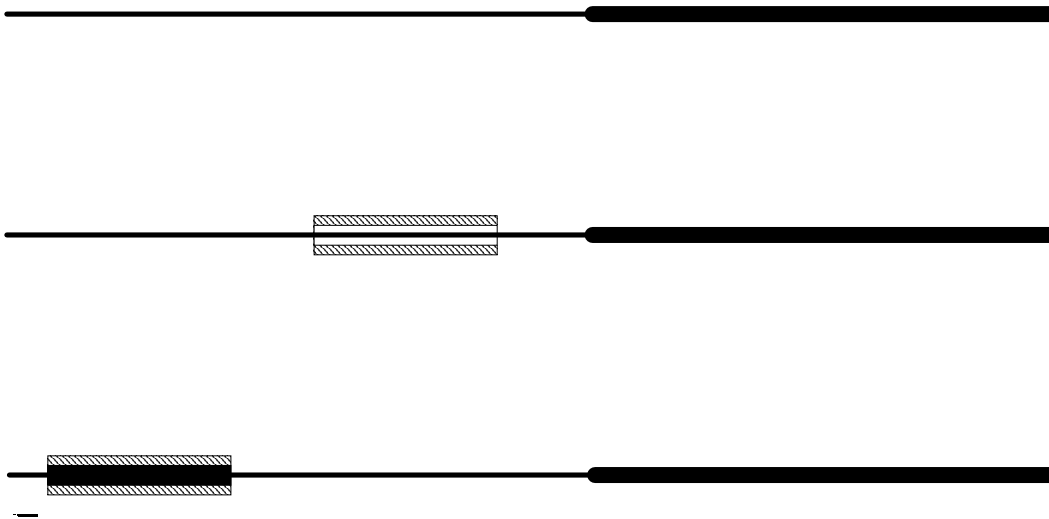
### 2.4.1 Mounting single fibres for polishing

Optical fibre has tremendous tensile strength, but any bending or shearing forces will cause it to break. Fibre can be wrapped around the surface of a smooth cylinder, but if the cylinder has a small enough diameter the fibre will break. The radius of this cylinder then defines the 'minimum bend radius' of the fibre. To prevent any such bend occurring the fibre needs a tough outer supporting jacket.

Polishing also requires the fibre to be held rigidly so that it can be polished down to an optically flat surface. To make the fibre mechanically stronger a hollow stainless steel tube is fixed over the fibre buffer with epoxy. This supports the end of the fibre in a rigid steel tube and makes the fibre suitable for easy handling - these thin steel tubes are made from the same process as hypodermic needles and are called 'ferrules'. This ferrule is then mounted in a polishing jig and the fibre/ferrule combination are both polished together to form a single flat surface. The method for fixing ferrules onto a fibre is now presented.

**Attaching a single ferrule to a fibre.**

First, the outer layer of acrylic is stripped off after soaking the fibre end in acetone.



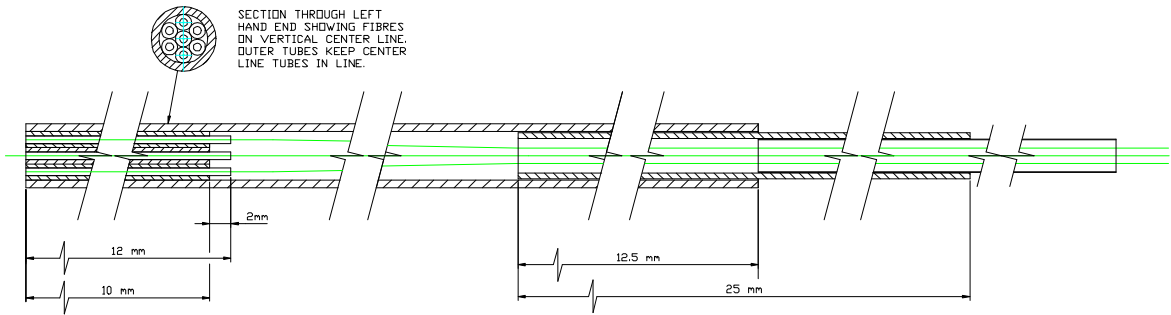
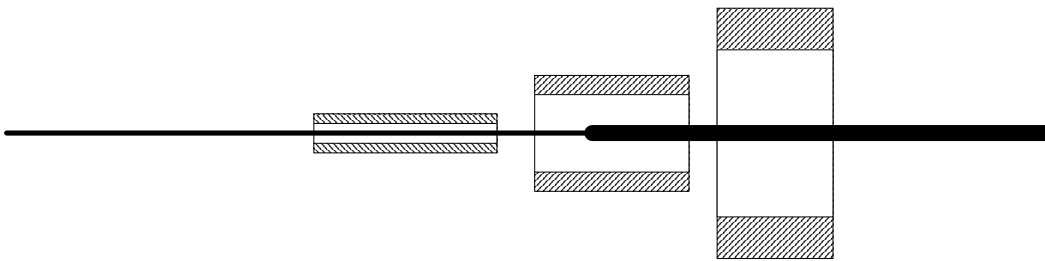


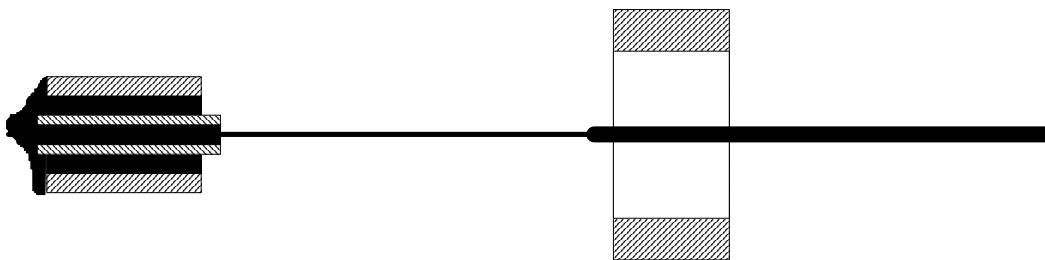
**Figure 2-8** Diagram showing arrangement of ferrules for the SPIRAL lens array.

**Attaching many ferrules to a fibre**

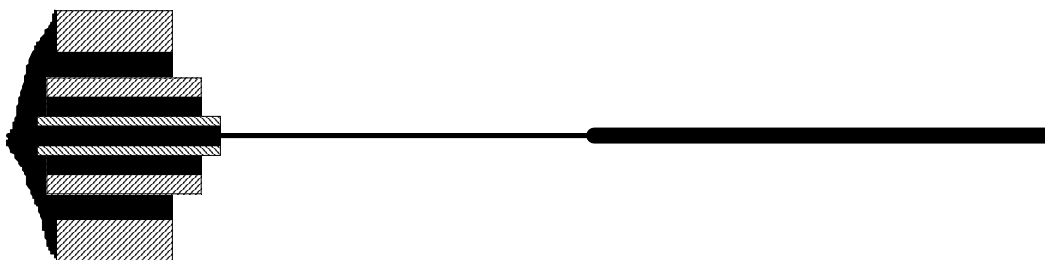
The three ferrules are threaded onto the fibre. Note that the length of the ferrules has been shortened for clarity.



The first ferrule is put into place and fixed with epoxy. Another layer of epoxy is put onto the outer surface of the first ferrule and the second ferrule is pulled over into place. It is always useful to let the inner ferrule protrude slightly out from the larger ferrule.



The last ferrule is put in place. The assembled fibre and ferrule can be left on a sheet of paper and excess epoxy scraped off with a scalpel when cured.



Ferrules such as these are then fixed rigidly in a metal polishing block that has pre-drilled holes for the ferrules (see Figure 2-9). The polishing block is heated up by sitting on top of a hot plate. Two small brass risers make thermal contact between the block and hot plate whilst providing a small gap for the fibre ferrules to protrude from the front surface of the metal block. To hold the ferrules in place a heat resetting adhesive (called ‘General purpose hot melt’ in the RS Supplies catalogue) is used.

Heat resetting adhesive is solid at room temperature but turns into a viscous fluid when heated to 70 degrees Centigrade. Upon cooling the glue reverts to a solid with a strong mechanical bond. The adhesive can be put through many thermal cycles with no degradation of its resetting properties. When the metal block is hot, the adhesive is added into the holes drilled through the block. Ferrules are then pushed into the holes and through to the front surface of the metal block. After all ferrules are put in, the hot plate is allowed to cool and the adhesive then holds the ferrules firmly in place. The polishing block and fibres are then polished together as a single unit. After polishing the re-heating of the block releases the ferrules and excess adhesive is then cleaned off by using a soft cotton cloth soaked with acetone.

This technique is used for when many optical fibres need to be positioned individually onto an optical surface. This is the case for the SPIRAL and COHSI lens arrays.

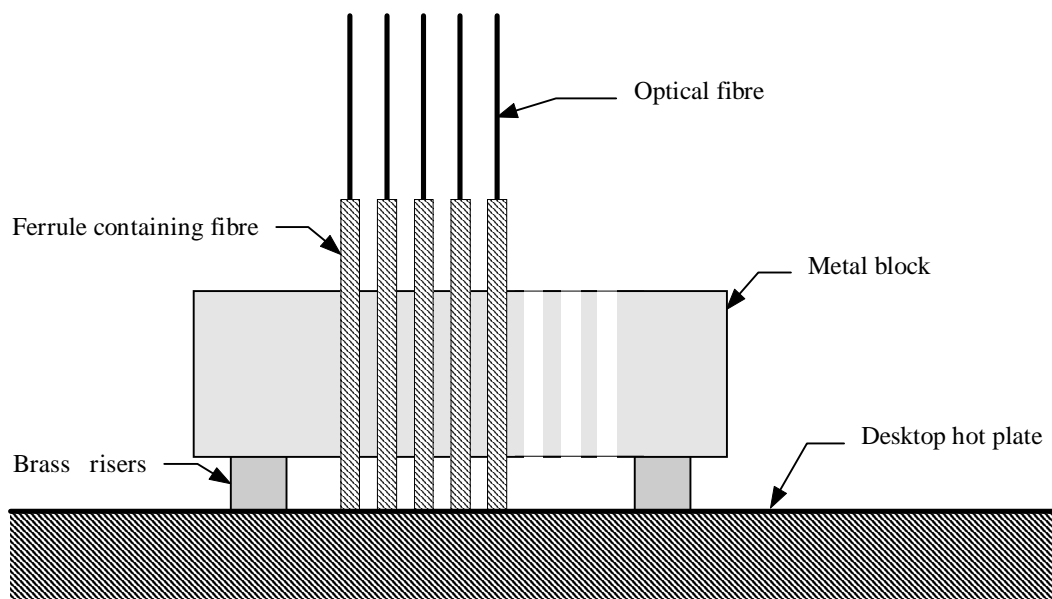


**Figure 2-9.** Putting ferrules into the metal polishing block. The brass blocks allow the ends of the ferrules to stand proud of the polishing block’s surface. If any fibres are recessed in their ferrules, they can then be carefully filed back to the metal block revealing the fibres ready for polishing.

#### 2.4.2 Mounting many fibres into fibre slits for polishing

An alternative method for mounting fibres is to fix them into a metal block such that they are in their final optical configuration after polishing. This considerably reduces the construction time of the fibre feed as the fibres do not need to be subsequently separated, cleaned and repositioned. This process

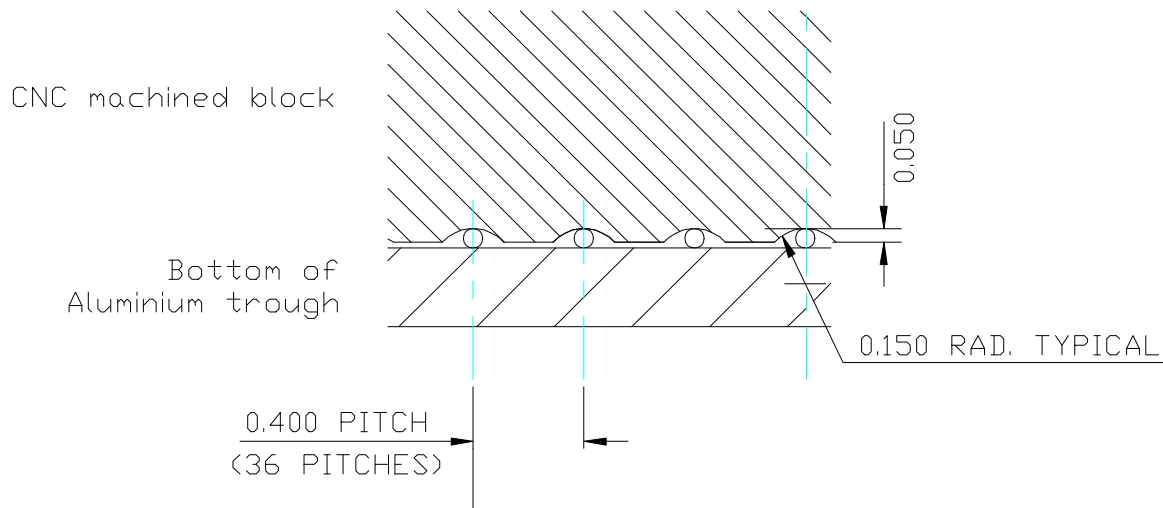


**Figure 2-10** Detail of the *SPIRAL* fibre slit. Spark eroded grooves are cut into an aluminium block and fibres are held in place against a flat aluminium surface. Epoxy is then run into the inter-fibre spaces.

is used in the manufacture of fibre slits, where the polishing block becomes part of the final fibre feed. The *SPIRAL* fibre slit and three *COHSI* fibre slits all use this technique of assembly (see §4.5.3 and §5.4 respectively). An enlarged section of the *SPIRAL* fibre slit is shown in Figure 2-10, where a CNC machined block holds the object fibres against the bottom of the fibre slit trough (see also Figure 4-20).

The surface area of the fibres in their block is of the order of a few square centimetres concentrated into a rectangular or circular shape. Polishing this is impossible without a wide and stable base for the optical surface to sit on the polishing plate, so the block is mounted into a polishing jig (Figure 2-11). Metal files are used to level the fibre ferrules down to within a millimetre of the metal polishing block, and then the block is mounted into the polishing jig. Emery paper is used for the last half millimetre of ferrule protruding above the block.

#### 2.4.3 First time use: Conditioning the polishing jig and polishing plate

The first time the polishing jig was used, the milled surface was found to be too rough to polish with. A small amount of water with carborundum powder formed a coarse abrading paste that is used to ‘condition’ the jig. The polishing jig was then placed on the polishing plate and manually moved for the first ten minutes - during this time metal swarf fell off the milled edges of the jig onto the polishing plate, causing scratches on the ring and plate surface. When this occurred, the plate and jig were washed off with water and the conditioning process resumed.

Over half an hour the sound of polishing becomes smoother and examination of the feet of the polishing jig showed fine grey patches where they were being conditioned. Although the finish looked dull, examination under a microscope revealed a much smoother finish compared to the milled areas. Only when all of the feet were this gun-metal grey colour were the fibres mounted in the polishing jig.

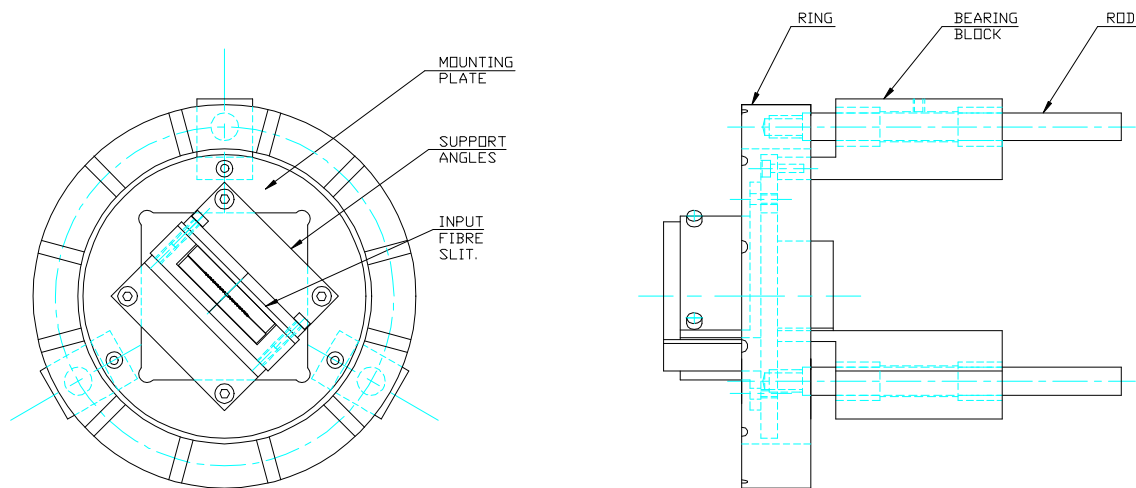


**Figure 2-11** *The polishing jig.* The mounting plate holds the fibre slit securely onto the bearing blocks, which can raise or lower the input fibre slit with respect to the ring. It is the ring which provides the stable support on the polishing plate for the slit.

#### 2.4.4 The polishing itself

Before every polishing attempt, water was used to thoroughly wash and clean all surfaces that would be in contact with the polishing plate. Cotton buds were used to reach into any bolt holes or crevices that were not readily reached by the first water wash. After wiping down all surfaces excess water was removed with disposable paper towels. The reason for the cleanliness is that the polishing technique relies on abrading the active surfaces with successively finer pastes. Any particles larger than those in the current polishing paste are regarded as ‘contamination’, causing scratching across the active surfaces and destroying the polishing achieved. The only course is to return to the rougher paste and begin polishing again to remove the scratches incurred.

It is hard to underestimate the care needed as the pastes contain micron sized particles of silicon oxide or diamond and the slightest contamination from a more coarse paste or from metal swarf from the polishing surface produces prominent scratches in seconds.

Each polishing grade proceeded as follows:

The jig and plate were washed down, taking care to clean off all paste from the polishing machine. For rough grinding and smooth grinding (see Table 2-3) the paste was supplied in dry powder form and had to be mixed with water first. A clean 100ml beaker had two tablespoons of powder added and then water was added up to the 80ml mark. A spatula was then used to stir the powder into a suspension, the consistency of which could be varied by either adding more powder or more water.

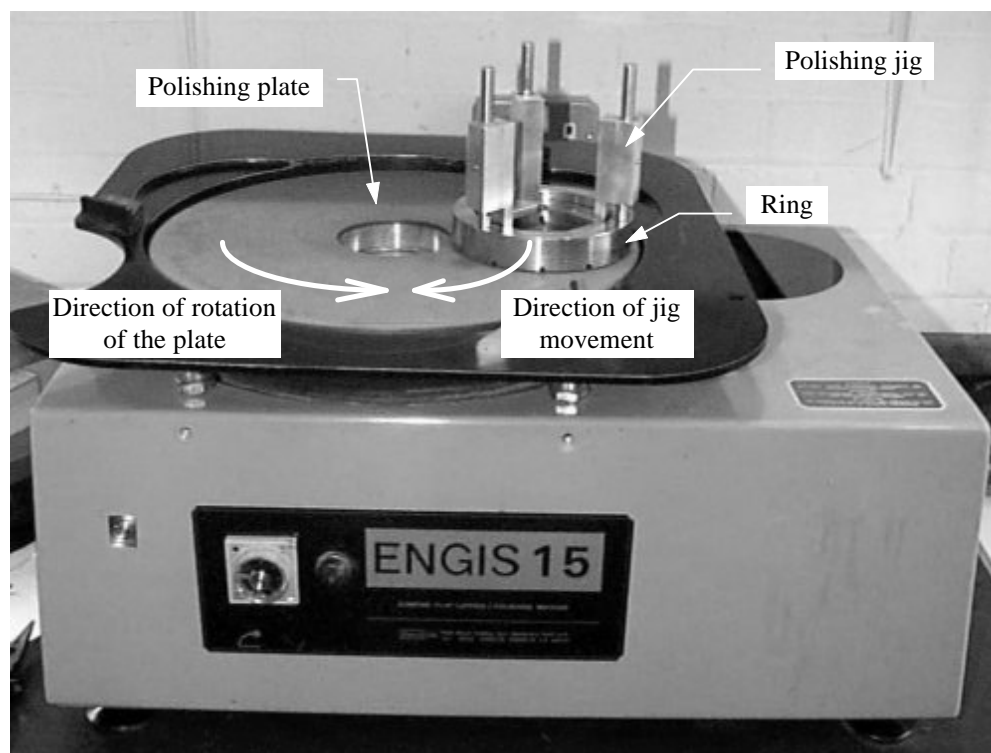
The paste was then poured onto the plate and distributed evenly by placing the jig on the paste and pushing the paste over all areas of the plate with the leading edge of the jig. When the plate was

covered, slow manual polishing was carried out for three or four revolutions, making sure that the movement of the jig over the surface of the plate produced an even ‘hissing’ sound. The electric motor underneath the polishing plate was then switched on and the jig moved in a circular motion on the plate, moving against the rotation of the plate (Figure 2-12).

Care was taken with the moving plate as it rotated over two revolutions per second. The jig sits

Process	Material used	Disk used	Time (minutes)
Emery papering	600P, 300P wet/dry glass paper	-----	variable
Rough grinding	F600 Carborundum powder - Kemet 2320 (as alternative)	Metal Pb/Sn plate	10-20
Smooth grinding	12 $\mu$ m Aluminium Oxide - Kemet 2900 (as alternative)	Metal Pb/Sn plate	10
Rough polish	6 $\mu$ m Diamond solution - 6(Type K) STD Kemet, Hyprez	Silk cloth	10
Smooth polish	3 $\mu$ m Diamond solution - 3(Type K) STD Kemet, Hyprez	Silk cloth	10
Finishing off	1 $\mu$ m Diamond solution - 1(Type K) STD Kemet, Hyprez	Silk cloth	5

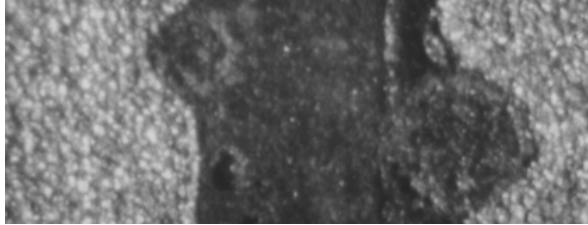
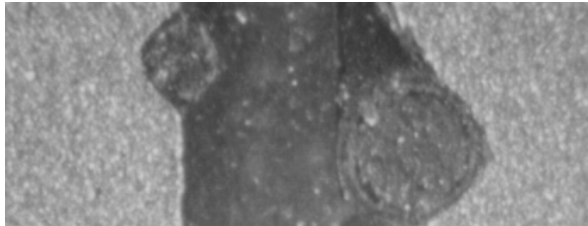
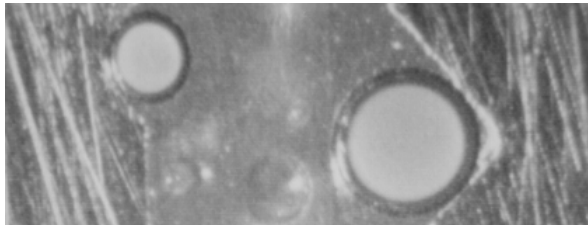
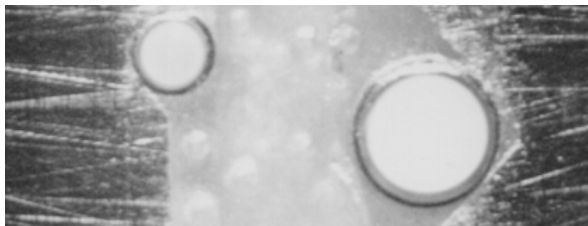
**Table 2-3** Polishing pastes used for the optical fibres.



**Figure 2-12** The polishing jig sitting on top of the polishing plate.

on a thin film of water/paste and any metal swarf or excess pressure down on the plate would cause the jig to suddenly 'stick' to the plate and subsequently cause deep scratches. This was avoided by not pressing down too hard on the plate with the jig and by making sure that the paste did not become too 'dry' or 'wet'. The paste typically dried out over a period of minutes, signalled by the grinding sound increasing in volume and the jig becoming harder to move smoothly over the plate.

Examining the fibres underneath a T.V. microscope (see Figure 2-13) gave the best indication as to when the current stage of grinding/polishing was completed. This was signalled by an even, finely grained texture appearing over all the fibres and metalwork (see Table 2-4). It is important to note that although the metal finish appeared to vary in quality, the fibres surfaces themselves showed successively better finishes as finer pastes were used.

The COHSI curved fibre slit during polishing	Comments
	<p><i>Rough (carborundum) grinding.</i> An input fibre and output fibre in the curved double slit after being abraded with the carborundum grit. Note how irregular the fibre surfaces are.</p>
	<p><i>Smooth (12µm) grinding.</i> The surrounding metal now looks dull grey, but the fibre surfaces still look very irregular.</p>
	<p><i>Rough (6µm) polishing.</i> The metal now begins to get a mirror finish and the fibres begin to look smooth. Light can be seen coming out of the fibres as the contrast in the image decreases.</p>
	<p><i>Smooth (3µm) polishing.</i> The scratches that appear in the 6µm image now disappear and air bubbles in the glue can be seen. A slight rounding of the fibre ends can be seen due to the silk cloth.</p>
	<p><i>Finishing (1µm) polishing.</i> Now the mirror surface of the metal looks black, and only with the brightest illumination can scratches be made out. These fibres show some rounding at the edges - the metal abrades faster than the core fibre material.</p>

**Table 2-4** *Microscope images at the different stages of polishing*

Below 12 $\mu\text{m}$  Aluminium Oxide powder, an oil-based diamond suspension impregnated in a silk cloth was used to polish the fibre surfaces. The cloth was fixed onto an aluminium disk and the diamond/oil paste was absorbed into the cloth. For each diamond paste a separate plate and cloth were used, three cloths and plates in total.

From powder at 12 $\mu\text{m}$  to diamond at 6 $\mu\text{m}$  there was a distinct change in the colour of the metal block from matt grey to a metallic mirror finish. Even though more scratches seemed to appear on the metal block, this was thought to be an illumination effect from the swan-neck lamps, a hypothesis borne out when the improvement in the fibre surface was seen. Polishing with 3 $\mu\text{m}$  diamond paste showed another improvement in the fibres as well as a reduction of scratches on mirrored surface of the metal.

The polishing process is completed using 1 $\mu\text{m}$  diamond suspension.

## 2.5 Optical testing

### 2.5.1 Examining the surfaces of the fibres

The fibre faces needed periodic inspection and so a microscope objective and CCD camera was connected to form a TV microscope (see Figure 2-13). Placed beside the polishing machine, this

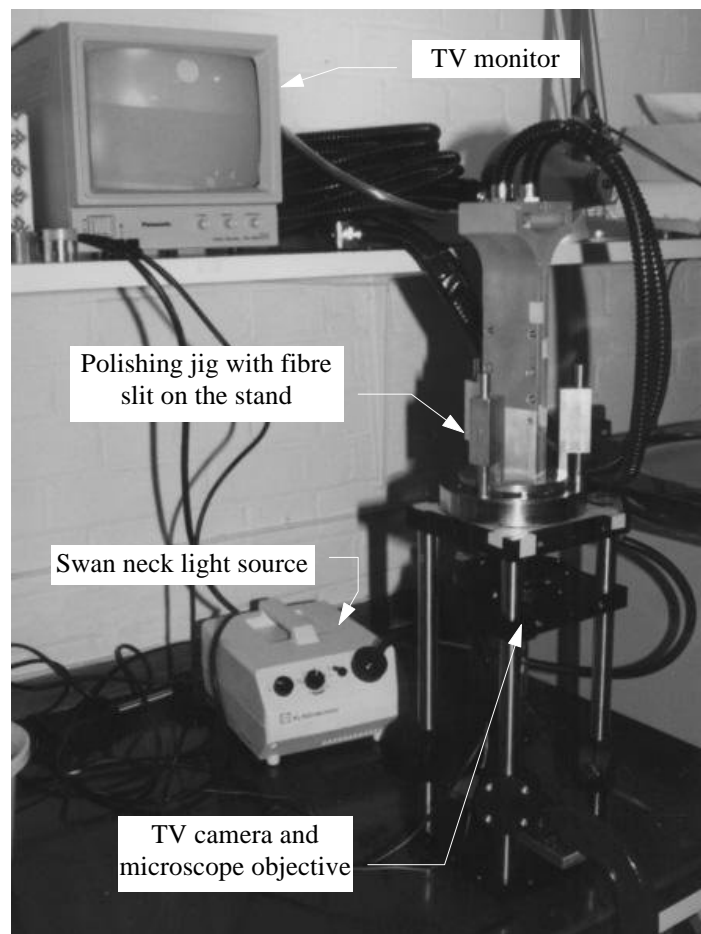


**Figure 2-13** *The microscope and camera used for examining the fibre faces.*

allowed the jig and fibre surface to be examined periodically. Due to the magnification used (approximately  $\times 100$ ) a powerful light source was needed to illuminate the polished surfaces. Two fibre-optic crane-neck halogen lamps were used, one on either side of the microscope objective. The fibre-optic necks allowed two sources of light to be positioned anywhere near the fibre surface.

With the microscope, any chips or scratches in the surface of the fibres was easily visible. Two other checks on the fibres performed were:

- (i) **Checking for micro-pits.** Micro-pits are small pits in the fibre surface about  $2\mu\text{m}$  in size that are thought to be caused by contamination from rougher pastes. The light source was positioned to shine light onto the fibre faces at a large angle of incidence. After the  $3\mu\text{m}$  polishing the fibre face appeared black, except for micro-pits that showed as bright spots of light due to the scattered light from them (see Figure 2-14). By counting these on each fibre and checking after each stage of polishing a check on quality could be made.
- (ii) **General fibre structural integrity.** The light source is taken away and light shone down the far end of the fibres. By slowly increasing the incident angle out towards the N.A. of the fibre, a single spot in the centre of the output end of the fibre appeared and expanded into a ring which moved out towards the edge of the fibre, eventually disappearing at the cladding boundary (see Figure 2-14). Any structural defect in the core a few millimetres below the fibre surface would be readily apparent as an unevenly illuminated ring of light or visible as dark cracks.

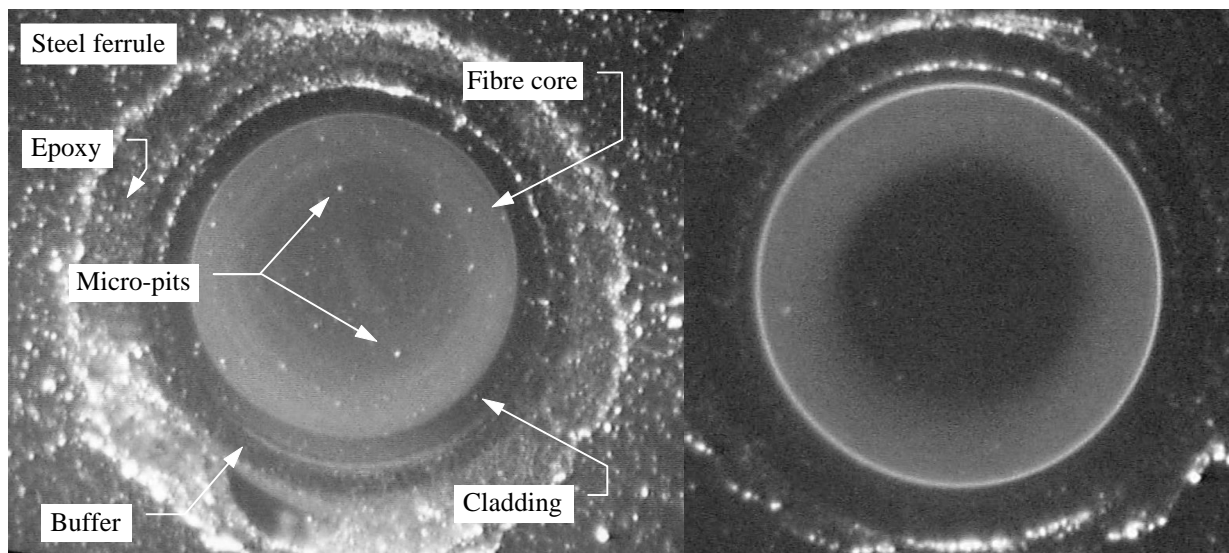


**Figure 2-14** Examining the fibre faces. On the left the fibre face is checked for micro-pits - several can be clearly seen. On the right the back-illuminated fibre shows a clean ring of light across the face of the fibre.

### 2.5.2 Tests for FRD and throughput

With any fibre it is important to characterise the throughput and FRD properties. FRD is strongly dependent on how the fibre is glued in its ferrule and on the type of adhesive used to hold the

fibre in optical position. A test apparatus for FRD and throughput measurements is shown in Figure 2-25.

The general principle for measuring FRD involves putting a beam of known focal ratio into the fibre to under test and then measuring the fraction of light emerging from the fibre for a given focal ratio. A graph of relative transmission versus output focal ratio shows the effect of FRD (see Figure 2-15).

A halogen light bulb illuminates a monochromator and the emerging light then passes down a 50 $\mu\text{m}$  diameter fibre. Two lenses then re-image the 50 $\mu\text{m}$  fibre onto the end of the test fibre, arranged so that the spot of re-imaged light is approximately 20 $\mu\text{m}$  across. An input aperture in front of the lens selects the input focal ratio. A pellicle in the beam from the 50 $\mu\text{m}$  fibre allows a TV camera with a microscope objective to look at the face of the test fibre and help position the spot of light.

The light passes through the test fibre and the focal ratio of the emerging light is fixed by the output aperture stop. A Pentax  $f/1.2$  lens then refocuses the beam onto a light sensitive detector and an electronic amplifier produces a digital output. However the flux from the 50 $\mu\text{m}$  diameter fibre is small. Even with all the lights in the room turned off, a light emitting diode in a power supply on the far side of the room can dominate over the signal from the fibre.

To avoid contamination from ambient light sources in the room the light from the 50 $\mu\text{m}$  fibre is modulated by an optical chopper. A rotating metal disk between the monochromator and the halogen lamp provides the source of modulation. The detector now sees a large D.C. background level due to the

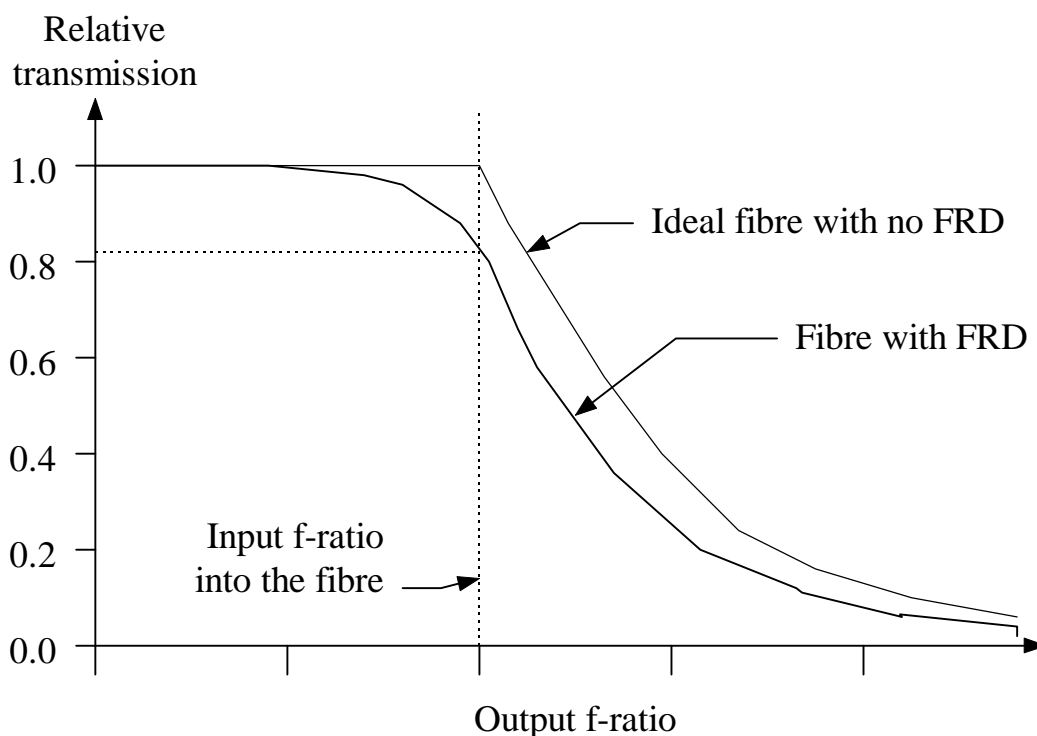


**Figure 2-15** A typical FRD plot. An ideal fibre has 100% transmission until the output aperture closes down to the input f-ratio, whereupon the curve follows a typical inverse-square law. A fibre with FRD always has a curve lying below this ideal curve.

ambient light in the room with a modulated signal from the fibre. A phase-locked amplifier takes the detector signal with the frequency of modulation from the optical chopper, and the level of light from the input fibre is produced. The amplifier is sensitive to modulated signals only, so to prevent any scattered modulated light from reaching the detector by indirect means, the monochromator is placed in a light-proof box. Blocking the 50 $\mu$ m fibre with a piece of card then demonstrates that the lock-in amplifier gives a null signal.

FRD tests are performed with the diameter of the input aperture set to give a particular input focal ratio for the fibre. The signal level is plotted as a function of flux within a particular focal ratio, determined by the diameter of the output aperture. The flux is normalised by opening the output aperture to give the fastest beam possible (and therefore collect all the emergent light from the test fibre).

By replacing the input fibre with the detector a direct comparison can be made between the flux incident on the face of the fibre and the output flux, allowing a direct throughput of the fibre to be calculated for a given wavelength. Different wavelengths are selected with the monochromator and the variation of transmission with wavelength can also be calculated.

For the infra-red fibres, the monochromator is used in 2<sup>nd</sup> order, with a 850nm blocking filter between the monochromator and 50 $\mu$ m fibre. The TV camera is sensitive beyond the red so realignment and refocusing of the spot on the test fibre is possible.

Assuming that the input aperture is evenly illuminated by the 50 $\mu$ m fibre, the input aperture diameter is varied and the resultant signal is noted. To ensure all flux is collected by the output of the fibre, the detector is butted up against the detector window. The 3mm<sup>2</sup> IR detector sits back from the detector window by approximately 5mm, so any output beam larger than  $f/2.0$  does not completely fall within the bounds of the detector, but it is enough for this test. For an evenly illuminated aperture, the flux is inversely proportional to the square of the input focal ratio, so by plotting the reciprocal of the square root of the flux against the input focal ratio, a straight line should be obtained (see Figure 2-16). As can be seen, the apparatus is reliable down to  $f/2.5$ , with departures from uniform illumination for any faster input ratios.

## 2.6 Results of optical tests on the fibres

The first section is composed of tests performed on the COHSI fibres in the fibre feed from the lens array to the curved fibre slit (see Chapter 5). These demonstrate some of the properties of FRD. The results for the SPIRAL and COHSI fibres are then discussed and further investigation of the FRD properties of infra-red fibres then follows.

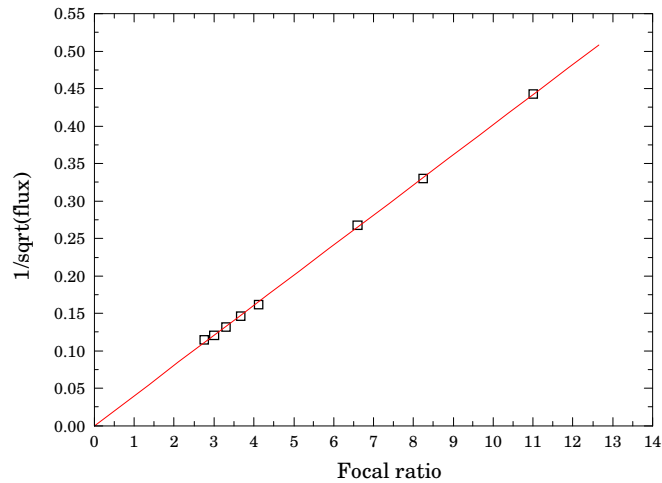


**Figure 2-16** *Testing the fastest input aperture beam.* This graph shows how the measured signal varies as a function of input focal ratio.

**2.6.1 Optical properties of focal ratio degradation**

FRD is independent of wavelength and independent of the position of the input spot on the end of the fibre (Ramsey 1988). This is examined with the COHSI long fibre feed that extends from the telescope to the OH suppressor (see Chapter 5 for details about COHSI). This fibre feed was used to test these two observations - the results are seen in Figure 2-17.

These results confirm the suitability of the test apparatus, and also suggest that the slight difference between the two wavelengths may be due to fibre ends rounded off by the polishing process. This convex rounding of the fibre ends leads to the ends of the fibre acting as a low power lens.

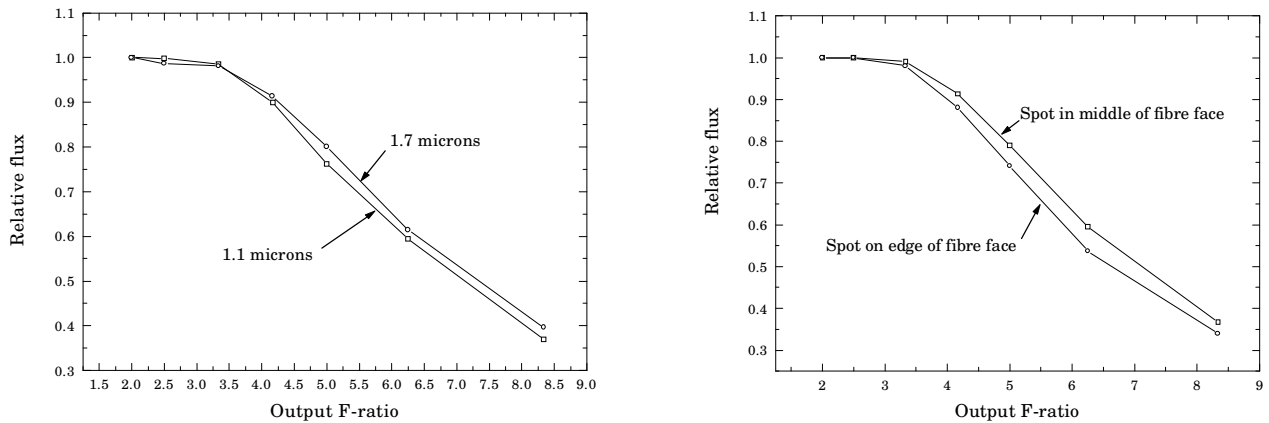


**Figure 2-17** *Varying the wavelength and position of the input spot.* These graphs show that the FRD does not significantly change with wavelength or position of the input spot on the end of the fibre.

**2.6.2 The SPIRAL fibre feed**

The fibre feed was tested after assembly, using a simplified form of the FRD apparatus and a more basic phase locked amplifier. Since the lens array was permanently fixed to the fibres FRD tests could not be performed on the fibres alone. Instead the lens array was illuminated with a collimated

beam using the IFS field lens as seen in Figure 2-18. FRD measurements were made for seven fibres and the results are shown in Figure 2-19. Although the graph implies a very good geometric throughput of  $(89\pm 5)\%$  for an  $f/5.0$  input beam to  $f/4.8$ , there is now some doubt as to whether the actual value is this high. The lock-in amplifier used for this test was found to have a fault which was only discovered a year after the measurements were made. Unfortunately the fibre feed was unavailable for further testing, and so the conclusion is that the throughput is more realistically around the 80% transmission level.

The conclusion is that the SPIRAL fibres have a geometric throughput of  $(80\pm 5)\%$  for an  $f/5.0$  input beam into an  $f/4.8$  output aperture, which constitutes an acceptable loss for the SPIRAL system.

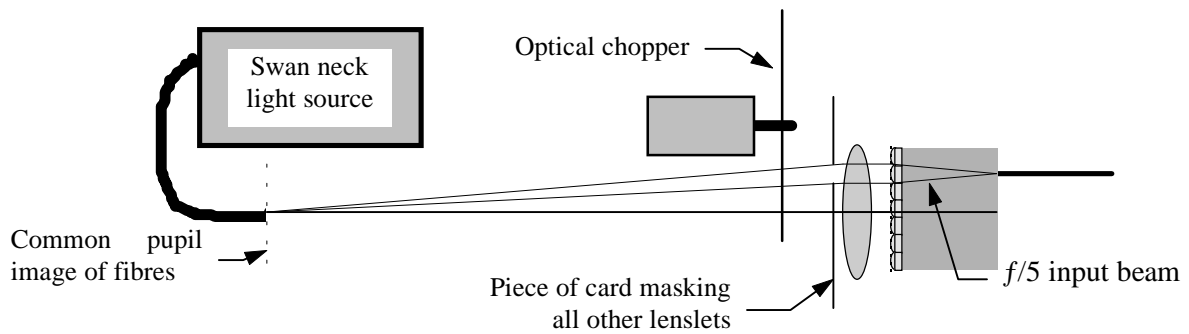


**Figure 2-18** Layout of the SPIRAL FRD test apparatus. The light is fed into the fibre by illumination from the common fibre pupil.

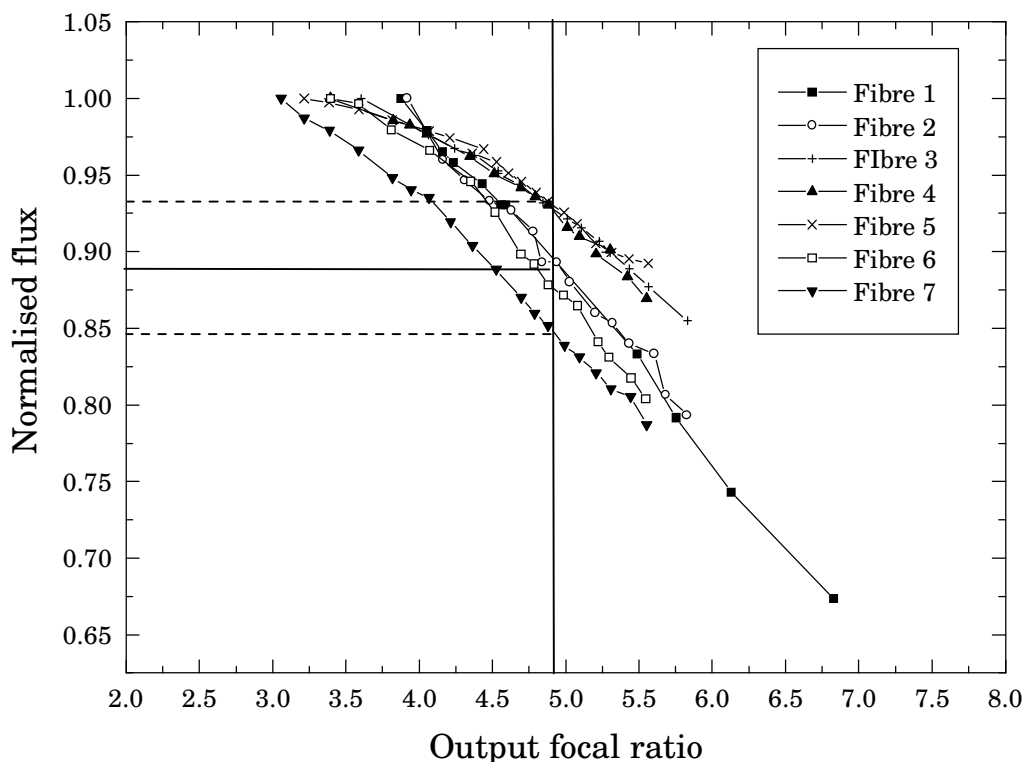


**Figure 2-19** FRD test results for seven SPIRAL fibres. This is for a 16m length of Polymicro 50/70/90/110 $\mu$ m fibre measured at 600nm.

### 2.6.3 The COHSI fibre feeds

The short fibre feed and long fibre feed were both tested after the March 1998 observing run as part of the investigation into the low measured efficiency of the Cambridge OH Suppression Instrument (Ennico 1998). Both fibre feeds use the ultra-low OH absorption Optran WF fibre from CeramOptec - the details of each fibre feed are listed in Table 2-5. As can be seen, the output focal ratio is faster than the input focal ratio to accommodate for FRD effects in the fibres (see Chapter 3 for further discussions on other design considerations using fibres).

COHSI fibre feed	Long fibre feed	Short fibre feed
Length of fibre optic	12.50 metres	4.50 metres
Core/buffer diameter	110/135 $\mu$ m	200/244 $\mu$ m
Input focal ratio	$f/6.5$	$f/5.5$
Output focal ratio	$f/5.5$	$f/5.0$
Core/buffer diameter	110/135 $\mu$ m	200/244 $\mu$ m

**Table 2-5** Physical details of the two COHSI fibre feeds

The results of the FRD tests on both the COHSI fibre feeds are shown in Figure 2-20. Both fibre feeds were expected to deliver >95% of the input flux into the required output f-ratio. The high expectation of the fibre throughput was due to the larger difference in f-ratios between the fibre-fed units - a difference of one stop for the long fibre feed and a difference of half a stop for the short fibre feed, in contrast to the 0.2 difference in SPIRAL. It was hoped that this extra margin would ensure transmission of flux with minimal loss.

The actual measured figures were 72% for the long fibre feed and 78% for the shorter fibre feed,

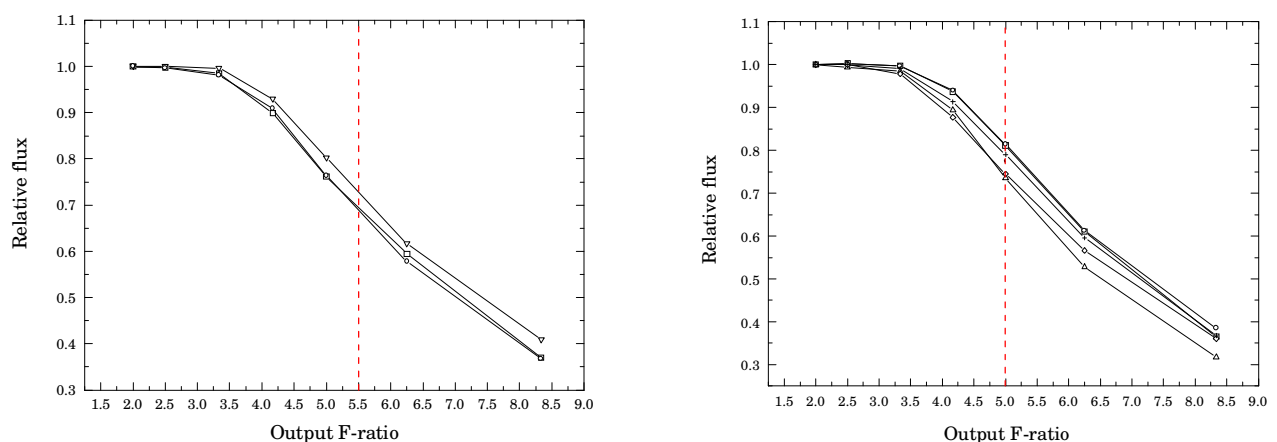


**Figure 2-20** FRD measurements for the two COHSI fibre feeds. The left-hand graph is for three fibres in the long fibre feed (fed at  $f/6.5$ ) and the right hand graph is for five fibres in the short fibre feed (fed at  $f/5.5$ ). The dashed line indicates the output focal ratio for each fibre bundle respectively.

representing a total geometrical throughput of 56% for the combined fibre feeds. Combined with other losses in the COHSI spectrograph, this represented a significant loss in efficiency. FRD is known to be worse for smaller diameter fibres and (to a lesser extent) for longer pieces of optical fibre. It was therefore a surprise to see that the shorter, larger core diameter fibre feed had a greater FRD loss than the long fibre feed.

Since a new make of fibre had been used for the COHSI fibre feeds it was then decided to investigate two different types of low OH fibre to see if the FRD was inherent in the manufacturing process.

#### 2.6.4 Comparison of CeramOptec and Polymicro fibres

Two lengths of optical fibre were threaded into a protective conduit, both twelve metres long. One was CeramOptec WF fibre and the other was Polymicro Low OH fibre. Both fibres were sleeved with ferrules and fixed in place with Araldite Standard adhesive. The fibres were then polished and their FRD measured, with an input beam of  $f/6.5$  (see Figure 2-21).

The transmission into an  $f/5.5$  beam was 77% for the Polymicro fibre and 71% for the CeramOptec fibre, lower than expected. Examining the ends of the fibres mounted in their ferrules showed signs of stress induced FRD with poor radial scrambling clearly visible in the CeramOptec fibre (see Figure 2-22).

#### 2.6.5 Measuring FRD in an unmounted fibre

The possibility of the FRD being due to the contraction of adhesive around the last 20mm of fibre was considered. A CeramOptec fibre was held in the polishing jig by using steel ferrules and heat

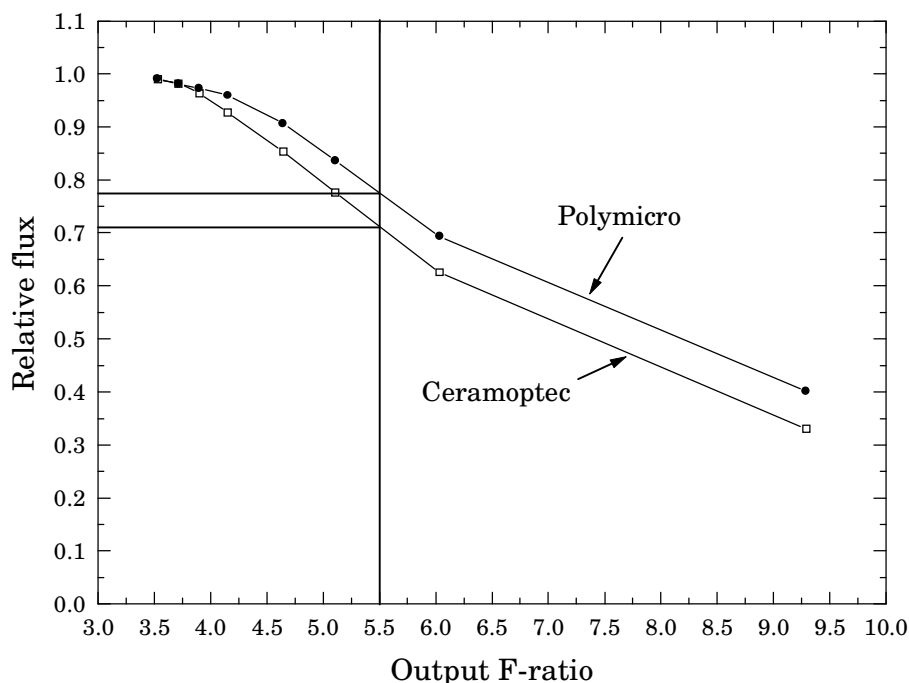


**Figure 2-21** FRD plots of CeramOptec and Polymicro test fibres. Both have a core diameter of  $110\mu\text{m}$ .

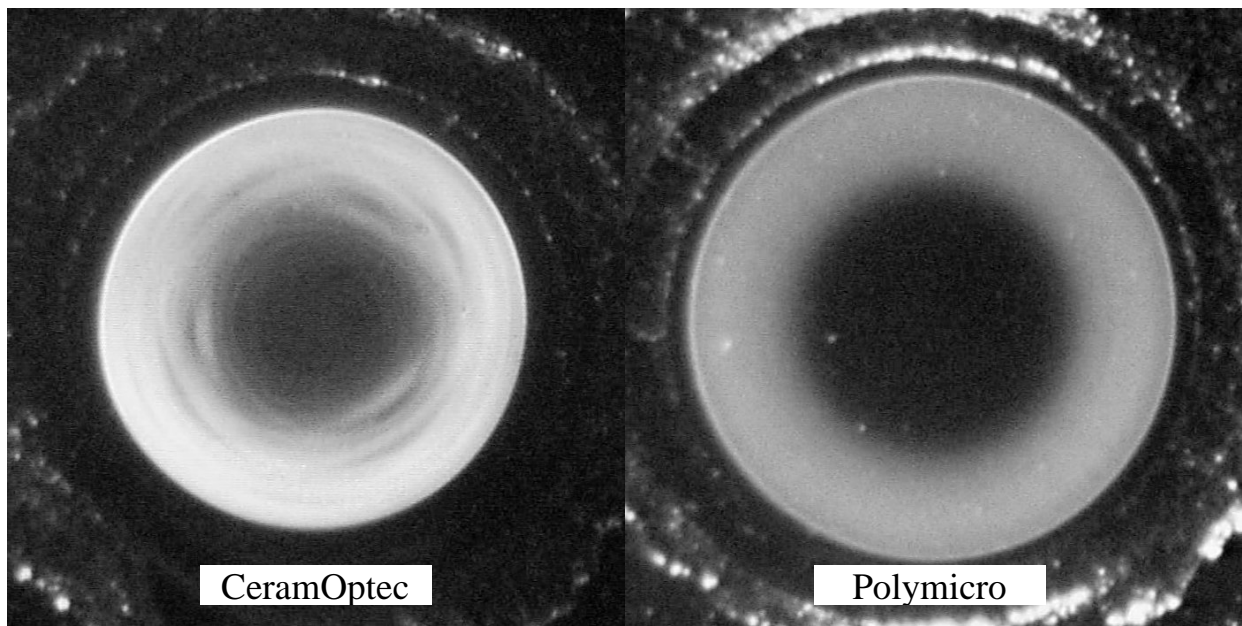


**Figure 2-22** Images of the Polymicro and CeramOptec test fibres in steel ferrules. Both fibres are 110 $\mu\text{m}$  in diameter. The CeramOptec fibre has no outer buffer layer.

resetting adhesive used to temporarily fix the fibres in place. After the polishing was completed the ferrules were removed and the fibre ends carefully cleaned with acetone. The resultant FRD curve is shown in Figure 2-23. Although the fibre shows a slightly improved transmission of 75% at  $f/6.5$ , this is still much lower than the expected transmission for the fibre.

Currently other fibres are being investigated to determine a more suitable substitute, and one idea is that these low OH 'dry' fibres have inherently large FRD. It is possible that normal 'wet' fibres

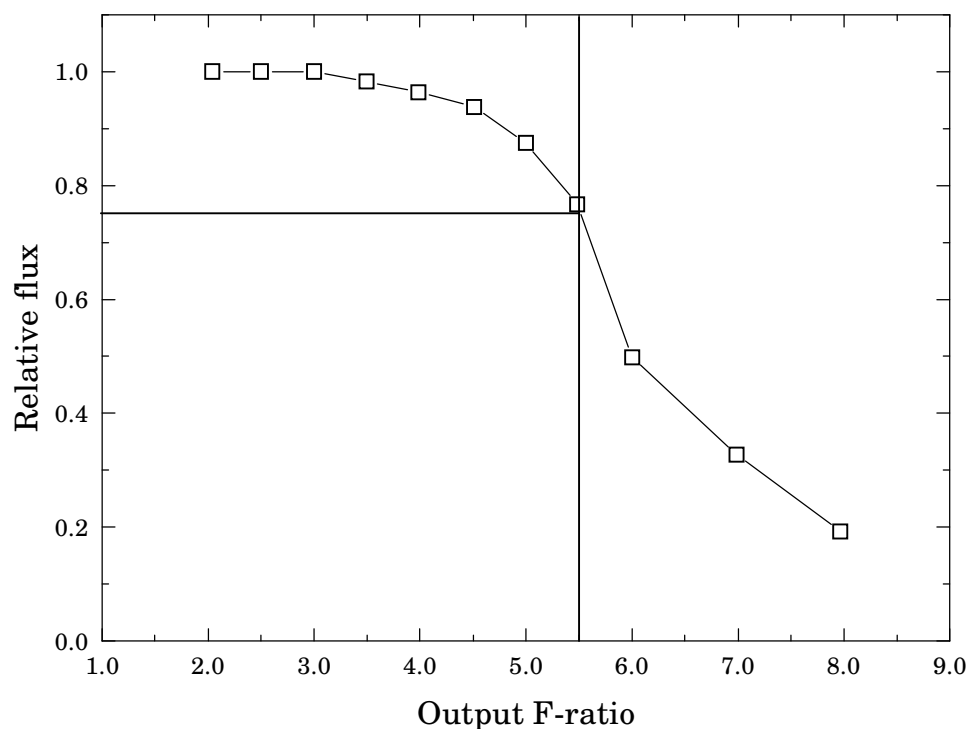


**Figure 2-23** FRD plot for an unmounted CeramOptec fibre. The input focal ratio is  $f/6.5$ .

will have better FRD properties and that the losses from internal absorption with these fibres will not be as great as the FRD losses measured from these 'wet' fibres.

### 2.6.6 FRD as a function of temperature

Stress induced on a fibre is a well known source of FRD (Angel 1980). This stress comes in the form of contraction onto the optical fibre by the surrounding adhesive holding the fibre in place. Part of the short COHSI fibre feed passes from room temperature surroundings and into a cryogenic dewar, at an average working temperature of 80K.

It was thought that the metalwork forming the cryogenic fibre feed was contracting as it was cooling down and inducing extra FRD, so this idea was tested during one of the 'cool down' runs of the cryogenic dewar.

Heating resistors and a thermocouple were attached to the fibre slit, and the throughput of the fibres was determined with an  $f/5.5$  input beam. The resistors were used to heat the fibre slit and the thermocouple monitored the temperature of the slit. The results are shown in Figure 2-24.

The 'increase factor' is the ratio of the throughput at a given temperature to the throughput at 110K. Increasing the temperature of the fibre slit improves the throughput but only by a factor of 0.10. This shows that the FRD is a weak function of temperature, and it was considered that the throughput gain from heating the slit was more than offset by the increase in thermal background it would incur.

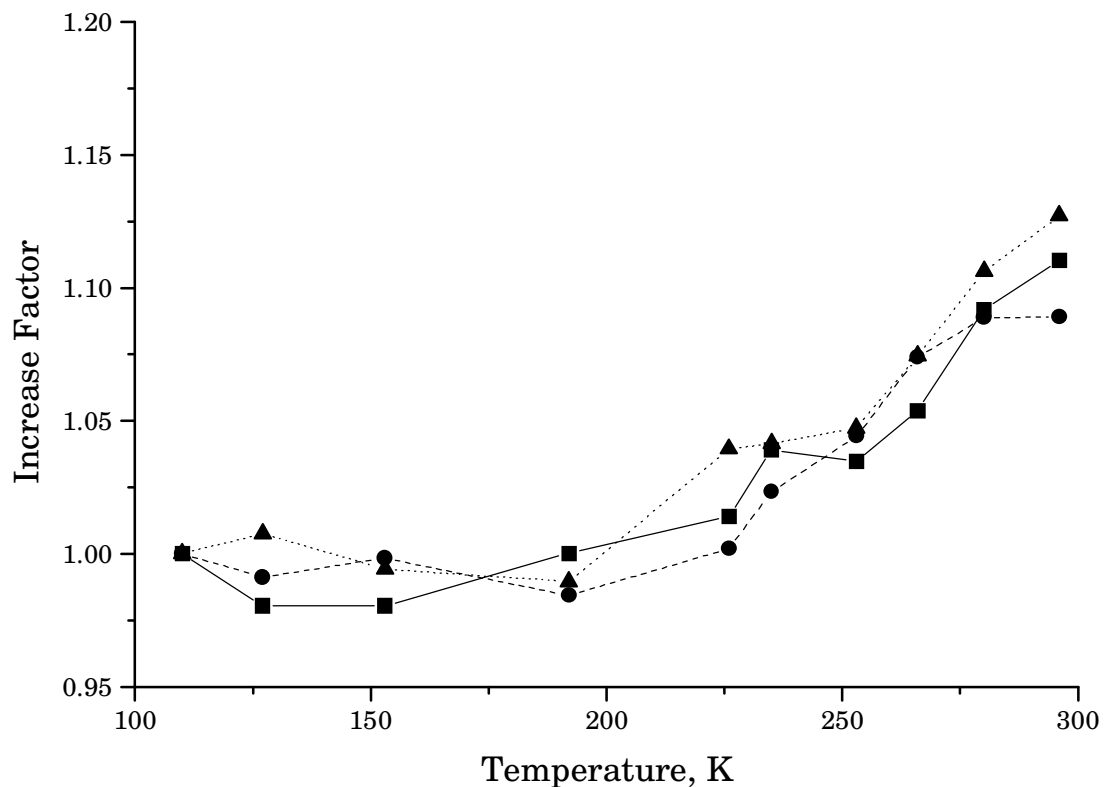


**Figure 2-24** Variation of FRD with temperature. The data is taken from three different regions on the J band camera array.

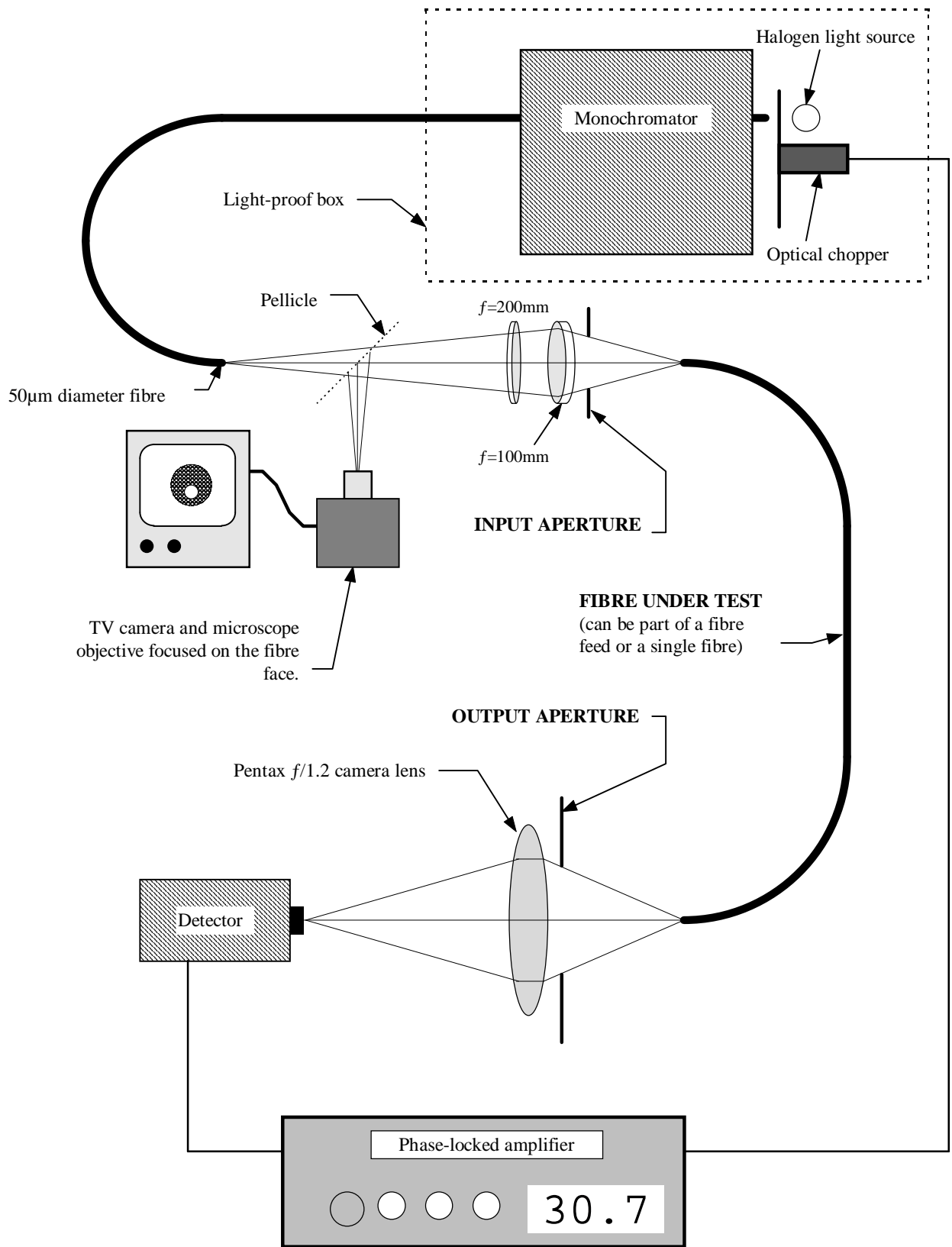


**Figure 2-25** Layout of the FRD test bench.

## 3. The Design of Fibre-fed I.F.S.

---

### 3.1 Introduction

This chapter discusses the issues involved in designing spectrographs to work most efficiently with optical fibres (§3.2.2) and explains why fibres overcome problems involved with slit-based spectrographs (§3.4.1).

Slit based spectrographs produce spectra by dispersing the image of the slit onto a detector (§3.4.2). This means that many fundamental parameters of spectrographs are related to each other, such as an increase of slit width on the sky results in a decrease of spectral resolution. The inter-related parameters mean that slit-based spectrographs for eight-metre telescopes require larger optics and larger gratings along with the new technology required to realise them.

Using fibres between the telescope and spectrograph enlarges the design parameter space, and some interdependent relations (such as the slit-width/resolution relation mentioned above) disappear altogether (§3.4.1). Using fibres with small core diameters naturally leads to high spectral resolutions, a common science driver for large telescope spectrographs.

To highlight the issues concerned with the optical design involving fibres (§3.2.1) a spectrograph fed with one fibre is discussed and the equations relating the angular extent of a single fibre/slit are derived and examined (§3.2.3). Telescopes work at f-ratios which match poorly with the range of f-ratios optimal for fibres (§3.2.2) and require the introduction of optics for optimal matching. From the fundamental optical invariant of area/solid angle product (§3.2.4) it is shown that a lenslet in front of the fibre allows an optimal input focal ratio of the fibre to be selected. A close-packed array of such lenslets can then sample an area of sky, giving two-dimensional spectroscopic (integral field spectrograph - IFS) capabilities. Two different methods of matching lens arrays to the telescope are examined (§3.3) with the macrolens array and re-imaging fore-optics method giving the best performance. The fibres lead down to a spectrograph fixed on the floor of the observatory and are reformatted into a single line of fibres (a 'fibre slit').

A fibre-fed spectrograph design is effectively decoupled from the parent telescope by the introduction of the fibre image slicer, and this allows very efficient Littrow designs to be used (§3.4) and good matching of the fibre slit to the detector pixel size (§3.4.3).

## 3.2 Optimising designs for use with optical fibres

### 3.2.1 Layout of a fibre-fed spectrograph

Optical fibres are often the largest constraint in a design - one of the only properties that can be easily changed is the input focal ratio of light into the fibre,  $f_{\text{fibre}}$ . A typical layout for a fibre-fed spectrograph is shown in Figure 3-1. This can be broken down into two sections - a focal plane unit (FPU) that feeds the light from the focal plane of the telescope into the fibre, and a fibre-fed spectrograph that can sit on the floor of the observatory.

The simplest FPU is one with no optics - many multi-object spectrographs have bare fibres as their fibre input. In this simplified spectrograph however, the starlight is focused in the focal plane of the telescope with the focal ratio of the telescope  $f_{\text{tel}}$ . The FPU then either re-images the star or the telescope pupil onto the end of the fibre. These optics determine the focal ratio of light fed into the fibre,  $f_{\text{fibre}}$ . The fibre then passes down to the spectrograph.

Focal ratio degradation dilutes the emerging light into a faster beam, and the input focal ratio into the collimator,  $f_{\text{coll}}$  is designed so that  $f_{\text{fibre}} > f_{\text{coll}}$  and the collimator can accept the FRD degraded beam. The collimated beam has a diameter  $D_{\text{coll}}$  and this passes through the dispersing element, typically a diffraction grating or grism. The dispersed beam is then focused onto a detector via a camera with focal length  $f_{\text{camera}}$ .

The size of the image of the fibre on the detector is given by:

$$d_{\text{image}} = D_{\text{fibre}} \cdot \frac{f_{\text{camera}}}{f_{\text{coll}}} \quad (3-1)$$

Where  $D_{\text{fibre}}$  is the diameter of the core of the fibre.

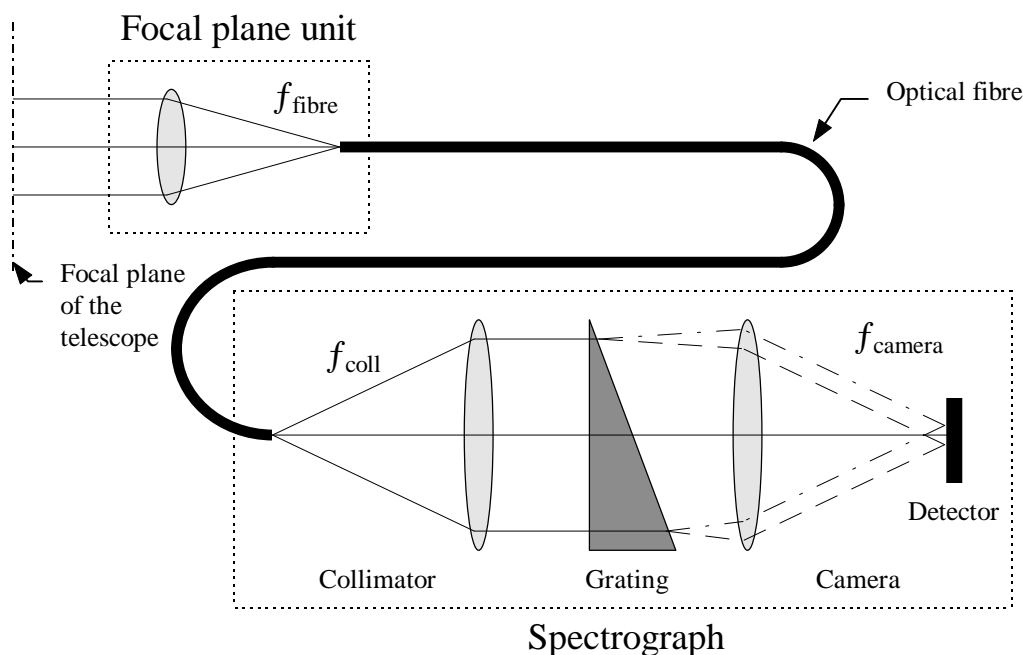


**Figure 3-1** Schematic layout of a fibre-fed spectrograph with one fibre.

The separation of the spectrograph from the back of the telescope allows a much simpler structural design to be introduced. Designs that require major structural support of optical components are now no longer necessary, and the spectrograph can be permanently mounted in a separate room with the optical fibres feeding in the light from the telescope.

Other points which affect the design are the diameter of the fibre, the diameter of the collimated beam in the spectrograph and the size of the detector pixels.

The diameter of the fibre and input focal ratio of the fibre dictate the amount of sky seen by the fibre (see §3.2.3 for the derivation). The size of the detector pixels  $d_{\text{pixels}}$  also has a bearing on how well sampled the fibre images are, and for very high spectral resolution applications the diameter of the collimated beam with the fibre diameter has a bearing on the instrumental spectral resolution (see §3.4.3).

### 3.2.2 The optimum focal ratio for working with fibres

The most important consideration is to see what focal ratios are most suitable for transmission through an optical fibre. To find out what f-ratio is most suitable, a sample of optical fibre was tested in the laboratory. A beam from an aperture defines an input f-ratio for the light entering test fibre. The amount of light exiting the fibre into the same beam size is measured and is calculated as a fraction of the total light emerging from the fibre (see Figure 3-2).

For an ideal circular aperture the graph would show 100% transmission for all f-ratios, but the presence of FRD in the fibre causes the emerging flux to spread into a wider beam. As shown in the figure the fibre is more efficient for faster f-ratios.

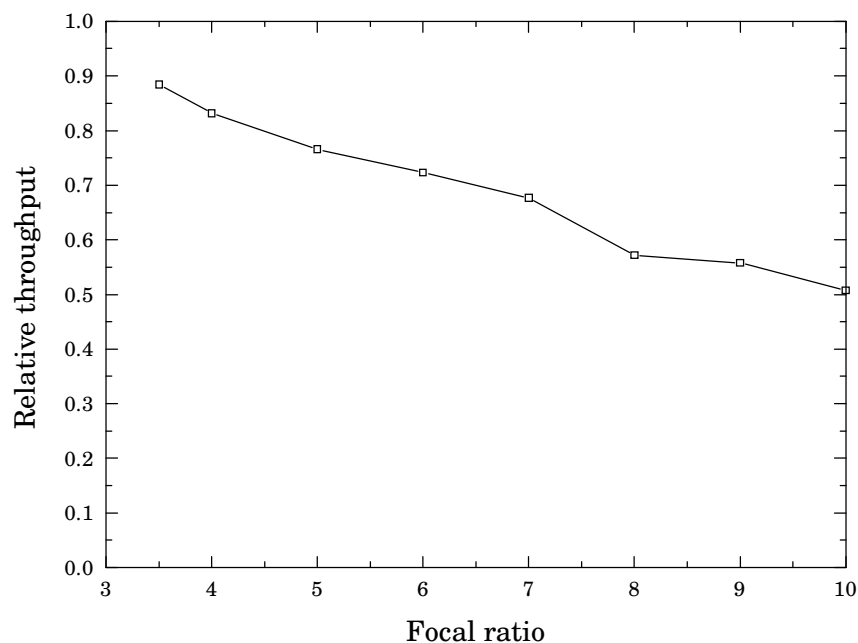


**Figure 3-2** *The loss of flux in a beam due to FRD.* The fibre used was a 12 metre length of Polymicro Low OH fibre with a core diameter of 110 $\mu\text{m}$  and tested at 1.1 $\mu\text{m}$ . The graph shows that the efficiency of a fibre is lower for larger focal ratios.

Considering that most telescopes have Cassegrain foci anywhere from  $f/8$ - $36$ , Figure 3-2 shows that a bare fibre feed with no re-imaging fore-optics is inefficient. Having a re-imaging lens in front of the fibre allows  $f_{\text{fibre}}$  to be chosen by the designer. In order to collect as much flux from the fibre as possible, the output spectrograph then has an acceptance focal ratio  $f_{\text{coll}}$  faster than the input focal ratio of the fibre  $f_{\text{fibre}}$ . The suggestion is to then build a spectrograph with fast optics. However, very fast achromatic refractive optics ( $<f/3.0$ ) are difficult to design and align.

There is a balance between choosing a beam that is not too slow to be inefficient for the fibre and not too fast to design suitable collimator optics for. The focal ratio  $f_{\text{fibre}}$  chosen for the SPIRAL fibres was  $f/5.0$  with the spectrograph operating at  $f/4.8$ , and the COHSI fibres used  $f/6.5 \rightarrow 5.5$  between the telescope and the suppressor and  $f/5.5 \rightarrow 5.0$  between the suppressor and the spectrograph.

### 3.2.3 The angular extent of a fibre on the sky

The angle of sky subtended by an individual fibre  $\alpha_{\text{fibre}}$  is determined by the diameter of the telescope  $D_{\text{tel}}$ , the focal ratio of the light entering the fibre  $f_{\text{fibre}}$  and the diameter of the fibre  $D_{\text{fibre}}$ .

With reference to Figure 3-3, two relationships can be deduced:

$$\alpha = \frac{D_{\text{fibre}}}{F_{\text{tel}}} \text{ and } f_{\text{fibre}} = f_{\text{tel}} = \frac{F_{\text{tel}}}{D_{\text{tel}}} \quad (3-2)$$

By cancelling out  $F_{\text{tel}}$  (the focal length of the telescope) the result obtained is:

$$\alpha_{\text{fibre}} = \frac{D_{\text{fibre}}}{D_{\text{tel}} \cdot f_{\text{fibre}}} \quad (3-3)$$

where  $D_{\text{fibre}}$  and  $D_{\text{tel}}$  are in millimetres and  $\alpha_{\text{fibre}}$  is in radians.

With  $D_{\text{tel}}$  fixed and  $f_{\text{fibre}}$  within a limited range of efficiency ( $4 < f_{\text{fibre}} < 10$ ) a simple relation is generated between the angular extent of the fibre and its diameter.

In the case of SPIRAL where the instrument is for a 3.9 metre telescope,  $f_{\text{fibre}} = 5.0$  and  $\alpha_{\text{fibre}} = 0.5$  arcseconds (matching the seeing of the telescope) this gives us a fibre core diameter of  $\sim 50\mu\text{m}$ . Fibres range in diameter from  $10\mu\text{m}$  for single mode fibres up to  $500\mu\text{m}$  and higher.

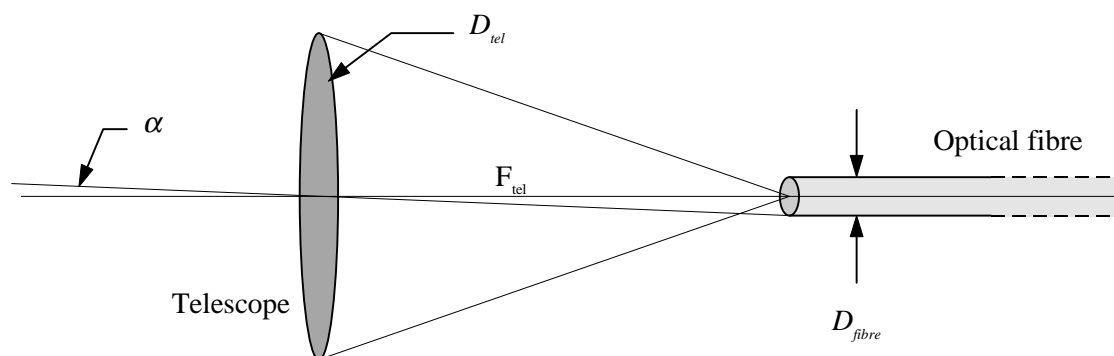


**Figure 3-3** Diagram of telescope and fibre. The angle  $\alpha$  subtended by the aperture (in this case, a fibre with diameter  $D_{\text{fibre}}$ ) is related to the diameter of the telescope and its focal ratio.

### 3.2.4 The A- $\Omega$ product

Throughput, optical extent, light-gathering power and etendue are all names for the optical invariant known as the A- $\Omega$  product (see Figure 3-4) which relates how flux passes through an optical system. It is the area A multiplied by the solid angle  $\Omega$  subtended by the flux incident on that area, and this applies for any pupil plane or image plane in an optical system. A derivation from first principles is given in Boyd (1983).

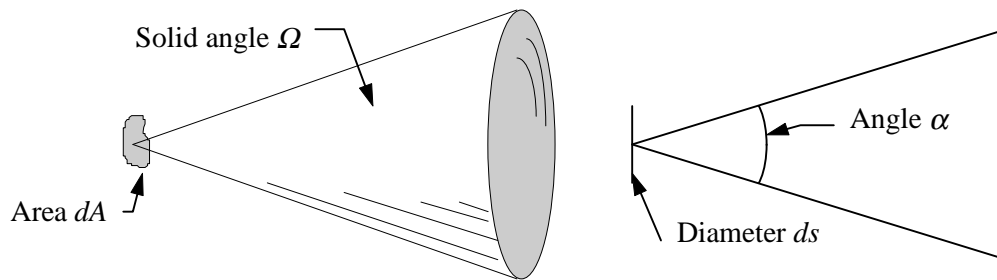


**Figure 3-4** *The area/solid-angle product.* Here the optical surface is composed of small elements of surface  $dA$  each seeing a beam of solid angle  $\Omega$ . For systems that are radially symmetric about the optical axis it can be simplified as in the diagram on the right.

This product is important as it is conserved for all optical surfaces in an ideal optical system. Optical aberrations such as focal ratio degradation and diffraction always increase the value of A- $\Omega$  through a system, and this has led it to be likened to a form of entropy for optical systems.

Although the formal definition of the optical extent is a double integral involving  $d\Omega$  and  $dA$ , it can be simplified to A- $\Omega$  for the rest of this thesis. If all optical components possess radial symmetry about their optical axis, a further simplification can be made (see Figure 3-4). It can be rewritten as the diameter  $d$  of the optical element multiplied by the subtended angle of the incident flux  $\alpha$ .

In determining the A- $\Omega$  product a useful approximation for  $\Omega$  can be given as:

$$\Omega \cong \frac{\pi}{4 \cdot (f/\#)^2} \quad (3-4)$$

This approximation over-estimates  $\Omega$  for a given f-ratio, but the error in the estimate is less than 5% for  $f/3.0$  and rapidly diminishes for slower beams.

This invariant can be demonstrated for the diagram shown in Figure 3-3. The A- $\Omega$  product can be defined as:

$$A\Omega = (\pi \cdot D_{\text{fibre}}^2) \cdot \left( \frac{\pi}{4 f_{\text{fibre}}^2} \right) = \left( \frac{\pi \cdot D_{\text{fibre}}}{2 \cdot f_{\text{fibre}}} \right)^2 = \frac{\pi^2}{4} \cdot \left( \frac{D_{\text{fibre}}}{f_{\text{fibre}}} \right)^2 \quad (3-5)$$

So if  $f$  and  $D$  represent the input focal ratio  $f$  and diameter  $D$  of any aperture in the system then by these quantities can be linked by the A- $\Omega$  invariant by:

$$\frac{D}{f} = \frac{D_{\text{fibre}}}{f_{\text{fibre}}} \quad (3-6)$$

This relation is used later on in §3.4.3.

### 3.3 The focal plane unit (FPU)

#### 3.3.1 From one fibre to many fibres: the packing fraction problem

By packing many optical fibres together into a close-packed array, an area of sky can be spectrally sampled in one exposure resulting in integral field spectroscopy. The input beam of the fibres  $f_{\text{fibre}}$  is the focal ratio of the telescope,  $f_{\text{telescope}}$ . If circular fibres are close packed together then the maximum packing fraction PF (defined as the total light collecting area of the array divided by the total area covered by the array) is less than 91% for fibres with no cladding and typically <60% for fibres with a core-to-cladding ratio of 1.2 (See Figure 3-5).

$$PF \approx 0.91 \cdot \left( \frac{d_{\text{core}}}{d_{\text{cladding}}} \right)^2 \quad (3-7)$$

This geometric loss of flux is avoided by using a close packed lens array in front of the fibre bundle to achieve  $PF > 98\%$ . The introduction of a lens array also means the input focal ratio for the fibres can be chosen, as  $f_{\text{lens array}} = f_{\text{fibre}}$ . This is the basis for the focal plane unit (see Figure 3-1).

A lens array consists of regularly spaced lenses that form a contiguous surface and the individual lenses in the array are commonly referred to as ‘lenslets’. The three simple polygons that can tessellate to form a continuous imaging surface are the triangle, the square and the hexagon. Of

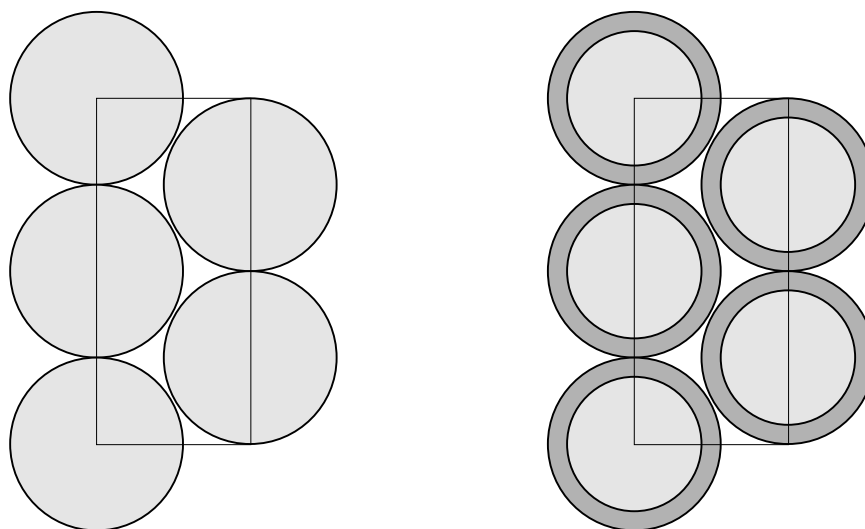


**Figure 3-5** The packing fraction for fibres. On the left is the arrangement for a set of fibres with no cladding. By considering the area in the box drawn over the fibres it can be shown that the packing fraction is ~91%. In reality fibres need a cladding layer and this decreases the packing fraction further.

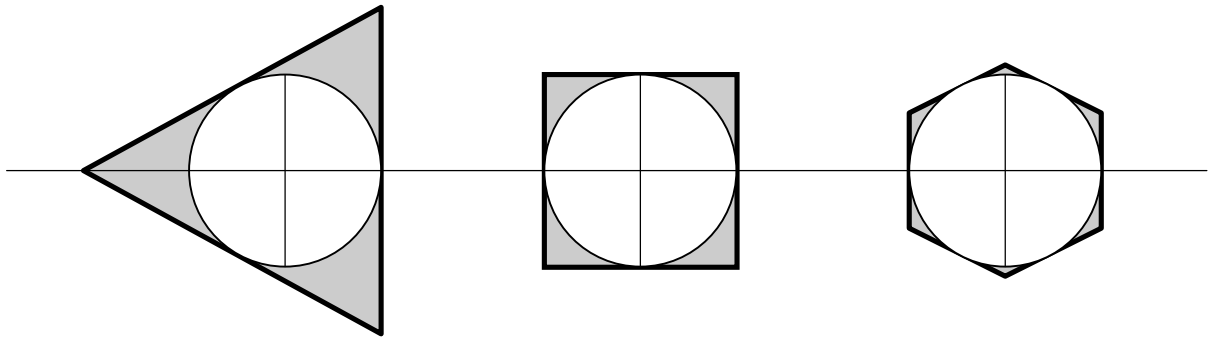


**Figure 3-6** Comparing the different polygons. The polygons above can be characterised by the diameter of the largest circle that can be drawn within their area. Any rays in the shaded areas of the polygons enter the fibres at a faster f-ratio than those rays passing within the circle, producing an effect similar to FRD.

these three shapes, lens arrays are commonly manufactured with hexagonal or square lenslets.

A subtle consideration with polygonal lenslets is the introduction of an effect known as geometric FRD (see Figure 3-6). This effect means that light rays entering near the corners of the lenslet then pass into the fibre at a larger incident angle than rays at the midpoints of the edges. These rays mean that the averaged input focal ratio  $f_{\text{fibre}}$  is faster than the f-ratio defined by the pitch of the lenslets. The more sides a polygon has, the closer the polygon approximates to a circular aperture, so hexagonal lenslets were chosen for the COHSI and SPIRAL lens arrays.

The next two sections describe two alternate ways of matching a lens array with the telescope. In the first case the size of the lens array is chosen to match the image scale at the telescope plane, and in the second case the lens array size is chosen to optimise optical performance and quality of the lens array, with the image scale of the telescope matched to the lens array scale by using fore-optics.

### 3.3.2 Microlens arrays

For telescopes such as the WHT, the plate scale of the Cassegrain focus is 4.46 arcseconds per mm. If the lenslets are matched to 0.5 arcseconds (matching to the typical seeing at the telescope) then the pitch of the required lens array is 110 $\mu\text{m}$ . Such small lenses (or ‘lenslets’) cannot be made using conventional polishing techniques. Instead the whole lens array is fabricated *en masse*, e.g. from metal moulds filled with a UV setting resin. After curing the metal former is then removed to produce the microlens array. The fibres are then positioned onto the back of the array where the lenslets form images of the telescope pupil on the ends of the fibres (see Figure 3-7). Extensive tests on different types of microlens arrays and their performance are recorded in Lee (1998).

Lee’s conclusions are that microlens arrays have intrinsic losses on the order of 20-40%, predominantly due to poor surface quality causing light to be scattered in the array. but as the degree of co-operation between industry and optical designers increases, the quality of microlens array manufacture is expected to improve in the near future.

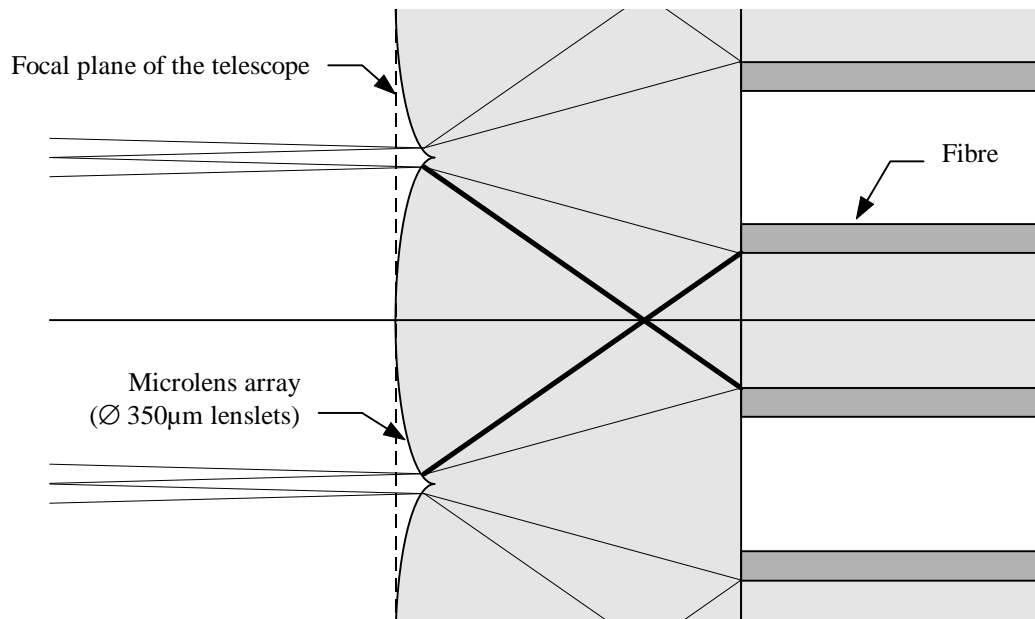


**Figure 3-7** Cross section of a microlens array feeding optical fibres. Light from the telescope comes in from the left, passes through the microlens array and the telescope pupil is re-imaged onto the end of the fibres.

Ideally the optical axis of a fibre is aligned with the optical axis of its respective lenslet. For a microlens array where the diameter of a lens is on the order of hundreds of microns it is difficult to position all the fibres on the array individually. A technique developed by the Durham Instrumentation Group (Allington-Smith 1997) is to put all the fibres into a close-packed array of metal tubes with the same pitch and spatial geometry as the lenslets. Fibres are positioned in the tube array and joined to the back of the lens array with UV curing epoxy. However the pitch of the lenslets in such arrays have RMS errors on the order of  $3\mu\text{m}$ . The tube arrays can also have errors of up to  $3\mu\text{m}$ . The fibres themselves are undersized to allow easy insertion into the tubes, and this introduces an extra  $5\mu\text{m}$  RMS error. Finally, the fibre cores themselves are not concentric with their outer buffer introducing a further  $4\mu\text{m}$  error. These lead to total decentering errors of up to  $8.6\mu\text{m}$  and a loss of light due to the image from the lenslet not aligning with the core of the fibre.

Another problem is that of non-telecentricity. The thicker rays in Figure 3-7 indicate that rays from the edge of the lenslet enter the opposite edge of the fibre at a larger angle of incidence (faster speed) than one would expect. If the input f-ratio of the fibre is taken to be the ratio of lenslet diameter to focal length then this underestimates the actual mean f-ratio of light entering the fibre. This is sometimes referred to as 'geometric FRD' and is an important consideration in microlens array design. Coupled with fibre FRD this leads to a lower throughput and needs a faster spectrograph. The microlens array is also fixed to a particular plate scale making it difficult to transport the fibre feed to other telescopes.

### 3.3.3 Fore-optics and macrolens arrays

By using two lenses to enlarge the plate scale of the telescope a larger macro lens array can be used (see Figure 3-8). Instead of an array composed of microlenses, larger diameter discrete lenses are used to build up a macrolens array (see Figure 3-9). A small magnifying lens near the focal plane of the telescope performs the enlarging of the focal plane, with the field lens providing a slight correction to form the enlarged image scale of the telescope at the plane of the macrolens array.

The advantages of using the macrolens design are:

- Lens surface quality - these larger (typically millimetres in size) lenslets are made with classical polishing techniques, resulting in fewer scratches, higher surface tolerances and less scattered light. Broadband anti-reflection (AR) coatings can also be applied.
- Quality control - by building the lens array from individual lenses they can be checked for surface quality and focal length, with sub-standard ones rejected before they can be part of the lens array.

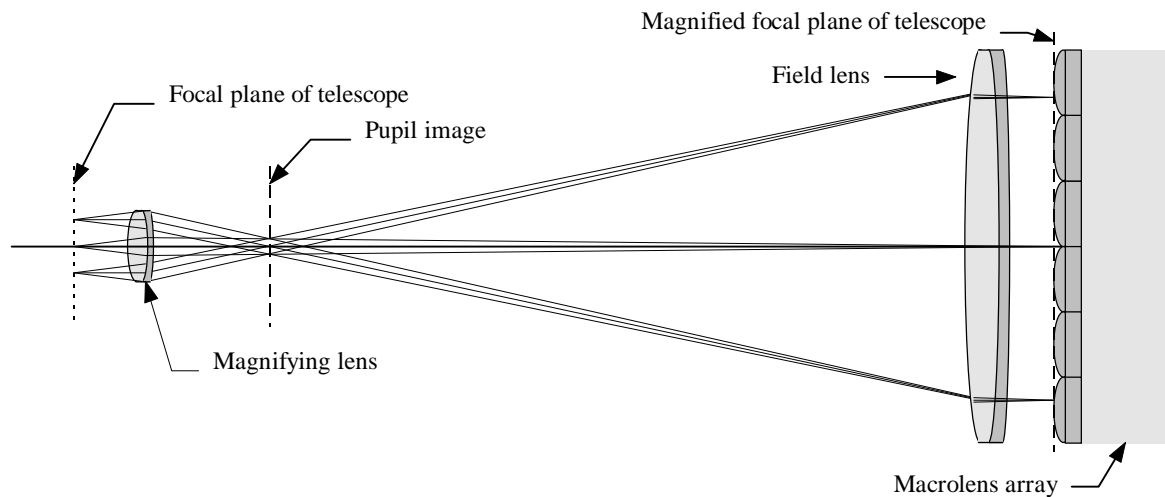


**Figure 3-8** Using fore-optics to increase the plate scale of the telescope.

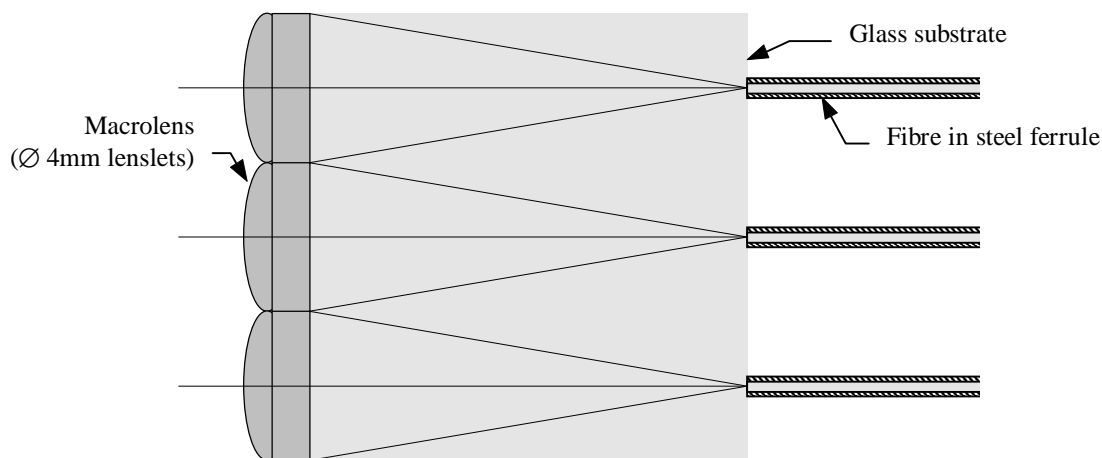


**Figure 3-9** Detail of the macrolens array. With the diameter of the lenslets  $\gg D_{fibre}$  the telecentric problem is considerably reduced. There is enough room on the back of the array for fibres to be individually positioned.

- Achromatic doublets - these can be used as an alternative to the singlet lenses in microlens arrays for when aberration correction over a greater wavelength range is required.

Fibres can now be individually placed on the back of the lens array substrate, substantially reducing systematic decentering errors (see §5.6 for the accuracy obtained with the COHSI lens array). With the larger lens diameter the fibres are now telecentric with the lenses, eliminating the geometric FRD losses inherent with microlens arrays. With a simple change of magnifying lens the array can then be transferred to other telescopes, enhancing the versatility of the instrument.

In conclusion, using fore-optics and a macrolens array removes most of the mechanical and geometric losses inherent from using microlens arrays in the focal plane of the telescope. Combined with broad-band anti-reflection coatings the losses from introducing two extra lenses is minimal compared to the losses incurred by using microlens arrays.

### 3.4 Fibre-fed spectrographs

The issues relevant in the design of a fibre-fed spectrograph are presented - first the problems inherent with a slit-based spectrograph are presented, showing how seeing-limited observations can be difficult for consistent high-resolution work. The advantages of using a lens array as an 'image slicer' show how the spectral resolution of a fibre-fed spectrograph can remain high, regardless of the seeing at the telescope.

Even with corrective optics to minimise atmospheric distortion, the typical angular size of distant galaxies (such as those observed in the Hubble Deep Field) are on the order of 1 arcsecond (Piche, private communication). The fundamental limits of optimally matching the detector and collimator optics to such objects show that efficient high resolution slit-based spectrographs are difficult to implement on 8m telescopes.

#### 3.4.1 The problems with a slit-based spectrograph

Shown in Figure 3-10 is the input slit of a spectrograph and the resultant dispersed spectrum on the detector. The image of the star is placed in the middle of the slit and the collimator then produces a collimated beam which passes through the dispersing element of the spectrograph. A camera then images the dispersed light onto a suitable detector. What can be seen is that each monochromatic image on the detector is an image of the slit, so any variation in illumination of the slit is reflected in the dispersed images.

The width of the slit is matched to the seeing at the telescope so that the maximum possible stellar flux enters the spectrograph. The spectral resolution of the spectrograph is defined as  $\lambda/\delta\lambda_{\text{instrument}}$ , where  $\delta\lambda_{\text{instrument}}$  is the width of the slit image on the detector multiplied by the linear dispersion ( $d\lambda/dx$ ) of the spectrograph. This width is varied according to the seeing, and for bad conditions the spectral resolution of the spectrograph is smaller.

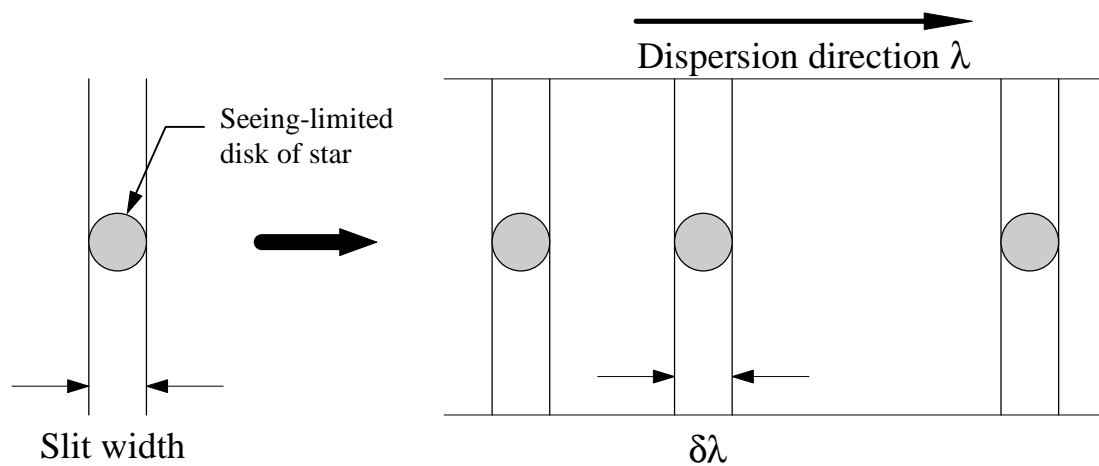


**Figure 3-10** *The input and output of a slit based spectrograph.*

Keeping the width of the slit narrow to maintain the high spectral resolution then results in loss of star light on the edges of the slit, known as ‘slit jaw losses’. This is a well known problem for the slit based spectrograph.

If the image of the star moves from the centre of the slit, the corresponding images of the slit on the detector also move with respect to the edges of the imaged slit. The corresponding centroids of the spectral lines are therefore shifted with respect to the edges of the slit. When wavelength calibration is performed, a dispersion solution to a known set of emission line wavelengths is fitted to the spectrum of an arc lamp. If the slit is illuminated by the arc lamp in a different manner to the illumination by the stellar observations, the image centroids of the calibration lines will be different to those of the star. The result is a systematic error in the wavelength calibration of the stellar spectra, which without due attention can lead to incorrect radial velocity measurements of the star.

The slit-based spectrograph needs to be stationary with respect to the optical path of the telescope focus, requiring that the spectrograph is fixed on the telescope for Prime and Cassegrain foci. This introduces a changing three dimensional gravity vector into the spectrograph that can cause misalignment of optical components, introduction of systematic errors and loss of resolution. The problem can be reduced somewhat by use of Coudé or Nasmyth foci.

Large echelle spectrographs can be fed by a set of 3 extra relay mirrors from a Coudé focus (for an equatorially mounted telescope) or by one extra relay mirror at a Nasmyth focus (for an altitude-azimuth telescope). Both systems have some form of field rotation, and so either the spectrograph is rotated along one axis during the exposure or the duration of the exposure is short enough that field rotation is not significant. Restricting the movement of the spectrograph to one dimension reduces the problem but does not remove it. The unique properties of optical fibres make it possible to completely decouple the motion of the telescope from the spectrograph and eliminate the problems due to flexure.

### 3.4.2 The advantages of a fibre-fed spectrograph

Figure 3-11 shows how the introduction of a square lens array and fibre feed changes the properties of the spectrograph. The disk of the star falls on the lenses of the lens array. The light from each lens is then focused onto the end of an optical fibre which then is fed into a fibre slit. The fibre slit is composed of all the fibres from the lens array arranged into a single vertical line. It is this line of fibres that is dispersed by the spectrograph and imaged onto the detector.

The width of the imaged slit is fixed by the diameter of the individual fibres used, meaning that the spectral resolution of the spectrograph is now independent of stellar image size. If the seeing disk of the star becomes larger, more lenslets are illuminated along the slit, and if the stellar image moves across the lens array, a different set of fibres will be illuminated.

Since the lens array covers a larger area of sky, all the flux from the star enters the spectrograph, allowing high resolution photometric observations to be made, something difficult to do with slit based spectrographs.

Another property of optical fibres that is useful for high resolution work is their image scrambling properties (see §2.3). The radially symmetric images on the ends of the optical fibre formed by image scrambling give rise to spatially symmetric profiles on the detector, regardless of the spatial illumination on the input face of the fibre. The consistency of the fibre profile image combined with the stability of a floor mounted spectrograph lends fibres to high resolution work.

By effectively decoupling the slit from the telescope, the parameter space that defines slit-based spectrographs is enlarged by the removal of the slit/sky relationship. However all spectrographs ultimately encounter the limits set by the throughput invariant discussed in the previous chapter.

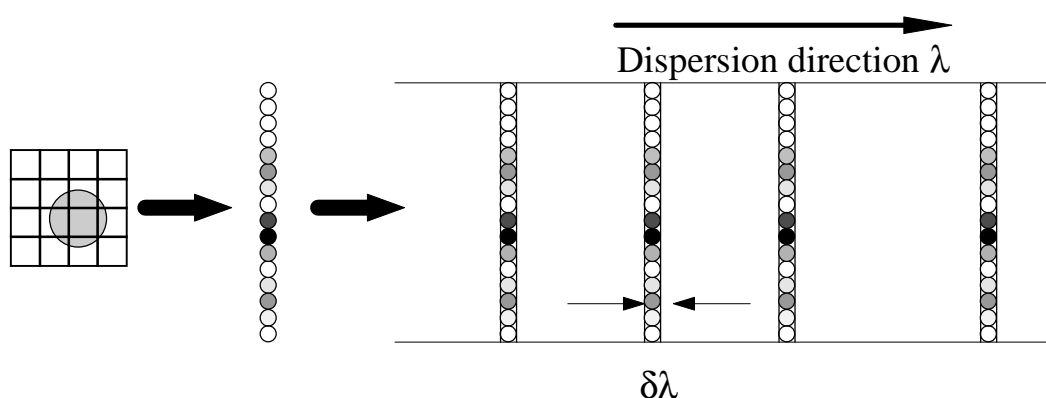


**Figure 3-11** *The input and output of a fibre-fed spectrograph with square lens array. The seeing disk of the star is sub-sampled with a lens array. The optical fibres then reformat the image into a ‘fibre slit’ which then passes into the spectrograph.*

### 3.4.3 Optimal matching to the detector pixels

The most efficient and cost effective spectrograph is one where all optical components are being optimally used. The amount of information recorded with the spectrograph is directly dependent on the number of pixels being used in the detector. The image of a monochromatic emission line on a spectrograph detector is optimally sampled when the width of the image is matched to two pixels on the detector (the Nyquist criterion), so the expression relating pixel size to angular width on the sky is derived for a slit based spectrograph below.

- Pixel matching for a slit based spectrograph

Equation 3-3 can be manipulated to give the size a detector pixel subtends on the sky by using the optical invariant as described in Equation 3-6.

Rearranging Equation 3-3:

$$\alpha_{.sky} \cdot D_{telescope} = \frac{D_{fibre}}{f_{fibre}} \quad (3-8)$$

Using the optical invariant in Equation 3-6:

$$\frac{D_{fibre}}{f_{fibre}} = \frac{d_{pixel}}{f_{camera}} \quad (3-9)$$

Combining the two equations above gives:

$$d_{pixel} = \alpha_{.sky} \cdot f_{camera} \cdot D_{telescope} \quad (3-10)$$

With knowledge of the telescope diameter, the typical size of pixels in large format arrays and the angular slit width on the sky this equation gives the focal ratio needed for the spectrograph camera. For example, an 8 metre telescope with an angular slit size of 0.5 arcseconds and detector pixel size of 20 $\mu$ m gives a camera focal ratio of 0.93. This is an extremely difficult design to realise, possibly requiring a combination of non-spherical reflecting and refracting optics for the large fields of view that modern detectors require.

The focal ratio becomes even faster for larger telescopes and smaller pixel sizes, showing that slit based designs quickly reach fundamental limits for optimal designs.

The spectral resolution  $R$  is defined as  $R = \lambda/d\lambda$ , where  $d\lambda$  is the smallest wavelength difference that can be measured by the spectrograph. Diffraction effects due to the finite size of the grating give a minimum image diameter on the detector, which is the diameter of the first minimum of the Airy diffraction disk  $d_{Airy} = 1.22 \times f_{camera} \cdot \lambda$ . However, in many cases  $d_{pixel} \gg d_{Airy}$  so the spectral resolution is purely limited by the pixel size and  $R \propto \lambda/d_{pixel}$ .

Substituting in the value of  $d_{pixel}$  from Equation 3-10 then gives:

$$R \propto \frac{\lambda}{\alpha_{sky} \cdot f_{camera} \cdot D_{telescope}} \quad (3-11)$$

and now  $f_{camera}$  can be replaced with  $F_{camera}/D_{coll}$  where  $F_{camera}$  is the focal length of the spectrograph camera.

$$R \propto \left( \frac{\lambda}{F_{camera}} \right) \cdot \frac{D_{coll}}{\alpha_{sky} \cdot D_{telescope}} \quad (3-12)$$

so for a given wavelength:

$$R \propto \frac{D_{coll}}{\alpha_{sky} \cdot D_{telescope}}. \quad (3-13)$$

Equation 3-13 shows that increasing telescope diameter or widening the slit (and hence increasing  $\alpha_{sky}$ ) both lead to a decrease in the spectral resolution, and the only improvement then is to increase the diameter of the beam incident on the grating. For 8 metre telescopes working in the optical and matching to 0.5 arcsecond objects in the sky, this results in the need for gratings that are much larger than the typical gratings used in spectrographs. With the Keck 10m telescope, the slit based echelle spectrograph HIRES (Epps 1993) uses a mosaic of three gratings to form a large grating which can accept a collimated beam diameter of 12 inches and uses an  $f/1.0$  camera to optimally sample the image of the slit. This shows that slit based designs for large telescopes are possible to build, as long as one has the budget to spare - the cost of HIRES was 4 million dollars (Vogt 1993).

- Pixel matching for a fibre-fed spectrograph

The introduction of the fibre feed means that the detector is matched to the image of the diameter of one fibre in the fibre slit. A larger aperture on the sky is equivalent to a larger number of fibres being illuminated along the fibre slit, so the relation in Equation 3-10 does not hold anymore - instead the fibre diameter is related to the pixel size by Equation 3-1:

$$d_{image} = D_{fibre} \cdot \frac{f_{camera}}{f_{coll}} \quad (3-14)$$

Similarly the expression for the spectral resolution now changes and depends solely on  $d_{fibre}$ , as long as  $d_{pixel} \gg d_{Airy}$ .

The detector most commonly used at the AAT is the  $1K^2$  TEK detector, which has a pixel size of  $24\mu m$ . By choosing a fibre with a core diameter of  $50\mu m$  (which matches the Nyquist 2 pixels/resolving element criterion) the spectrograph does not have to magnify the fibre image on the detector, so from Equation 3-14 it is seen that  $f_{camera} = f_{coll}$ . This means that the fibre-fed spectrograph design for SPIRAL can use a double pass system, where one set of optics is used for both the camera and the collimator.

By using the flexible reformatting qualities of the fibres to position the fibre slit as close as possible to the detector the grating is used in a near Littrow configuration. A grating is said to be used in Littrow conditions when the angle of incident light and angle of diffracted light are the same. This mode is the most efficient mode of operation for a grating.



# 4. SPIRAL Phase A

---

## 4.1 Introduction

This chapter discusses the design, construction and testing of the ‘Segmented Pupil Image Reformatting Array of Lenslets’ (SPIRAL) Phase A spectrograph. The SPIRAL project is composed of two parts - Phase A (hereafter referred to as ‘SPIRAL’) is a prototype fibre-feed and lens array built to test techniques that can be taken and used in the construction of Phase B, which consists of a larger fibre-feed and lens array (Figure 4-1). The techniques developed were also used in the construction of the COHSI IFU (see Chapter 5).

The two observational modes of SPIRAL are described. One is an integral field mode and the other uses the array in a single object mode called pupil imaging. This mode allows the spectrograph to be matched to the seeing disk of a star whilst keeping a high spectral resolution capability, something which is not possible with a slit-based spectrograph (Chapter 3). The theory behind the pupil imaging mode (§4.3.2) shows how additional fibres next to the object fibres on the back of the lens array simultaneously sample the sky background.

The physical layout of the whole instrument is broken down into the four main components and the design parameters for each component are then described. Following the philosophy of the previous chapters the design is based around the properties of optical fibres. The choice of fibre input focal ratio ( $f_{\text{fibre}}$ ) the seeing, and the diameter of telescope set the diameter of the fibre (§4.4.1). The size of the lens array can then be chosen with relatively little constraint, and design of the fore-optics for both modes then follows from the scale set by the physical size of the lens array (§4.4).

The diameter of the fibres combined with the length of the fibre slit (~ cladding diameter multiplied by the number of fibres) then influences the spectrograph design (§4.4.4), which for SPIRAL was realised as a double-pass spectrograph with the grating in a near-Littrow configuration. After describing the assembly and testing of the fibre-feed (§4.5-4.6), the alignment procedures for both modes on the telescope are discussed and the performance of the spectrograph is evaluated (§4.7).

SPIRAL A is a prototype and during the course of its construction and testing, several problems were discovered with the stability of the spectrograph and the fixing of optical fibres to the

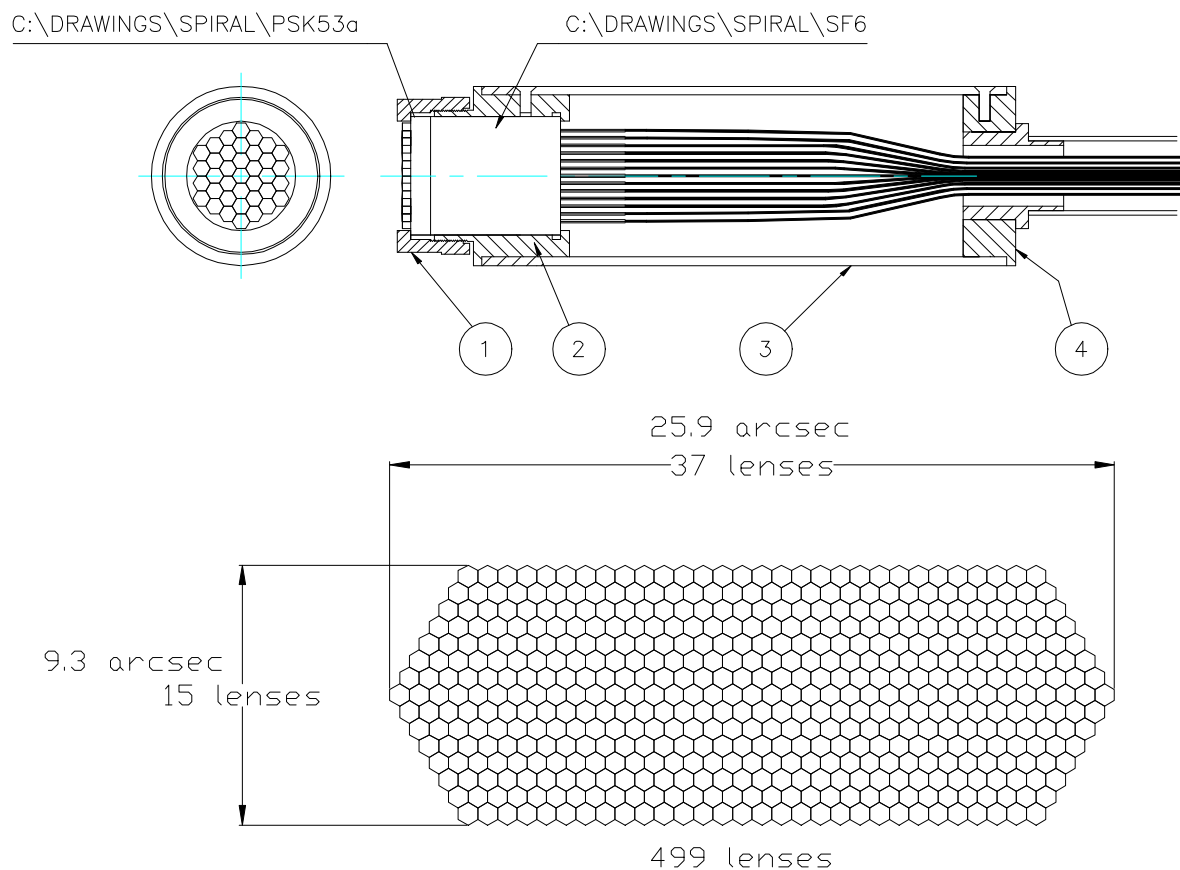


**Figure 4-1** Diagram of the SPIRAL Phase A and Phase B lens arrays. The upper figure shows the lens array unit design for Phase A with its 37 lenslets and the lower diagram shows the proposed lens array for Phase B.

back of the lens array. A discussion of the practicality of the pupil imaging mode and suggestions for avoiding the problems discovered in Phase A form the conclusions in this chapter (§4.8).

## 4.2 Overview of the design

SPIRAL consists of 37 close-packed lenslets forming a hexagonal array (Figure 4-1). Phase B is the large scale instrument, containing 499 close packed lenslets arranged in a ‘fat slit’ configuration. Techniques were developed for the building of macro lens arrays, the alignment of the lens array with appropriate optical fibres and the construction of fibre slits suitable for spectrographs. By building the SPIRAL prototype the full expense of a large lens array was avoided whilst allowing for the testing of the novel technique.

### 4.2.1 Physical layout of the fibre feed

A layout of SPIRAL on the AAT is shown in Figure 4-2. The design is split into four main components: the fore-optics, the lens array, the fibre slit and the spectrograph. The spectrograph was constructed independently at the Anglo-Australian Observatory (AAO) and the rest of the system was constructed in Cambridge. The preliminary optical design was done by Ian Parry and the detailed

design was performed by Damian Jones (private communication). The spectrograph lenses were manufactured by INOAE in Puebla, Mexico.

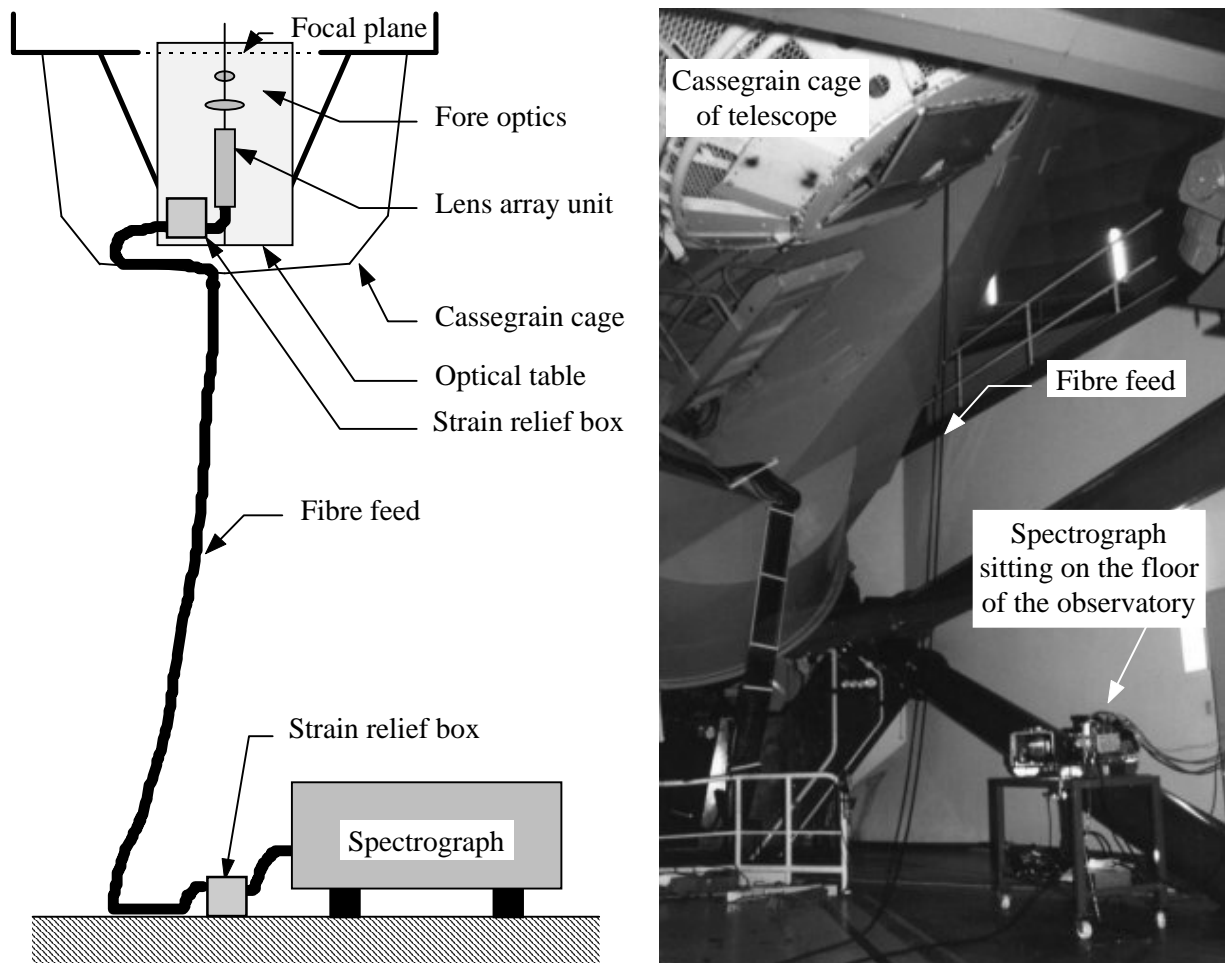


**Figure 4-2** Layout of the fibre feed on the Anglo-Australian Telescope. The spectrograph in the image is shown without light-proof covers. The strain relief box for the fibre slit end is mounted underneath the spectrograph framework.

Light enters the Cassegrain focus from the telescope and passes through fore-optics into the lens array, all of which are fixed onto an optical table in the Cassegrain cage. Optical fibres connected to the back of the lens array pass through the first strain relief box and out of the cage down to the spectrograph sitting on the floor of the observatory. A second strain relief box on the outside of the spectrograph leads to a fibre slit where the fibres are reconfigured into a suitable straight slit. The light is dispersed in the spectrograph and the fibre spectra imaged on a Charge Coupled Device (CCD) mounted inside a liquid nitrogen cooled vacuum dewar.

### 4.3 The observational modes

There are two observational modes in SPIRAL - one for integral field spectroscopy (IFS), and one for single object spectroscopy (SOS). Each mode requires a different optical arrangement of fore-optics in front of the lens array.

#### 4.3.1 Integral Field Spectroscopy

The IFS mode uses all 37 lenses to spatially sample the sky in a close packed hexagonal pattern. Optimum sampling occurs for two spatial elements matching the seeing of the telescope (Nyquist sampling) and with a median seeing of one arcsecond on the AAT this corresponds to a scale of 0.5 arcseconds per lenslet, giving a hexagonal array that is 3.5 arcseconds across the corners.

Light from the telescope focus passes into a magnifying lens which produces an image of the telescope pupil (the primary mirror) behind it and an image of the sky at a larger scale onto the lens array. The large field lens in front of the lens array images the common pupil to infinity so that the pupil images formed by the lens array all fall directly on the axis of the lenslets and onto the end of each fibre (Figure 4-3).

The image of the telescope pupil completely fills the 50 $\mu$ m core of the fibre, but by adjusting the power of the magnifying lens the sampling on the sky can be changed. By making the image scale less than 0.5 arcseconds per lenslet, the image of the telescope pupil becomes smaller and under-fills the fibres. On the other hand, increasing the image scale causes the telescope pupil to become larger

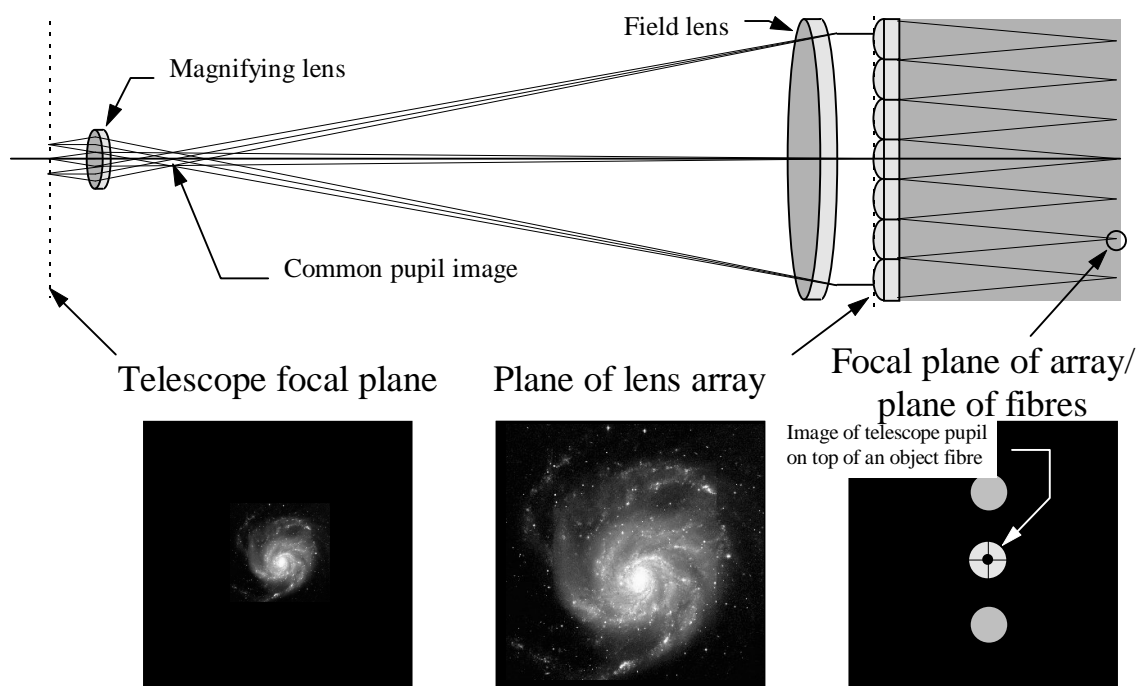


**Figure 4-3** *Layout of the fore-optics for the integral field mode.* In the integral field mode, the fore-optics magnify an extended object to match the plate scale of the lens array with the seeing. At the focal plane of the fibres each lenslet projects an image of the pupil onto the end of the object fibre. The two sky fibres (above and below the object fibre) are not used in this mode.

than the fibre and the light is lost. One can always go to a finer sampling scale without light losses, but not to a larger one.

### 4.3.2 Single Object Spectroscopy (Pupil imaging)

Single object spectroscopy (SOS) is classically performed with a long slit (LS) spectrograph. The slit is placed across the star's image and an exposure taken - in the resultant spectral image the object's spectrum can be seen superimposed on a long slit image of the night sky spectrum. It is this large spatial sampling of the night sky which leads to an accurate estimation of the sky background, and makes the LS spectrograph suitable for faint objects where sky background subtraction is needed. However, there are certain problems associated with LS spectroscopy.

SOS with a slit suffers from transmission variations due to slight pointing and focus errors and accurate spectrophotometry is very difficult to achieve (see Chapter 3). The width of a slit is a compromise between obtaining more throughput flux or increasing the spectral resolution. In LS spectroscopy the adjustment of the slit to the telescope point spread function (PSF) is difficult - one would like to minimise the light loss with a slit width significantly larger than the PSF, but small displacements of the object with respect to the slit centre lead to asymmetric illumination and produce a systematic wavelength error (§3.4). With a fibre fed spectrograph this is not the problem due to the radial scrambling properties of the fibre (§2.2).

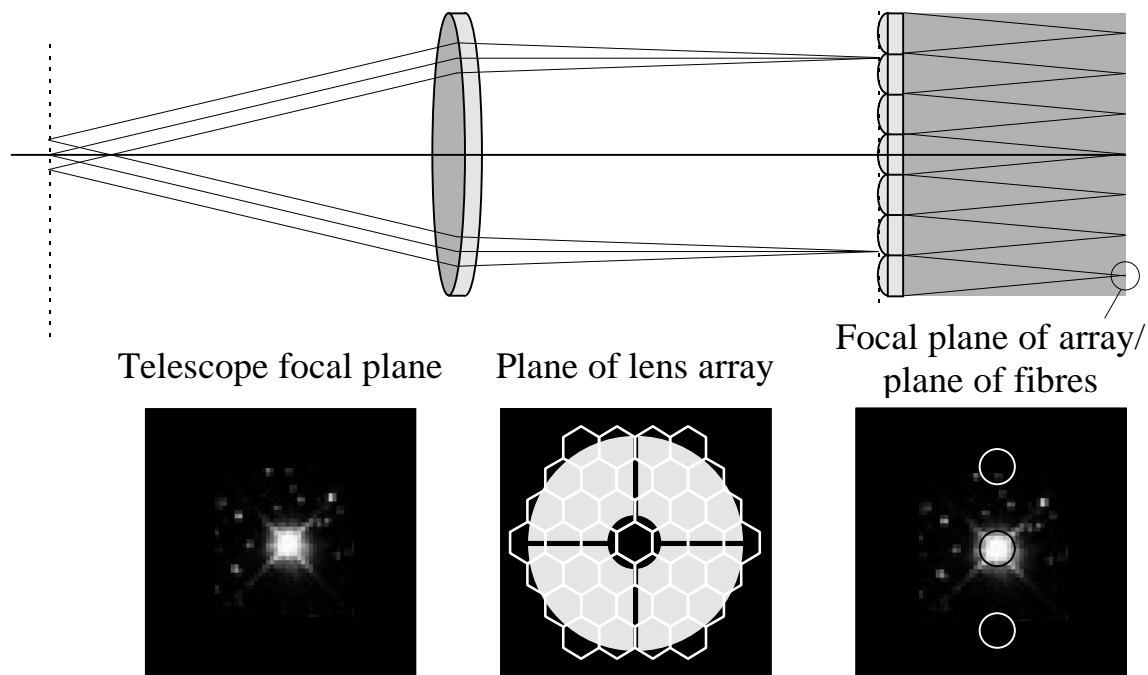


**Figure 4-4** *Pupil imaging mode.* The telescope looks at a single unresolved object (such as a star) blurred only by seeing conditions. By projecting the pupil image of the telescope onto the lens array, the plane of the sky is then imaged in the fibre plane. The image scale at the fibres is dependent on the size of the pupil image on the lens array. The stellar image can be matched to the fibre diameter and the two sky fibres sample the sky background subtraction.

With SPIRAL, ‘pupil segmentation’ (PS) or ‘pupil imaging’ can perform high spectral resolution faint object spectroscopy in moderate seeing conditions. By imaging the pupil of the telescope onto the lens array, the spatial resolution of IFS is lost but now an image of the sky is located in the plane of the fibres (Figure 4-4). The diameter of a star image on the end of the fibre is described by Equation 3-3. By adjusting the power of the fore-optics the image scale of the sky in the plane of the fibres is changed to match the object fibres with the current seeing conditions at the telescope. The angular diameter of the fibres on the sky is given by rearranging Equation 3-3 to give:

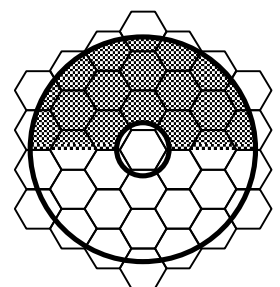
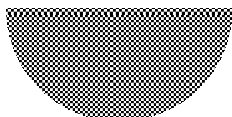
$$\alpha_{fibre} = 206265 \times 10^{-6} \cdot \frac{D_{fibre}}{D_{sub} \cdot f_{fibre}} \quad (4-1)$$

where  $D_{sub}$  is the diameter (in metres) of the mirror subtended by one lenslet in the lens array and  $D_{fibre}$  is the diameter of one fibre (in microns). Hence the image scale (as arcseconds/mm) in the focal plane of the fibres can be written as:

$$scale = \frac{206.265}{D_{sub} \cdot f_{fibre}} \quad (4-2)$$

This combined with the distance between the sky fibres on the back of the lens array determines the separation of the fibres on the sky. Specific examples are given in Table 4-1.

Only the object fibres need to be positioned accurately on the optical axis of their respective lenslets, as the sky fibres could sample any arbitrary patch of sky nearby for the background. Having a spatial spread of sky fibres about the object fibres would give a better estimate of the local sky



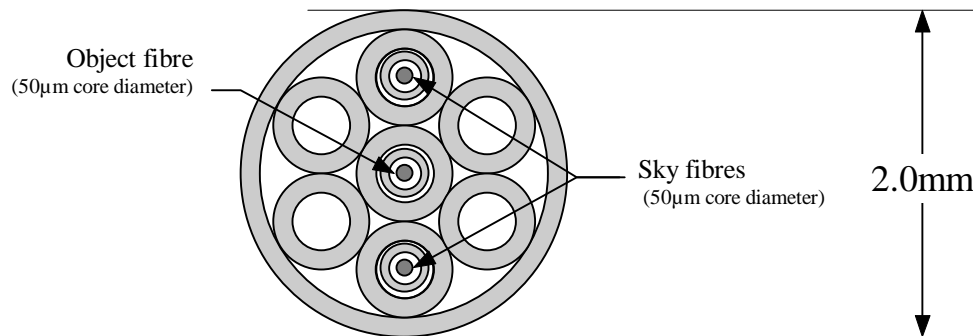


**Figure 4-6** Face-on view of a SPIRAL fibre ferrule. This diagram shows how the two sky fibres and one object fibre are kept in a straight line. The three small ferrules are supported in a close-packed formation by the addition of four empty ferrules.

background, but if a nearby star falls on the background fibres then signal from those fibres is lost. The placement of sky fibres for SPIRAL is shown in Figure 4-6.

The ferrules that hold the fibres in a single SPIRAL fibre ferrule unit do not form a tightly-packed hexagonal array (see Figure 4-6). The outer diameter of the ferrules has a limited accuracy due to their manufacture, on the order of 2 microns (Lee 1997). If the ferrules were made perfectly then they could be assembled to form a perfectly regular array. However the small manufacturing errors cause tightly fitting ferrules to stick together during assembly and lead to fibre breakage. By choosing stock catalogue ferrules that can form loose packed arrays, assembly is more rapid.

There are two sky fibres per object fibre in SPIRAL, but this number could be as large as packing space on the back of the lens array permits. The separation of all the fibres on the sky also scales with the power of the fore-optics lens. With the SPIRAL ferrules, if the sky fibres are 60 arcseconds apart on the sky when the object fibre is matched to 3 arcsecond seeing, they will be only 20 arcseconds apart if the fore-optics are then chosen to match to 1 arcsecond seeing. As can be seen from Figure 4-5, the size of the pupil image changes for matching the fibres to different seeing conditions. Table 4-1 lists the various sub-apertures selected with different fore-optics. Here the versatility of the pupil imaging mode can be seen - by changing one simple lens the spectrograph can be matched to the seeing conditions at the telescope.

#### 4.4 Design parameters

The optimum input focal ratio for optical fibres is combined with the diameter of the telescope (Table 4-2) and typical seeing in Equation 3-3 to give the required fibre diameter. In this section implications for the design of the lens array and fore-optics are discussed, in addition to the mechanical design parameters for the conduit and fibre slit.

Diameter of the primary mirror	3.9 metres
Effective focal length of $f/8$ Cassegrain focus	$f_{\text{cass}} = 30.78\text{m}$ , $f/7.91$
Image quality for $f/8$ Cassegrain focus	With a perfect secondary, this gives a geometrical image with 80% of the light within 0.3" diameter and 99% within 0.65" diameter. 0.18" and 0.3" for 80% and 99% enclosed energy.
$f/8$ image scale and size	6.67"/mm and 40' diameter
Obscurations in $f/8$ configuration	The obscuration with the $f/8$ top end is 1680mm diameter (19%). Support vanes obstruct about a further 1% of the primary area. Unobscured area = $9.56 \times 10^4 \text{ cm}^2$ .
Typical seeing	1 - 2 arcseconds

**Table 4-2** Parameters of the Anglo-Australian Telescope

#### 4.4.1 The choice of fibre diameter, lens array and fore-optics

- Choice of fibre diameter

From Table 4-2,  $D_{\text{tel}} = 3.9$  metres and the typical seeing is on the order of 1 - 2 arcseconds. Choosing a reasonable input focal ratio for the fibres to be  $f/5.0$ , and matching the angular size of a fibre for optimal spatial sampling (the Nyquist condition) to be 0.5 arcseconds, Equation 3-3 gives the diameter of the fibre to be  $50\mu\text{m}$ .

The typical size of detector pixels in modern CCDs (typically  $25\mu\text{m}$  or less) means that for Nyquist sampling of the fibre spectrum, the fibre image should be  $\sim 50\mu\text{m}$ . This matches almost exactly with the diameter of the fibre and means that the spectrograph can be a double pass system. The width of a typical slit on an 8 metre telescope spectrograph is about  $250\mu\text{m}$  (§3.4.3), resulting in the need for a very fast camera to reduce the image scale to match that of the detector. Since the width of the fibre is only  $50\mu\text{m}$  then the camera and collimator optics can be the same set of lenses and the grating can be used in a near Littrow configuration (§4.4.4).

- The lens array

The lens array design follows from the fixed diameter of the fibres. The constraints are that the fibre is fed with an  $f/5.0$  beam and that optical fibres are able to be individually positioned with respect to the optical axis of lenslets in the array. To ensure a stable optical alignment of fibres with the optical axis of their respective lenslets, a solid glass substrate is used for the base of the lens array (see Figure 4-7). 37 hexagonal lenslets each with a nominal height of 2.0mm and a point to point distance of 4.0mm are close packed to form a hexagonal array pattern. Two pieces of glass form a flat onto which the lenslets are fixed and their thickness is optimised to minimise chromatic aberration. The total thickness of the flat is such that the focal plane of the lenslets is formed on the back surface. It is onto this surface that the fibres are fixed permanently in place.

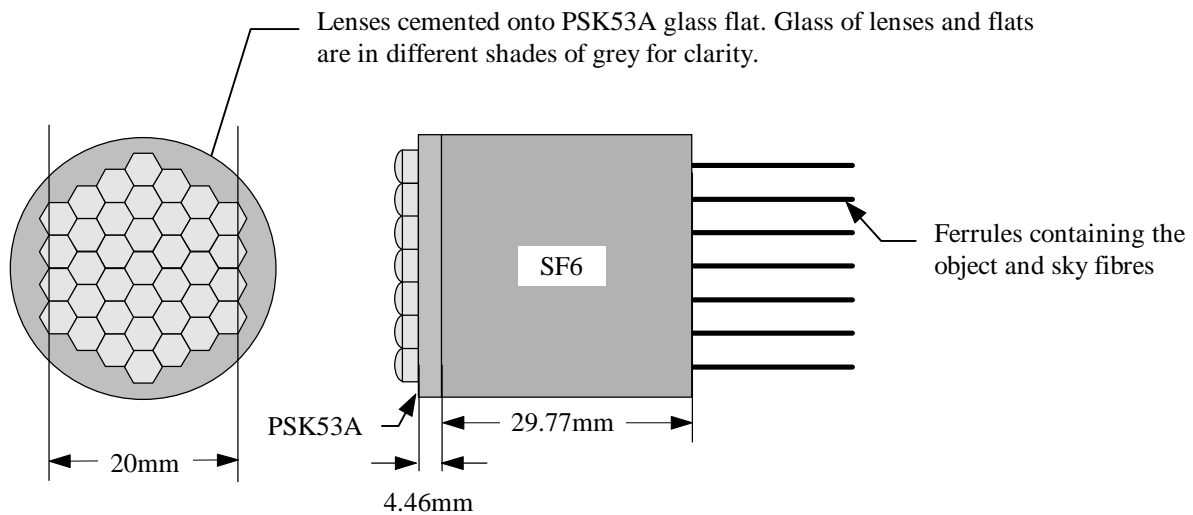


**Figure 4-7** Layout of the SPIRAL lens array and fibre ferrules. The lenslets are fixed onto a cemented glass flat whose thickness is equal to the focal length of the lenslets. Fibre ferrules are fixed onto the back of the lens array by means of UV curing epoxy.

The two glasses used in the design are PSK53A (a crown glass) and SF6 (a flint glass). The detailed dimensions of the glasses are determined by using the ZEMAX optical design program.

The optical fibres need to be fixed onto the back surface of the flat with a suitable mechanical support, not only for their final fixing on the back of the array but also for when they are being polished. A design using nested concentric stainless steel ferrules was introduced, where epoxy held the fibres in place within a tough capsule - the design used is shown in Figure 4-6, Figure 4-8 and Figure 4-16.

- The IFS fore-optics

The schematic for the IFS fore-optics design is shown in Figure 4-9. Here the two lenses enlarge the image scale of the telescope to match the size of the lens array. The field lens (FL) and magnifying lens (ML) act as an image enlarger, with the magnification approximately equal to the ratio of their focal lengths, i.e.  $m \approx F_{FL}/F_{ML}$ . The AAT Cassegrain plate scale has a scale 6.67"/mm and the lens array requires a scale of 0.125"/mm to correspond to 0.5"/lenslet. This sets  $m = 53.36$ .

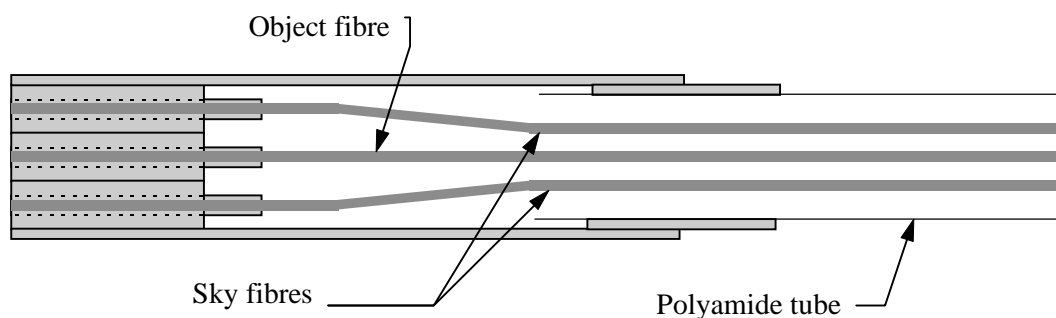


**Figure 4-8** Cross-section of a SPIRAL fibre ferrule.

The next consideration is the FL with its diameter and focal length. For the whole lens array to be covered in the field, the FL has to have  $D_{FL}$  greater than the diameter of the lens array. The focal length of the FL is the most unconstrained parameter, with its constraints being that the focal ratio is slow enough for a simple design, its focal length large enough to define a realistic focal length for the ML (see next paragraph) and that it is short enough to fit the whole arrangement onto the optical table.

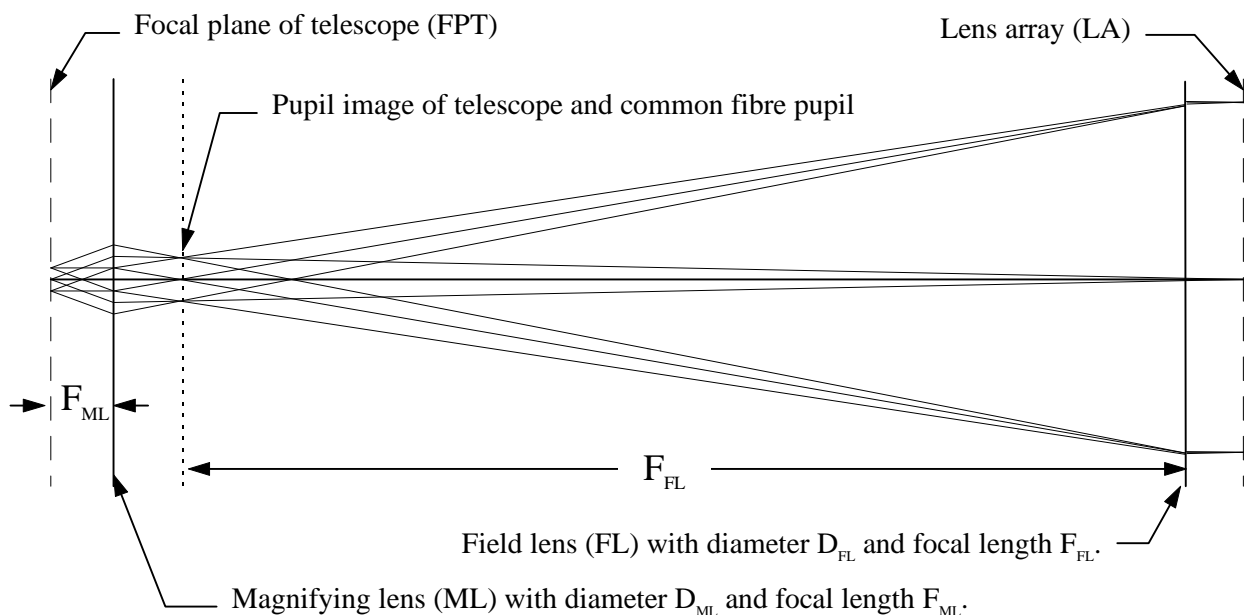


**Figure 4-9** Schematic of the IFS fore-optics. This diagram shows the relevant dimensions of the optics involved in the design.

Setting  $F_{ML}$  to be 10mm gives  $F_{FL}$  to be approximately 600mm.

The final number is the diameter of the ML - the minimum size of this is determined by the size of the pupil image it produces. The primary mirror can be considered to be at infinity since its effective focal length is much larger than the focal length of the ML (30.78 metres compared to  $F_{ML} = 10\text{mm}$ ) - this makes the pupil image (i.e. the image of the primary mirror) to be  $F_{ML}/7.91 = 1.26\text{mm}$  in diameter. These numbers are entered as the 'ideal' lenses in Table 4-3 and the optical design program is then used to optimise and select suitable lenses for the design.

	Ideal lens		Chosen lens		
	Diameter (mm)	Focal length (mm)	Diameter (mm)	Focal length (mm)	Model of lens
ML	> 1.4	10	6	10.39	S+H 322260
FL	> 25	533.6	31.5	598.55	S+H 322277

**Table 4-3** Ideal and real lenses for the IFS mode.

- The PS fore-optics

The pupil segmentation mode has a simpler design with the fore-optics consisting of only one lens. The schematics are shown in Figure 4-10. One lens re-images the pupil onto the lens array and the size of the pupil image on the array dictates the image scale in the plane of the fibres as discussed in §4.3.2.

The fibres have the largest angular diameter on the sky when the image of the telescope primary mirror fits just within the area of the lens array (see Figure 4-5a). For the AAT, this occurs for an image of diameter 20mm, so the diameter of the pupil imaging lens (PIL) needs to be at least 20mm. Given that the input focal ratio from the telescope is  $f/7.91$  this gives a focal length of 158.2mm. Any lens with the same diameter and a shorter focal length will give a smaller angular diameter for the fibre on the sky and fewer illuminated fibres (see Figure 4-5b and c).

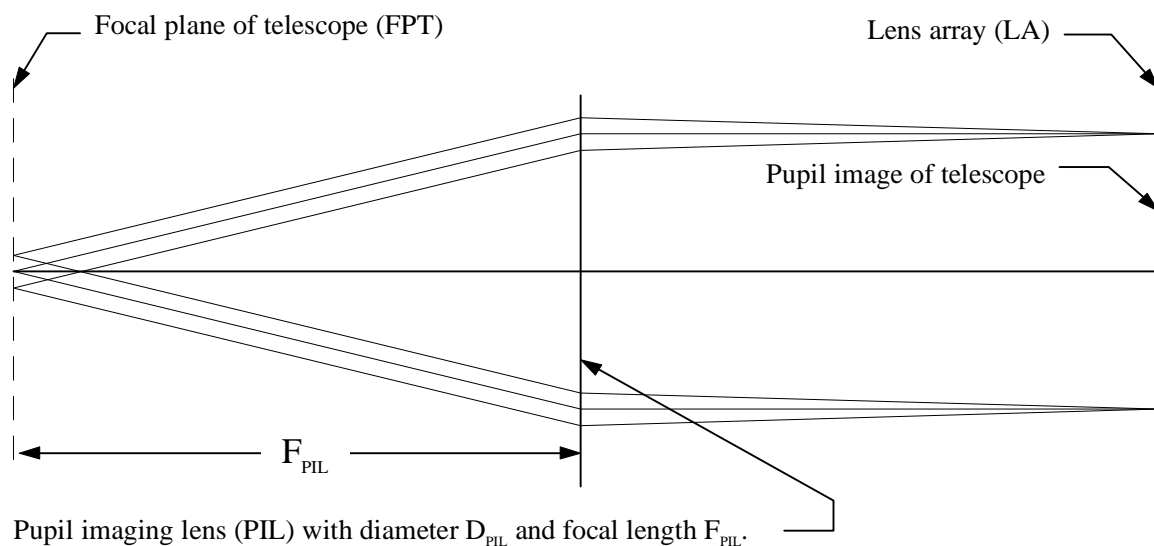


**Figure 4-10** Schematic of the PS fore-optics. The pupil imaging lens re-images the telescope pupil directly onto the lens array.

#### 4.4.2 Conduit and strain relief boxes

The minimum length of optical fibre needed is determined by the distance between the bottom of the Cassegrain cage and the location of the spectrograph sitting on the floor below (see Figure 4-2). The floor of the observatory is approximately 8 metres below the bottom of the Cassegrain cage with the telescope pointing at the zenith, and an extra 5 metres of clearance is needed to allow for telescope access to the rest of the sky, giving an absolute minimum length of 13 metres. Optical fibre is inelastic and although the breaking strain can be very high, shear forces can easily damage and destroy a fibre, so a covering that can protect the fibres from any undue stress and protection from the environment is needed.

Most conduit available can undergo longitudinal extension and compression of the order of 10% of their length. To prevent the fibre being put under tension or being compressed as the conduit

flexes, strain relief boxes are put into the optical fibre path as part of the conduit (see Figure 4-15). These boxes contain a loose coil of the optical fibre, and the coil can expand or contract as the conduit moves around with the telescope. In the case of SPIRAL it was thought necessary to have one box near each end of the fibre feed considering the length of conduit used.

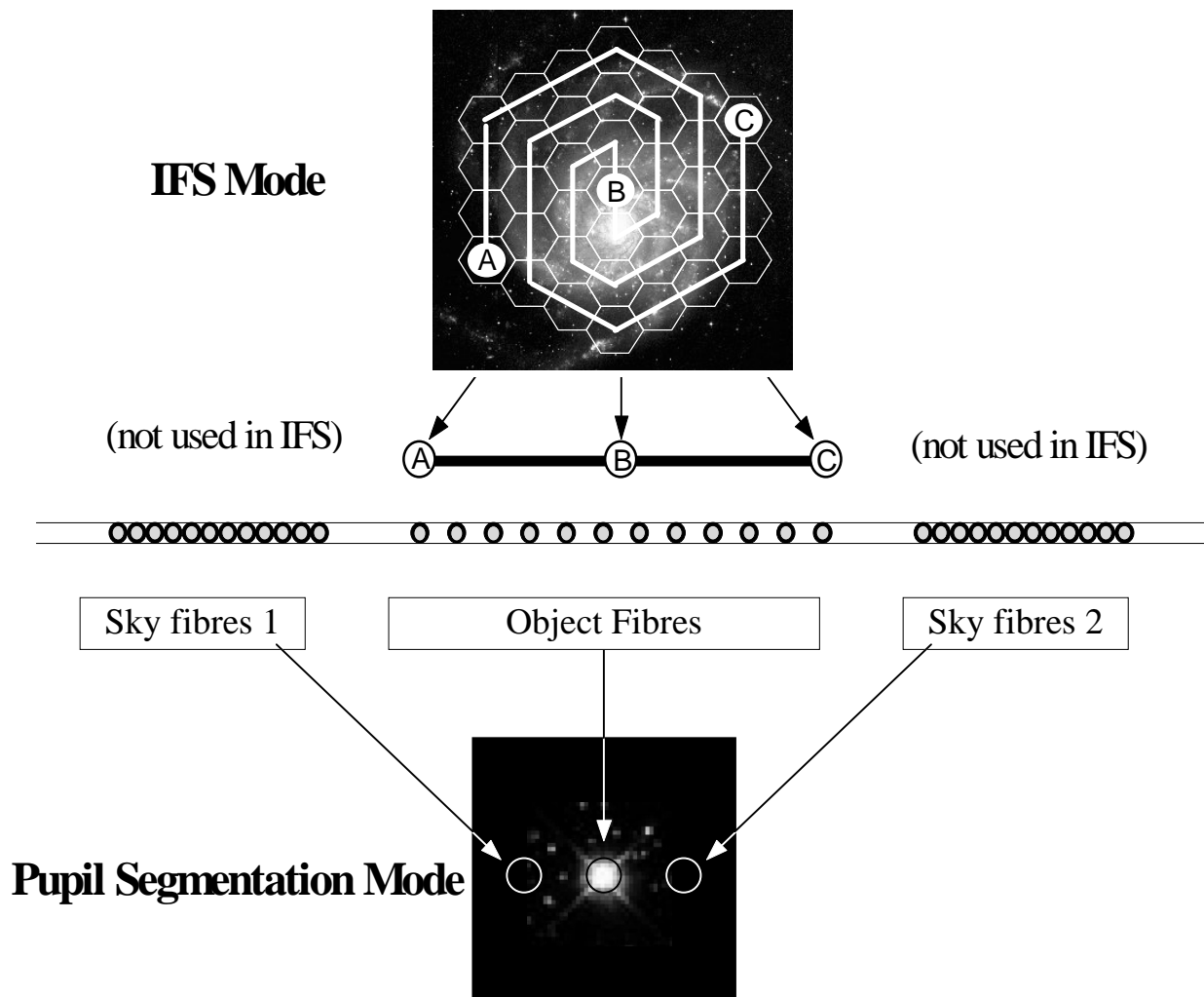


**Figure 4-11** Schematic layout of the SPIRAL fibre slit. This diagram shows how the fibres are used in the two modes. If pupil imaging was the only mode in use on SPIRAL then the object fibres could be close-packed together like the sky fibres, as all the object fibres receive light from the same area of sky in that mode.

#### 4.4.3 The fibre slit

The fibres in the fibre slit correspond with lenslets in the array in a pre-defined pattern, so that images of the sky can be reconstructed from reduced fibre spectra at a later date (see Figure 4-11). The fibres are arranged in such a way that fibres in the fibre slit are contiguous on the sky. In this way, any cross-talk introduced from the extraction of overlapping fibre spectra was from adjacent areas of the sky. This effect is discussed further in §6.7.

In the PS mode each group of fibres contains the same signal, so the sky fibres can be packed together on the fibre slit as close as possible. Since the object fibres are used in the IFS mode they have to remain spatially distinct on the slit for image reconstruction purposes.

The PS mode is used for faint objects at high resolution - in this spectral domain this means that the number of photons per unit wavelength is distributed over many pixels on the detector, and it may be the case that readout noise from the CCD is the dominant source of noise. CCDs can be operated in mode called ‘on chip binning’ where the charge in a given number of pixels can be added together and this ‘super-pixel’ incurs the same readout noise as a single pixel. This means that a higher signal to noise ratio can be achieved. By close-packing the fibres the number of pixels added together is reduced, and the potential gain for faint object spectroscopy is increased. This is discussed further in Chapter 6.

#### 4.4.4 The spectrograph

The design brief for the spectrograph given to Damian Jones is shown below in Table 4-4.

Wavelength range	370-900nm
Total input slit length	25mm
Spectral imaging area	24.6mm x 24.6mm for Tek 1024 <sup>2</sup> CCD (24µm pixels) 30.7mm x 61.4mm for MIT/Lincoln Lab 2Kx4K array (15µm pixels)
Input focal ratio and focal length	$f/4.8$ , spectrograph pupil 150mm diameter, focal length 720mm
Input fibre width	50µm

**Table 4-4** Parameters for the SPIRAL Pupil Spectrograph (SPS)

As can be seen from the table, the input focal ratio for the spectrograph is  $f/4.8$ , slightly faster than the  $f/5.0$  beam entering the fibres. This is to allow for FRD broadening of the beam as described in §3.2. The spectrograph also has to produce monochromatic images over the whole area of the Tek CCD, requiring imaging of a slit length of 25mm.

With the diameter of the fibres (50µm) matching well to the Nyquist sampling of 2 pixels ( $2 \times 24\mu\text{m} = 48\mu\text{m}$ ), the camera and collimator can be combined to make a double pass system, with a total magnification of unity. This then allows the grating to be used in a near-Littrow configuration. A Littrow configuration is where the incident angle of light equals the diffracted angle of light from the grating. In this mode, the grating is used at its highest theoretical efficiency. For a double pass system the Littrow condition is exact only for object and image superimposed on each other, but by separating the fibre slit and detector beams by 22.5mm, the deviation from the Littrow configuration is minimal. The resultant design is shown in Figure 4-12.

The most suitable optical configuration for the spectrograph is a field-flattened Petzval system, otherwise known as a P1 Petzval configuration (Figure 4-12). This consists of two separated positive doublets (L2 and L3) followed by a field flattening singlet (L1) near the focal plane. A small reflex prism brings in the fibre slit close to the optical axis of the system, and the grating G1 sits in the collimated space beyond L3.

The design also allows for a rotation and tilt of the dewar, eliminating the need for an extra field correcting lens and thus reducing the cost of the system - a plot of chromatic focal shift shows the range of travel and tilt needed to refocus the CCD from one wavelength range to another (Figure 4-13).

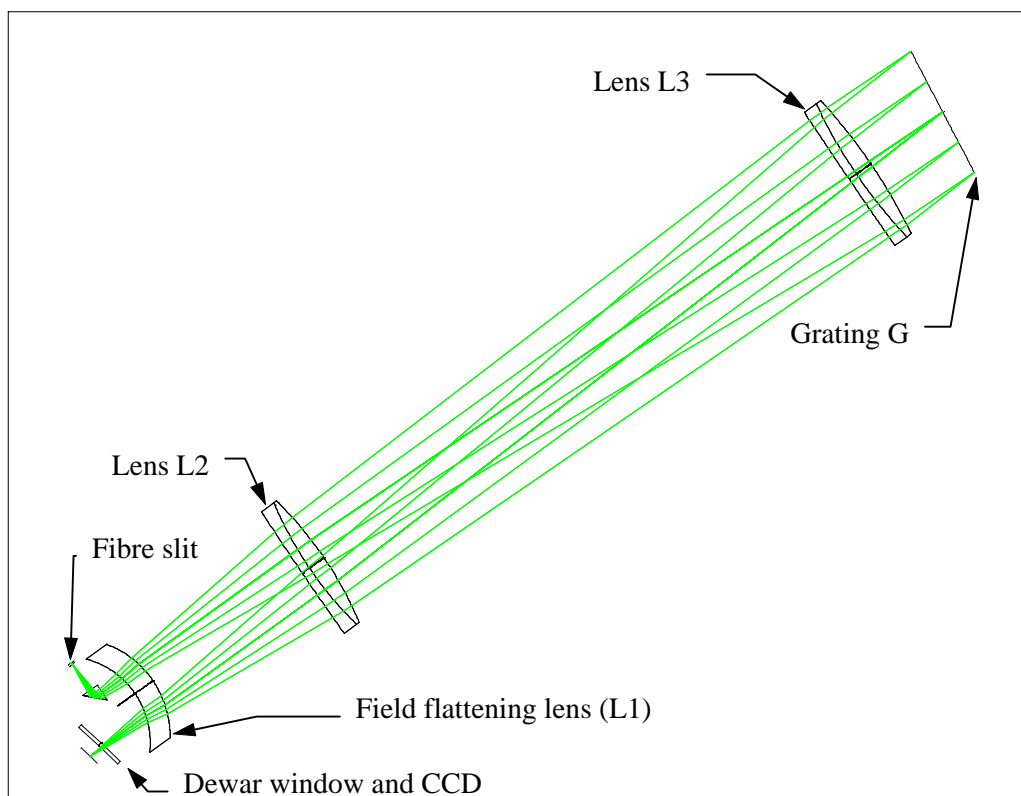


**Figure 4-12** *Layout of the SPIRAL spectrograph.* This ray-traced diagram shows monochromatic light emerging from the fibre slit (lower left) passing through the Petzval system (L1-3) acting as a collimator, onto grating G and back through L3-1 to be focused on the detector inside the dewar (not shown).

## 4.5 Construction of the fibre feed

### 4.5.1 Conduit and strain relief boxes

The first component built was the optical fibre conduit. A steel wound PVC covered conduit (supplied to RS by Adaptaflex) was used - the conduit flexes freely but locks tight with any attempt to bend it below a minimum radius of 25mm<sup>1</sup>. Its wound steel construction can withstand a crushing

<sup>1</sup> Taken from 1996 RS Catalogue.

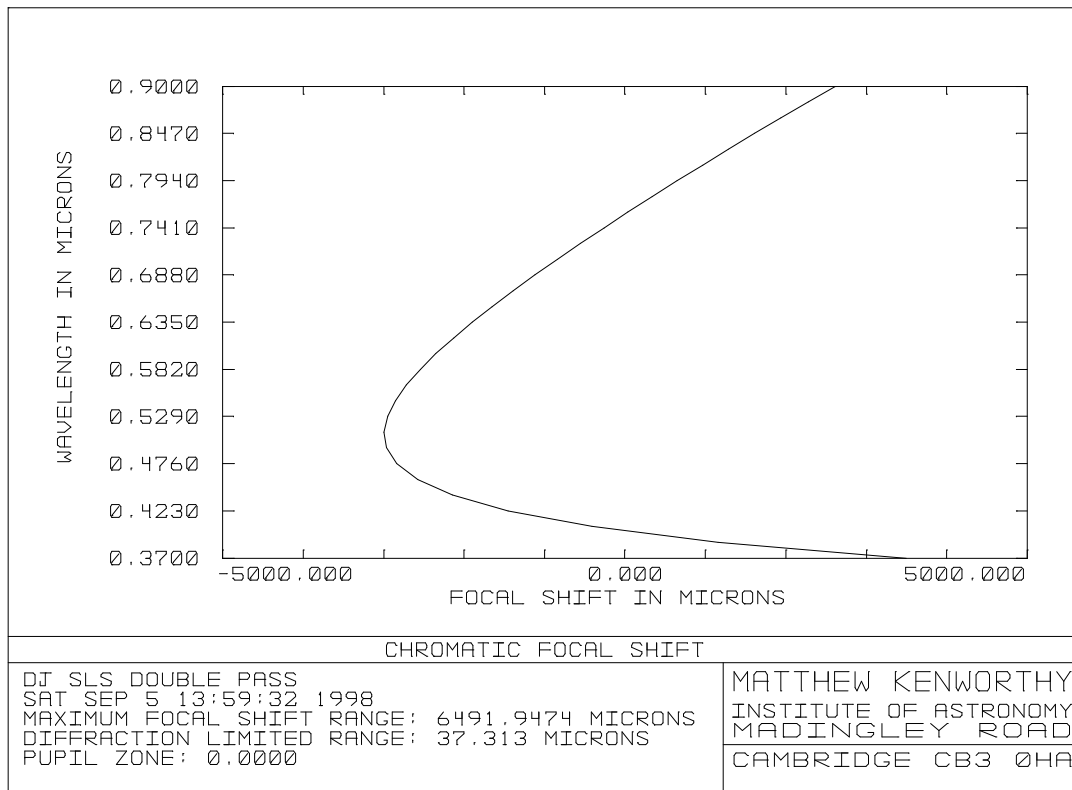


**Figure 4-13** The chromatic focal shift for the SPIRAL Littrow spectrograph. This graph shows how the focus varies with wavelength. For 500nm it is difficult to select an optimum focus and tilt for the CCD.

force of up to 1250 Newtons over 50mm<sup>1</sup>. Another useful property was that it could not be easily twisted longitudinally, thus ensuring that any handling did not twist and put extra strain on the optical fibres. The total length of conduit cut was 17.5 metres, enough for two strain relief boxes to be put into its length a metre in from either end. The conduit was cut with a hacksaw and fitting rings allowing coupling to aluminium fittings were glued in place. The lengths cut for the final SPIRAL conduit are listed in the Figure 4-14.

As can be seen from Figure 4-15, the fibres entered and left each spare length box near the corner. This allowed the fibres to loop around with the minimum of stress inside the box before passing out again on the other side. Both boxes were made out of die-cast aluminium and were emery papered inside so as to remove any rough surfaces that might damage the outer layers of the fibres and ultimately damage the fibres themselves. Extra care was taken to ensure that the fibres could not

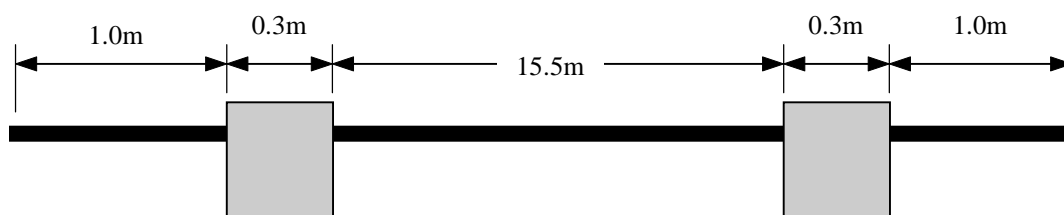


**Figure 4-14** The fibre feed. This diagram shows the layout of the SPIRAL fibre conduit. Two strain relief boxes compensate for the expansion and contraction of the conduit.

be trapped underneath the edges of the lid and consequently be broken.

After constructing the conduit complete with the spare length boxes, a small wooden bead attached to strong nylon thread was blown through the conduit with compressed air. This thread was then used later on to draw the fibres through the conduit and into their final position. The optical fibre was supplied on three reels each containing a kilometre of the fibre. The fibre needed to be laid out, cut to the required length and fed into the protection of the conduit.

Five tables were placed end to end and covered with computer fan-fold paper. 120 strands of optical fibre were laid out and taped to the ends of the table which were 18 metres apart. To help gather the fibre strands together, a one inch strip of paper was wrapped around one end of the fibres and cyanoacrylate (trade name of 'Super Glue') was run into the paper roll to form a strong fixed end from which all the fibres could be drawn from.

The conduit was laid out next to the fibres and the nylon thread attached to the fibres. By slowly drawing the nylon thread through, the fibres were pulled into the conduit. Care was taken that no fibres were tangled up - if any loops of fibre were seen the process was paused whilst the fibres were untangled. With the fibres in the conduit and 50cm of fibre hanging out of each end, the fibres were now protected and were ready for the assembly of the lens array.

#### 4.5.2 Lens array unit and fore-optics

All the fore-optics used were standard Spindler and Hoyer lenses and were mounted together with the lens array unit on an optical table fixed at the Cassegrain focus of the telescope. For the lens

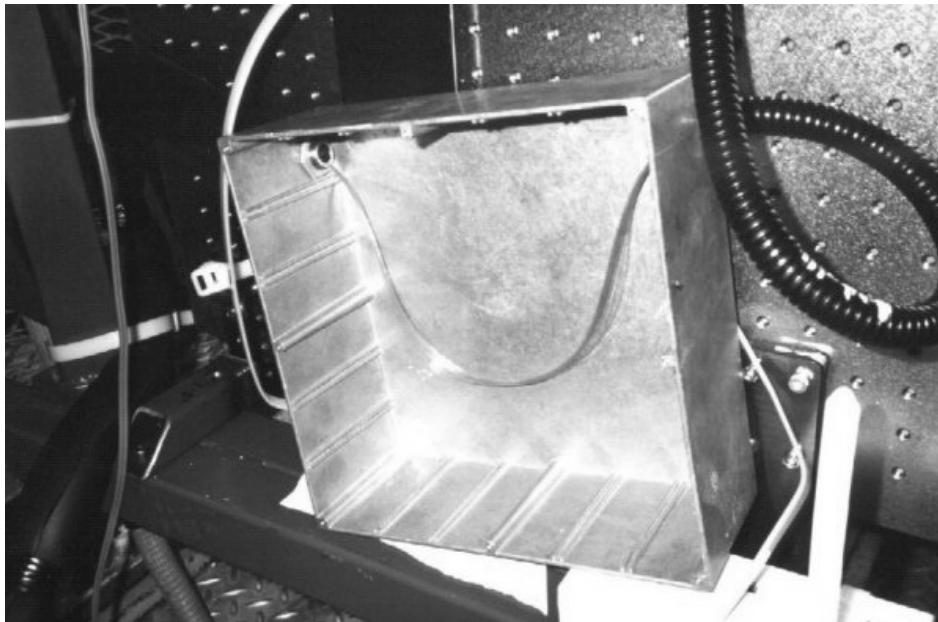


**Figure 4-15** *The strain relief box at the lens array end of the conduit. Here the lid of the box has been taken off to show the fibre strands partially retracted into the conduit. This picture was taken with the telescope tilted over to its most Northern declination as part of the optical table flexure test.*

array unit, the lens array substrate was constructed first, then this was put into a Hoyer mount suitable for fixing to an optical table, suitable for the placement of optical fibres on the back surface. The fibres were then assembled into ferrules, polished and fixed onto the back of the lens array substrate.

37 singlet lenslets made of PSK53A glass were selected by their surface quality and focal length from an initial batch of 50. The most critical parameter was the distance between the focal plane of the lenslet and the back surface of the lenslet. The focal length of all 50 lenslets were measured before selecting 37 lenses with their focal lengths closest to the mean. The mean focal length in air of all 50 lenslets at 639nm (a No.29 Grub Parsons interference filter with 12nm bandwidth) was  $(19.27 \pm 0.02)$  mm. The thickness for the two flats was then calculated using the mean focal length of the lenses.

An aluminium former in the shape of the lens array was placed over the PSK53A substrate (see Figure 4-17). This former allowed the lenses to be held in the correct configuration during the lens array construction.

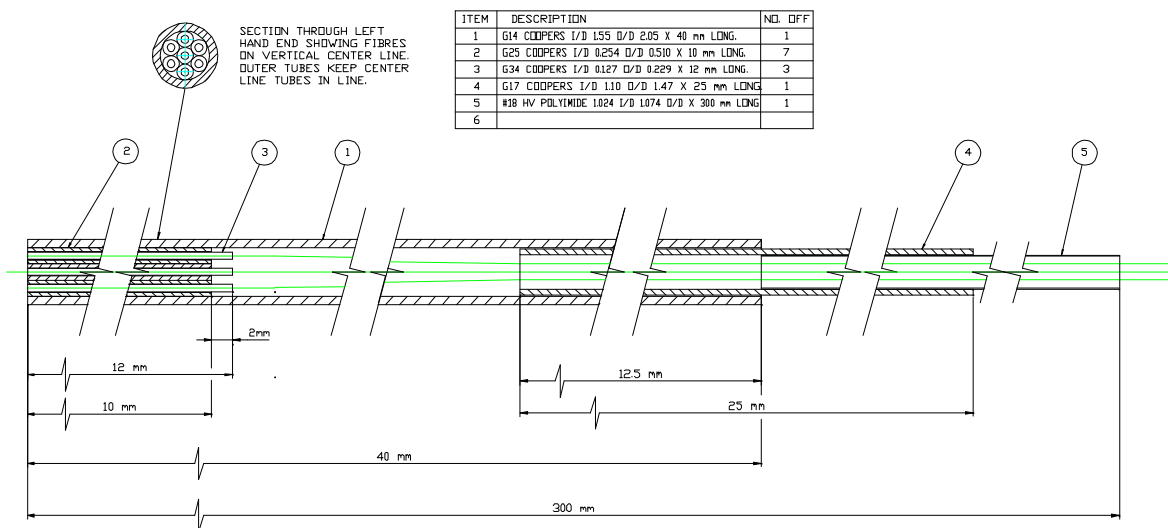


**Figure 4-16** Diagram of the SPIRAL fibre ferrule. This drawing shows the layout of the different ferrules used. The text uses the numbering convention in the table on the diagram.

Each lens was carefully cleaned with acetone and then a small drop of UV curing epoxy was put onto the back surface. A pair of tweezers then transferred the lenslet onto the substrate, making sure that no excess epoxy ran between the lenslets. If the epoxy was cured whilst on the upper curved surface of the array then this would lead to scattered light losses. Any excess seepage from crevices required the affected lenses being removed and cleaned thoroughly with a moist cloth before reassembling. After all the lenses were in place and carefully checked, the epoxy was cured with a UV lamp. The aluminium former was removed and the completed lens array PSK53A substrate was

fixed to the SF6 substrate before being inserted into the brass lens array holder. The completed solid lens array unit was held in its brass holder by a flange around the top edge.

The unsorted fibres were then divided into three groups of 37 - one group would be the object fibres and the other two groups would be the sky fibres with one sky fibre either side of each object fibre. There were three fibres per lenslet - in the IFS mode only the object fibre was used, but in the PS mode the sky fibres used to sample the sky background (Figure 4-6, Figure 4-8 and Figure 4-16). The fibre ferrules were then fixed onto the back of the lens array substrate as described in detail below. The fibres then ran from inside the ferrules into a set of flexible polyamide tubes. These tubes then guided the fibres safely into the steel-wound conduit, ensuring that if any tension was put onto the fibres then they were pulled laterally onto the inside of the polyamide tubes (see Tube Number 5 in Figure 4-16) and not onto any sharp metal edges at the ends of the ferrules (4). The long polyamide tubes also kept the triplets of fibres separate and prevented them from being tangled together during handling.

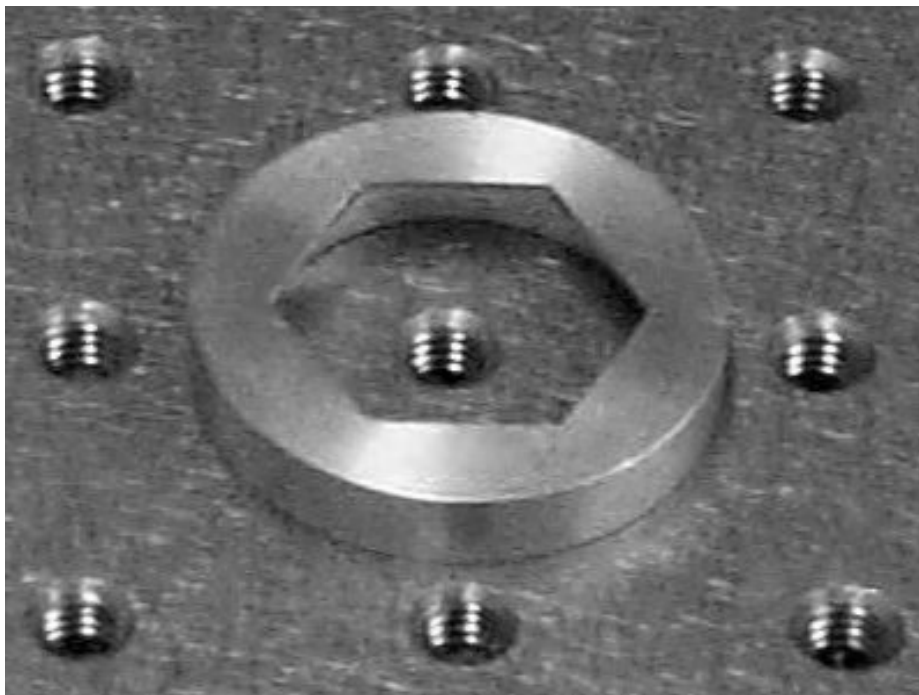


**Figure 4-17** Photograph of aluminium former used for SPIRAL array. The distance from one side of the picture to the other is approximately 50mm.

Although the general procedure for putting on fibre ferrules has been discussed in Chapter 3, the SPIRAL ferrules were more complicated to assemble due to their structure. First, the long polyamide tubes were threaded on over all three fibres, then the two outermost ferrules that thread together to form the outer ring (1,4) were slid on over the polyamide tubing (5). Two small ferrules

(3,2) were then slid on to each of the three fibres, completing the ferrule threading prior to fixing with epoxy.

There were two stages to the ferrule assembly process - firstly the fibres had to have their individual ferrules glued on. The three ferrules were then pushed together on a piece of paper to form a line. After curing, a scalpel was used to carefully lift the line of ferrules off the paper and to clean excess epoxy off the outside circumference of the ferrules. Care was taken not to break any fibres off at the end of the ferrules, as a slip of the scalpel led to easy breakage.

The second stage was to assemble the rest of the ferrule. To keep the three fibre ferrules (2) in a straight line within the larger ferrule (1), four empty ferrules (2) were used to pack together into a hexagonal pattern. Using the partially cured epoxy the fibres were fed into ferrule (1) along with the four extra ferrules. Tube (5) was connected to ferrule (4) and fed into the back of ferrule (1), completing the SPIRAL ferrule construction.

The fibre ferrules were now mounted, ready for their polishing. A machined metal block was used to hold the SPIRAL ferrules within the polishing jig and heat resetting resin was used to hold the ferrules in place (see §2.3). After removing the fibres and cleaning them of resin they were ready for alignment with the lens array. The layout of the apparatus is shown in Figure 4-18.

The lens array was mounted into the Spindler and Hoyer equipment and held the lens array parallel to the optics table. The field lens used in the IFS mode was fixed in front of the lens array and a graticule was fixed in front of the lens array and a graticule was fixed at the focal plane of the field lens. A TV camera connected to a TV monitor (not shown) used a microscope objective to produce an image of the graticule. The graticule defined

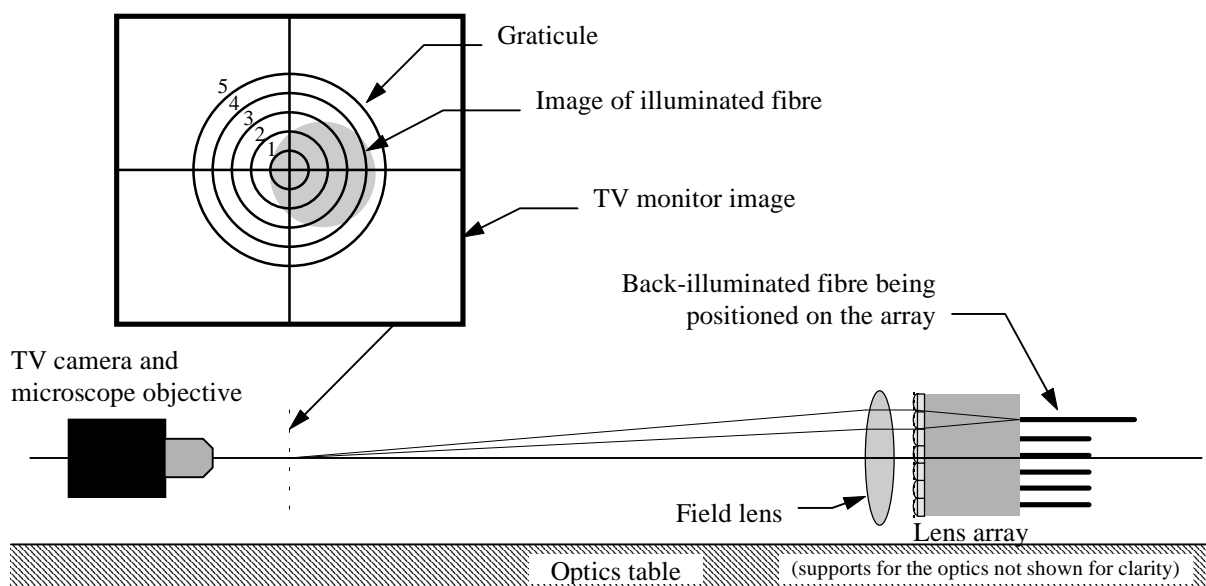


**Figure 4-18** *Aligning the SPIRAL fibre ferrules on the lens array.* The mounting post and supports used in the construction of the alignment optics were also used in the observing runs, so as to ensure a similar optical alignment on the telescope as possible.

the focal plane of the field lens, the position of which was determined by the method of auto-collimation.

Auto-collimation was performed by replacing the lens array with a mirror flat. Using the microscope to look at the image of the graticule the field lens was moved back and forth along the optical axis of the field lens until a superimposed inverted image of the graticule appeared on the graticule itself - the graticule was now in the focal plane of the field lens.

The flat was then replaced with the lens array in its brass holder. Any back illuminated fibre correctly aligned with the optical axis of a lenslet produced an image of the fibre on the graticule. By using a small metal arm attached to an x-y-z stage the fibres could be positioned onto the back of the lens array (Figure 4-19).

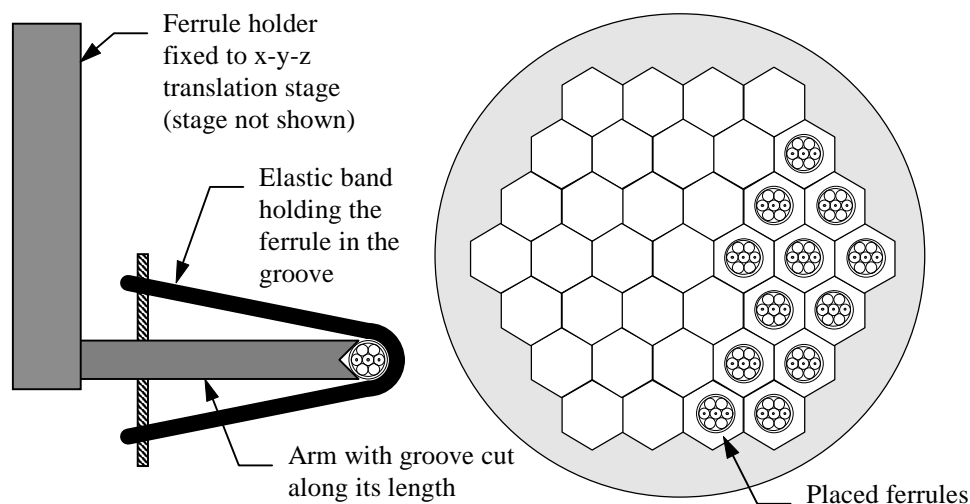


**Figure 4-19** *The order of fibre placement on the lens array.* This is a face-on view of the SPIRAL lens array, showing the projection of the fibre ferrules on the back surface of the lens array substrate. As the arm of the ferrule holder and x-y-z stage extend to the left, fibres must be placed on the array starting from the right-most edge.

Before fixing the ferrules permanently on the back of the lens array it was important to orient the ferrules so that the sky fibres were all aligned with respect to one another. By back-illuminating the sky fibres with a red filter the sky fibre image could be easily identified on the TV monitor and the ferrule rotated so that all the sky fibres lay in a horizontal plane parallel to the optical bench.

After fixing all the ferrules to the lens array the whole lens array was carefully rotated through a vertical plane until it was face down toward the optical bench. The metal sleeve of the lens array unit was carefully screwed into place on the brass lens array holder and the conduit arranged so that it could be easily sealed with the lens array unit. To provide mechanical support for the fibre ferrules, a potting compound was poured into the cavity formed by the metal sleeve and lens array unit. The potting compound (called 're-enterable polyurethane') cured into a soft, dense sponge that

held the fibres in place on the back of the lens array and protected the ferrules from snapping under any mechanical shock.

This completed the assembly of the lens array unit.

### 4.5.3 The fibre slit

All the fibres needed to be reformatted into a slit configuration that was perpendicular to the dispersion direction on the spectrograph CCD. The object fibres were spatially separated on the CCD as they contained different spatial information of the sky in the IFS mode (see Figure 4-11).

The object fibres were held between a polished aluminium plate and a custom made aluminium block with grooves cut by a CNC machine - this is indicated as the 'middle block' in Figure 4-20. Two separate side blocks held the sky fibres on the aluminium base of the slit either side of the object fibres.

An elastic band wrapped around the end of the fibre slit held all three blocks whilst the object fibres were inserted into their correct places. The grooves were numbered from 1 to 37, starting with the left hand side of the slit in Figure 4-20. Two short lengths of scrap fibre were inserted under grooves 3 and 37 so that the other fibres could be inserted under the middle block with the minimum of force. If fibres were pushed in too hard then they had a tendency to suddenly buckle and break, shortening the length of the available fibre. If this occurred too many times the fibres had to be rearranged from within the strain relief box to ensure all fibres lay flat in the metal trough.

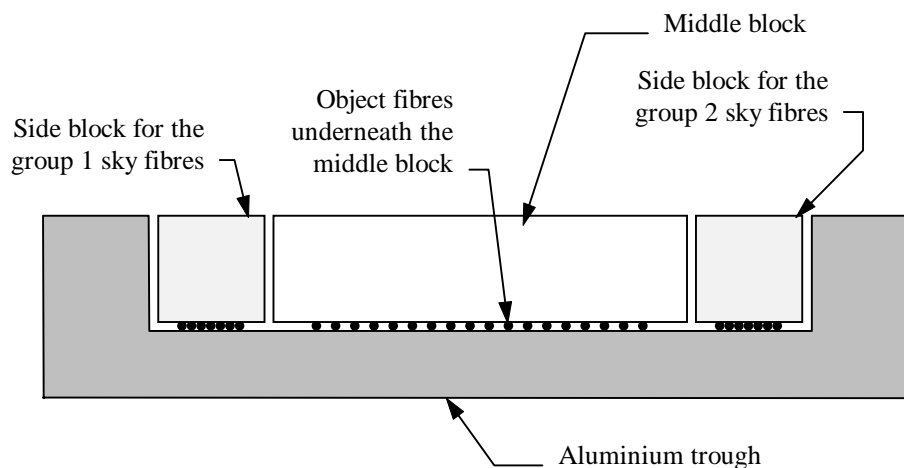


**Figure 4-20** End-on view of the SPIRAL fibre slit during assembly. This schematic drawing shows the relative positions of the blocks that hold the fibres in place. When the assembly was completed a cover was fixed across the top of the aluminium trough and blocks.

An object fibre was selected from the others by shining light into its associated lenslet on the array. The configuration of the fibres is seen in Figure 4-11, with A to C indicating the order from left to right. All but one of the lenslets were masked with card - a hole in the card allowed light to reach

the specified lenslet. After selection, the object fibre was inserted into the appropriate groove. The scrap fibres were removed and were replaced with their relevant fibres and consequently all fibres were correctly arranged under the middle block.

The object fibres were now fixed into their grooves with Araldite Standard epoxy resin, which had a typical cure time of 24 hours. The method for fixing the fibres in place was as follows:

- The middle block was moved backwards to leave ~5mm of trough in front of it.
- Epoxy was run along the front of the block.
- A small metal ruler placed underneath the overhanging fibres lifted the fibres up off the trough, allowing epoxy to run underneath them.
- The middle block was slowly moved forwards until it was flush with the front edge of the trough.

During the curing process the side blocks were removed and excess epoxy carefully wiped off. The epoxy was left to cure before assembling the sky fibre slits.

A different technique was pioneered for the placement of sky fibres. The requirement from design was that the sky fibres were close packed along the trough and that none of them deviated from this straight line. With the middle block fixed in place, the block and inside edge of the trough formed a smaller 'canyon' into which the sky fibres would lie flat. A small drip of UV epoxy was placed in the bottom of the trough and the sky fibres randomly placed on top of it. Capillary action now held the fibres down in position in the trough. By adding more epoxy and carefully stroking the fibres with a small brush the epoxy was dispersed evenly around the fibres and any overlapping fibres were naturally reorganised into a flat line by the brushing process. No side block was needed to hold the fibres in place as the epoxy provided enough surface tension. The seating of the fibres was checked occasionally by back-illumination of the lens array and examination with a hand held eyepiece.

When the fibres were satisfactorily positioned, a UV lamp was used to temporarily fix the sky fibres in position in the bottom of the trough. The side blocks were then fixed in place with Araldite. The last step in assembling the fibre slit was to attach the two top plates that enclosed the trough, checking that no fibres were sitting proud of the side of the trough and were not trapped by the lid.

The fibre slit was now polished using the techniques in Chapter 2. Two metal brackets with bolts threaded through the fibre slit were used to hold it firmly in the polishing jig.

## 4.6 Laboratory testing

Before the fibre feed was shipped to Australia, tests were performed on the fibre feed. The accuracy of the fibre alignment on the back of the lens array was measured along with accuracy of the

placement of the fibres in the fibre slit and focal ratio degradation (FRD) tests were performed on a selection of fibres.

#### 4.6.1 The fibre slit

To determine how well the fibres were placed in their respective grooves, a travelling microscope was used to measure the pitch between adjacent fibres. The results for the distances are shown in Figure 4-21. The graph shows pitch difference versus fibre number, and as can be seen the fibres towards one end of the fibre slit show a significant departure from the expected pitch. The conclusion to be drawn from the graph is that the fibres were not rigidly held between the middle block and the bottom of the fibre slit trough. Two possible causes are:

- 1) The aluminium trough did not have a flat base, and
- 2) The middle block was not sitting squarely on the fibres and a fibre moved from underneath its groove, causing one side of the block to be lifted up and allowing nearby fibres to move out of place.

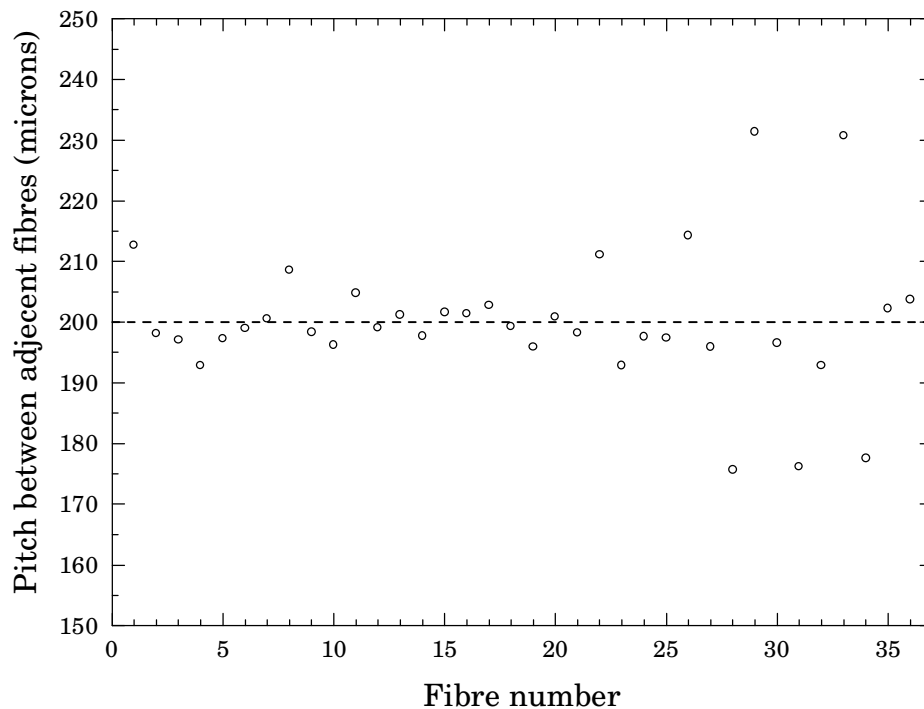


**Figure 4-21** Graph of measured fibre pitch on the SPIRAL fibre slit. The fibre number corresponds to the naming of the fibres from left to right as looking at the fibre slit face on. The measured errors are  $1\mu\text{m}$ . See Figure 4-20.

#### 4.6.2 The lens array

The optical arrangement shown in Figure 4-18 was used to measure the alignment of the fibres on the back of the lens array. Ideally, all 37 fibres produced a fibre image such that so they

were all superimposed exactly in the centre of the graticule cross-hairs. The graticule was mounted inside a small x-y stage that could move the cross-hairs anywhere in the fibre image plane by means of two micrometers, enabling the position of a fibre image to be measured. The procedure to measure all the fibre positions was as follows:

- One lenslet was selected by using a light source at the fibre slit and light was prevented entering adjacent fibres by covering with metal foil.
- The position of the illuminated lenslet was double checked with reference to the lens array/fibre slit arrangement.
- The graticule was moved with x-y micrometers until the cross-hairs were aligned with the centre of the fibre image and the readings on the side of the micrometers were noted.

This was performed for all 37 fibres. The graticule was used to measure the diameter of one illuminated fibre - knowing that the fibre core was 50 microns across gave the image scale at the graticule. The results are shown in Figure 4-22.

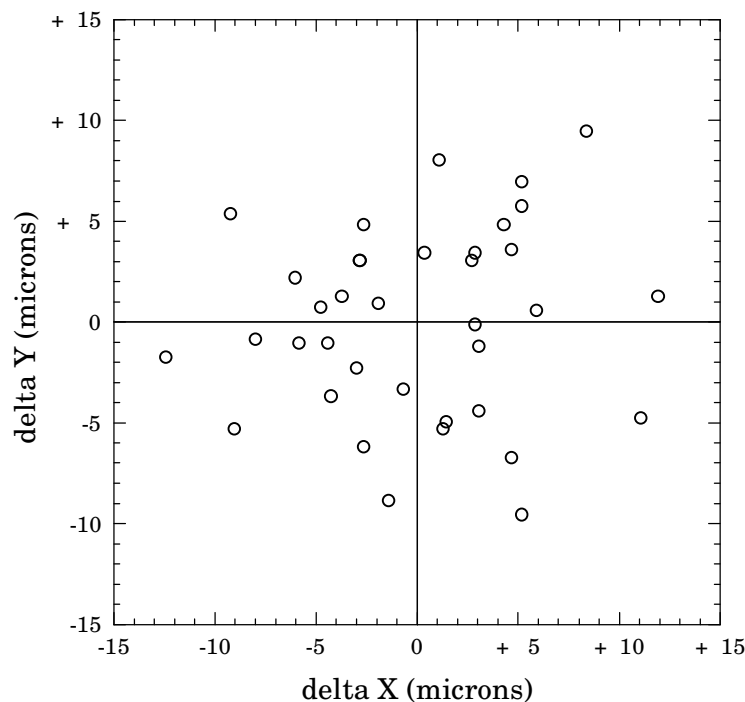


**Figure 4-22** *The measured fibre position errors on the SPIRAL lens array. The measuring accuracy is 0.1 $\mu$ m.*

The results show that the fibres are aligned with an average decentering of 10 $\mu$ m with the largest being 13 $\mu$ m. From visual examination when the fibres were being put on the lens array, a positional accuracy of better than 2 $\mu$ m was being achieved. It was concluded that something had made the fibres shift laterally on the back of the lens array, probably the potting compound used to hold the fibres in place. To investigate this, the fibres were arranged according to their mean distance

from the centre of the lens array. The idea was to see if the mean displacement of the ferrules was proportional to radial distance, implying that the potting compound had expanded or contracted during curing and moved the ferrules in the process. The results of this are shown in Figure 4-23.

The left hand graph shows a histogram where the bins represent radial distance from the mean fibre position. There are three groups of fibres shown on the graph - the widest bars represent the 18 outermost ring of fibres in the SPIRAL lens array, the narrowest bars the innermost ring of six and the middle ring of twelve fibres are the remaining set of data bars. The graph on the right shows the cumulative encircled fraction of fibres for a given radius, with the largest circles representing the outermost ring and the smallest circles the innermost ring.

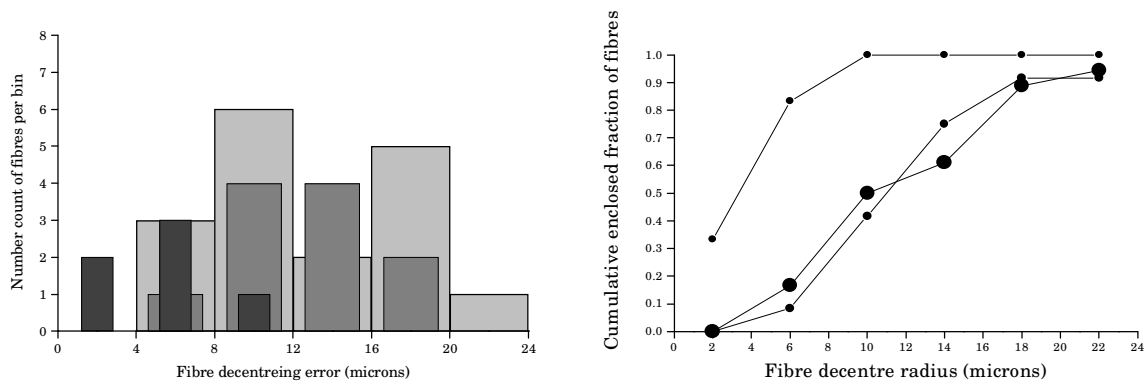


**Figure 4-23** Fibre decentering errors in the SPIRAL lens array.

As can be seen, the outer two rings of fibres follow the same scatter of radial errors, but the innermost ring of fibres have a much smaller scatter, implying that the bulk expansion of the compound induced displacements proportional to their radial distance. This offers some indication to what happened with the ferrules, but is only marginally indicative of an expansion/contraction of the potting compound.

Another issue was why the ferrules were able to be moved off their aligned positions. The UV curing epoxy formed a strong tensile bond between glass and metal, as was tested in the laboratory beforehand, so the fibres should not have been shifted at all.

The true cause of the SPIRAL lens array misalignments was due to the fact that the SF6 glass that formed part of the lens array was opaque to UV radiation below 400nm. Thus, when UV light was being shone through the lens array in order to fix the epoxy, the UV light was being absorbed by the intervening glass instead and the UV epoxy remained in liquid form. Later examination of the fibre ferrules revealed that the epoxy was still liquid, and that the fibres had been held on only by the cured epoxy around the edge of the ferrule. The horizontal ferrule was then aligned whilst acting like a horizontal beam sagging under its own weight. When the lens array was rotated vertically to pour in

the potting compound, the ferrules then moved out of alignment and were fixed in their current positions by the surrounding epoxy.

This design flaw was only discovered and fully understood after the two SPIRAL observing runs. After this discovery, the COHSI lens array substrate was chosen carefully and the technique successfully modified (see Chapter 5).

## 4.7 Alignment of SPIRAL on the telescope

SPIRAL Phase A had two observing runs in 1997, both of which investigated the techniques needed for setting up an IFS on a telescope (§4.7). The first issue dealt with was target acquisition and alignment of the lens array with an object on the sky. For a slit-based spectrograph, the starlight scattered off the edges of the slit acts as a visual reference for initial telescope alignment and subsequent guiding. The layout of the guiding unit and the TV slit viewing camera that looks at the spectrograph slit in the AAT is shown in Figure 4-24. For SPIRAL there was no such slit edge to act as a mirror to observe the position of objects in the focal plane of the telescope, so custom-made pick off mirrors (POM) were used for initial acquisition (Figure 4-25).

The IFS mode was the more difficult of the two to align because of the greater number of

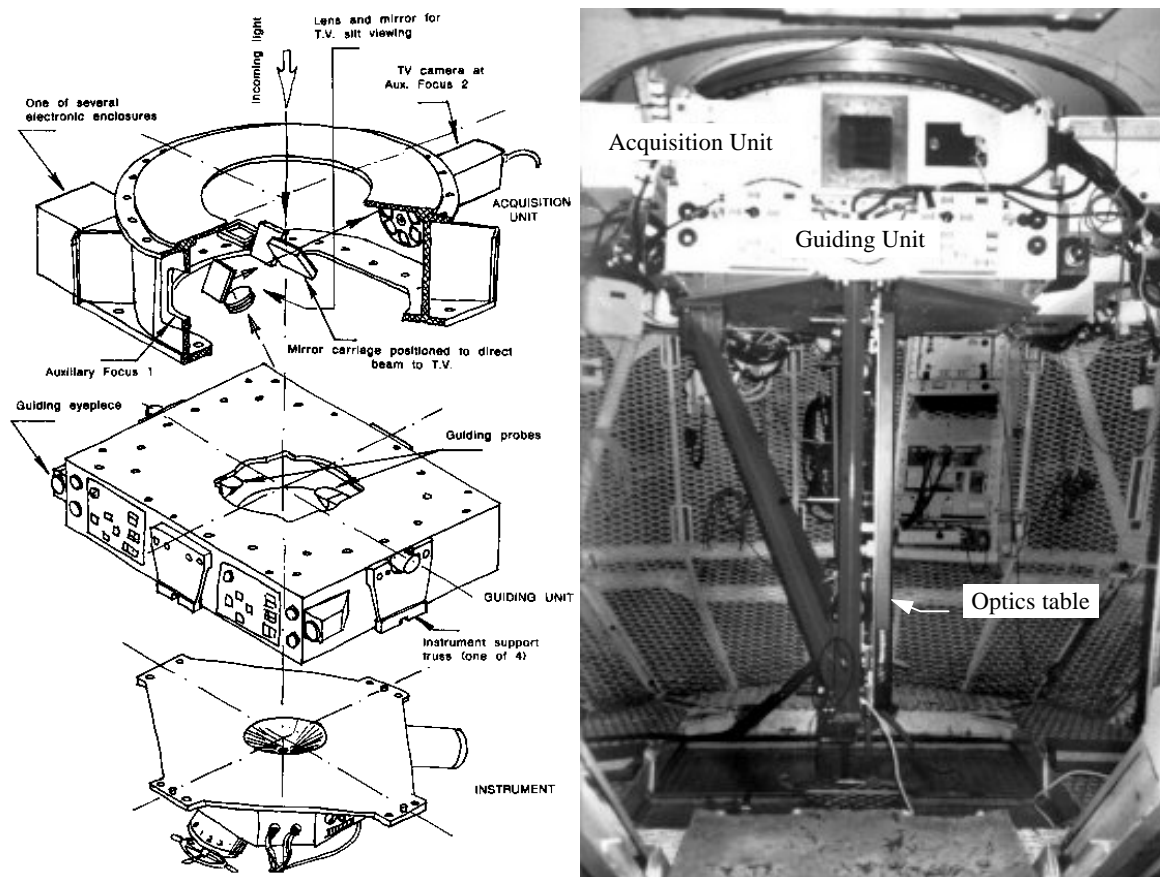


**Figure 4-24** Layout of auto-guider unit and TV slit viewing camera for the AAT. The photograph on the right shows an edge-on view of the optical table (see also Figure 4-26) bolted onto the Cassegrain focus. The TV slit viewing camera focuses on the pick-off mirror mounted on the table.

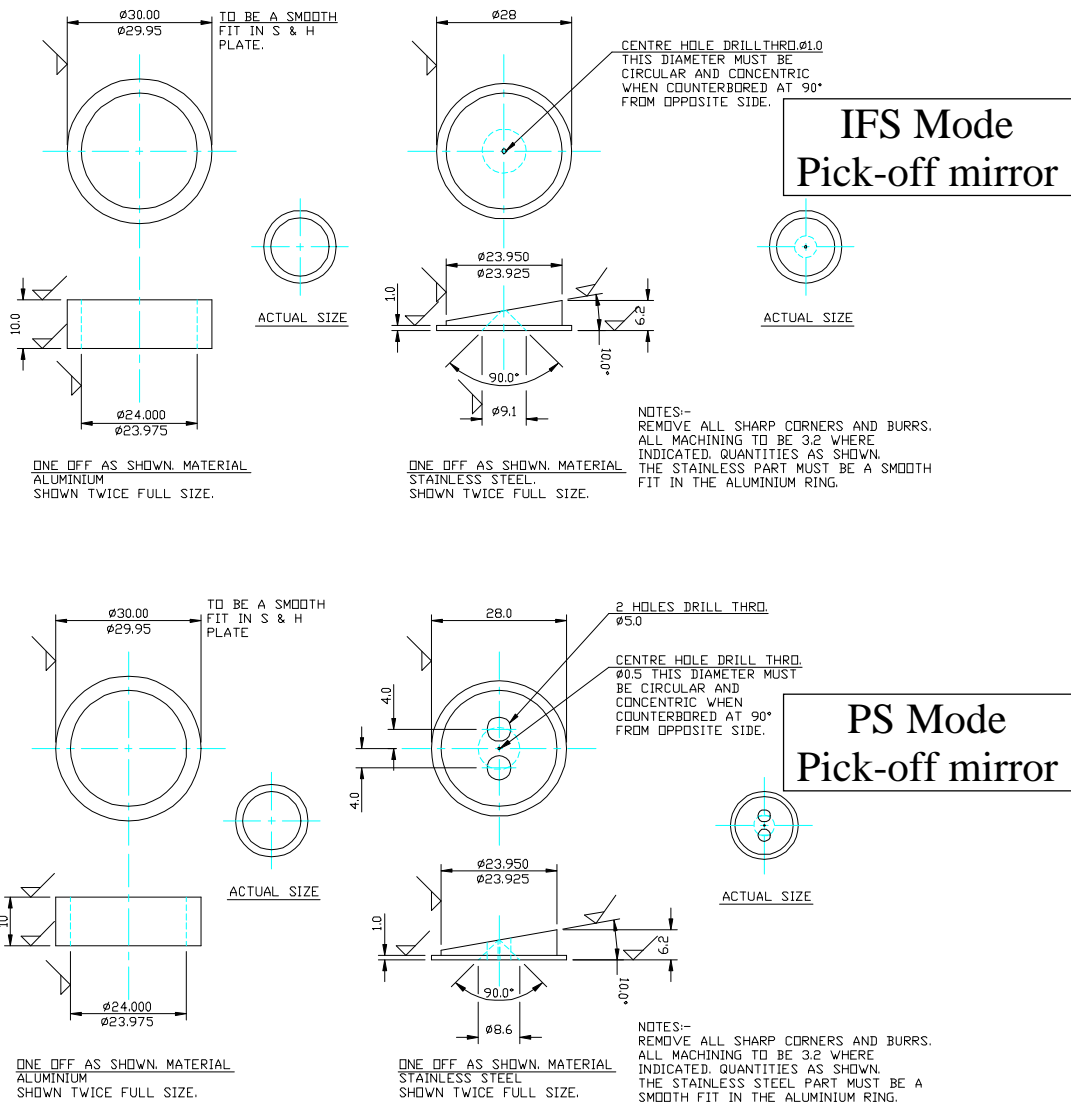


**Figure 4-25** Technical drawings of the two pick-off mirrors used with SPIRAL.

fore-optics involved, but either set could be aligned within ten minutes of gaining access to the telescope Cassegrain cage, allowing future users easy inter-change of the two modes. In the observing runs, one mode was aligned during twilight and was not altered during the remainder of that night.

Flexure of the optics table was an issue that was resolved by monitoring the back-illuminated fibres in the Cassegrain cage as the telescope travelled across the sky to various declinations and zenith distances (§4.7.4). An observed shift in the POM position during the night was discovered to be due to the warming up of the TV camera tube in the autoguider. The solution was to switch on the camera early in the afternoon and by the evening the TV image had stabilised.

#### 4.7.1 Alignment of IFS mode

The layout of the optical table as fixed onto the telescope is shown in Figure 4-26 and Figure 4-27. Light from the telescope came to a focus in the Cassegrain focal plane (see Figure 4-28). Here

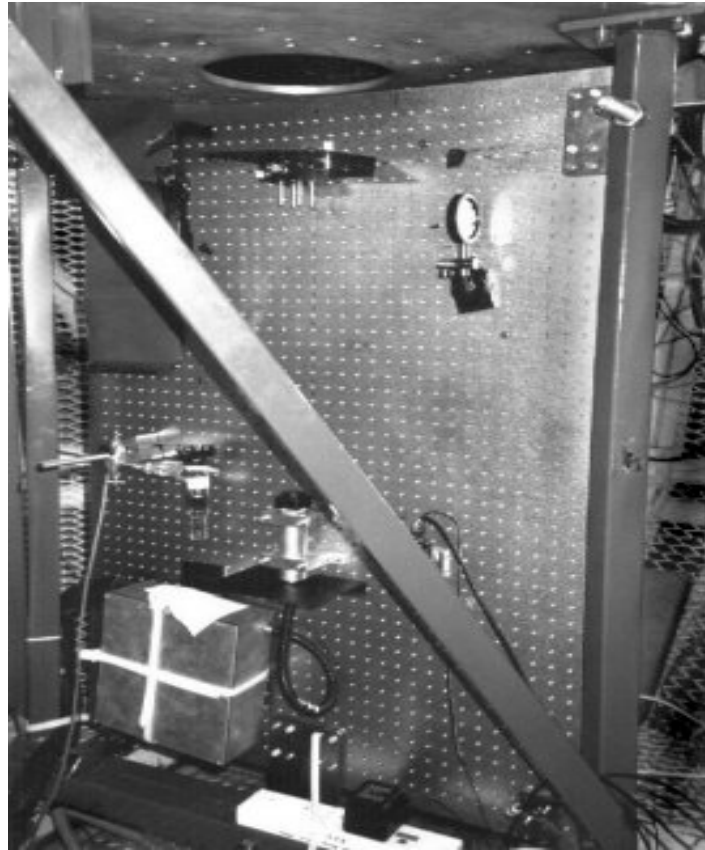


**Figure 4-26** *Fore-optics and lens array mounted on the optical table in the Cassegrain cage. This is the typical layout of the optical table for alignment of the IFS mode, including the pellicle and arc lamp used for calibration.*

the POM was oriented such that the light from the sky was reflected back up towards the TV slit viewing camera. A 2mm hole in the middle of the POM allowed light to pass through into the magnifying lens on the optical table. An image of the pupil (the primary mirror) was formed 10mm below the magnifying lens. The light then passed to the field lens and lens array some 600mm further down the optics table and into the optical fibres.

The first step in the alignment was to mark the optical centre of the POM in the control room using one of the computer controlled markers used for autoguiding of the telescope. By rotating and moving the POM up and down in its mount, the mirror was brought into sharp focus on the TV slit viewing display, bringing the focal plane of the telescope coincident with the hole in the middle of the POM. The centre of the POM hole now defined the optical axis for the lens array and fore-optics lenses, and so was not moved out of position for the rest of the alignment procedure and subsequent observations.

The lens array and field lens were fixed together in a single mount. Without the field lens, the back-illuminated fibres and lens array produced a collimated beam of light, but with the field lens a common fibre image was formed in front of the field lens. This was placed on the optical table in the approximate position prescribed by the fore-optics design. By inserting a piece of paper in the optical

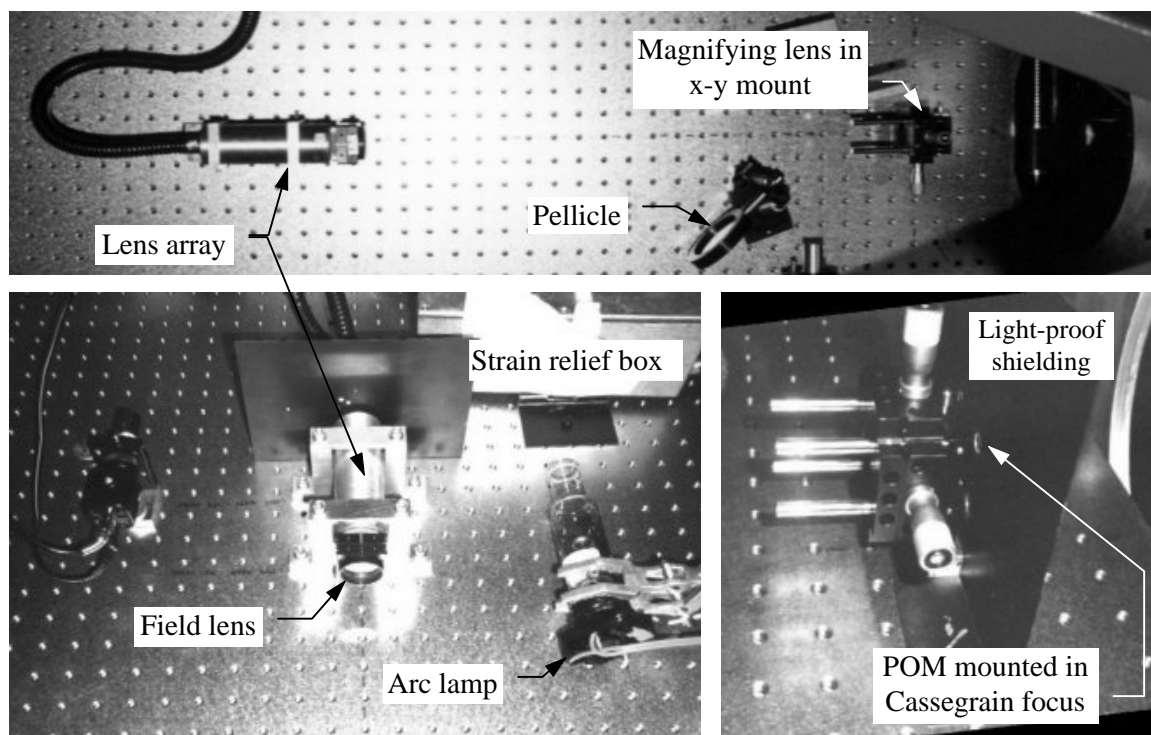


**Figure 4-27** *Layout of the IFS mode optics on the telescope.* The top photo shows the whole optical train for IFS, and the lower two panels show the lens array and magnifying lens unit in close-up.

beam the common focus of the fibre images was revealed and this beam was then aligned with the hole in the POM. The magnifying lens was now put into position.

The next part of the alignment required the telescope to point at a bright star in order to fix the x-y-z positions of the magnifying lens. The telescope was set to point at a star near the zenith, to the spot earlier defined as the centre of the POM by the TV slit viewing camera.

Light from the star now passed down through the magnifying lens and onto the lens array, producing an enlarged image of the star. The magnifying lens was moved with the x-y mount until the stellar disk was in the centre of the lens array. At this point the telescope focus and the magnifying lens focus were not coincident, so the telescope was refocused to give a sharp stellar image which aided with the magnifying lens alignment.

When this part of the alignment procedure was done, the telescope was re-set to its nominal focus and the z motion of the magnifying lens was adjusted to produce the sharpest possible image of the star on the lens array. Sometimes a slight adjustment of the x-y was needed to re-centre the star. The magnifying lens was now aligned.

The final part of the alignment required the pupil image of the telescope to be aligned accurately with the common fibre pupil image. A pellicle and TV camera were introduced into the optical path of the telescope as shown in Figure 4-28. A small piece of ground glass was introduced into the beam to make the pupil image of the telescope visible. Back illuminated fibres now produced the fibre pupil in the form of a small circle of light. Careful tip-tilt adjustment of the lens array moved

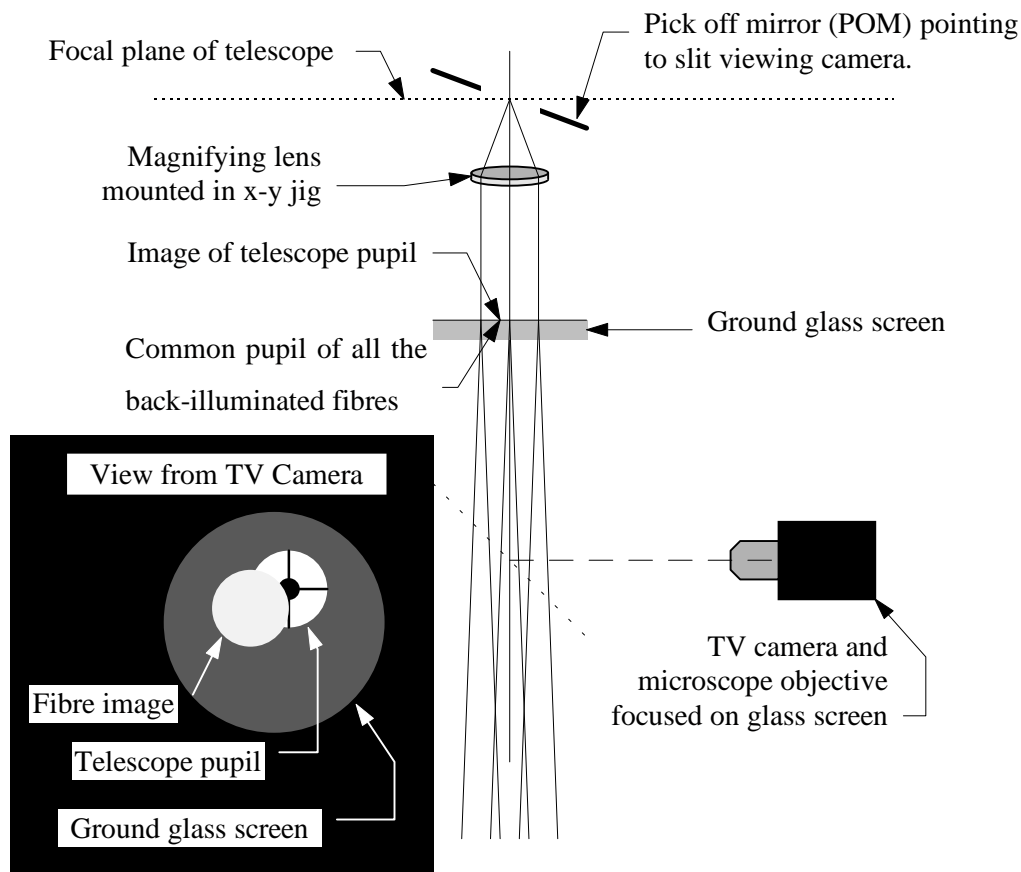


**Figure 4-28** Schematic of the pick-off mirror arrangement. This schematic shows how the pick-off mirror and magnifying lens are arranged and where the pellicle and ground glass screen were inserted to examine the alignment.

the fibre pupil into alignment with the telescope pupil. The alignment of the IFS mode was now complete.

#### 4.7.2 Alignment of the PS mode

The alignment of the PS mode was similar to that of the IFS mode but required a different POM to be inserted and aligned with the same method as in the last section.

The lens array was fixed to the single fore-optics lens with rods (see Figure 4-29) and the array was carefully set to the prescribed distance. Back-illumination of the fibres produced a single sky fibre image three arcseconds in diameter, along with two groups of sky background fibres imaged either side of the sky fibres. The lens array was then rotated so that the sky fibres would align with the sky background holes drilled into the POM. Moving the lens array to align the object fibres with the hole in the POM was assisted by using the pellicle and TV camera to ensure that none of the fibres was vignetted by the edge of the POM. Placing a thin piece of paper over the top of the POM also helped identify the centre of the object fibre images.

The last part of the alignment was to wait for twilight and a bright star near the zenith. With the star centred on the control room TV camera, an image of the primary mirror was imaged onto the

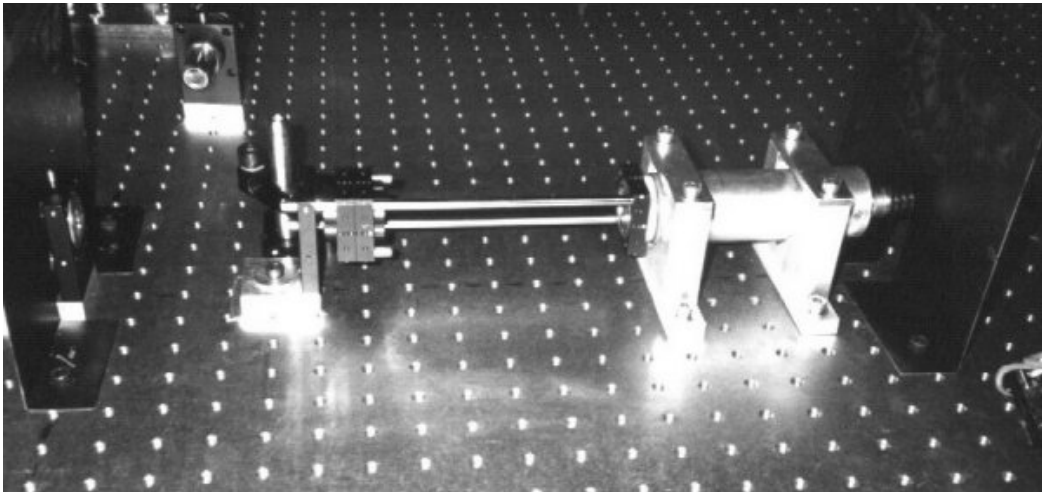


**Figure 4-29** *Aligning the pupil imaging mode on the telescope.* The telescope focus is on the left, with the POM in the middle of light-proof shielding. The fore-optic is held to the lens array by two rods and the mount for the lens array itself can be clearly seen.

lens array. The image of the mirror was then centred on the lens array by moving the body of the lens array. However this caused the fibre image in the middle of the POM to become severely misaligned, and it was simpler and more time efficient to simply leave the lens array in its current position. Usually it was found that the pupil image was very well aligned with the centre of the lens array and the extra realignment needed for the fibre pupil in the POM did not merit the extra effort.

### 4.7.3 Calibration of the SPIRAL spectrograph

There were four micrometers on the spectrograph that allowed movement of the different optical components (Figure 4-30). These were labelled M1 to M4.

- M1 moved the fibre slit with respect to lens L1
- M2 adjusted the table upon which L1, L2, L3 and the fibre slit were attached
- M3 adjusted the tilt of the dewar containing the CCD
- M4 rotated the dewar about its optical axis.

The dewar was first rotated to align the spectra as closely as possible with the pixel rows on the CCD and this rotation was not altered any further during the course of the run. M1 and M2 were used together to make sure that the path length from the CCD to L1 was as close as possible to the path length from the fibre slit to L1. This was done by measuring the distances involved beforehand and adjusting M1 and M2 to match. Focusing was controlled with micrometer M1 and the tilt of the CCD with M3, and each time a new wavelength range was selected, the M3 tilt and M1 focus had to be readjusted to produce the sharpest images.

After connecting the slit, the lens array was back illuminated with a tungsten lamp. This helped define the tracks of the fibre spectra on the CCD. Replacing the tungsten lamp with an arc discharge lamp, images of arc emission lines were taken for wavelength calibration. After fitting the spectra produced with a known list of emission lines, the resolution and spectral coverage was

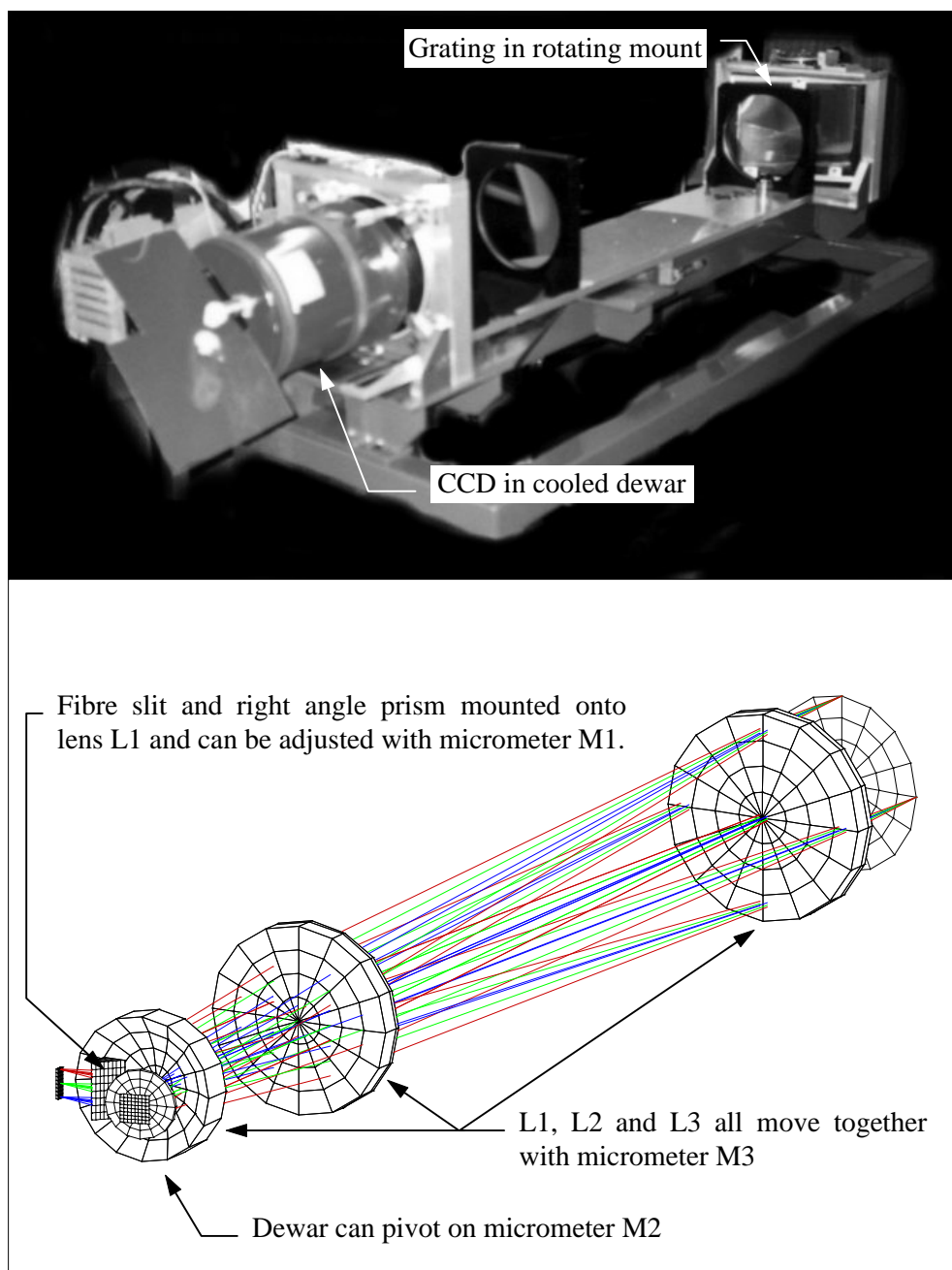


**Figure 4-30** Arrangement of micrometers for adjustment on the *SPIRAL* Littrow Spectrograph.

calculated and tabulated (see Chapter 7 for the results). The gratings used were the RGO spectrograph reflection gratings, thus saving on producing new gratings and allowing a wide range of choice. They were inserted into the grating holder at the back of the spectrograph and held with two restraining clips.

#### 4.7.4 Flexure of the fore-optics table

One concern of *SPIRAL* was that of flexure in the fore-optics table in the Cassegrain cage. Earlier it had been noted that the image of the hole in the POM drifted by half an arcsecond during the night on the telescope, and the hypothesis was that the table was undergoing slight movement

under different gravity vectors. To resolve this, the optics table was monitored as the telescope was sent over to large zenith angles in all four points of the compass. The fibres were also back-illuminated and the pupil images examined with the TV camera and ground glass screen used in the alignment of the IFS mode (Figure 4-28).

No flexure of the optics table was observed, and it was recognised later that the image shift seen in the control room was due to the thermal expansion of the imaging tube in the auto-guider.

The opportunity was also taken to see if the fibres underwent any strain at large zenith distances. The cover of the strain relief box was removed and whilst the telescope was moved towards the horizon the fibre decreased in size to a coil approximately 10cm in diameter but did not become taut, indicating that the strain relief boxes contained an adequate length of fibre.

## 4.8 Conclusions

### 4.8.1 The construction of the fibre feed

The construction of the lens array was quick and relatively simple to perform, posing no problems in assembling the lenslets together. Similarly the fibre polishing technique proved efficient for dealing with the triplets of fibres *en masse*, although some fibres were broken by careless handling and were subsequently replaced.

In principle the fibre alignment technique for the ferrules on the back of the lens array gave very good positional accuracy, but due to the error in the glass chosen, the UV curing epoxy that held the fibre ferrules in place did not cure properly. It is a mixed blessing that the subsequent introduction of potting compound into the lens array unit shifted the fibres out of alignment during the curing period but that once cured, held the fibres rigidly in place. With carefully chosen UV transmitting glasses this method was still considered a viable option for optical alignment of fibres with a lens array. Alternative methods still have positional errors of 10 $\mu$ m or more, so it was considered worth pursuing a method with a potential positioning accuracy of 2 $\mu$ m.

The assembly of fibres in the fibre slit proved to be a relatively simple, if time consuming task. For the 37 object fibres it took approximately a day to insert all fibres in their correct order. For considerably larger fibre slits, it is worth considering grouping the fibres into batches of 100 or so, and fixing each set one at a time. In this way if a fibre block is disturbed and the fibres move out of position, only a day or so of work is lost.

The sky fibres were particularly easy to position with the brush/surface tension technique. This provides an easy method for lining up many fibres that don't need to be spatially arranged, e.g. a fibre image slicer for very high resolution stellar work that can slice up the image of a star and format the output as a long thin fibre slit.

### 4.8.2 Alignment on the telescope

Fore-optic alignment on the telescope proved to be relatively easy, but working out the methodology so as to ensure the best possible alignment for the IFS mode was more difficult. Many attempts at alignment were made before it was realised that the critical step was the defining of the telescopes pointing position. As soon as a point on the TV control room screen was defined to be the centre of the field of view of the telescope and the pick off mirror was adjusted and brought into the telescope focus, the alignment procedure followed naturally from there.

The pupil imaging mode was considerably simpler to align, but some care had to be taken to ensure that the back-illuminated fibre pupil image was aligned with the hole in the pick-off mirror. As there was no spatial information in the pupil imaging mode it proved difficult to ensure that the light from the star was completely entering the fibres. Unlike a slit based spectrograph where all light entering the slit passes through to the detector, the POM pupil imaging hole was slightly oversized to prevent vignetting from fibre misalignments. As a result it was difficult to determine when the pupil imaging mode was optimally aligned.

The techniques in the assembly of SPIRAL A proved essential in the assembly of the COHSI fibre feeds described in the next chapter, and the different problems encountered led to successful modifications and simplifications in the COHSI design.

# 5. The COHSI fibre-feeds

---

## 5.1 Introduction

The Cambridge OH Suppression Instrument (COHSI) is an infra-red spectrograph designed to optically filter out ~200 of the OH lines which dominate the 1.0-1.8 $\mu$ m night sky spectrum (Figure 5-2) so that the redshifts of high  $z$  faint star-forming galaxies can be determined (§5.2). COHSI is comprised of three spectrographs - the first two are part of an OH suppression unit and the third is a cryogenically cooled low dispersion spectrograph, with two optical fibre bundles feeding light between the telescope, OH suppressor and cryogenic spectrograph.

The mechanical and optical design of COHSI has been based around the use of optical fibres both as image slicers and as means of making the instrument as telescope independent as possible (§5.3). Its cryogenic spectrograph (§5.3) allows simultaneous observation of the J and H bands whilst the bright, variable OH emission of the atmosphere is suppressed by the OH suppressor module. The layout of the separate sections of COHSI are individually described and the optical requirements of each one is discussed along with their construction and assembly in the laboratory (§5.4). Various tests performed after the first commissioning run showed the efficiencies of the optical fibre used was not as high as expected (§2.6.3), but the rest of the techniques used in the construction and alignment of the fibre feeds were a complete success (§5.6).

## 5.2 The scientific case for COHSI

COHSI is designed to identify the redshifts of selected faint galaxies in the range of  $1 < z < 2$ . This redshift regime is important as this is thought to be the major epoch of star formation in the Universe. This parameter space has previously been very difficult to explore as the optical emission lines that identify a galaxy's redshift ( $\lambda\lambda 3727-6731$ ) are red shifted amongst the OH night sky emission lines redward of 1.0 $\mu$ m. By imaging both the J and H bands all galaxies with  $0.5 < z < 1.8$  and at least two emission lines can be identified (Ennico 1998).

There are two observational modes for COHSI. The first is an IFS mode using a 100 element lens array (see Figure 5-1). Two different sampling scales allow COHSI to image small extended objects, such as galaxy nuclei and gravitationally lensed galaxies. The complete spatial mapping of

gravitational arcs combined with the spatial resolution also leads to image reconstruction of the original galaxy (Franx 1997).

The second mode is a multi object spectrograph mode. With a list of candidate galaxies, COHSI will be able to perform long integrations of distant galaxy fields. This is realised by using a plug-plate system to position optical fibres on images of galaxies within a given field of view, with a different plug-plate for each different field. The multiplexing combined with the OH suppression and large band coverage make COHSI a competitive instrument on a 4 metre telescope (Ennico 1998).

The construction of the COHSI IFU fibre feeds are the main subject of this chapter.

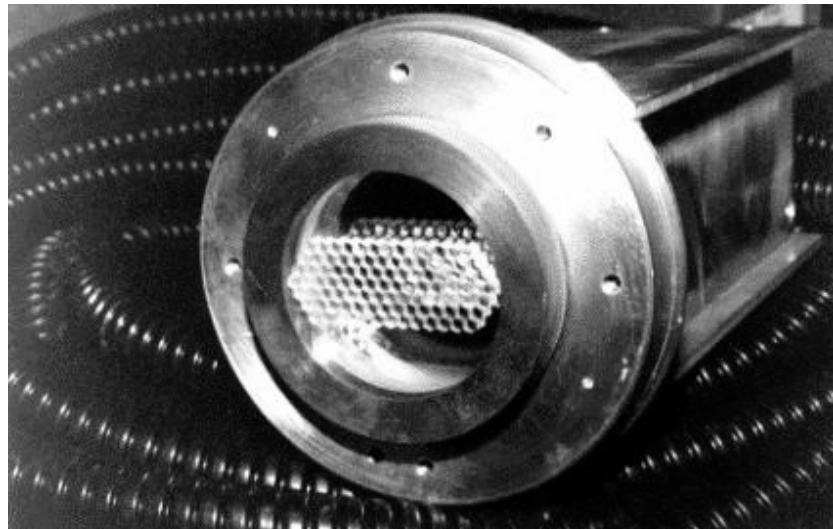


**Figure 5-1** *The COHSI IFU lens array. The IFU is shown resting on the fibre conduit.*

### 5.2.1 The infra-red night sky

Hydroxyl molecules (OH) lie in a tenuous atmospheric layer ~80-100km above sea level (Bates & Nicolet 1950) and are put into excited electronic states by sunlight during the day. After sunset these states slowly decay into lower rotational and vibrational energy states, emitting infra-red photons in the process.

As there are many vibrational and rotational combinations of energy states, a distinctive forest of emission lines is produced (Figure 5-2). During the night, this total OH sky emission lowers by a factor of 3 (Ramsay-Howat 1996) but is still large compared to the galaxies under observation. The intensity of the lines is not constant (Taylor & Hill 1991, Ramsay 1992) as pressure waves travelling through the upper atmosphere cause variations in brightness over tens of seconds and on small spatial scales, making accurate beam switching and subsequent sky subtraction very difficult to perform.

The accurate removal of OH emission is the largest problem in performing faint object spectroscopy in the near infra-red. Two methods of removing it are discussed in the next section.

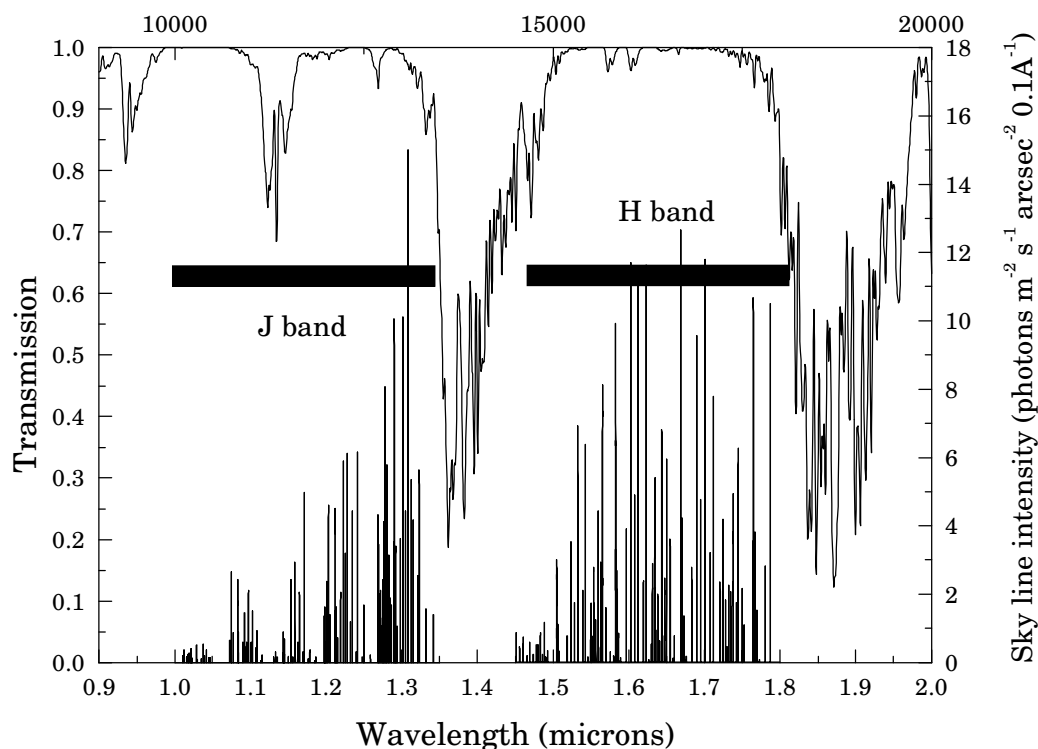


**Figure 5-2** *The infra-red sky above Mauna Kea.* This graph shows the atmospheric transmission above Mauna Kea (the upper curve) and the OH emission line forest that is approximately 100 times brighter than the continuum sky.

### 5.2.2 OH Suppression techniques

There are two main techniques for OH suppression - software suppression and hardware suppression. Both rely on the observation that the OH emission lines have well defined frequencies and their intrinsic line widths are very narrow ( $\sim 80$  metres/second) (Turnbull 1983).

Software suppression uses a high dispersion spectrograph to image the band at high spectral resolution and then ignore pixels that contain OH emission lines. This method suffers from several drawbacks:

- To cover both bands at a high dispersion a large number of pixels is needed. At the time COHSI was designed, only  $256^2$  arrays were available.
- The OH emission is typically 1000-10000 times brighter than the galaxy emission line signal being looked for (Ennico 1998).
- Scattered OH light from the spectrograph makes the galaxy emission line less detectable, and since the OH lines vary in strength, no simple scattered light model can be used to subtract it off.
- IR arrays are read noise and dark current limited - high dispersions mean fewer photons per pixel from the galaxy, resulting in lower signal to noise.

Hardware suppression attempts to overcome these difficulties by using a separate suppression spectrograph to remove the OH lines. By using optical fibres the exit apertures in the OH suppressor are very small, resulting in considerably reduced levels of scattered OH light being transmitted into the cryogenic spectrograph. The principle of hardware OH suppression is shown in Figure 5-3.

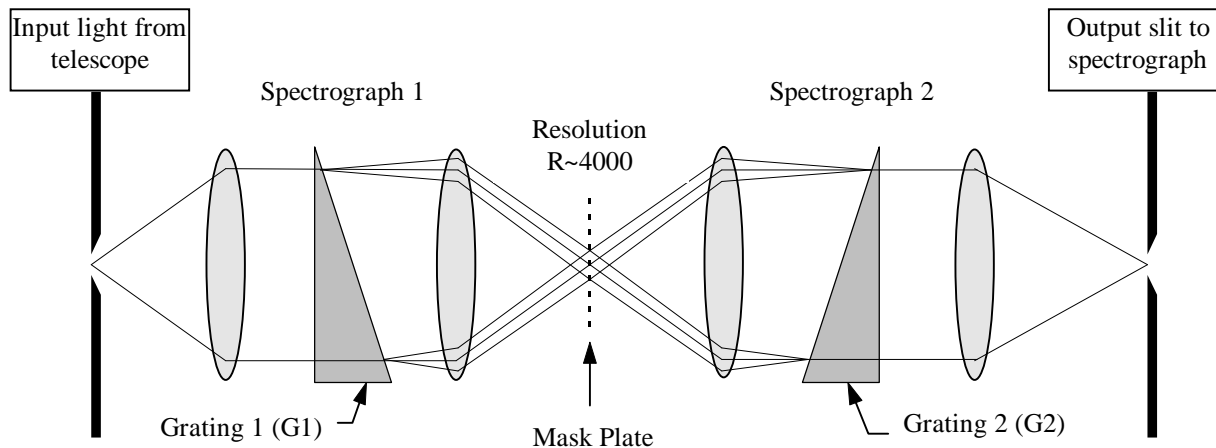


**Figure 5-3** Principle of OH hardware suppression. Incoming light is dispersed by Spectrograph 1 onto a mask plate which then cuts out the night sky lines. Spectrograph 2 then redisperses the ‘cleaned’ light into a white slit image and passes out to a low resolution cryogenic spectrograph.

Light from the telescope enters a high resolution dispersion spectrograph (Spectrograph 1) which images a dispersed spectrum onto a mask plate. The plate has black IR absorbing lines drawn on it in the positions of the intrinsically narrow skyglow lines. The rest of the light passes through and is redispersed with Spectrograph 2 into a white slit image, which passes into a low resolution cryogenic spectrograph.

By making the hardware unit a separate module fed only with optical fibres, the amount of scattered light introduced into the cryogenic spectrograph is minimised.

Using optical fibres makes the design of COHSI modular, leaving the suppressor and cryogenic spectrograph on the floor of the observatory. Simple optics, similar to those used in the SPIRAL lens array (see §4.4) feed light into optical fibres at the Cassegrain focus.

### 5.3 The design parameters for COHSI on UKIRT

COHSI uses hardware suppression to remove 196 OH night sky lines in the J and H bands. It is comprised of a lens array unit (containing fore-optics and a fibre-fed lens array similar to SPIRAL), an OH suppression spectrograph, and a cryogenic spectrograph. The detailed design of COHSI is given in Ennico (1998) and what is presented here is a simple description of the light path within COHSI.

The layout of COHSI on the United Kingdom Infra-Red Telescope (UKIRT) is shown in Figure 5-4.

The image scale of COHSI was chosen to sample the median seeing of Mauna Kea, typically 0.75-0.35". Two IFU image scales were chosen - 0.35" per lenslet and another with 0.67" per lenslet. The lens array itself was composed of hexagonal lenslets in the configuration shown in Figure 5-5.

The IFU is fixed to one of the ports of the UKIRT Instrument Support Unit with a rigid metal framework (see Figure 5-6). This framework also holds the fore-optics in front of the IFU. The layout of the fore-optics is similar to the fore-optics used for SPIRAL, with two lenses acting to enlarge the

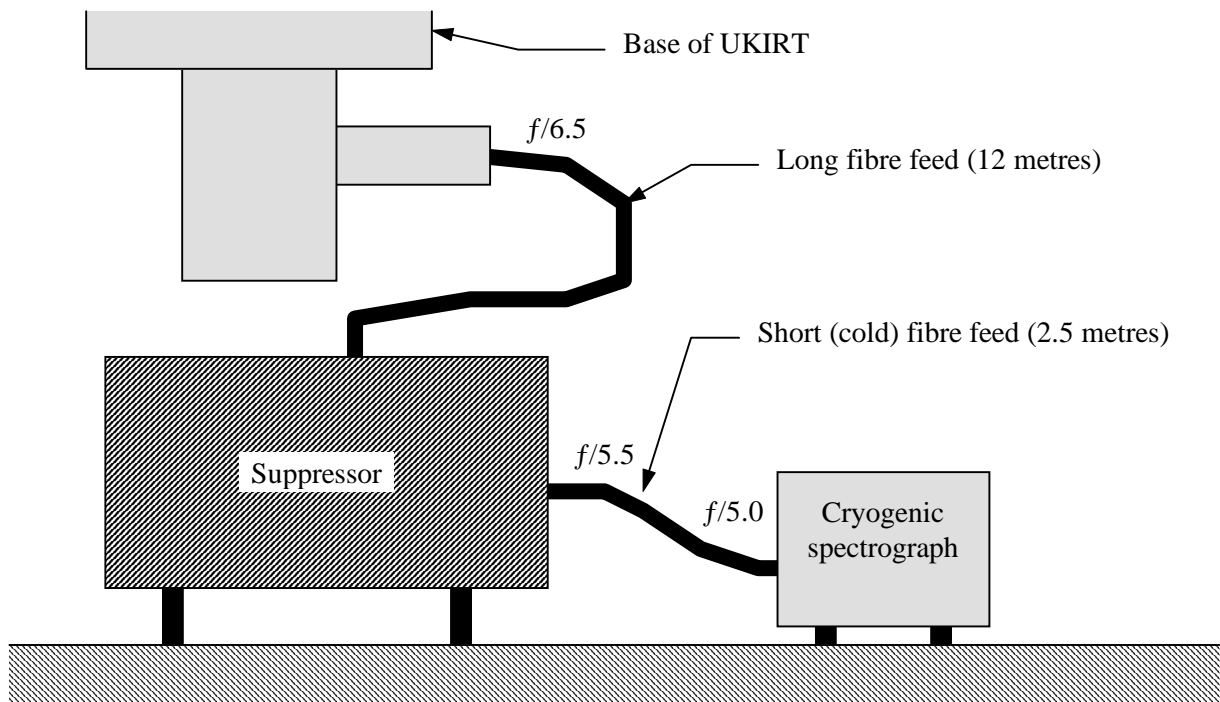


**Figure 5-4** *Layout of COHSI.* Here the lens array is mounted on the Cassegrain focus with the long fibre feed leading down to the suppressor and cryogenic spectrograph on the floor of the observatory. The OH cleaned light is transferred to the cryogenic spectrograph via a short fibre feed.

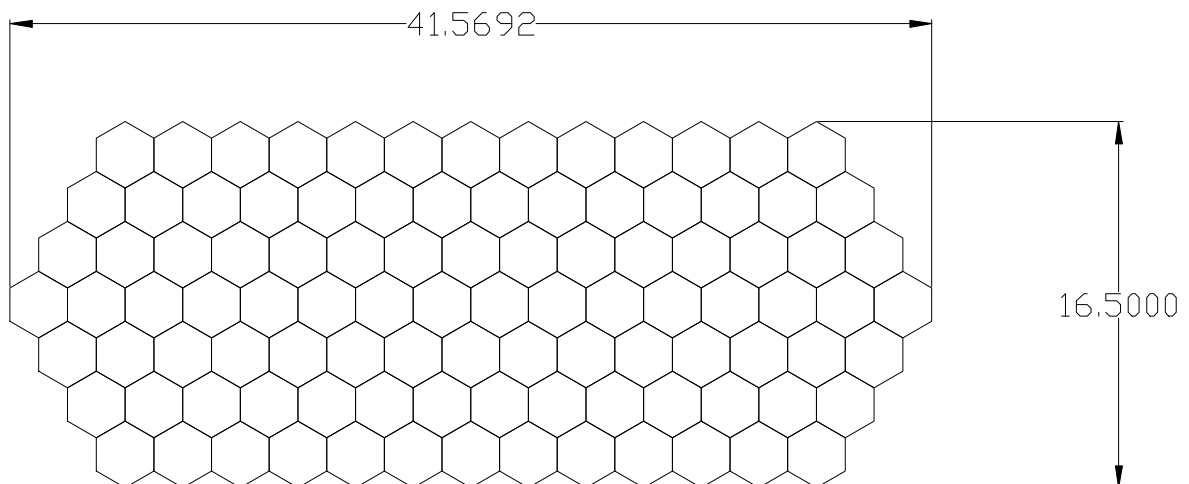


**Figure 5-5** *Layout of the COHSI lens array.* The figures refer to the size of the array in millimetres.

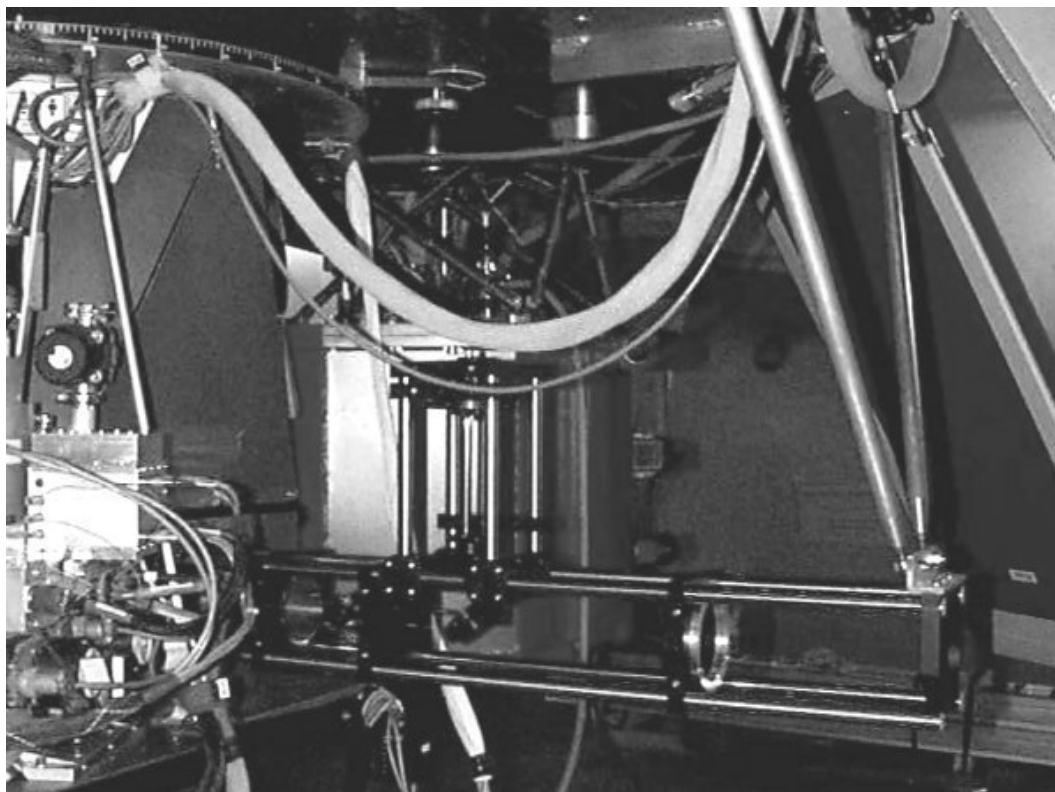


**Figure 5-6** Framework holding the COHSI fore-optics on UKIRT.

telescope image plane to match the scale of the lens array. The framework also holds the optics and TV camera required for the alignment of the fore optics with the telescope.

Each of the 100 lenslets in the lens array is aligned with an optical fibre. This bundle of 100 fibres then runs down 12 metres of conduit to the OH suppressor unit sitting near the North edge of the UKIRT observatory floor. The OH suppressor sits in a light-proof metal framework (approximately  $1\text{m} \times 1\text{m} \times 2\text{m}$  in size). Inside is a Schmidt camera with its optical axis parallel to the floor.

The fibres enter the OH suppressor from the top of the light proof box and are reformatted into a long fibre slit. The curved focal plane of the Schmidt camera defines the surface on which the OH suppression masks, the input fibres and the output fibres all sit (see Figure 5-7).

The two spectrographs S1 and S2 are identified by the position of their gratings G1 and G2, and the mask mirrors. The first spectrograph is on the left hand side of the diagram, with the primary mirror and corrector plate acting as collimator and camera in a double-pass system. The dispersed spectrum is re-imaged on the focal plane of the Schmidt, with the J and H wavelength windows arranged to be on either side of the fibre slit. This spectrum is approximately 100mm long and has a resolution of  $\sim 4000$ , giving an instrumental line width on the curved focal plane of  $125\mu\text{m}$ . Here two mask mirrors have IR absorbing lines drawn on them in the locations of the OH night lines, cutting out  $\sim 17\%$  of each band.

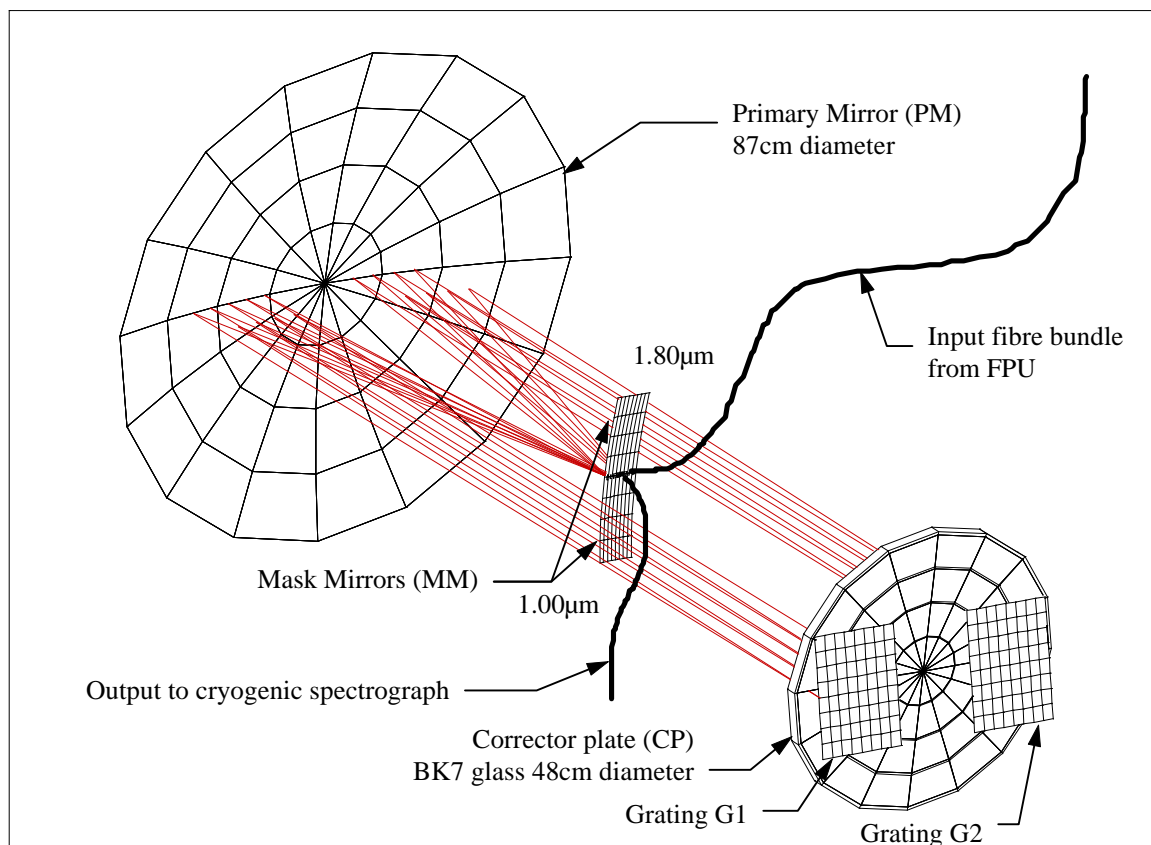


**Figure 5-7** *Layout of the COHSI OH suppressor.* This ray tracing shows the optical components of the suppressor. Between the two mask mirrors are the fibre slits, which are not shown for clarity.

The light then passes onto the right-hand side of the suppressor where a similar spectrograph (S2) redisperses the cleaned spectrum back into a white light image in the curved focal plane. The input fibre slit and output fibre slit do not sit on the optical axis of the Schmidt but are displaced either side by  $250\mu\text{m}$ . These output fibres have a larger diameter than their counterpart input fibres, to take into account optical aberrations and diffraction effects.

The output fibre feed then leads into the cryogenic spectrograph - the spectrograph is in a large rectangular dewar that is cooled down to 70K under a high vacuum. The fibres enter the dewar through a small hole filled with vacuum-proof epoxy and pass down a plastic conduit into the cryogenic fibre slit.

Throughout the whole system the optical beams become progressively faster -  $f/6.5$  to  $f/5.5$  from the Focal Plane Unit, though the suppressor through to the cryogenic spectrograph. This is an allowance for FRD in the optical fibres. A diagram of the cryogenic spectrograph is shown in Figure 5-8.

Further details of the optical design of COHSI, the alignment procedures and the performance of COHSI is found in Ennico (1998).

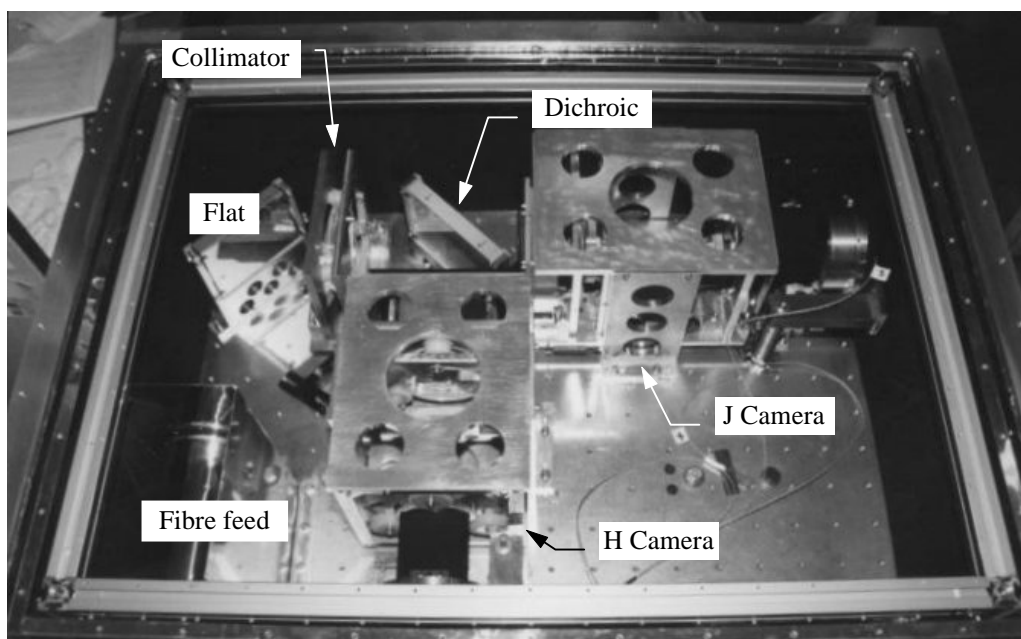


**Figure 5-8** Inside the cryogenic dewar. The fibres pass through the dewar wall in the lower left.

### 5.3.1 Protecting the fibre bundle

Optical fibre is fragile and can be easily broken without due care and attention, so a protective conduit is needed to ensure safe handling and transportation of the fibre bundle to and from the telescope. The conduit and fibre also needs to reach the Cassegrain focus for all possible pointings of the telescope. To prevent the optic fibre being stretched, strain relief boxes allow the fibre to move freely by seating a loose coil of optical fibre within a box that can contract as the conduit stretches and flexes.

In SPIRAL there were two spare length boxes, one near each end of the fibre feed. The length of fibre for SPIRAL was 18 metres, so two boxes were thought to be necessary to accommodate the conduit extension as a large length of the conduit was suspended off the telescope.

With COHSI, the Cassegrain focus is only a metre off the ground and the linear distance the UKIRT focus moves is smaller than that of the AAT. A conduit of 12 metres length is needed for the UKIRT telescope and so only one spare length box is used. The location of the strain relief box is near the OH suppressor. A redesign of the SPIRAL design now gives transparent side panels to the box, allowing visual inspection of the fibres movement as the telescope slews across the sky.

### 5.3.2 The lens array

As seen with the SPIRAL lens array, fore-optics are used to re-image the telescope focal plane onto a macro-lens array. COHSI covers the J and H band, meaning that the lens array has to produce achromatic images from  $1.0\mu\text{m}$  to  $1.85\mu\text{m}$ . Using macrolenses means that doublets can be specified, leading to an achromatic solution for COHSI (see Figure 5-9).

The lenslets image the telescope pupil (the secondary mirror) onto the fibres with an image size of  $92\mu\text{m}$ . To allow for any positioning error during assembly the fibres used are slightly oversized with a  $110\mu\text{m}$  core diameter.

### 5.3.3 The curved double slit

By using an optical fibre bundle instead of a classical slit-based design, a novel Schmidt camera design was used for the suppressor. The path of light from one fibre can be followed in Figure 5-10. Fibres enter the suppressor from the telescope above and pass into a fibre housing that feeds the light to the curved focal surface of the camera. Light passes from the fibres to the primary and back through the corrector plate onto the first grating. The dispersed spectrum is imaged across two mask mirrors that sit above and below the location of the fibre slit.

A second grating then takes the spectrum and redisperses it back to a series of white images on the output fibres of the slit. These output fibres are larger than the input fibres ( $200\mu\text{m}$  compared to the input fibres with a core diameter of  $110\mu\text{m}$ ) to allow for aberrations in the Schmidt system (see Figure 5-11). It is crucial that the vector from the output fibre to the input fibre is constant for all fibres as once glued in place, individual fibres cannot be moved to align their associated output images.

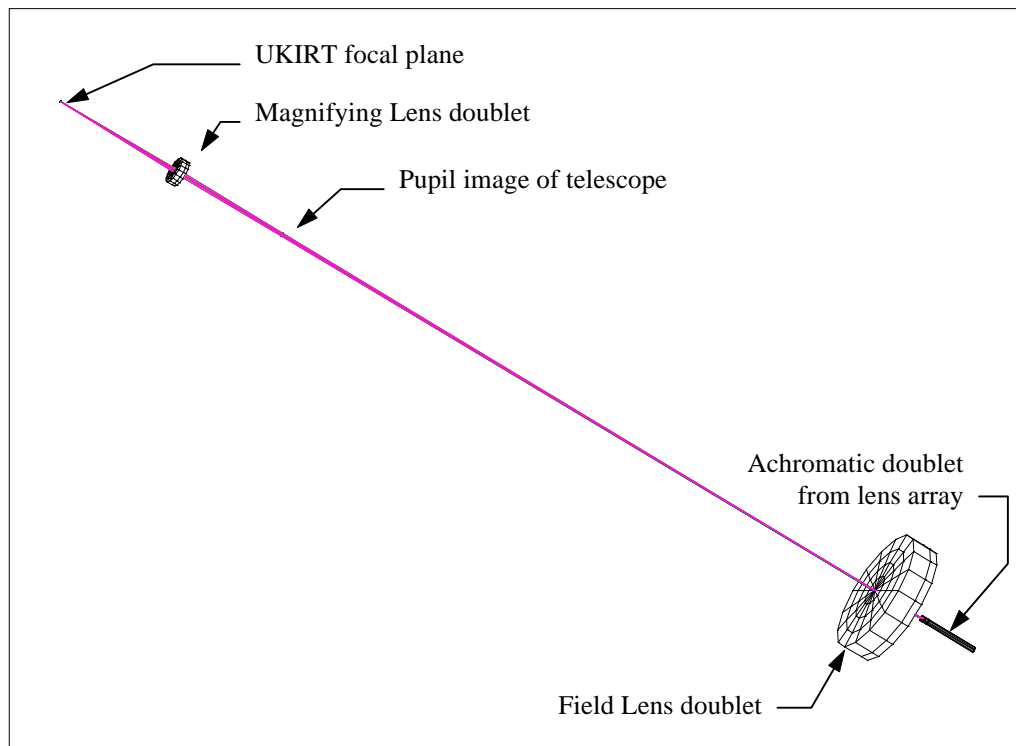


**Figure 5-9** Wire frame of the COHSI fore-optics.

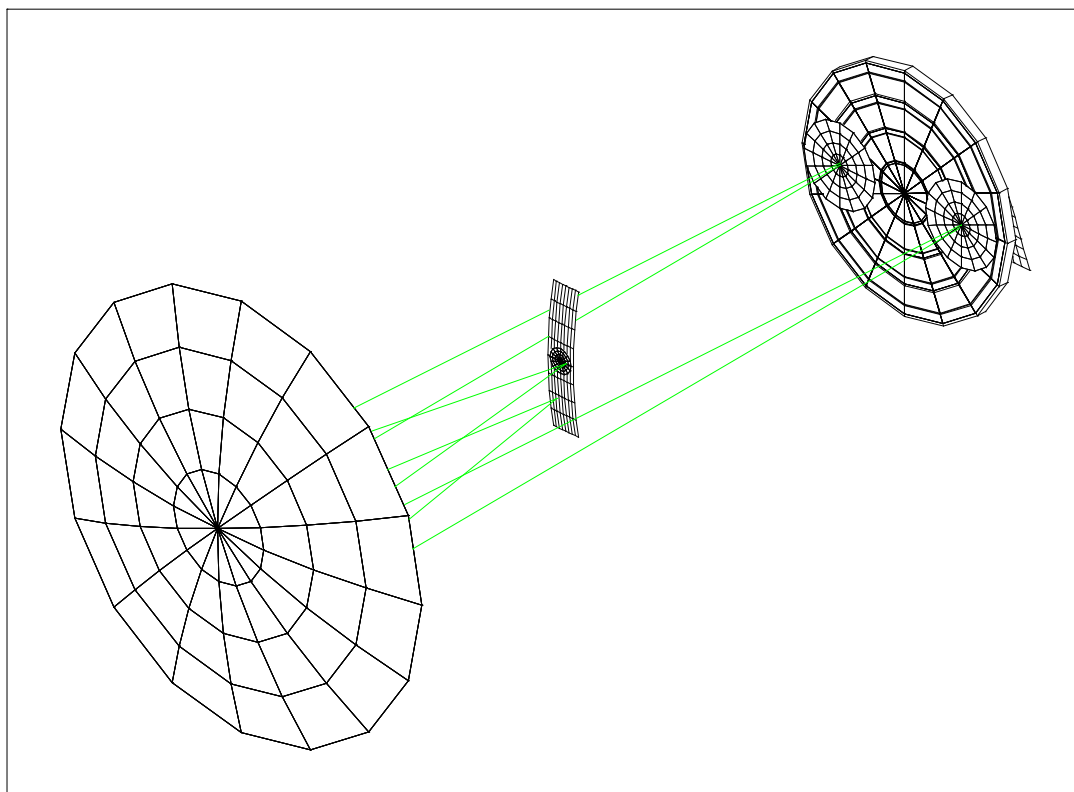


**Figure 5-10** A single fibre in the OH suppressor. This diagram shows the four passes that each fibre performs passing through the suppressor.

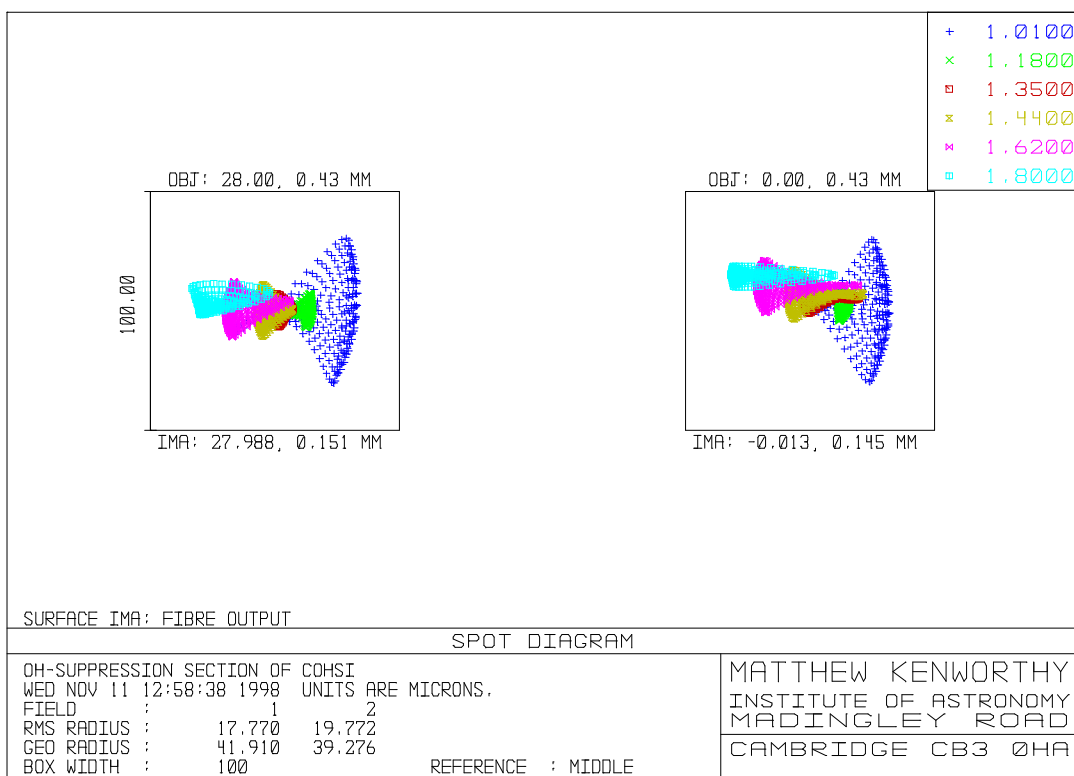


**Figure 5-11** Spot diagrams for the OH suppressor. These diagrams are the spot formed at the output fibre for a single polychromatic ray from the centre of an input fibre in middle of the slit (right diagram) and one at the end of the slit (left diagram).

Light is launched into the suppressor at an angle with respect to the normal of the focal surface and the output light is correspondingly accepted at another set of angles into the output fibres. These angles are crucial for correct pupil alignment on the gratings, so the fibres need to be accurately aligned along the correct optical line to ensure that there is no loss of light due to vignetting.

### 5.3.4 The cold fibre slit

The limiting magnitude of the faintest observable galaxies is determined by the dark current and scattered light inside the cryogenic dewar. Slit based spectrographs have an arrangement of cold aperture stops that prevent excess radiation entering the dewar, but any misalignment results in vignetting of the beam or an increase in the thermal background. By having a cold fibre feed instead of a slit with a cold aperture stop, the background level of scattered light drops below the dark current level of the PICNIC arrays. In COHSI the fundamental limit to detection is due to the dark current in the arrays ( $<0.5e^-/\text{pixel}$ ).

In order to pack the 100 fibres onto the 256 pixels across the array, the fibres themselves need to be arranged such that they are contiguous in the spatial direction. Arranging the fibres in a straight line is not the optimum packing strategy, as the cladding of the fibre introduces dead space between fibre images. To overcome the spacing introduced by the cladding layer, the fibres are staggered, with the fibre slit formed as two rows of fibres forming an alternate pattern (see Figure 5-12).

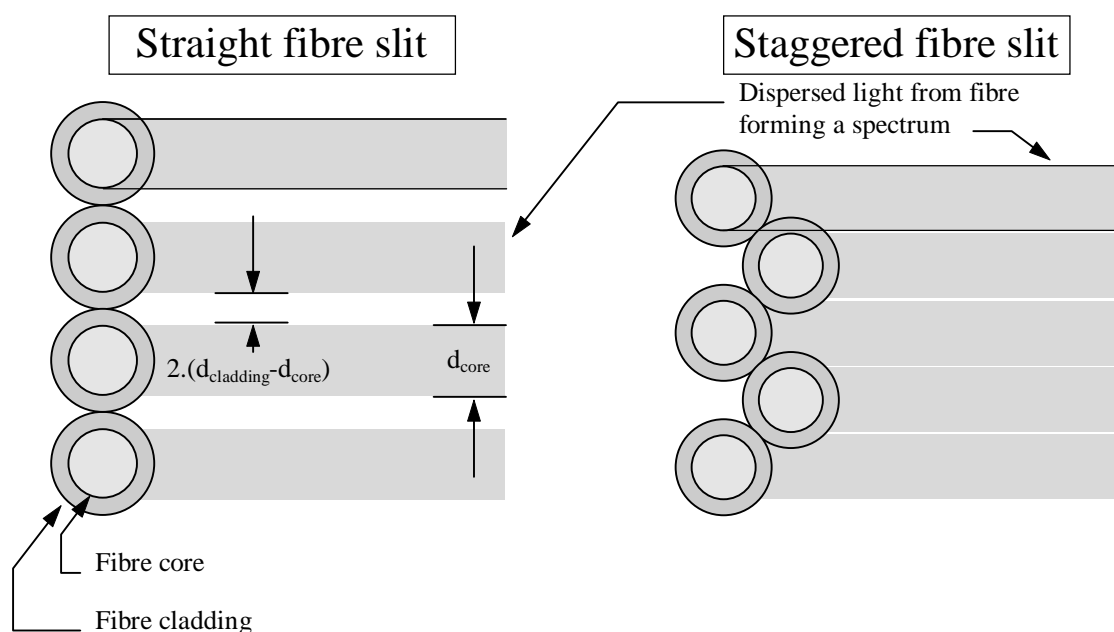


**Figure 5-12** *Inter fibre spacing reduced by a staggered fibre slit.* The spacing between fibre spectra can be reduced by putting the fibres in an alternate staggered pattern. Alternate fibres now have a systematic difference in wavelength offset.

## 5.4 Building the fibre feed

### 5.4.1 The fibre conduits

Two different diameters of optical fibre are used in the fibre feed - 110 $\mu$ m core diameter from the IFU to the suppressor, and 200 $\mu$ m from the suppressor to the cold fibre slit. They are supplied as two reels of continuous uncut fibre, which have to be cut to length and placed in the conduit.

First the total length of conduit and fibre needed is worked out by the geometry of the telescope. The length of the optical fibres was set at 12.50 metres for the long fibre feed and 4.30m for the short fibre feed, so a calculation is made to work out the remaining length of conduit needed (see Figure 5-13). The required length of conduit is cut, allowing for the room taken up by the spare length boxes and the conduit is fully stretched out so that when the fibre is in the conduit, there is no possibility that the fibres can become taut and break. Compressed gas is used to blow a strong cotton thread through the conduit and spare length boxes, so that the fibres can be pulled through.

Metal posts were fixed on two tables 12.50 metres apart, defining the length of fibre required. and after fixing down one end of the fibre with tape, the reels are unwound along the table, passing around the posts. When the number of required fibres is laid out (along with a few extra lengths in case of fibre breakage) the bundle of fibres are taped down and cut with a sharp scalpel. Care was taken to gather the fibres together, as tangled fibres can break whilst they are being drawn into the conduit.

One end of the fibre bundle is wrapped in a thin strip of paper and fixed together with cyanoacrylate to form a secure point with which to pull the fibres into the conduit. It is important that the fibres go into the conduit smoothly and slowly so that the process can be stopped quickly to rearrange tangled fibres.

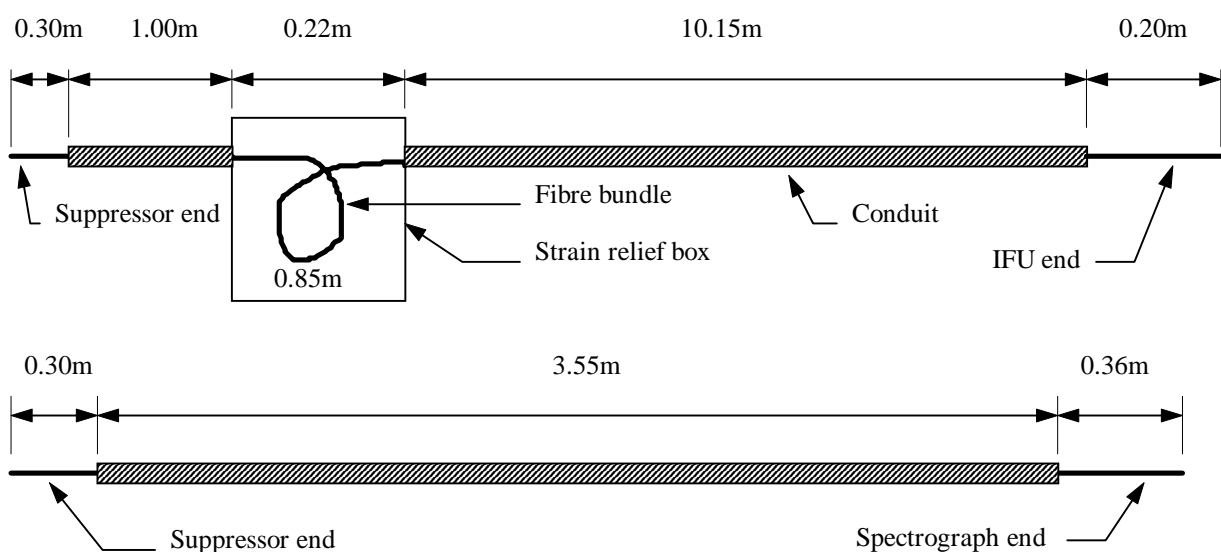


**Figure 5-13** Dimensions of the COHSI fibre feeds. The upper conduit is for the telescope to suppressor and the lower conduit for the suppressor to spectrograph.

In this way, both conduits are threaded with their respective fibre bundles. As the final step the fibre ends are soaked in acetone to remove the outer buffer and reveal the polyamide coating.

### 5.4.2 Lens array

The IFU comprises of 100 hexagonal achromatic doublets fixed onto an optically flat substrate of SF2 glass. This substrate is placed into mechanical contact with another flat of SF2 to form a lens array module whose thickness is equal to the focal length of the doublets (see Figure 5-14).

The achromatic lenslets have very poor transmission in the ultraviolet. This means that the epoxy used to fix the achromatic lenslets on the SF2 substrate cannot be cured by shining a UV lamp down through the lenslets. Instead the array is illuminated from underneath through the SF2 glass substrate, which has high internal transmission at the UV curing wavelength of 400nm.

To hold the lenslets in the correct pattern, an aluminium mask was manufactured which fits over the substrate (see Figure 5-15).

A hole cut in the shape of the lens array allows lenslets to be packed correctly onto the substrate. By assembling the array with the substrate on a slope of about ten degrees, gravity holds the lenses in a close-packed formation in the bottom of the array and allows easier assembly.

After the last lenslet is put in, a visual examination of the whole array is done to check for any air bubbles trapped between the lenslets and the substrate, and to see that no epoxy has seeped up between the sides of adjacent lenslets and run over the lens surfaces. The lens array is transferred to a glass tabletop and a UV lamp underneath the glass hardens the epoxy. The aluminium mask is then removed and the completed lens array has an anti-reflective I.R. coating deposited. The lens array substrate is fixed permanently into its aluminium holder with Araldite Rapid epoxy and bolted together with the other SF2 substrate to form the complete lens array (see Figure 5-16).

The fibres are now mounted in steel ferrules for polishing and fixing to the back of the lens array. For COHSI three ferrules are used for each fibre. The two inner ferrules ferrule are supplied from Coopers Needle Works and form a support for the outermost ferrule. This outer ferrule is

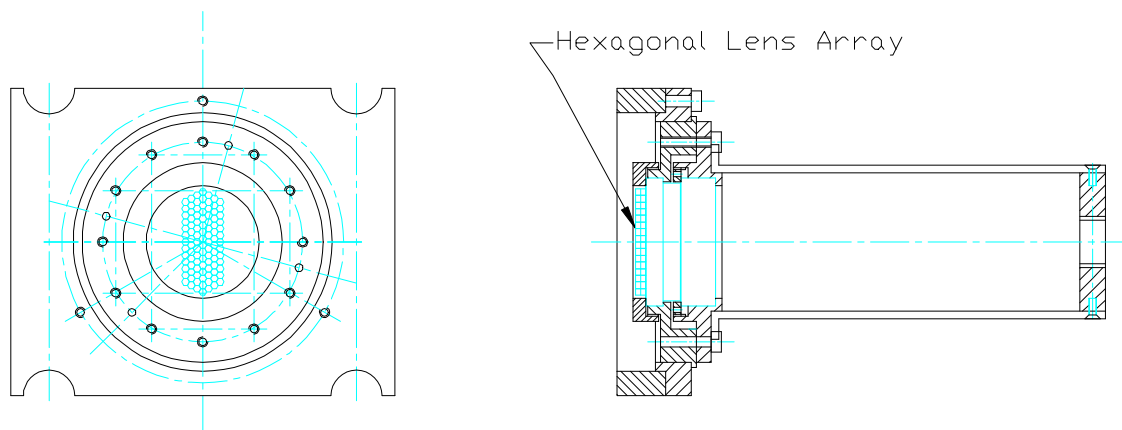


**Figure 5-14** *The COHSI lens array IFU.*

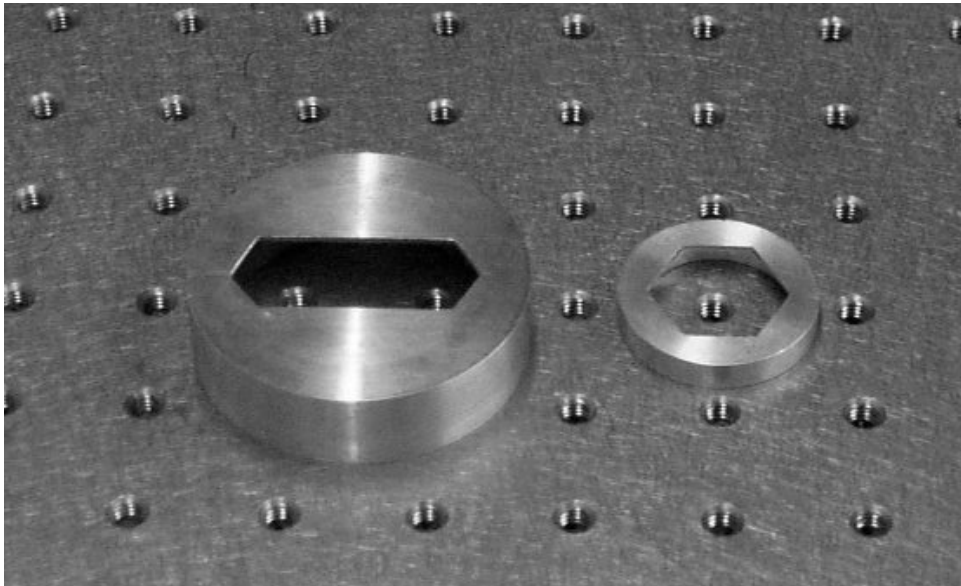


**Figure 5-15** Aluminium formers for the COHSI and SPIRAL lens arrays.

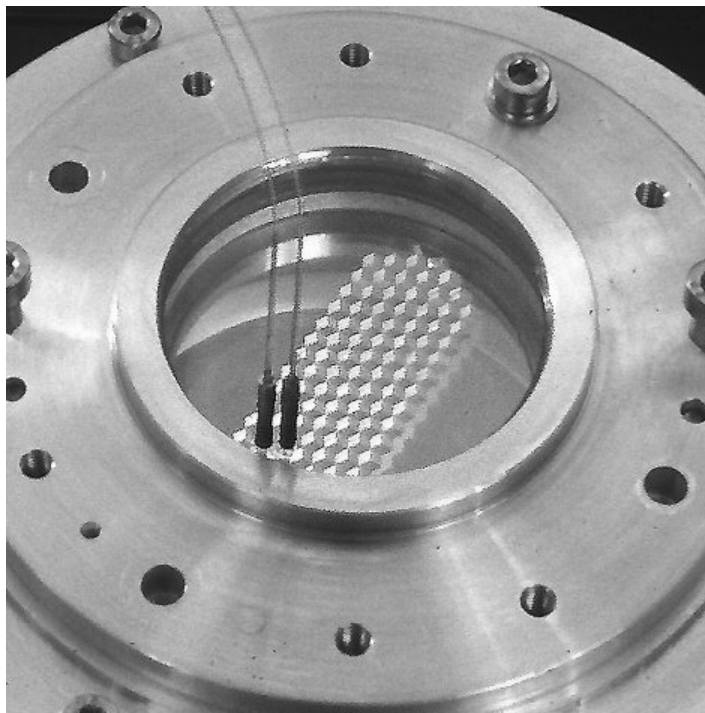


**Figure 5-16** Close-up of the COHSI lens array with two fibres in place. The lens array can be seen through the two substrates.

custom made for COHSI and they are manufactured using a wire machining process (see Figure 5-17). The layout of ferrules used for the COHSI lens array fibres is shown in Figure 5-18.

With all ferrules fitted to the fibres the ferrules are then mounted in a polishing jig and polished with the same method as used for the SPIRAL lens array ferrules (see §4.5.2 and §2.4). After removing and cleaning the fibre ferrules with acetone the ferrules are ready to be put onto the back of the lens array.

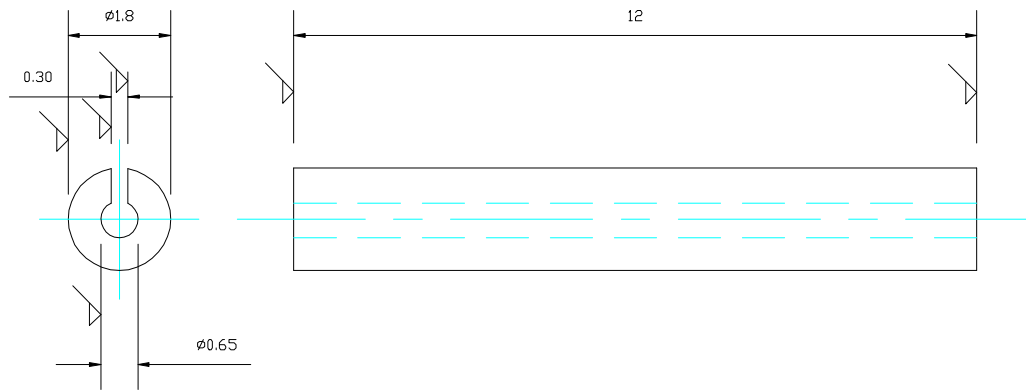


**Figure 5-17** The custom ferrule for the COHSI fibres.

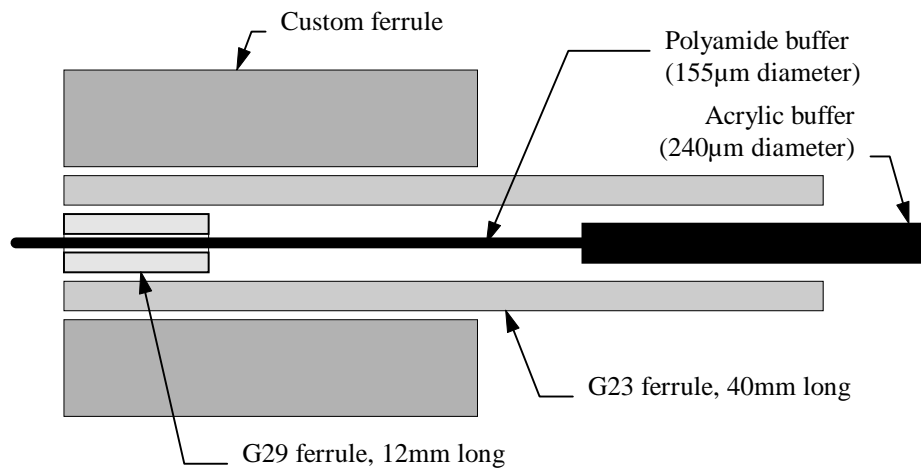


**Figure 5-18** The complete set of ferrules for the COHSI lens array fibres.

After the experience of the misalignments of fibres in SPIRAL, the process for aligning the fibres was slightly modified. Instead of the optical alignment equipment being horizontal along the optical bench, it is fixed vertically so that the COHSI fibres remain upright all the way through the optical alignment and potting process that holds them permanently in place. In this way it is hoped that the fibres are not put under any lateral stress that would cause alignment errors. The field lens from the fore optics is used to bring the fibre images to a common pupil image, which is then examined with a TV camera and microscope objective (see Figure 5-19).

The common pupil is marked with a circular graticule and the back illuminated fibre pupils are seen as a white spot that is aligned with the centre of the graticule.

It is vital that the graticule is in the focal plane of the field lens, so auto-collimation is used to adjust the graticule distance. A flat mirror placed across the back of the field lens mount produces an inverted image of the illuminated graticule only when the beam between the mirror and the field lens is collimated. This defines the focal plane of the field lens and the graticule is then fixed in place. The flat is removed and replaced with the lens array and substrate. An XYZ jig placed above the lens array holds and positions the fibre ferrules one at a time.

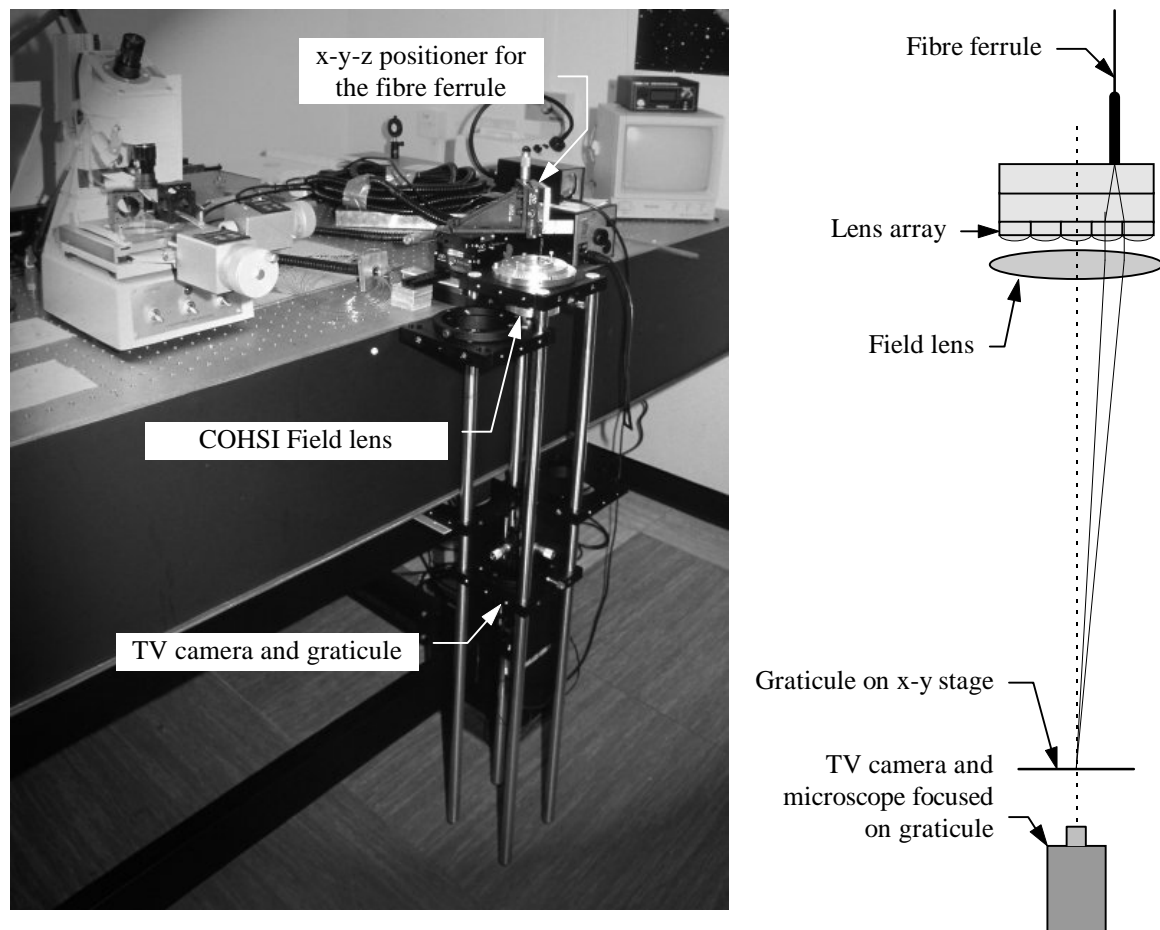


**Figure 5-19** Layout of the COHSI fibre alignment apparatus.

The lens array substrate and the fibre ferrule substrate are fixed in two separate metal holders which allow repeated removal and replacement of the two components. Two metal dowels ensure accurate and repeatable relocation of the lens array with the fibre ferrules. This design allows the fibre faces to be illuminated directly with UV light, thereby fixing each ferrule in turn on the array. It was this inability to illuminate the fibres on the SPIRAL array that led to the misalignment of the SPIRAL fibre ferrules.

The procedure for aligning a fibre with a lenslet is as follows:

- 1) A fibre from the suppressor end of the conduit is chosen and is back illuminated. The fibre ferrule is then easily identified and transferred to a microscope. The surface of the fibre is examined with a microscope and any excess epoxy is cleaned off with acetone. The ferrule is then fixed into the x,y,z stage (see Figure 4-19).
- 2) The fibre is brought down to the back surface of the lens array. Light from the fibre end passes through a selected lenslet to form a collimated beam. The field lens then produces an enlarged image of the fibre on the graticule and by moving the x,y,z stage the fibre image can be centred in the middle of the graticule.

- 3) The fibre is now lifted away with the z-motion of the stage and optical epoxy applied to the fibre face. As the fibre is moved back down onto the substrate the epoxy makes contact with the glass and spreads out over the substrate. The fibre usually requires some minor realignment at this point.
- 4) The UV lamp is used to 'tack' the fibre ferrule on the substrate by virtue of the meniscus of glue between the outside wall of the ferrule and the substrate surface. The SF2 glass with fibre attached is then lifted off the lower lens array substrate and placed on an adjacent stand. Light from a UV lamp is then shone from underneath the substrate through to the front face of the fibre. This illumination makes the epoxy harden across the whole fibre face, forming a strong mechanical bond (see Figure 5-16 for a close-up view of the fibre ferrules and substrate).
- 5) Placing the ferrule substrate back on the lens array substrate shows excellent re-alignment of the fibres with the lens array and the next fibre is selected.

As an extra alignment procedure, the first fibre on the lens array is used as a reference fibre - this back illuminated fibre is used every time to realign the graticule. Switching the light between the reference fibre and the aligned fibre then ensures that all the fibre pupil images are coincident.

For all 100 fibres this process takes approximately 30 hours, with an average of one fibre ferrule aligned and fixed on in twenty minutes.

After all the fibres are fixed into place, a small cylinder of plastic is constructed around the 100 fibres and a potting compound is poured into the inter-ferrule spaces. Potting compound is a liquid which cures over twenty-four hours to form a tough, environment resistant solid that provides mechanical support for the ferrules without putting undue lateral pressure on the ferrules that could cause misalignments. The name of the compound used is re-enterable polyurethane.

Assembling the protective box around the lens array completes the assembly of the integral field unit.

### 5.4.3 The curved double slit

The fibres pass through the conduit down to a strain relief box that sits on top of the suppressor unit. The fibre then passes through the suppressor to the curved fibre slit (see Figure 5-20), which sits in between the J and H mask mirrors. The design requires that the output fibres (200 $\mu$ m in diameter) sit less than 700 $\mu$ m away from their corresponding input fibres. These larger diameter fibres then pass on through the bottom of the suppressor to the cryogenic spectrograph nearby.

The fibres are held in the correct orientation and position by a series of radial grooves cut into two aluminium plates. The two plates are joined together and polished as one unit to form the curved double slit. The grooves are not perpendicular to the spherical slit surface (radius of 834.5mm), but

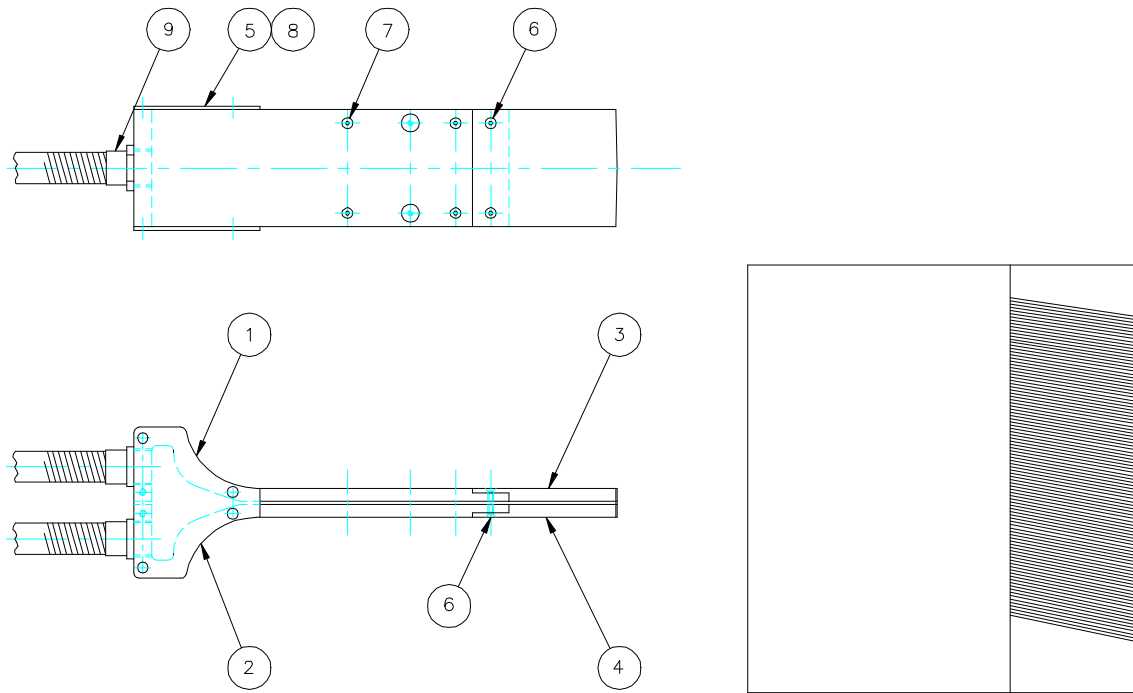


**Figure 5-20** *The curved fibre slit assembly.* The slit is assembled from two halves, each of which have one set of fibres connected to them. On the right is a detail of one fibre plate, showing the angled grooves which hold the fibres in the correct orientation.

they launch light into the suppressor at a mean angle of 6 degrees to the normal. The output fibre slit has a deeper grooves to accommodate the larger diameter output fibres.

Due to the close proximity of the two fibre slits, the input and output fibre slits are assembled separately before putting them together for polishing.

The relationship between the fibres on the lens array and their position on the fibre slit is such that adjacent fibres in the slit are adjacent on the sky. Since the lenslet fibres are fixed to the lens array this means that the input fibres have to be selected in the correct order for placement in the fibre slit (see Figure 5-21 for the fibre order).

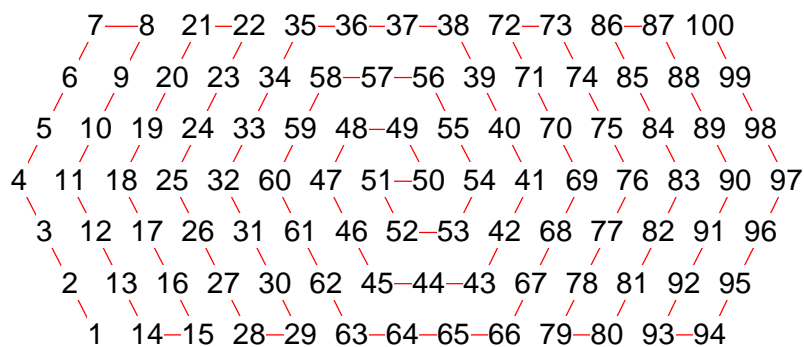


**Figure 5-21** *The order of the fibres in the curved fibre slit.* The fibres in the slit are numbered 1 to 100 from one end to the other. This picture shows the order of the fibres on the lens array.



**Figure 5-22** *The curved fibre slit on the spherical polishing plate.*

To hold the fibres in the grooved block during the insertion of all the fibres, a thin sheet of Teflon (PTFE) glued to a flat aluminium block provides a small but firm amount of pressure on the fibres. Each fibre is inserted into its allocated groove, held there under the Teflon sheet by the pressure of a rubber band encircling the fibre slit and Aluminium block. Initially two short lengths of fibre are used to hold up the other end of the block whilst the other fibres were inserted. These fibres are then removed when they are no longer necessary to provide support of the block.

After all 100 fibres are in place, the Teflon block is carefully pushed back along the fibres to reveal 10mm of the polishing plate. Epoxy is applied across the top of the fibre surfaces and grooves to hold them all in place. To help the epoxy reach underneath the fibres, a screwdriver is placed under the fibres and parallel to the slit surface. By raising the screwdriver the fibres are lifted up and epoxy runs around the fibres into the grooves. The Teflon block is now slowly moved forward over the fibres and epoxy applied to the exposed fibres at the back of the grooved slit. By moving the block slowly back and forth the epoxy reaches all fibres and grooves underneath the block.

The Teflon block is left overhanging the fibre slit edge whilst the epoxy cures. After carefully removing the rubber band the aluminium block is lifted off, leaving the Teflon sheet in place on the epoxy. Carefully peeling off the Teflon with small pliers reveals a flat surface of epoxy in which the embedded fibres sit fixed in their grooves. This process is repeated for the other fibre slit.

The input slit sits less than 700 $\mu$ m from the output slit, so it is important to clear any epoxy that protrudes above the plane of the fibres and can prevent the slits being brought together smoothly. Any excess epoxy is removed with a pair of tweezers and a scalpel.

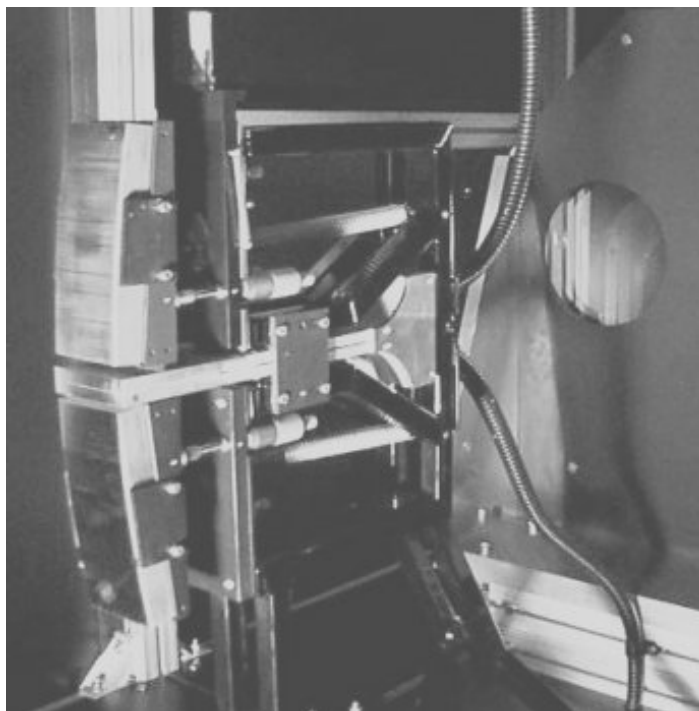


**Figure 5-24** *The curved fibre slit mounted in the middle of the OH suppressor.*

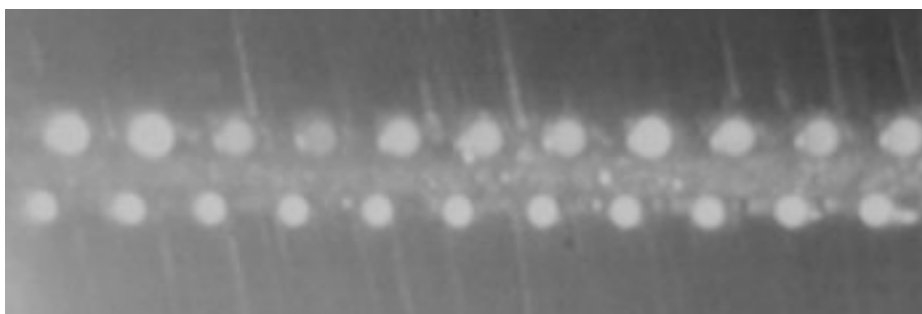


**Figure 5-23** *The finished curved fibre slit. The regularity of the fibre vector can be seen in the image. Higher magnification images are in Table 2-4.*

After checking that all the fibres are correctly placed in their respective plates, the curved fibre slit unit is assembled. The two halves of the curved fibre slit are now fixed together. The spacing between the two fibre slits is fixed by pieces of shim, and epoxy is run into the resulting gap. After curing, the fibre slit is ready for polishing.

The polishing jig is modified to hold the curved fibre slit and a spherical polishing plate with the correct radius of curvature is used to polish the curved fibre slit (see Figure 5-22). After conditioning the plate and polishing jig with carborundum powder, the completed curved fibre slit is successfully polished to a good surface finish (see Figure 5-24, Figure 5-23 and Table 2-4).

#### **5.4.4 The cold fibre slit**

The optical fibres pass from the output double slit inside the suppressor, through a small strain relief box on the outside fixing plate of the cryogenic dewar and into a flexible plastic conduit

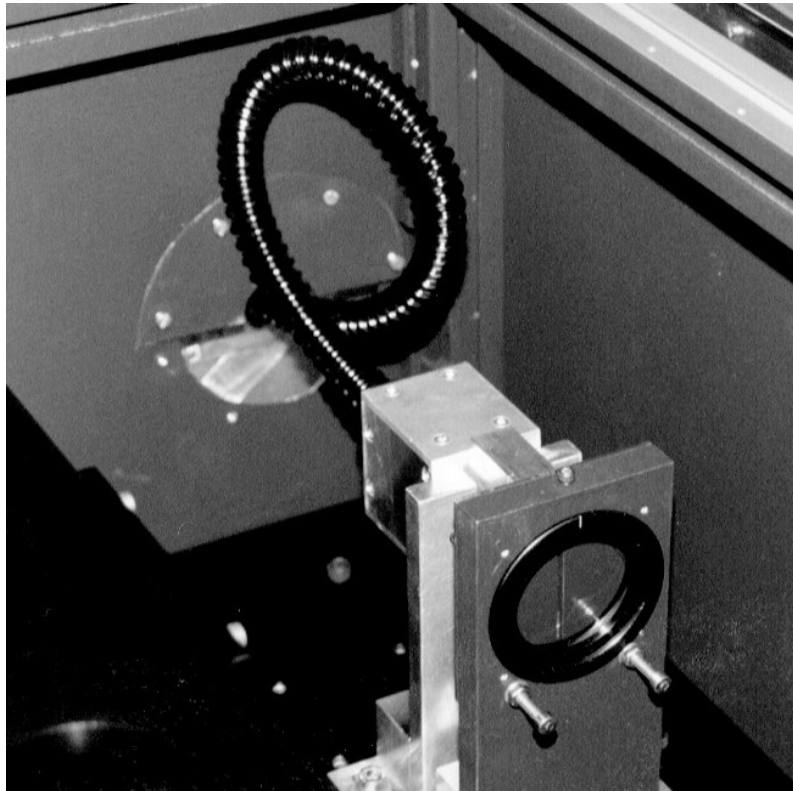


**Figure 5-25** *Cryogenic fibre feed inside COHSI dewar. The fibres pass through the wall of the dewar and into the fibre slit mounted on the optics table.*

that leads to the cold fibre slit (see Figure 5-25) Using a flexible plastic conduit with a cold fibre slit allows no background light to enter the dewar - the only thermal emission entering the cold spectrograph is that from the fibres themselves.

The fibres are arranged into a staggered pattern to fit all 100 spectra onto the PICNIC arrays as in §5.3.4. Figure 5-26 shows the design of the fibre blocks that hold the fibres in the correct configuration. Two grooved blocks are fixed together with two small G-clamps and small pieces of plastic shim set the correct spacing between the two blocks. This fibre slit is placed on two brass blocks on top of a metal heater in preparation for running epoxy between the fibres.

Two strands of fibre are used to test the groove block separation in the staggered slit. By varying the tension in the G-clamps holding the blocks together the correct spacing in the slit is selected. A knife edge held against the curved fibre slit casts a shadow from a bright light allowing the correct fibre to be selected from the fibre bundle. A binocular microscope and a pair of tweezers is then used to place the selected fibre into the staggered slit. All 100 fibres are eventually arranged in the slit in the correct order.

The heater is now switched on and the whole slit assembly is heated up to 70 degrees. The normally viscous epoxy becomes extremely fluid with heating, and application of the epoxy to the

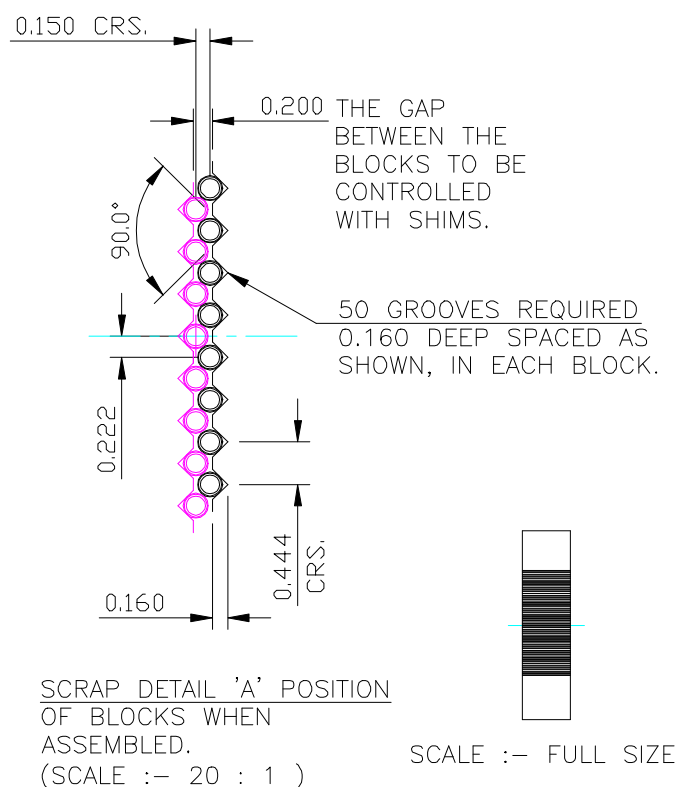


**Figure 5-26** Schematic drawing of the cold fibre slit. The staggered arrangement of the fibres shows how they are supported by two adjacent fibres and the fibre slit.

top of the slit allows gravity and capillary action to draw it through the completed fibre slit, ensuring a firm mechanical joint.

The slit is then taken and fixed into its metal housing with more epoxy. Any slack or variation in length in the fibres is taken out of the conduit by gently pulling on the appropriate fibres in the spare length box.

The fibres are then polished using the standard techniques covered in Chapters 2 and 4.

The fibres pass from the outside of the dewar into a small hole in the fixing plate which forms a seal with the dewar. It is here the fibres pass from room temperature and pressure into the vacuum of the dewar. This hole is made air-tight with Stycast, an epoxy with low out-gassing properties.

To make sure the fibres aren't inadvertently broken by stretching the soft plastic conduit too far, the conduit is kept artificially under tension whilst the epoxy cures. To do this the fibre slit is arranged vertically, with the outer mounting bracket held horizontally in a retort stand and the plastic conduit stretching downwards to the fibre slit. Weights on the cold fibre slit ensure that the conduit is kept under tension.

The curing of the epoxy and assembly of the cold fibre slit completes the building of the COHSI fibre feeds.

## 5.5 Measured performance of the fibre feeds

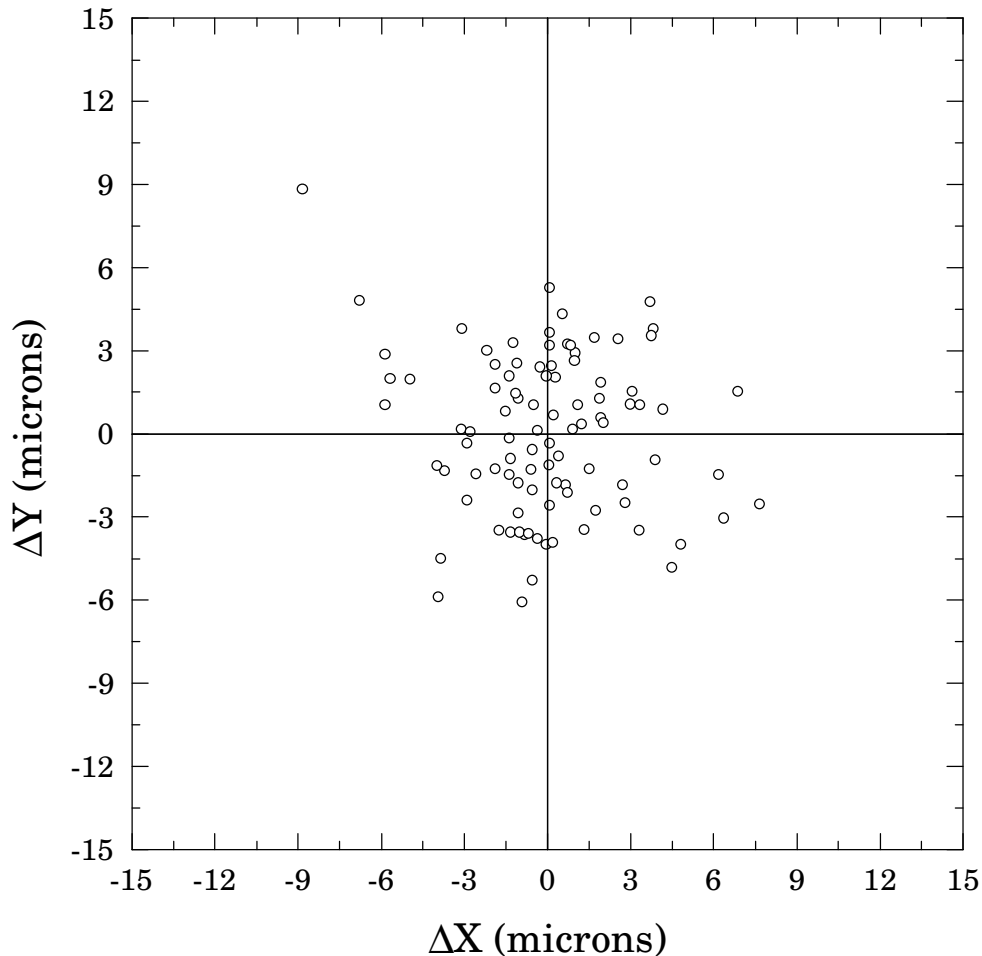


**Figure 5-27** *The positioning error of fibres on the back of the COHSI array. The errors on the measurements are 0.5 microns.*

### 5.5.1 The lens array

- (i) The lens array was glued together satisfactorily - however the Aluminium mask was found to be jammed onto the lens array by the edge-most lenslets in the array. Removing the Aluminium former cracked four of the lenslets in the removal process, causing their respective fibres to lose virtually all incident light. As the lenslets were all at the edge of the array and there was a considerable time constraint on the COHSI project, it was decided to keep with the lens array and avoid further delay by trying to replace the lenslets.
- (ii) Fibre positioning on the back of the lens array. The positions of the COHSI fibres were all within  $10\mu\text{m}$ , with 95% of the fibres falling within  $6\mu\text{m}$  of their average position (see Figure 5-27). A histogram of the fibre positioning errors is shown in Figure 5-28. The error budget for the fibres in COHSI is  $\pm 10\mu\text{m}$  so this means that all pupil images are aligned with their respective fibre cores.

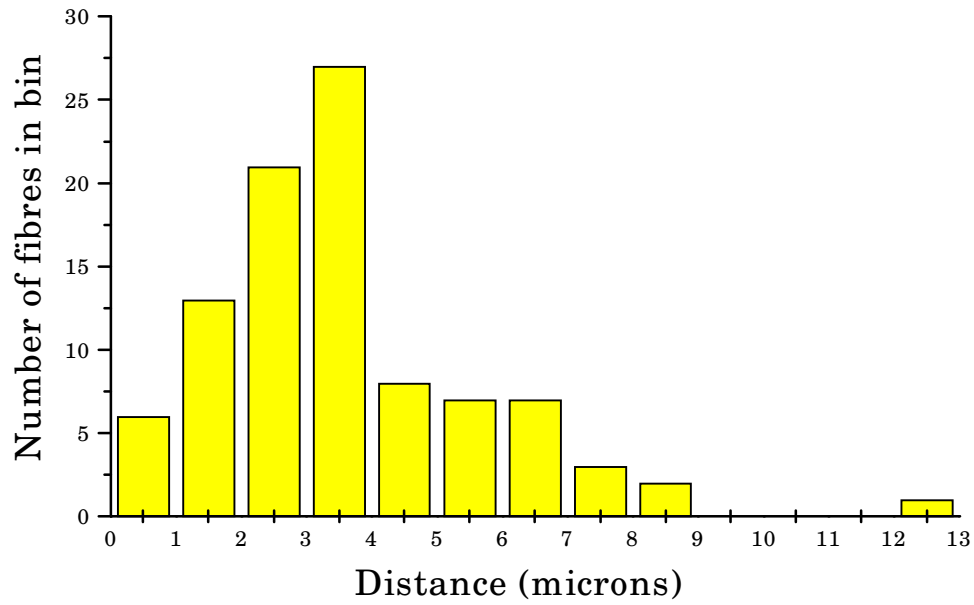


**Figure 5-28** Histogram of fibre positioning errors on the COHSI lens array.

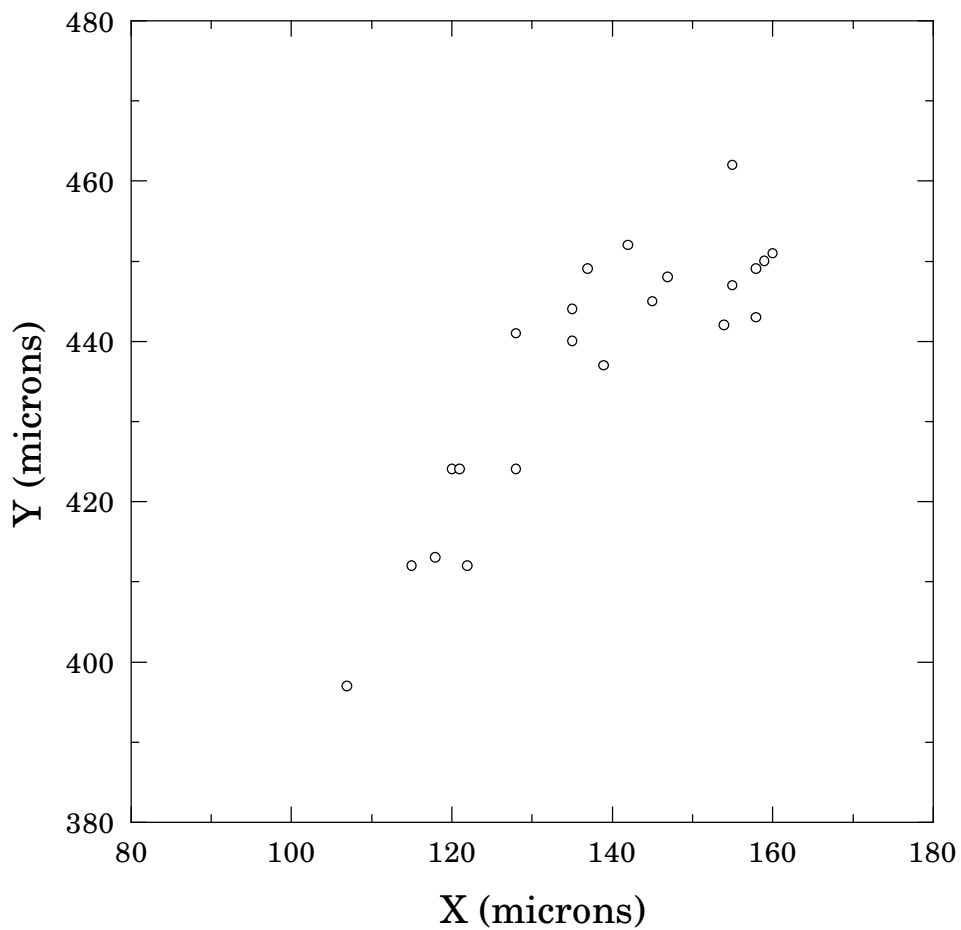


**Figure 5-29** COHSI curved fibre slit positioning errors. The points represent the vector from the centre of the large fibre to the small fibre.

### 5.5.2 The curved fibre slit

All 200 fibres in the curved fibre slit show no cracks or other surface defects when examined with a microscope. The most critical alignment in the fibre slit is the vector from the input fibre to the output fibre. If the vector is not the same for the fibres, then only the fibres with a given vector will be aligned in the suppressor.

A plot of the distance from the centre of the output fibre to the centre of the corresponding input fibre is shown in Figure 5-29. The plot shows the vector for 20 pairs of fibres evenly spaced along the fibre slit. The vector between the input and output fibres is not perpendicular to the fibre slits, but makes an angle of 72.5 degrees to the fibre slits. The x co-ordinate is the axis parallel to the fibre slits and the y co-ordinate is perpendicular to the fibre slits. The average separation of the two fibre slits is 437 $\mu\text{m}$  with the average distance between the fibre pairs is 458 $\mu\text{m}$ .

A plot of radial separation with fibre position along the slit shows evidence that one or both of the fibre slits is curved (see Figure 5-30). By fitting a curve to the data a standard deviation of 6.6 $\mu\text{m}$  was measured, meaning that if the slit curve effect is removed then the groove spacing technique has a positioning error of 6.6 $\mu\text{m}$ .

The error in the groove plate manufacture is enough to cause slight vignetting in fibres at the far ends of the fibre slit.

### 5.5.3 The cold fibre slit

All one hundred fibres were examined and found to be free of any cracks or surface defects and with a visual inspection all the fibres appeared to be regularly spaced with no fibres overlapping

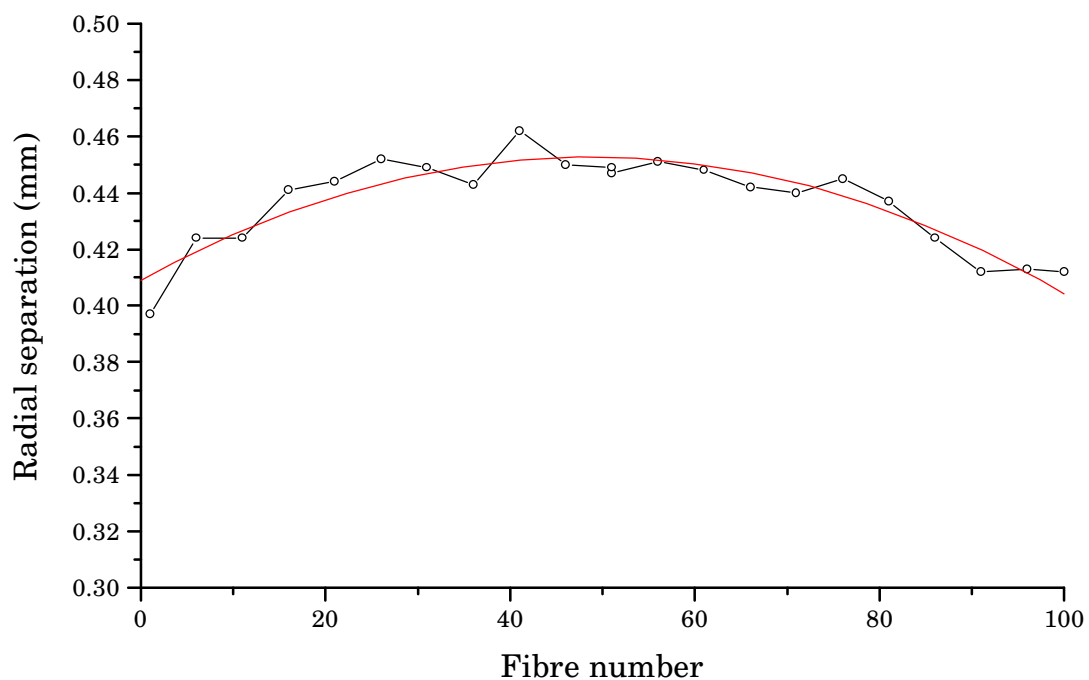


**Figure 5-30** Variation of the length of the fibre slit vector with position on the fibre slit. The curve fit is a second order polynomial, with a standard deviation to the fit of 6.6 $\mu\text{m}$ .

any other. The images of the fibre slit obtained from the spectrograph are near the critical sampling limit of 2.5 pixels per fibre, and for the purposes of the cryogenic spectrograph the fibre slit performs to specification.

## 5.6 Conclusions

All one hundred fibres have been accurately positioned on the back of the lens array with no geometric losses and no losses due to scratches or chipped surfaces. There are no geometric losses due to the positioning of the fibres either in the lens array or in the vector alignment of the fibres in the curved fibre slit.

All losses in the fibre feeds are due to FRD, which was measured in the throughput tests of COHSI on the UKIRT March 1998 run (Figure 5-31) and subsequent tests back in Cambridge. Clearly more research into FRD properties of infra-red fibres is required, but the technical assembly and construction of the COHSI fibre feeds (Figure 5-32) has been completely successful and has vindicated the techniques initially used and explored in the SPIRAL fibre feed.

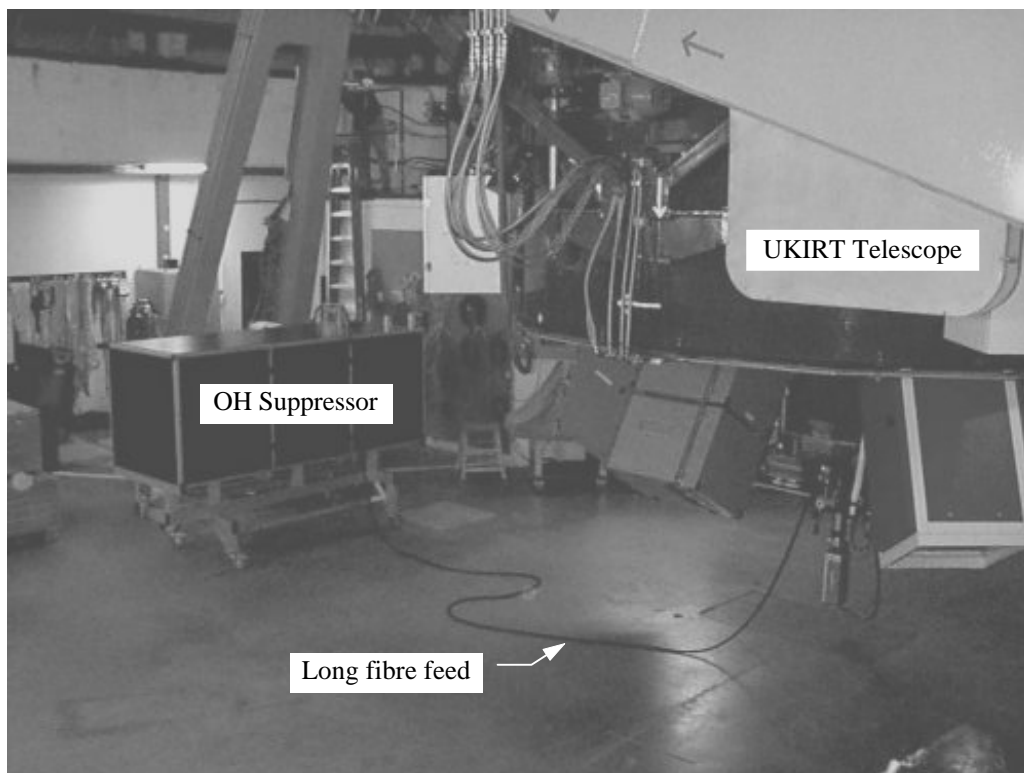


**Figure 5-31** *COHSI on UKIRT.*

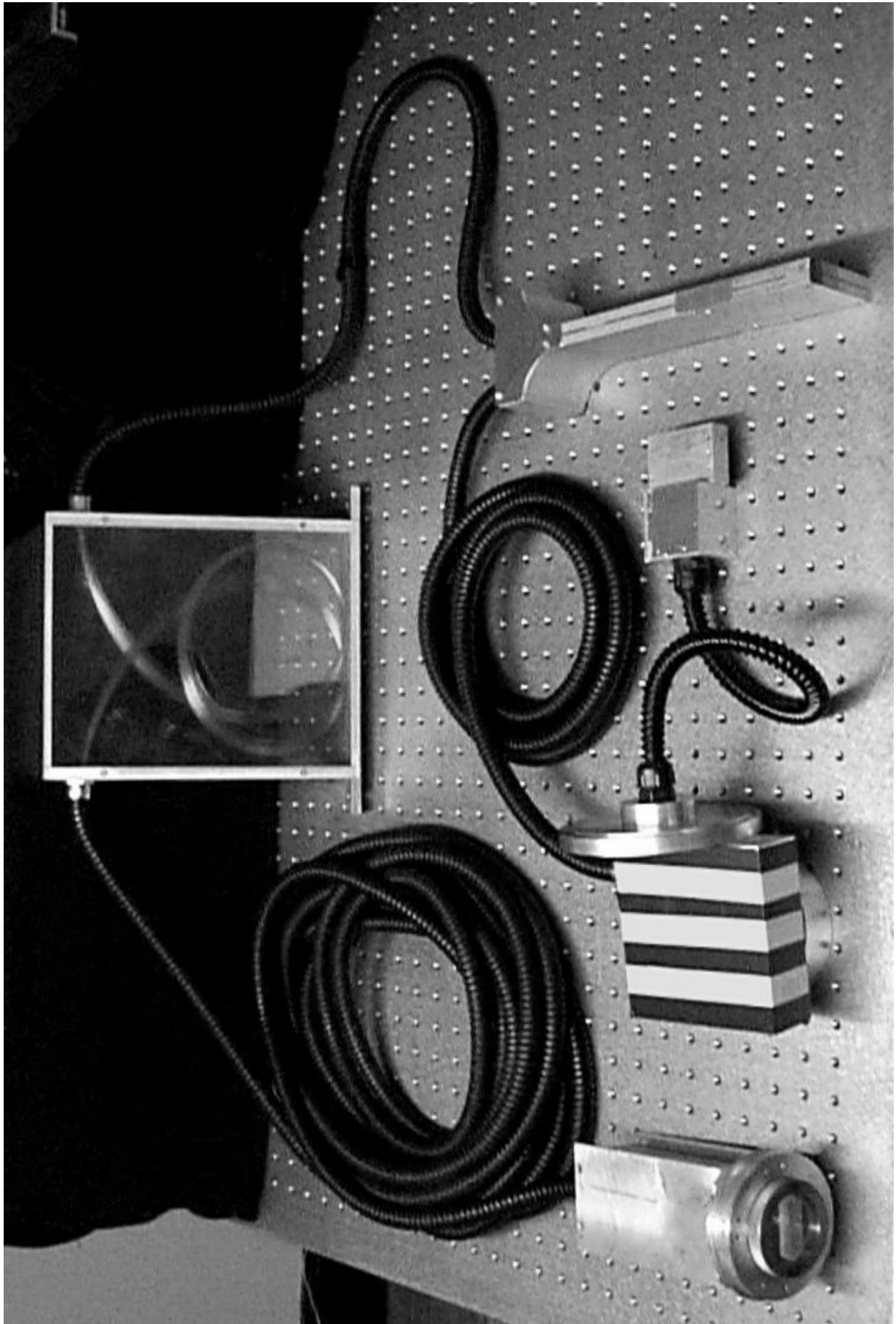


**Figure 5-32** *The completed COHSI fibre feed.*



## 6. Reduction of COHSI and SPIRAL data

---

### 6.1 Introduction

This chapter covers the steps needed to reduce fibre data from an integral field spectrograph (IFS) and the reduction of data from the pupil imaging mode of SPIRAL (§6.9.2). The format of the COHSI and SPIRAL data is an image containing rows of fibre spectra adjacent to each other (Figure 6-1). The order of the fibre spectra is related to the location of the fibre on the sky (see Figure 4-11), and with suitable software an image can be reconstructed from the fibre spectra (§6.8).

SPIRAL used an optical charge coupled device (CCD) to perform the imaging of the fibre spectra. On the two observing runs, two similar CCDs were used (the Tek 1024 and the MIT/LL 2kx4k) and the properties of these optical detectors are discussed (§6.2). For COHSI, an infra-red PICNIC array from Rockwell was used for the spectral imaging. Its readout modes and properties differ from a CCD and the resultant difference in data reduction is discussed (§6.3).

The location of fibre spectra in a data frame were identified and their centroids traced across the detector as a function of wavelength. All the two-dimensional spectra were extracted from the frame to produce one dimensional spectra, and they were then wavelength calibrated and resampled to a common wavelength scale and dispersion (§6.5).

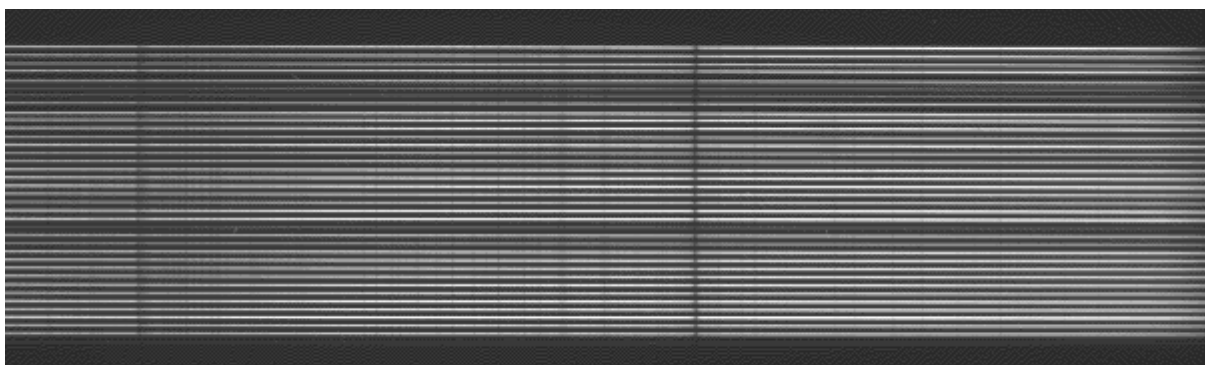


**Figure 6-1** A raw IFS data frame. In this data frame from SPIRAL the dispersion axis is across the page and the 37 separate fibre tracks can be seen. This is a twilight sky exposure, clearly showing absorption features in the atmosphere and the variation in throughput between fibres.

The COHSI fibre-fed cryogenic spectrograph had overlapping fibre spectra, resulting in signal cross-talk between extracted fibre spectra. Two issues arose from the overlapping of these

spectra and their small spatial profiles. The first was the tracing of the fibre spectra tracks (§6.6), and two methods were investigated - using a lens array mask, and interpolation from the two outermost defined tracks (§6.6.2). A set of simulations (§6.7) then showed that the cross talk could be minimised with use of a spatial filter (§6.7.2) and that interpolation of fibre tracks was a valid method for tracing COHSI spectra (§6.7.4).

This chapter finishes with a description of how to use the software for displaying IFS data (§6.8) along with an outline of the data reduction methods used in both COHSI and SPIRAL data (§6.9).

## 6.2 The MIT/Lincoln Lab 2kx4k CCD (SPIRAL)

The optical CCDs used with the SPIRAL spectrograph for the February 1997 and November 1997 runs were a TEK 1K<sup>2</sup> CCD and MIT/ Lincoln Laboratories 2048 by 4096 CCD, respectively. Their properties are listed along with the PICNIC array in Table 6-1. The CCD was housed in a vacuum dewar cooled to 80K, and was connected via an electronic controller to data storing computers in the observatory.

Detector	TEK CCD	MIT/Lincoln Labs CCD	PICNIC IR Array
Instrument used	SPIRAL	SPIRAL	COHSI
Pixel size	24µm	15µm	40µm
Array size (pixels)	1024 x 1024	2048 x 4096	256 x 256
Wavelength sensitivity	300nm - 900nm	300nm - 1µm	0.85µm - 2.5µm
Readout speed	Variable	55kpix/sec	190kpix/sec
Amplifier used	Single on-chip	Single on-chip	Individual for pixels
Readout mode	Destructive	Destructive	Non-destructive
Gain	2.74e <sup>-</sup> /ADU	1.11e <sup>-</sup> /ADU	10e <sup>-</sup> /ADU
Typical dark current	1.10e <sup>-</sup> /pix/4000s @ 170K	<0.3e <sup>-</sup> /pix/4000s @ 160K	<0.5 e <sup>-</sup> /pix/s @ 77K
Typical read-out noise	4.8e <sup>-</sup>	2.0e <sup>-</sup> (NORMAL)	15-20e <sup>-</sup> RMS/read

**Table 6-1** Physical parameters of detectors used for SPIRAL and COHSI

### 6.2.1 Physical description of the CCDs

A diagram of the layout of a charge coupled device (CCD) is shown in Figure 6-2. The light sensitive portion of the CCD is the rectangular area of silicon in the middle of the chip, with read-out microelectronics built to one side. A pixel is a square region typically tens of microns on a side on the active area and is defined by walls of impurities introduced into the silicon. It is made light responsive by applying an electrical current across a set of electrodes attached to the underside of the

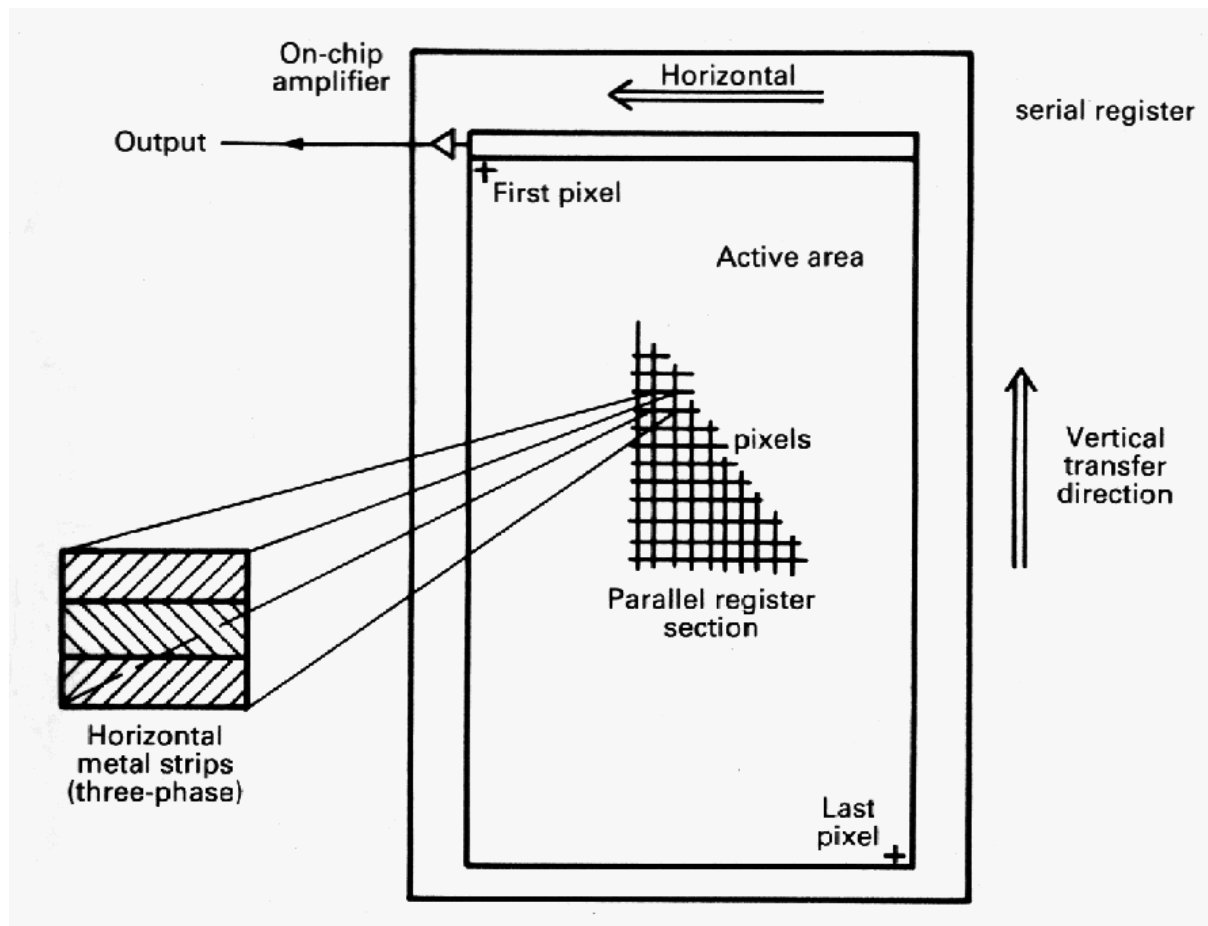


**Figure 6-2** Schematic of a CCD. Diagram taken from McClean (1997).

active area (Figure 6-3). Incoming photons liberate electrons from the silicon by the photoelectric effect, and the resultant electron/hole pair is separated by the electric field applied across the silicon. More charge accumulates as more photons are absorbed, and the charge is held in the confines of the pixel.

The CCD is read out a pixel at a time by adjusting the voltages in rows of pixels in a synchronised pattern - the effect is to move all charges in all the pixels one row up the CCD. The topmost row of the CCD is light-proofed, and is used to read out the row one pixel at a time. This is called the serial register, and a clock is used to transfer the charges from right to left into the on-chip amplifier (see Figure 6-3). Here an amplifier measures the charge of a single pixel and an output voltage that is directly related to the charge on the pixel is produced and recorded. During the readout sequence the pixels are still capable of receiving light, so a shutter is closed across the CCD during its readout (compare with the PICNIC array which does not need a shutter §6.3).

After one row is read out, the whole array of charge is shifted one row up and the readout process repeated for the next row. In this way, all the CCD pixels of the MIT/LL are read out through the on-chip amplifier.

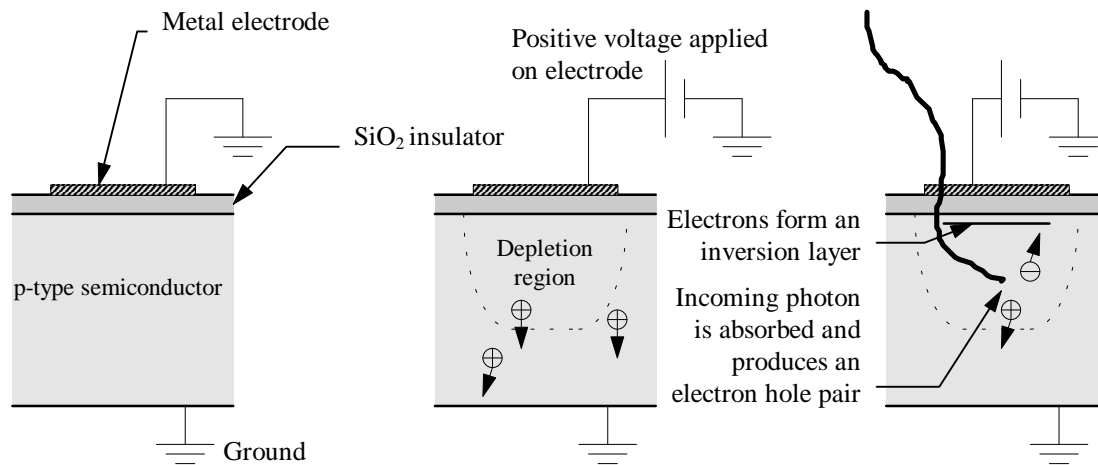


**Figure 6-3** A single metal-oxide-semiconductor (MOS) storage well. This is the basis of a pixel in a CCD. The CCD is made light responsive by applying a voltage across the silicon dioxide insulator. The excess of holes in the doped silicon cause a light sensitive depletion region to form near the electrode. (Adapted from McClean 1997)

The amplifier produces a read-out voltage for a given charge detected at the input of the amplifier. It is this voltage which is measured by the CCD controller and subsequently converted to a data number suitable for a computer.

### 6.2.2 The CCD controller and computer

A CCD controller is an electronic microcomputer that acts as an interface between the CCD and the host computer. It interprets the high level commands from the computer into sets of low-level commands that the CCD amplifier and shift registers use, and it also contains an analogue-to-digital converter (ADC) that converts the output voltage from the CCD into a digital number.

The number of bits used to represent a given voltage level in the controller dictate the dynamic range of the CCD. Most optical CCD controllers are 12-bit (4096 Data numbers) through to 16-bit (65,536 Data Numbers). The limit to the number of electrons that can be contained by a pixel is called the 'full well' limit, and depending on the operating mode of the CCD this can be many hundreds of thousands of electrons. The conversion factor between measured charge and data number is the gain of the ADC, and is measured in electrons per data number ( $e^-/\text{DN}$ ). Its value is set to a value such that the dynamic range of the ADC matches the application the array is intended for.

The amplifier introduces read noise to the measured voltage which can be positive or negative. For pixels with little or no charge in them this means that the read noise can give negative voltage values which are outside the range of the ADC. The solution to this is to add small positive voltage to the output of the amplifier that ensures that all pixels will give a positive non-zero voltage at the input of the ADC. An exposure of zero seconds with no illumination on the CCD during readout is called a 'black level image' and it gives the zero point values for all pixels in the CCD.

### 6.2.3 The black level and dark current of the MIT/LL CCD

The black level of an optical CCD is set to give a small positive value from the digital to analogue converter in the controller. Because the CCD uses the same amplifier for readout, the black level does not vary widely. For black level estimation the shift register is read out for an extra 32 pixels, located outside the main CCD area, called the overscan region. A good estimate of the black level for a row can be made by taking an average of the overscan region and taking off this value from that row.

In the SPIRAL November 1997 run this value was 170 data numbers, and varied by less than 1 data number along the length of the whole CCD. The black level is automatically subtracted as part of the first phase of CCD data processing, and presents no further concerns later on, in marked contrast to the situation with IR arrays.

A long exposure with no illumination on the CCD gives a black level subtracted image with non-zero pixel values. These electrons are generated in the silicon by sources other than photons, and the image produced is a 'dark current' image. The measured dark current varies from pixel to pixel and is measured in electrons per second. These currents are generated at the surface of the pixels where physical defects lead to the formation of intermediate electronic energy levels. Thermal vibrations in the lattice then liberate these electrons as dark current, leading to the observation that dark current is a strong function of temperature.

Early CCDs had large dark currents due to the transfer of charge across the silicon surface as the CCD was read out, but the latest series of optical detectors transfer the charge within the body of the silicon, leading to considerably reduced dark currents (e.g. the MIT/LL CCD has a dark current of less than  $0.3e^-/\text{pix}/3000\text{s}$  at 160K).

### 6.2.4 Flat fields

If the CCD is evenly illuminated with light the resultant image shows different data numbers (DN) recorded for each pixel. A combination of the CCD manufacturing process that determines their physical size and a variation of quantum efficiency (QE) leads to different sensitivities across the CCD. This image is called a 'flat field' and (for monochromatic light) can show variations on the order of 1-2%, usually in a systematic pattern. By normalising the pixel values in a flat field image, this normalised flat field can be divided into a data image to correct for the QE differences between pixels.

Flat fielding is well-behaved with the CCD but care is needed. A flat field image is effectively a map of quantum efficiency for the pixels in a CCD, and there is a marked variation of QE with the wavelength of incident light (see Figure 6-4). This variation can be as large as 10% for the lowest dispersions in SPIRAL where over  $2000\text{\AA}$  can be covered in one exposure with the MIT/LL CCD. Since there is a variation of wavelength with pixel number across the data images,

there is also a corresponding QE variation in the flat field, so it is essential that the flat field has the same spectral range and dispersion as that in the data images.

In fibre-fed spectrographs the fibre colour transmission and QE variation is corrected by taking a fibre flat field image. The dome is illuminated and the light passes down the fibres into the spectrograph and is dispersed in the same manner as light in a data exposure. The image produced is similar to that in Figure 6-1. This image can not be reliably used to perform two-dimensional flat fielding, however. The inter-fibre spaces in the flat field have few counts in them, usually only from scattered light from the optics. Attempting to divide this normalised flat-field image then results in inter-fibre pixel values with a large variance, and these values can cause problems for the fibre extraction. The solution is to first extract the fibre tracks from the flat field and data image separately and perform the normalising after. This solution is valid provided that both the data and flat field frames are reduced in the same manner.

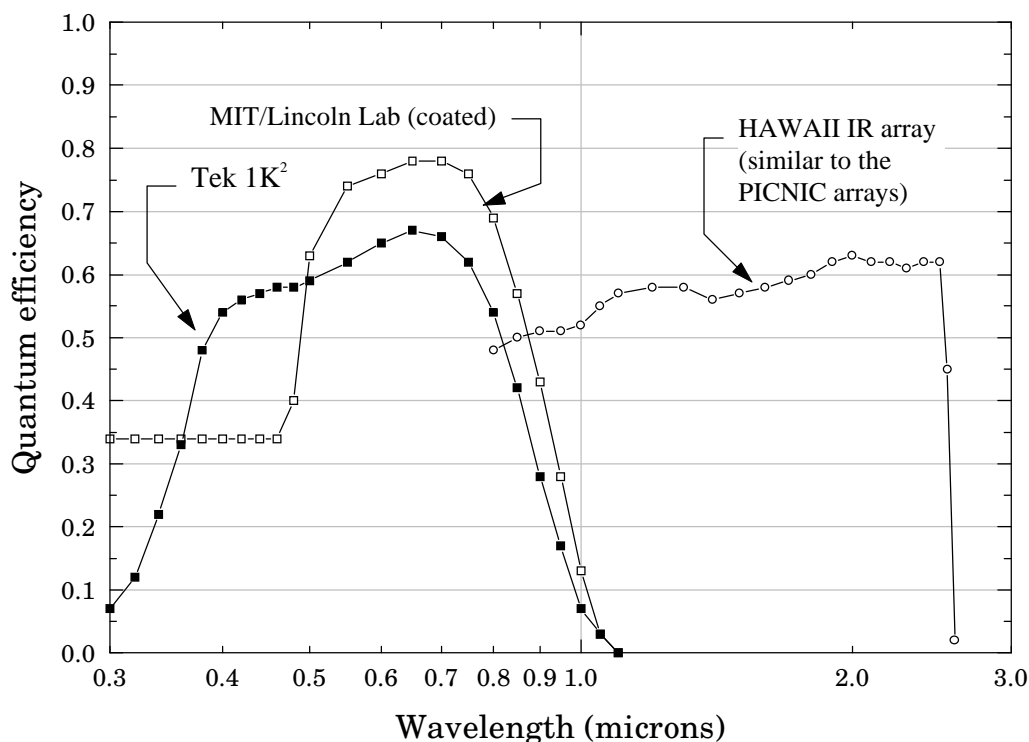


**Figure 6-4** Quantum efficiency curves for the MIT/LL CCD, the Tek 1K<sup>2</sup> and a HAWAII array<sup>1</sup>. There is no published QE curve for a PICNIC array but they are known to be similar in design and performance to the HAWAII arrays.

### 6.2.5 CRE removal and hot pixels

The manufacture of CCDs can result in a few pixels not properly connected to the shift registers, resulting in a loss of charge transferring capability. If this occurs near the end of the CCD

<sup>1</sup> Graph modified from data in [http://www.ast.cam.ac.uk/AAO/local/www/cgt/ccdimguide/mitll\\_performance.html](http://www.ast.cam.ac.uk/AAO/local/www/cgt/ccdimguide/mitll_performance.html) and <http://www.ast.cam.ac.uk/~optics/cirsi/hqe.gif>

with the shift register, then working pixels further down the array will lose their charge when entering the bad pixel. In the resultant image this results in a bad column of pixels for which no data can be collected. By looking at a flat field frame the bad pixels can be identified and their values replaced with values interpolated from surrounding pixels using various algorithms.

Cosmic ray events (CREs) are one or more pixels in the CCD that have a large amount of charge deposited in them by secondary showers of particles from high energy cosmic ray events high in the atmosphere. Algorithms can be used to identify and replace these anomalous pixels. Because of the wide spread of intensities that a CRE can produce, a simple and robust method is to median combine at least three exposures together. In this way, CREs are removed with minimum user intervention.

### 6.2.6 Summary of data reduction for SPIRAL

The data reduction procedure for the raw image frames using IRAF is:

- Image is trimmed and the overscan region is used to remove the black level with the routines in CCDPROC and ZEROLEVEL. Ten or so black level frames are median combined to remove sporadic CREs and this image is subtracted off all the subsequent data images. For each individual image the overscan region is used to make a further correction of black level if needed. If there are no large scale gradients in the combined black level frame and it looks uniform, then the overscan region in individual frames is used to define a correction for each row on the CCD.
- Data frames of the same object can be combined using IMCOMBINE with a median combine option to remove CRE. This requires at least 3 exposures of the same object. If three exposures have not been taken, other routines using the known gain and read noise of the CCD can identify anomalous events and clip them out of the data images. However, the median combining method is the most robust, requiring minimal user interaction.
- A fibre flat field image is used to identify the positions of the fibre spectra and apertures are defined for all the spectra (see §6.5). The scattered light in the image is then removed using APSCATTER.
- Flat fielding can be performed using an evenly illuminated image if a lamp is present in the spectrograph, but it is preferable to use a fibre flat field and perform the flat fielding after extraction of fibre spectra from the data image and fibre flat field image.

## 6.3 The PICNIC Infra-Red Array (COHSI)

A different technique for detecting photons longer than  $1\mu\text{m}$  is required, as the energy band gap of silicon is equal to  $1\mu\text{m}$ . Other semiconductors with lower energy band gaps are used instead.

### 6.3.1 Physical description

The PICNIC infra-red (IR) arrays have a fundamentally different design from optical CCDs. Instead of using the same silicon layer for charge storage and image readout, the IR arrays are composed of a two-layer sandwich (see Figure 6-5). The upper, light sensitive layer is referred to as the 'detector array' and is connected via small indium contacts to a lower layer called the 'multiplexer' which is not light-sensitive in the infrared region, though it is sensitive in the visible region. This readout method means that no shutter is required to cover the array as it is read out, and the array can continue an exposure during the read-out of the multiplexer.

The act of reading out a CCD causes the charge in the pixels to be lost as the charge is moved over to the shift registers and read out from the on-chip amplifier. With IR arrays the charge is not moved across the silicon, but instead the multiplexer can individually and non-destructively sample the charge in the detector array above. Each pixel has an individual amplifier associated with it in the multiplexer. Additionally the whole multiplexer is fully addressable and each pixel is sampled independently via two positional shift registers.

This fundamental difference in design of the read-out modes allows multiple reads during a

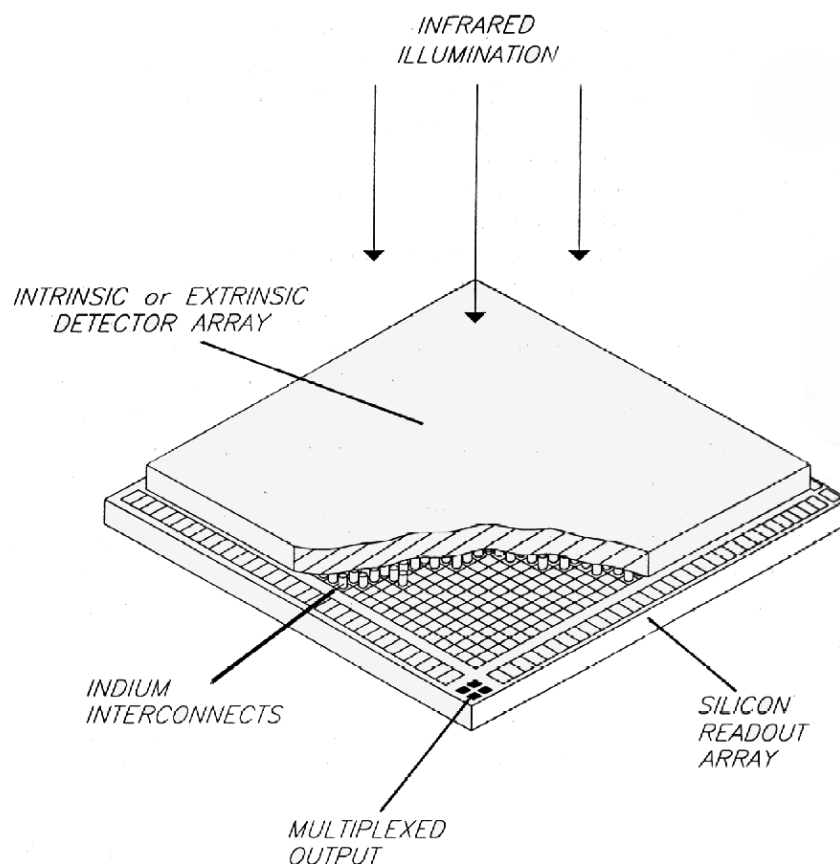


**Figure 6-5** Layout of the IR array. The light-sensitive detector is connected to a multiplexer underneath. The multiplexer is completely addressable and can non-destructively sample the charge in the array via indium connections (Diagram taken from McClean 1997).

typical exposure and different consequences for read-out noise, black levels and QE variations in the array. These differences are discussed and the multiple reads during an exposure allow removal of CRE and hot pixels.

The PICNIC array detectors used in COHSI are composed of a Mercury Cadmium Telluride mixture and so are known as ‘MerCadTel’ devices. They are sensitive from 850nm to 2.5 $\mu$ m and therefore they detect thermal radiation from room temperature objects, so the optics of the spectrograph have to be cooled to remove their thermal glow. A short band pass filter is also used to cut out any other thermal emission from beyond 1.8 $\mu$ m, and the dark current (which is a strong function of temperature) is reduced by cooling the array to liquid nitrogen temperatures.

### **6.3.2 The PICNIC controller and computer**

The array is interfaced to the data logging computer by an array controller, in this case an Astrocam 4100 controller working on a PC with Windows95 software. The controller deals with the array as a single unit, allowing simple commands that influence the whole array to be performed e.g. the RESET command and the READ command. The controller then uses clocking pulses to manipulate the shift registers for reading out of the array.

The RESET command causes the multiplexer to discharge all the charge stored on the array pixels whilst the READ command allows the charge to be measured by the multiplexer from the array above without destroying the charge residing within the array. These reads are called ‘non-destructive reads’ and allow the array to be sampled many times during an exposure.

The charge accumulated by a pixel is amplified by the multiplexer and digitised by an analogue to digital converter (ADC) in the controller. The numbers from the ADC are called ‘data numbers’ (DN) and the constant relating the number of electrons measured in the pixel to the DN is called the ‘gain’ or  $g_{\text{pixel}}$  often defined as electrons/DN. Care must be taken to note how the gain is defined for an array of pixels, since each pixel has its own amplifier.

### **6.3.3 Black level and dark current**

When a RESET is immediately followed by a READ in conditions of no illumination, the result is a ‘black level’ frame (see Table 6-2). The pixels have a distribution of non-zero values, the modal value of which is set by a DC voltage offset in the controller. This value is adjusted so that all the pixels have a positive value associated with them.

Black levels are almost always subtracted from subsequent exposures to produce a resultant image, and as a consequence are rarely dealt with directly by the user.

A simple exposure is composed by:

The array is RESET, immediately followed by a READ.

	Zero exposure time (first READ)	Non-zero exposure (second READ)
Frame readout with no black level frame subtraction		
Frame after black level frame subtraction		

**Table 6-2** The RESET-READ-READ mode of the PICNIC arrays.

The array is read out again with another READ after a defined exposure time, and the initial READ is subtracted from it. The resultant image has the black level subtracted off. This method also ensures equal exposure for all the pixels since they are read out in a raster format.

An exposure made with a RESET, READ, READ of a few minutes with no illumination will show non-zero values across the array. This is dark current, and is an introduction of electrons into the pixels from sources other than photons. The dark current is measured as electrons/second or DN/second, and varies strongly with the temperature of the array. It is important to take a dark frame of equal exposure length to any science exposure taken with the array, as the effects of dark current need to be subtracted off. In the case of COHSI, it is this dark current and the noise it contributes that determines the limiting magnitude of the instrument - COHSI is unusual in that other IR instruments are sky background limited.

**6.3.4 Flat fielding**

A RESET, READ, READ is performed with a source of even illumination over the whole array, and another exposure as a dark frame is taken. The difference of these two frames gives a ‘flat field’ (FF) showing the variation of quantum efficiency (QE) across the array from pixel to pixel. This can be represented as a QE flat that can be used repeatedly for calibration techniques but is rarely used in practice as the variation in QE across an array is on the order of 3%, as measured from tests on the IR arrays.

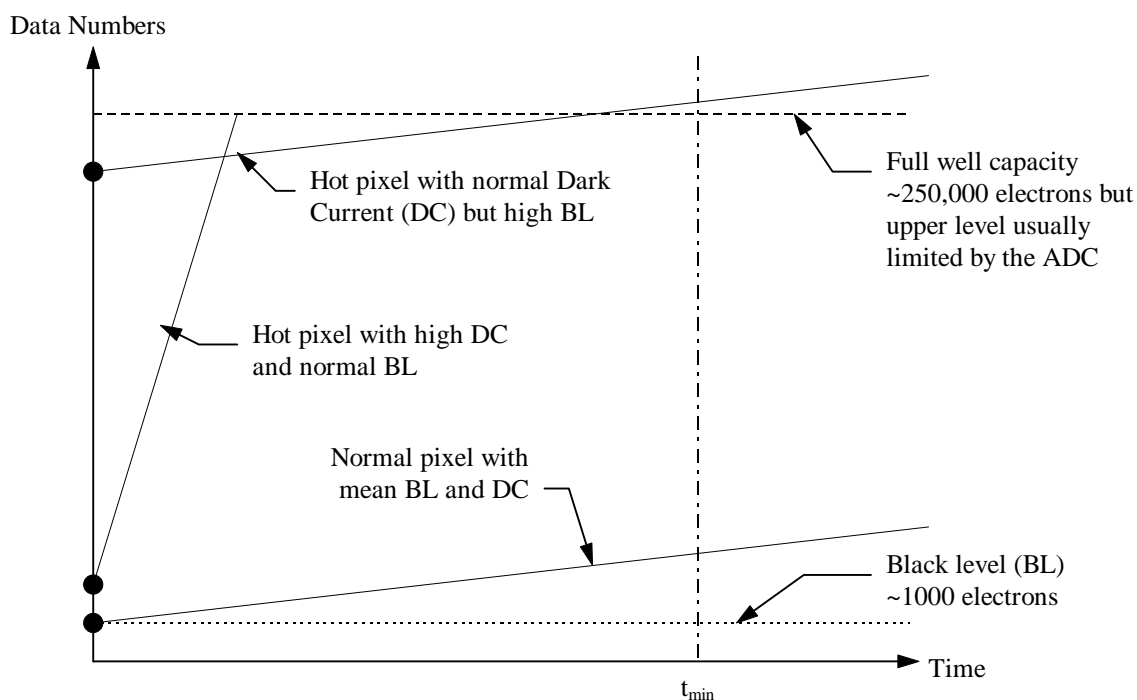


**Figure 6-6** What defines a hot pixel in a PICNIC array. The three pixels illustrated in the picture above show different combinations of black levels and dark currents.  $T_{\min}$  is defined to be the minimum time that should be allowed between useful exposures.

### 6.3.5 Hot pixels in IR arrays

Due to cosmetic defects and imperfections in the manufacture of the array, some pixels have an intrinsically high black level or have an excessively high dark current. These pixels tend to saturate and reach ‘full well’ capacity within a short period of time (see Figure 6-6). Because of this, they enter the regime where the pixels are non-linear in response (particularly within 80% of well capacity) and have to be discarded from further data reduction. These pixels are referred to as ‘hot pixels’ and an image file that contains the positions of such pixels is sometimes referred to as a ‘hot pixel mask’ or ‘bad pixel mask’.

Other pixel defects include dead pixels, which are pixels that have no response to light whatsoever and these can be catered for with dead pixel maps showing their location, and by using software to interpolate over these regions later on. The most difficult cosmetics to remove are those caused by ‘warm’ pixels and cosmic ray events (CRE).

Cosmic ray events are groups of very hot pixels that appear randomly across a frame from exposure to exposure. They are caused by energetic photons from various sources (mostly space) that are continually passing through the atmosphere. Occasionally one will interact with a pixel in the array and deposit a large amount of charge into the array. There are various techniques used by CCDs which can identify them, but the technique of performing many non-destructive reads (NDRs) during a long exposure provides a method of removing them.

### 6.3.6 Non-destructive reads and CRE removal

All reads of the array are non-destructive - this means that reads during an exposure can be taken and stored as frames showing the cumulative charge on the pixels. Three different readout methods are shown in Figure 6-7.

The first method is the RESET-READ-exposure-READ method, where NDRs are performed at the start and end of the exposure on an object. The difference of the two reads then gives the total number of electrons accumulated during the exposure. Electrons are collected from incoming photons, dark current from the detector itself, and cosmic ray events (CRE). An equal exposure taken with the detector covered (a dark frame) allows the contribution from dark current to be subtracted.

Every read of the array has an associated noise added by the on-chip amplifier, and so the resultant simple exposure is limited by the shot noise of the signals (photons, dark current, etc.), and read noise of each read.

The charge on a pixel can be represented as a line on a graph of DN versus time (Figure 6-7) and NDRs represented as measured points on this line. The read noise causes the points on the graph to have a given error bar associated with it. Ideally the error bar would be limited by photon statistics, so one solution is to have many NDRs taken in quick succession at the beginning of an exposure and a similar number at the end of an exposure. By averaging the DN for these reads a better estimate of the actual DN is provided, and this technique is known as Fowler sampling. However, CRE are not accounted for and can not easily be differentiated from hot pixels and high photon rates.

The third method combines the advantage of Fowler sampling and allows detection and removal of CRE. By taking reads at regular intervals during the exposure the accumulation of charge on the pixel can be seen. The effect of a CRE is to virtually instantaneously add a large charge to a given pixel (see Figure 6-8). However the charge added rarely takes the pixel to its full well limit, and the pixel continues to accumulate charge at the same rate after the CRE.

By looking at differences of sequential frames, the rate of charge accumulation can be plotted

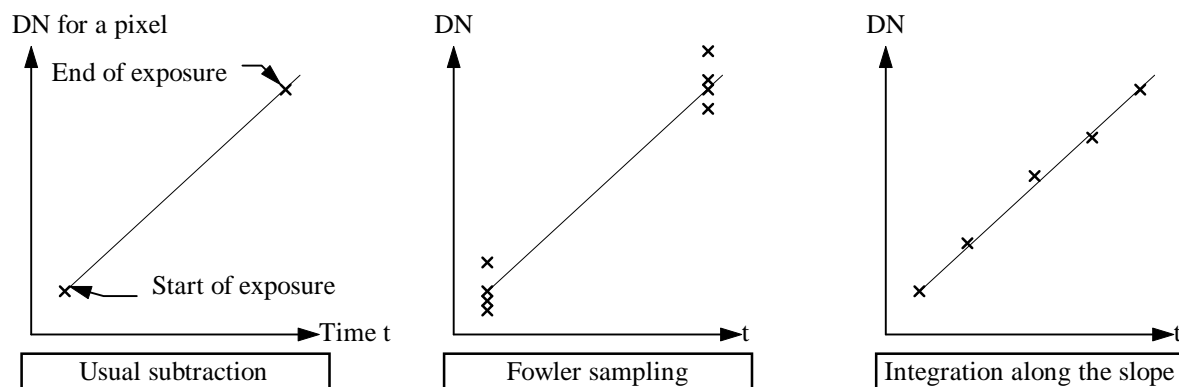


**Figure 6-7** The different NDR methods for an exposure. Three different modes for reading an astronomical exposure are shown, with the advantages and disadvantages discussed in the text.

as a function of time (Figure 6-8). The result is a horizontal line fit with an anomalously high value from the pair of frames surrounding the CRE. This method allows a ‘confidence of fit’ image to be generated for a given exposure, giving the least squares fit error for each pixel and aiding error estimation later on with data analysis.

The number of reads per exposure is limited by two processes. Firstly, for objects with low photon rates the readings will have Poisson statistics associated with them, and if the read noise of the array becomes comparable with the Poisson noise then there is no advantage to performing many reads. Secondly, the NDR requires an on-chip amplifier to be operating whilst the chip is read out, thermal and/or light emission from this causes a distinctive ‘amplifier glow’ to appear on the edges of the frames.

The NDR method can also be used to extract useful data from pixels with high black levels - if the first few reads are below the full well capacity then a value for the total exposure can be extrapolated from the exposures before the pixel reached full well capacity.

With the combined advantages of CRE removal, the production of an error map for individual pixels and better estimates of the errors on each pixel, the integration along a slope method provides a very useful method for producing cleaner science images. The only drawback is the addition of amplifier luminescence which can be minimised by using as few reads as possible.

### 6.3.7 Summary of data reduction for IR array

- Every data frame produced will always have at least two READS after the RESET and be created by a subtraction of these non destructive reads.

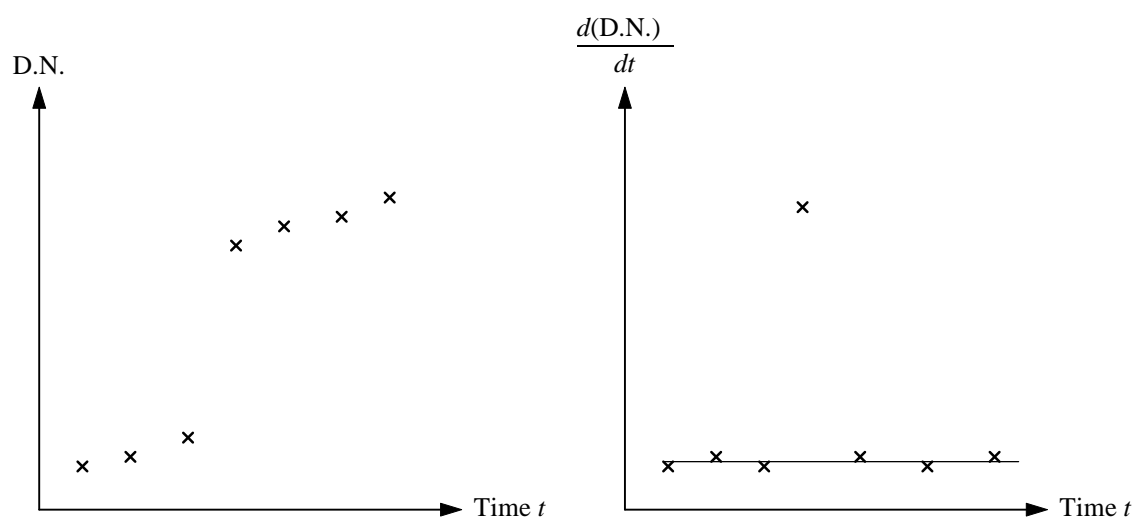


**Figure 6-8** *Detection of CRE in pixels using NDRs.* Here is a plot of data number (DN) of a single pixel versus time. An NDR is taken at evenly timed intervals during the exposure, and a CRE occurs between the third and fourth read but does not saturate the pixel. Subtracting two sequential frames from each other gives a horizontal line fit with the CRE as an anomalous point which can be identified and rejected.

- All data from the IR array is taken in NDR multiple reads per exposure format, and corrections for CRE and hot pixels are performed via a data processing program to produce a CRE cleaned science image with an associated ‘confidence of fit’ image.
- A dark current image of equal duration to the science exposure is taken and subtracted from the science image to produce a corrected scientific image.

## 6.4 Beam switching and other techniques

In beam switching the telescope is ‘nodded’ regularly so that two lenslets in the array alternately measure the object and an adjacent region of sky, so that the object spends exactly half the total exposure time in each lenslet aperture.

The advantage of the beam switching scheme is that an identical instrumental set up is used in both the object and the sky measurement, and many of the systematic errors due to the detector (such as relative pixel QE and dark current) cancel out in subtraction of the two signals.

For one half of an exposure the total signal in one fibre is:

$$F_{1A} = Q_1 + S_1 \quad (6-1)$$

in Fibre A and

$$F_{1B} = fS_1 \quad (6-2)$$

in fibre B. The factor  $f$  represents the difference in efficiency between the two apertures, combining detector response, fibre throughput, etc.  $Q$  represents the signal from the object and  $S$  the signal from the sky, where the sky is assumed to be the same in both apertures. This is a valid assumption for COHSI provided that the OH suppression unit is optimally suppressing during both exposures.

There are similar expressions for the other half of the exposure:

$$F_{2A} = S_2 \quad (6-3)$$

and

$$F_{2B} = f(Q_2 + S_2) \quad (6-4)$$

Now the result from beam switch ( $R_{BS}$ ) is calculated:

$R_{BS} = F_{1A} + F_{2B} - F_{1B} - F_{2A}$ , hence:

$$R_{BS} = Q_1 + fQ_2 + (1-f).(S_1 - S_2) \quad (6-5)$$

A non-beam switched exposure is one where the object remains in aperture A for both exposures.

The result for the non beam switch exposures is:

$R_{NOBS} = F_{1A} + F_{2A} - F_{1B} - F_{2B}$  so giving:

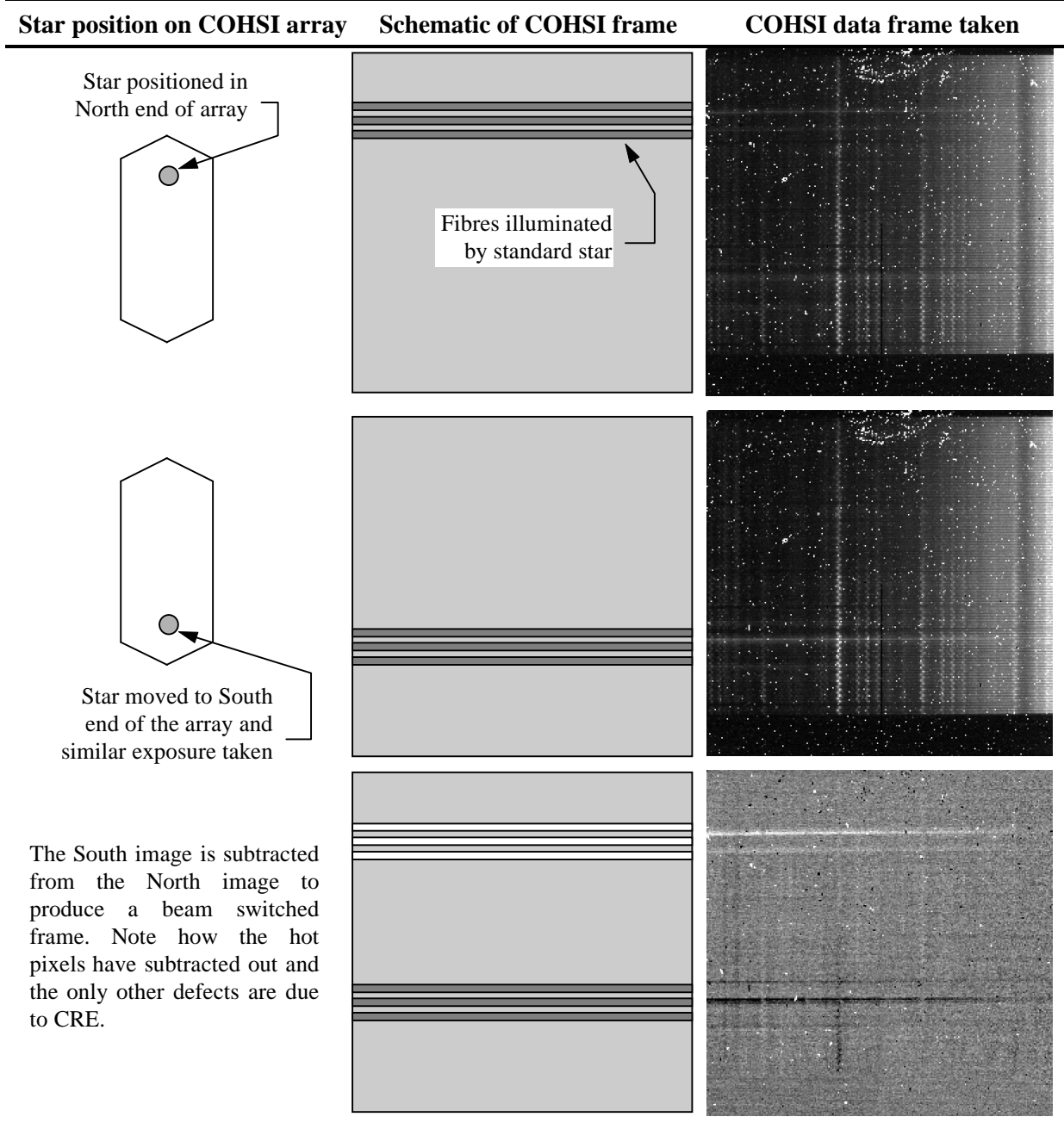
$$R_{NOBS} = Q_1 + Q_2 + (1-f).(S_1 + S_2) \quad (6-6)$$

For a perfect instrument (where  $f=1$ ) both expressions give the desired result of  $Q_1 + Q_2$ . However, it is rare that the apertures have identical responses, so  $f \neq 1$  - and this is when beam

switching wins out. It can be seen that if  $S_1=S_2$ , beam switching still returns a nearly ideal signal of  $Q_1+fQ_2$ , as the sky signal is cancelled out, but not for the normal case. For sky limiting cases where  $S>Q$ , the residual sky signal  $S_1+S_2$  dominates, and the signal is not recovered.

The principle is shown in Figure 6-9. Here two exposures of the same duration are performed on the same object, with the object in different regions of the lens array. Subtracting the two images then gives two sets of spectra, one with positive values and the other with the same magnitude but with negative values, in frame with a mean value of zero. To complete the beam switch, the negative spectra are combined with the positive spectra to complete the beam switch as written on Equation 6-5. The subtraction of one frame from another cancels out all the consistent time-independent systematic contributions, such as warm and hot pixels, the throughputs of the different fibres, the

**Figure 6-9** Beam-switching with COHSI.



detector dark current and sky background.

To show the sensitivity of this technique, the flux from one fibre in the North image is compared in the plot below to the same fibre spectra extracted from the beam switched image (see Figure 6-10). The fibre in both frames was looking at a region of blank sky. As can be seen from Figure 6-9, the single frame has hot pixels, and the thermal contribution appearing towards  $1.8\mu\text{m}$ . With the beam switched images, the fibre spectra has a mean value of zero with a deviation consistent with the combined read noise and photon noise - this represents accurate sky fibre subtraction, a goal crucial for faint object spectroscopy.

Subtracting the flux from different fibres in the same image can be seen in Figure 6-11. With the different throughput of the fibres and the different regions of the array used the systematic effects dominate the spectrum - hot pixels dominate as large spikes and the thermal background is not perfectly subtracted, resulting in a colour variation across the spectrum. With beam switching a simple technique can cancel out many of the systematic errors found with IR arrays and lead to effective sky subtraction.

The only other effects noticed on the difference frame apart from the fibre spectra are the

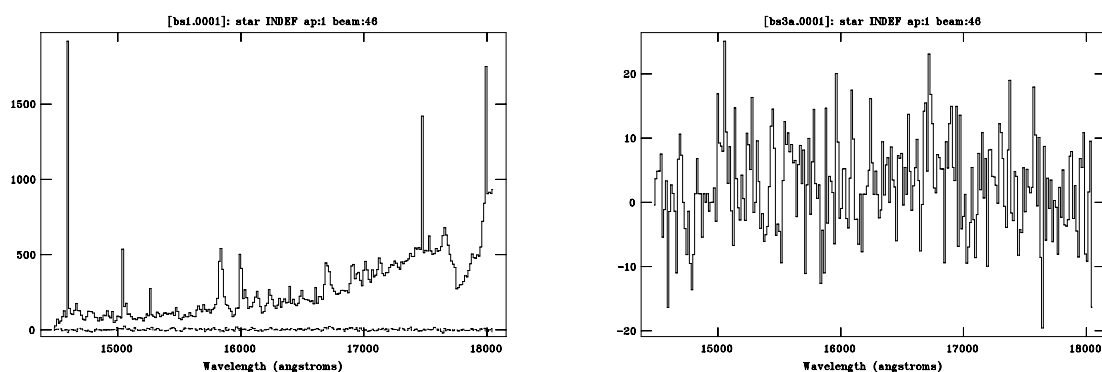


**Figure 6-10** Comparison of beam-switching. On the left is a graph with the spectrum of a single fibre. Notice the thermal background and hot pixels. Underneath it is the same fibre after beam switching. An enlarged version of this spectrum is shown on the right.

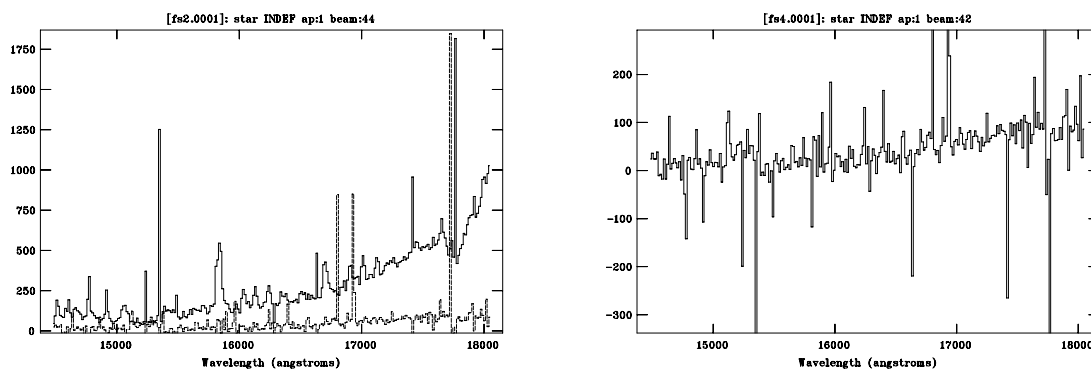


**Figure 6-11** Alternate fibre subtraction. The graph on the left shows one of the fibre spectra plotted with a graph of the subtraction of two separate apertures. The spectra on the right are an enlarged view of the subtracted apertures.

CRE across both frames. Since CREs are random events they are not cancelled out by the beam switching process, however techniques such as NDR slope fitting techniques can reject them efficiently and effectively.

## 6.5 Extraction of fibre spectra for COHSI and SPIRAL

After systematic effects have been corrected for in the data, the 2D image frames are ready to have the fibre spectra extracted from them. The frame is defined by two axes - a spectral (dispersion) axis where pixel number is correlated with wavelength, and a spatial axis along which the fibre spectra are spaced (Figure 6-12). The first stage is to identify the position of the fibre spectra on the image and define extraction apertures for all the fibres. The estimated position of the fibre spectra is represented by a low order polynomial curve fit, sometimes called a ‘tramline’ fit. By using this tramline and a defined aperture a one-dimensional spectra can be extracted.

By using the same tramline to extract an arc-lamp exposure the fibre spectrum can be wavelength calibrated such that each pixel in the spectra has the same wavelength interval. Finally, the spectra can be flux calibrated using a standard star observation if needed.

All of this data reduction is performed with IRAF software provided by the NOAO. The routines used are the APEXTRACT routines found in the `noao.twodspec` module.

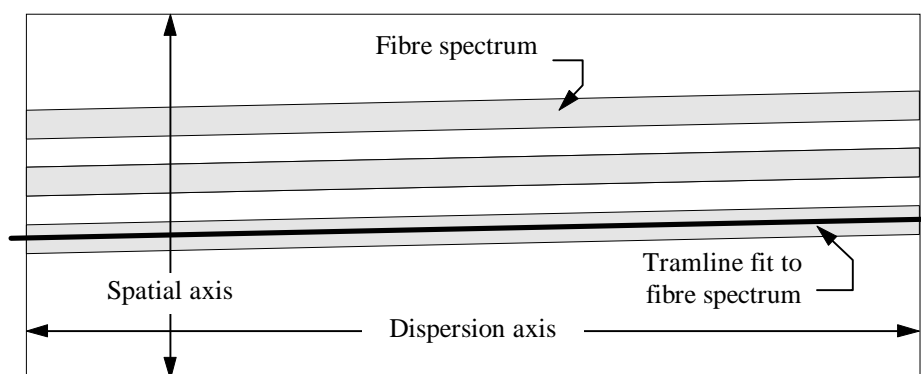


**Figure 6-12** A stylised version of an IFS frame. Three fibre spectra are seen next to each other on the image frame.

### 6.5.1 Scattered light subtraction (SPIRAL)

The presence of dust on the surface of optical components and impurities within various glasses cause light to deviate from its expected path. This light can then land on the detector in a pixel other than the expected one, leading to a diffuse background level of light to appear on the data image. This is scattered light, and needs to be removed from the image before further spectra extraction can be performed. The COHSI cryogenic spectrograph was an on-axis single pass system which helped minimise the scattered light possible within the spectrograph. The fibre slit design of the spectrograph also cut down the amount of scattered light passed to the cryogenic spectrograph from the OH suppressor unit.

By using low order function fits in both the dispersion and spatial directions, and by ignoring the pixels containing light from the fibres a scattered light image can be produced (see Figure 6-13) for a given frame and then subtracted off. The effect of scattered light needs to be considered when designing a spectrograph, and double pass systems are prone to scattered light. For example, the SPIRAL spectrograph has a highly curved field correction lens (L1) near the CCD and fibre slit, and light can be scattered off the inner concave surface of L1 directly into the CCD dewar. The addition of anti-reflective coatings helps reduce the scattered light fraction, but only with broadband anti-reflection coatings can scattered light be reduced to a minimum.



**Figure 6-13** *A scattered light image.* This image is a fit to the scattered light in a twilight sky exposure from the SPIRAL spectrograph. The values range from 246 DN in the middle to 26 DN at the edges. The optical axis of the spectrograph passes through the middle right of the frame.

### 6.5.2 Tracing and extraction

A cut along the spatial axis of a twilight sky image clearly shows the position of all 37 fibres in the SPIRAL lens array (Figure 6-14). This image also gives an indication of the variation in transmission between fibres and the presence of scattered light in the spectrograph. The extraction apertures can be defined in various ways, either by a fixed width for all fibres or by the limits when the counts in the pixels reach a small fraction of the peak value.

The centroids of the fibre images are quickly located in the spatial direction by `APFIND` and the width of the apertures are defined by `APEDIT` (see Figure 6-15). From this single cut in the spatial direction the program then seeks to trace the fibre images in the spectral direction and attempt to fit a polynomial curve for extraction in the next step.

The program `APTRACE` then steps along the dispersion axis and attempts to relocate the centroids of the fibres. By stepping across the whole image the variation of spatial pixel number with dispersion pixel number can be calculated and a low order polynomial fitted to the resultant plot.

NOAO/IRAF V2.11EXPORT mak@cass00 Tue 13:12:21 06-Oct-98  
 Line 975 of twi\_raw  
 Twilight sky

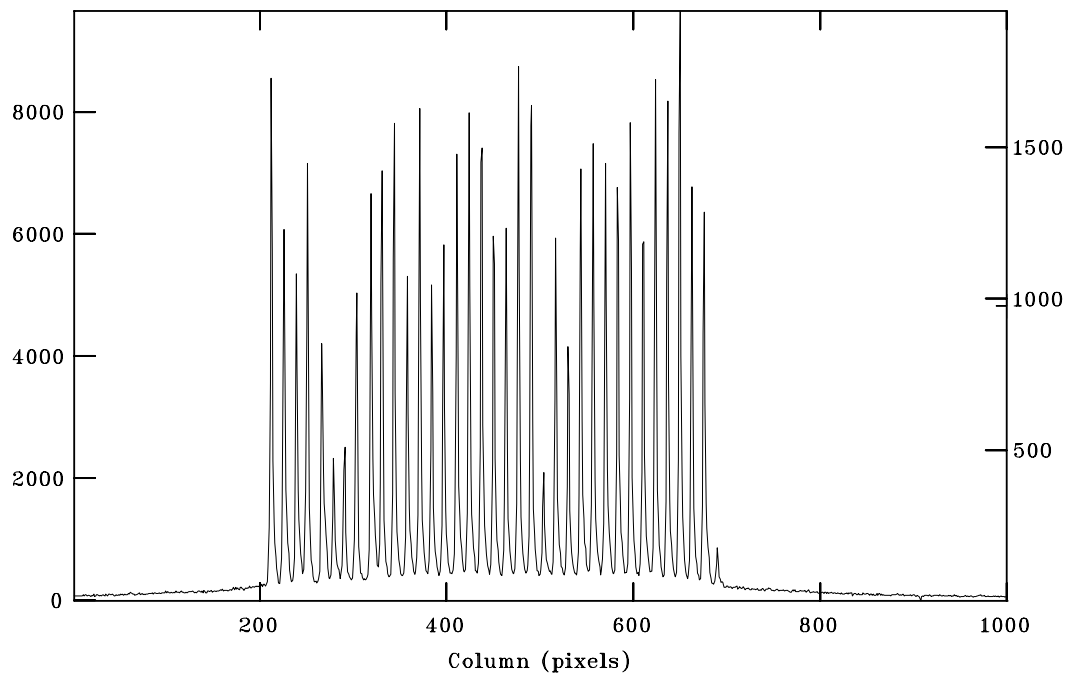


**Figure 6-14** A cut across the spatial axis of a SPIRAL twilight image. This image shows all 37 fibres being illuminated by the twilight sky. Note the scattered light to the left and right of the fibres.

NOAO/IRAF V2.11EXPORT mak@cass00 Tue 13:09:03 06-Oct-98  
 Image=twi\_raw, Sum of lines 969-978  
 Define and Edit Apertures

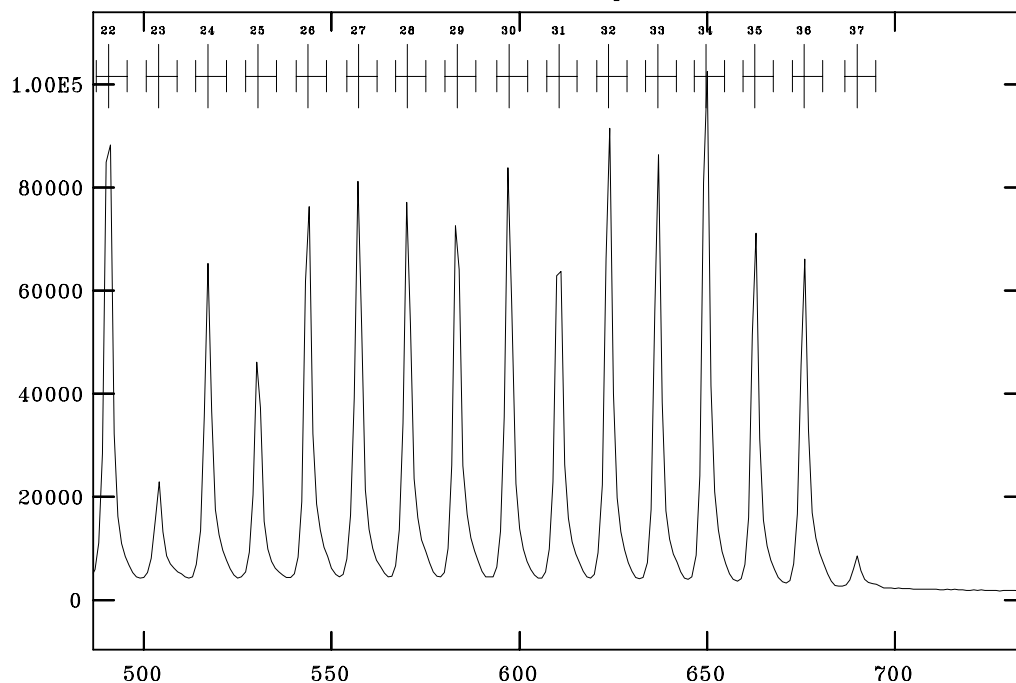


**Figure 6-15** Fitted apertures in APEDIT. The last few apertures have been identified and their widths have been determined as where the spatial flux falls to a fraction of the peak value. As can be seen, the spatial profiles are not symmetric.

Care is needed whilst fitting a curve to this plot - the centroid locating technique introduces a periodic error in the spatial pixel position of the centroid, as seen in Figure 6-16. Note the ordinate scale as being 0.05 pixels and that the RMS fit is less than  $1/30^{\text{th}}$  of a pixel. With all the fibres processed a table of extraction apertures and tramline fits is produced by the software. All subsequent data files, flat fields and throughput images must be extracted using the same tramlines and apertures to avoid the introduction of systematic errors.

The fibre spectra are now extracted from the two dimensional images. Each tramline and aperture is used to produce one spectrum representing the flux from a single fibre. The spectra produced have the intensity measured in counts as the ordinate and dispersion pixel number as the abscissa. The spectra is computed by summing across the aperture at each point along the dispersion subject to the parameters defining the width of the aperture. The default extraction is to simply sum the pixels across the aperture and use partial pixels at the ends of the aperture. If two fibre spectra overlap each other in the spatial direction then light from one fibre can be mistakenly contributed to another fibre spectrum - this 'cross-talk' effect is not present in the well separated spectra of the SPIRAL spectrograph but it becomes an issue for the COHSI cryogenic spectrograph and this is discussed in §6.7.

### 6.5.3 Fibre throughput and flat fielding

Two instrumental effects need to be removed from the data. The first is the pixel-to-pixel

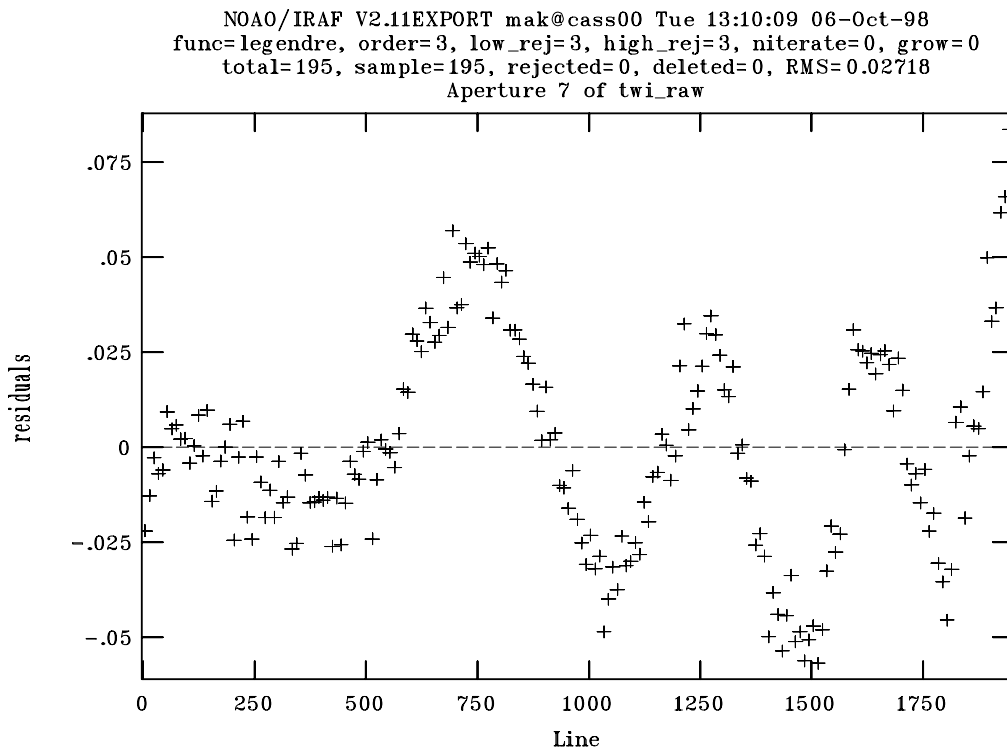


**Figure 6-16** A plot of residuals to a tramline fit on a SPIRAL fibre spectrum. The periodic effect seen in the fit is due to a combination of the centroid fitting routine and the aperture extraction width being narrower than the actual width of the whole fibre image.

variation in QE in the detector itself and the second is the different fibre throughputs. These two effects can be removed by using two different fibre-fed flat field images.

The first flat field is to correct the different fibre-to-fibre variations and other instrument alignments. An exposure of the twilight sky gives the most accurate representation of relative throughput of the fibres, but because the count level in individual pixels is usually very low, another flat field is needed to correct for the pixel-to-pixel variation - this is done using a dome/quartz lamp flat field. This dome flat field ensures that the number of counts per pixel is large enough to give a good signal to noise in the flat fielding process. Flat fields with low levels of flux contribute noise in the final reduced object spectrum.

The dome flat field is extracted to one dimensional spectra and all of the spectra are averaged together. A curve is fitted to this composite flat field spectrum and this is then divided back into the individual flat field spectra. This removes the mean flat field spectrum shape, thus avoiding introducing the inverse of the flat field spectrum into the object spectra and changing the approximate count levels in the object. The function fit should follow the overall shape using a fairly high order.

Now the twilight sky image is extracted - this helps define the relative throughput of the fibres. The extracted sky spectra are then divided by the dome flat field where each fibre spectra has been normalised to unity. The summed flux through each aperture is then found to define the relative throughputs of the fibre apertures themselves. These throughput values are then multiplied into the normalised flat field spectra to produce the final response spectra. This normalised flat field spectra image can then be divided into object spectra to produce spectra corrected for pixel variations and fibre throughput variations.

#### **6.5.4 Wavelength and flux calibration**

The flat-fielded object spectra can now be re-sampled to a linear dispersion by using extracted arc spectra (Figure 6-17). The process is to identify the wavelengths of emission arc lines and then fit a dispersion solution to them using the program `IDENTIFY` - a low order curve and higher order curve are fitted and the residuals to the fit are shown in Figure 6-18. This dispersion solution is a conversion between dispersion pixel number and wavelength, and by knowing the form of the solution the object spectra can be re-binned to a linear dispersion.

For a multi-fibre spectrum the fibre spectrum nearest the middle of the image has its dispersion solution determined and then this solution is automatically refitted to the other fibre arc spectra in the image using the program `REIDENTIFY`. In this way, each fibre has its own wavelength solution determined and by using the `DISPCOR` program the object spectra are wavelength calibrated and resampled with a linear dispersion whilst conserving the flux in the fibres.

With the data now wavelength calibrated the last stage is to flux calibrate the spectra. The preferred method is to take an observation of a standard star and reduce the observation in the same

NOAO/IRAF V2.11EXPORT mak@cass00 Tue 16:47:32 06-Oct-98  
 identify arc.ms - Ap 19  
 ThAr arc

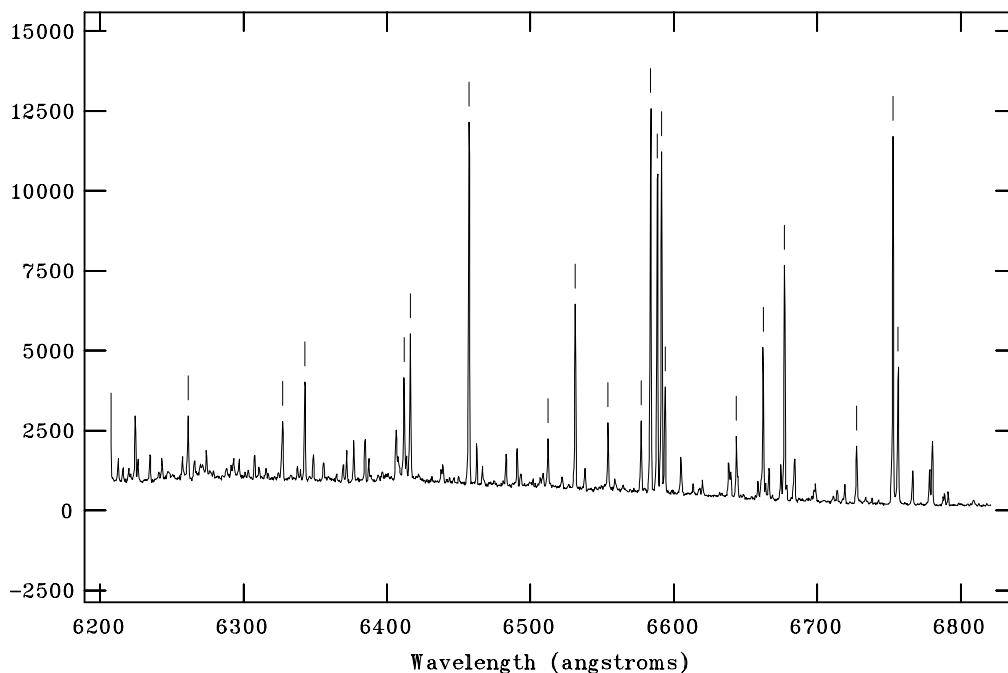


**Figure 6-17** An arc spectrum in the program *IDENTIFY*. The tick marks show lines that have been identified and are used in the dispersion solution.

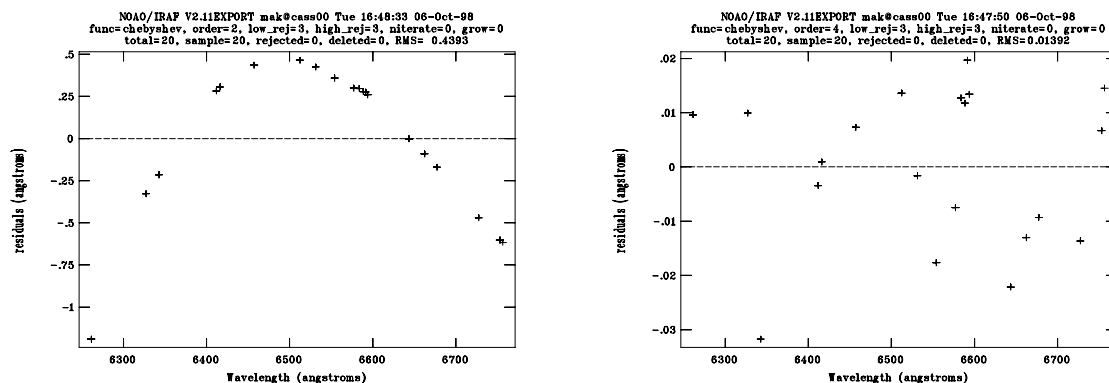


**Figure 6-18** Fitting the dispersion function. These two frames see the plot of residuals from successively higher order fits. In the case of the *SPIRAL* spectrograph a fourth order Chebyshev function produces a good fit.

manner as the object spectra. If the standard star has been centred in the middle of the IFU then all the light from the standard has passed through the instrument, and by adding all the spectra together the total amount of counts can be scaled to the known flux from the standard star for a given wavelength interval. Tables of fluxes for a given bandpass and wavelength have been produced for many standard stars across the whole sky<sup>2</sup>. By selecting a star close to the observed object a reliable flux calibration of the data can be performed.

A summary of the data reduction steps is shown in §6.9.

<sup>2</sup> for example - <http://www.hq.eso.org/observing/standards/spectra/optuvstandards.html>

## 6.6 Tracing the fibre spectra in COHSI data

The format of the data frames from the COHSI spectrograph and the SPIRAL spectrograph is similar, but the number of spatial pixels available compared to the number of fibres is very different. In SPIRAL, 37 object fibres are spaced over 800 pixels whilst with COHSI there are 100 fibres spaced over only 256 pixels. In order to sample the image point spread function (PSF) of the spectrograph the image of the fibre core must be sampled by at least 2 pixels (Nyquist sampling). For COHSI, each spectra occupies  $\sim 2.5$  pixels in the spatial direction, just above the critical sampling limit.

The fibre tracing algorithm encounters problems when trying to identify the centroids of the fibres when they are close-packed as they are in the COHSI spectrograph (see Figure 6-19). The fibre tracing algorithm relies on examining spatial cuts at different points along the dispersion axis and then re-fitting the centroid for the spectra concerned. However, the algorithm has problems keeping track of which peak in the spatial axis belongs to which fibre when the fibres are too closely packed—from the spatial cut in Figure 6-19 the distance between two fibres is only two pixels, leading to alternately high and low pixel values. The algorithm cannot trace the fibres in this case, and two methods are suggested with the aim to identify the tramline fits for all 100 fibres with minimal intervention.

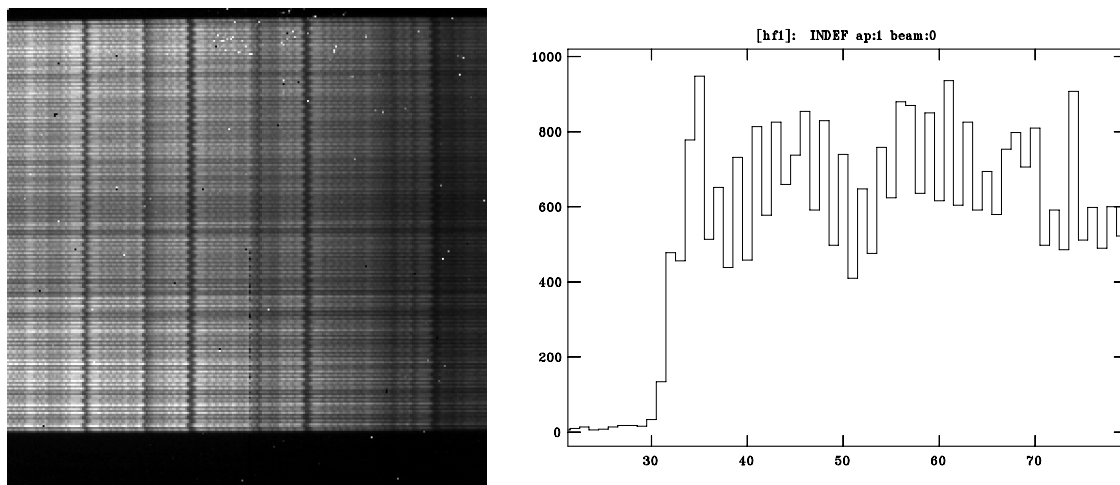


**Figure 6-19** Flat field in H band from COHSI. A cut along the spatial axis is shown on the right, with spatial pixel number along the x-axis and intensity up the y-axis.

### 6.6.1 Tracing using a lens array mask

A solution to this problem was to illuminate alternate fibres with a small mask placed over the lens array (Figure 6-20).

The mask was rotationally anti-symmetric, so by rotating the mask the other half of the fibres could be illuminated and subsequently traced. One of the two data images with the mask in place is shown in Figure 6-21. Now the fibre tracks are clearly defined and a measurement of the FWHM spatial

profile can be taken, which was measured as  $(1.64 \pm 0.18)$  pixels for 97 fibres, and the mean separation of two fibres was measured as  $(2.20 \pm 0.07)$  pixels.

This method proved successful but it took time to set up the mask properly on the lens array which was considered adequate for testing but impractical as part of a fully commissioned instrument.

### 6.6.2 Interpolation of fibre tracks

An alternative method was to take a trace of the fibres at the edge of the fibre field (fibre numbers 1 and 100), which the algorithm was able to perform as it could trace the outermost spatial profile of the edge fibres. With these two traces defined, the intervening 98 fibre tracks could be interpolated by smoothly varying the fitted track from the first fibre through to the last fibre.

This interpolation is a valid approximation only if the fibre spectra are evenly spaced. Figure 6-22 shows how well interpolated fibre track positions compare to the measured positions from a spatial cut across an H band image. As can be seen, there is a detectable third-order variation in the graph, but otherwise the interpolated values agree to typically within 0.1 pixels. The right-hand

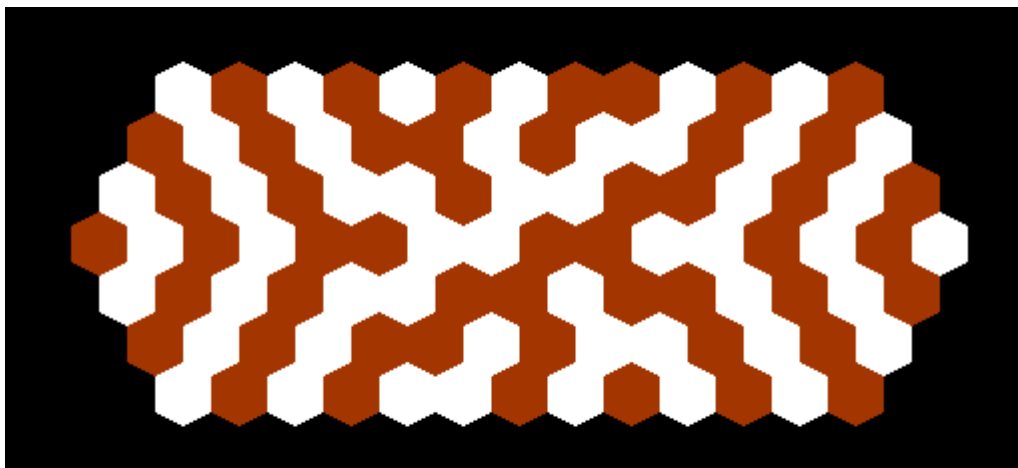


**Figure 6-20** *The mask for the COHSI lens array. This template was used to selectively illuminate alternate fibres in the cryogenic fibre slit.*

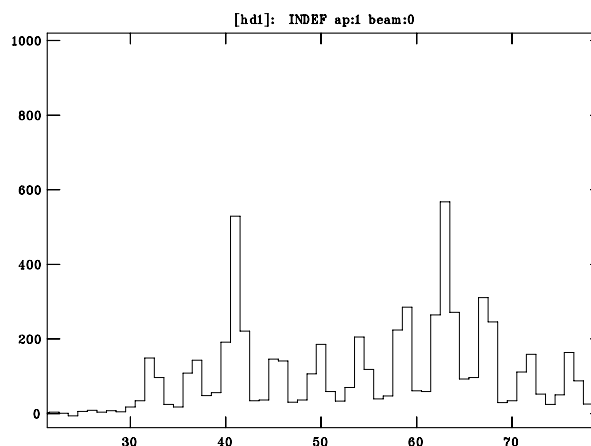
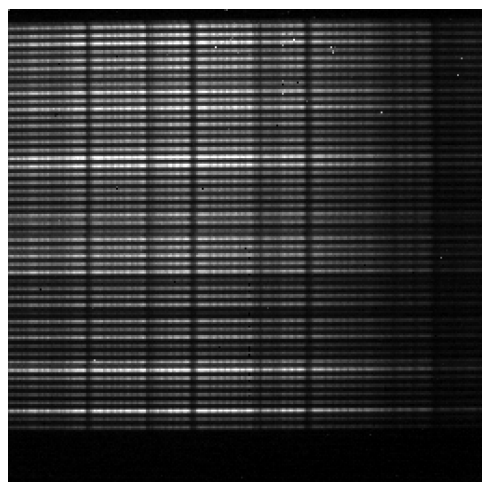


**Figure 6-21** *Illuminating alternate fibres in the H band to help define the tramlines. By using a mask on the front of the lens array every other fibre is illuminated. The tracing algorithm can now trace the fibre spectra successfully.*

chart in Figure 6-22 shows the FWHM of the fibre spectra spatial profile along a spatial cut - this is the other parameter that the interpolation routine must determine for aperture extraction. As can be seen from Figure 6-22 the typical value is 1.64 pixels, leading to extraction widths of typically 3.28 pixels.

The question is then whether the extraction of fibre spectra can withstand such misalignments and how sensitive the extraction process is to different extraction widths for a given fibre. This is discussed fully in §6.7 which deals with the effect of cross-talk in simulations.

## 6.7 Simulations of fibre cross-talk

The data images from COHSI are different from those taken with SPIRAL. Whereas SPIRAL had fibre spectra images that were much smaller than the distance between adjacent fibre spectra, the COHSI cryogenic fibre slit construction has the fibre cores adjacent to each one another in order to fit all one hundred fibres on the 256 pixels available on the PICNIC IR arrays. This results in overlapping fibre spectra images on the detector, and light from one fibre spectra falling into the pixels extracted as for fibre spectra. This is known as cross-talk, and results in a mixing of spectral information along the fibre slit. This then leads to a slight distortion of reconstructed IFS images, as shown in Figure 6-23.

This distortion can lead to incorrect morphological identification and may be important for certain applications, but it does not distort the spectral information in the fibres for fibre slits where all the fibre cores lie along a straight line. However the geometry of the COHSI cryogenic fibre slit is staggered, meaning that fibres do not have the same zero point on the dispersion axis. This means that the cross-talk now introduces a spurious spectral signature - the problem is shown in Figure 6-25.

For fibres in the COHSI fibre slit the question is whether the cross-talk is significant to cause mistaken identification of emission line features, and to what degree the cross-talk is sensitive to varying aperture extraction widths and errors in the determination of the tramline fit to the fibre spectra.

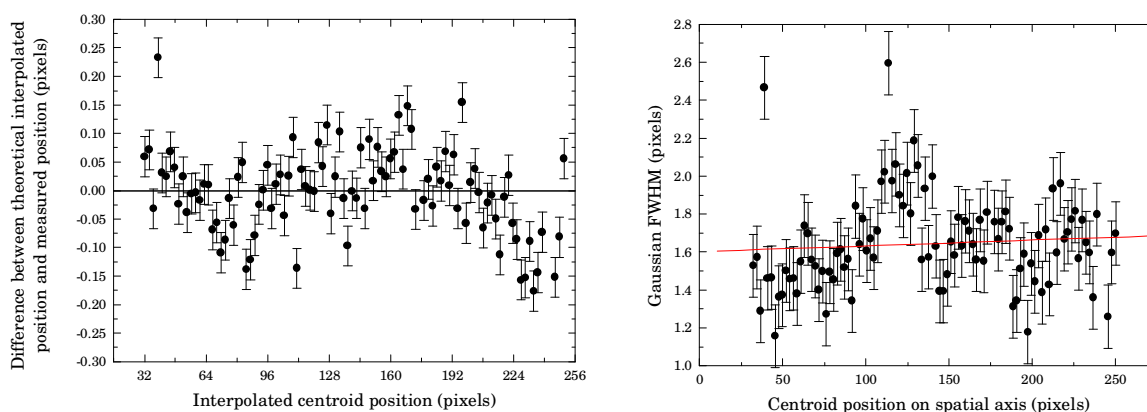


**Figure 6-22** A graph showing the interpolation technique, and a the variation FWHM across an  $H$  band camera image. The error bars on both graphs are due to the profile fitting routine.

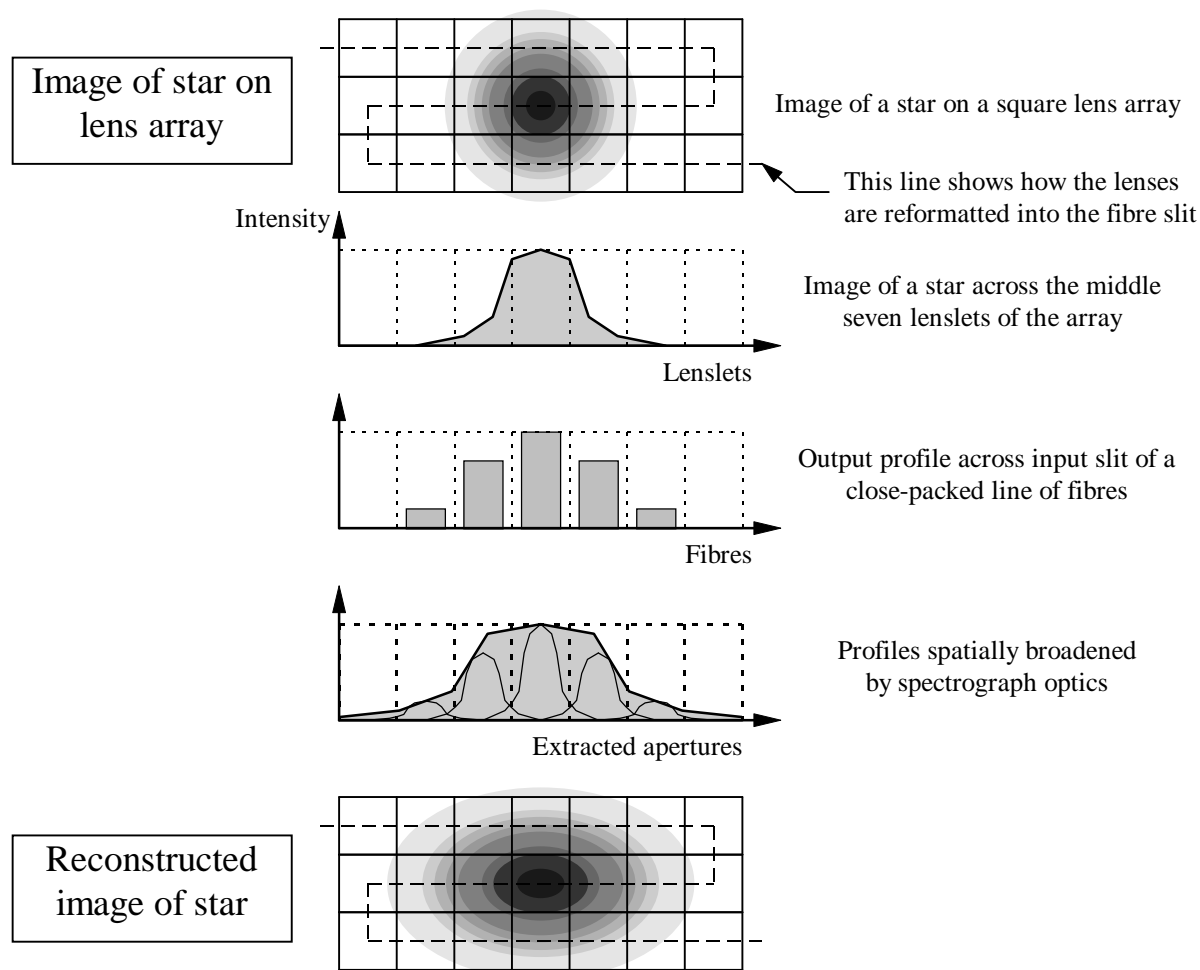


**Figure 6-23** *The effect of fibre cross-talk.* This diagram shows how the cross-talk causes the reconstructed images to be extended in the spatial direction along the fibre path.

### 6.7.1 Simulation of data and measurement of cross-talk

A simple model of a COHSI fibre spectrum was generated using the `noao.artdata` package in IRAF.

First, a reference spectrum was generated which would consist of a flat continuum - that way, any emission features from an overlapping fibre spectrum would become visible in the reference spectrum upon extraction. The 2-D spectral image was generated from a 1-D spectrum (Figure 6-24), consisting of a constant continuum of 100 data numbers (DN). The spectrum was noiseless and consisted of 256 wavelength bins covering the J band (1.00 - 1.35 $\mu\text{m}$ ). This spectrum was then used to create a 2-D fibre spectra on a blank image with a size of 40 pixels on the spatial axis by 256 pixels in the dispersion axis. The spectrum is tilted with respect to the dispersion axis and its centroid shifts by 0.01 spatial pixels per dispersion pixel, with the centre of the fibre spectra passing through the centre of the image.

The IRAF `apextract` routines were then used to trace and define the tramline needed to extract this reference spectrum.

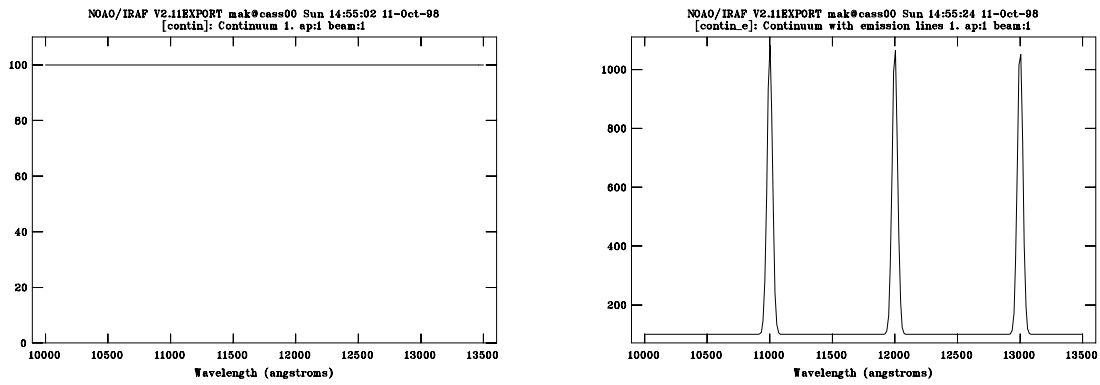


**Figure 6-24** *The reference spectrum and simulated emission line galaxy spectrum.*

The spectral profile of the reference spectrum with no emission line spectra on the frame with different extraction widths was examined. Somewhat surprisingly, a smooth continuum was NOT recovered for typical extraction width apertures. The mean flux for a given extraction width is consistent with the expected FWHM and shape of the Gaussian curve (see Figure 6-27), but the observed rippling effect is dependent on the tilt of the spectrum with respect to the dispersion axis and is an artefact of the software extraction process. This ‘ripple’ is removed when division by a flat field is performed, and is not a significant contribution to spectral errors in the final spectrum -

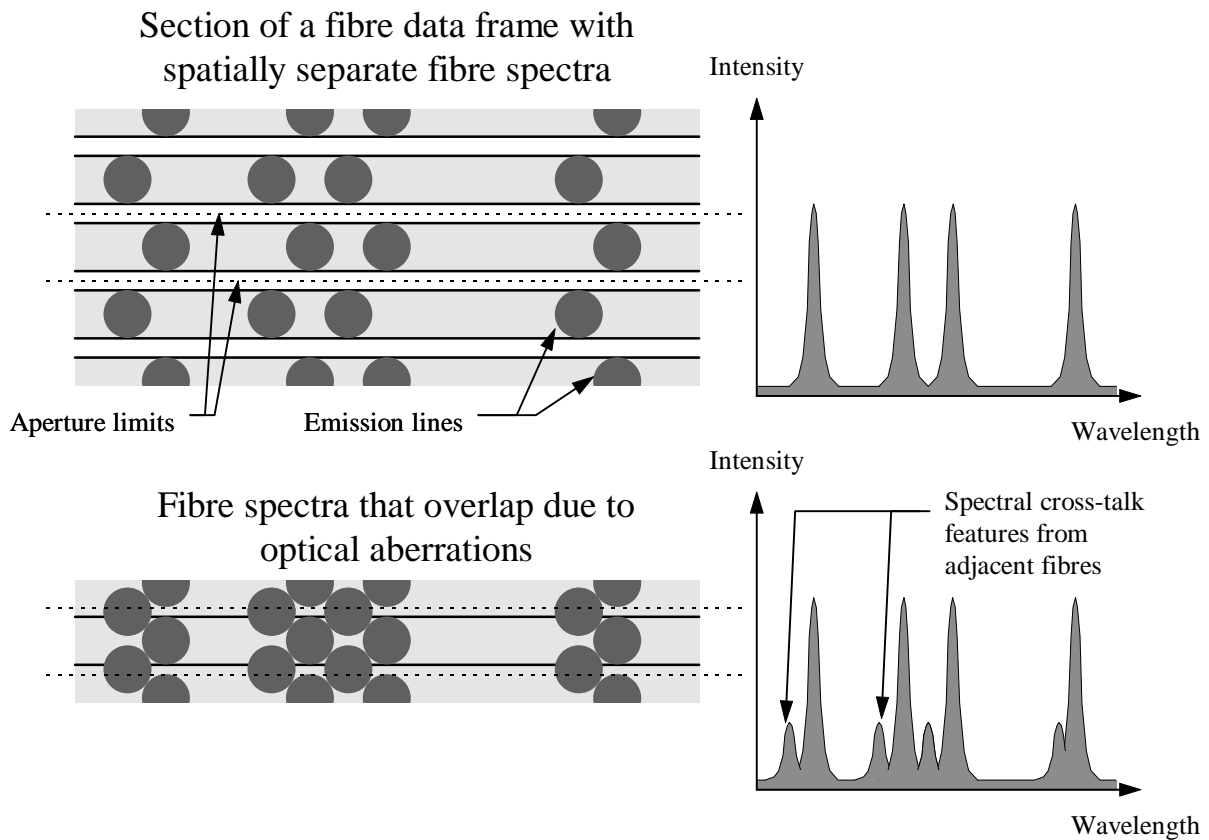


**Figure 6-25** *The cross-talk in COHSI data.* Here are two staggered fibre slits, one with the spectra well separated and the other with overlapping spectra. As can be seen, if the extraction aperture is kept to the same width then spurious spectral features appear near bright emission lines.

however it does emphasise the importance of using a flat field to divide out systematic errors from the extracted data.

A second 1-D spectrum with emission lines (Figure 6-24) was generated with its position and location exactly the same as the reference spectrum - this represented an emission line galaxy in the neighbouring lenslet. This image was shifted by a number of pixels in the spatial direction and added to the reference spectrum as in Figure 6-26. This new image with both the fibres added together now had the reference spectrum extracted using the earlier defined tramline, echoing the method used in reducing the COHSI data. The resultant 1-D spectrum showed cross-talk from the other spectrum in the form of anomalous emission lines on the smooth continuum.

Since the flux in the emission line is known, the 'cross-talk' for a given separation of fibres and a given extraction width can be calculated and is expressed as a fraction of the total flux in the emission line. The results of the simulations are shown in Figure 6-29.

### 6.7.2 Minimising the cross-talk with a spatial filter

Although the cross-talk can be a significant effect, it can be reduced by means of a spatial filter applied to the data image. This is in the form of an artificial fibre spectra generated with the same FWHM and tramline as the fibre spectra to be extracted (in this case, the reference spectrum). The 1-D spectrum is a constant with value unity. The 2-D image generated is then multiplied with the data image and the fibre is then extracted from this new image (Figure 6-28).

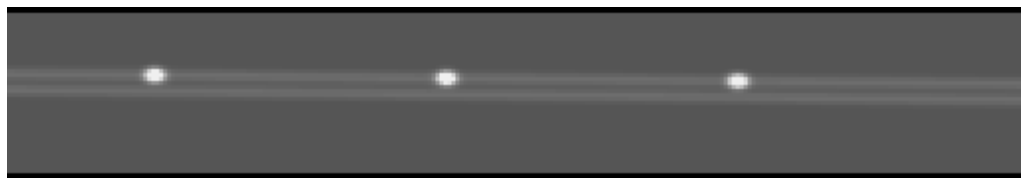


**Figure 6-26** Frame showing reference spectrum and simulated galaxy spectrum. The galaxy spectrum is above the reference spectrum with three emission lines.

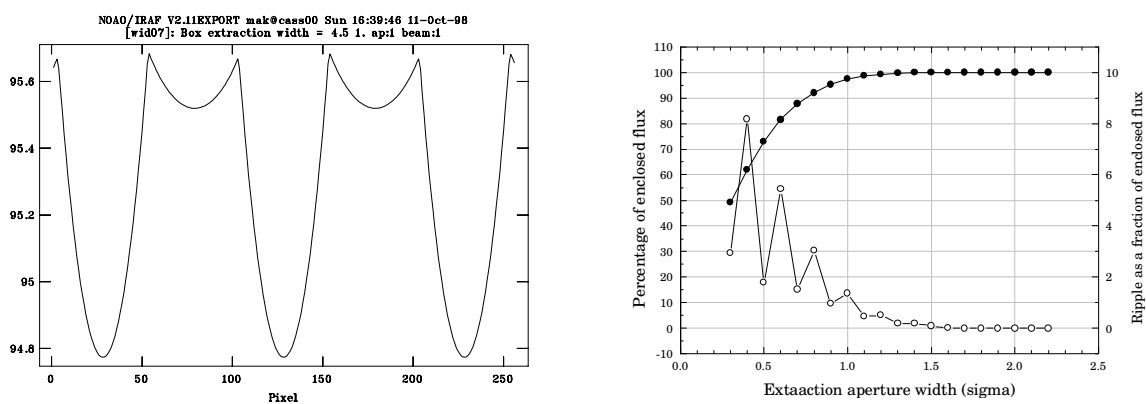


**Figure 6-27** Ripple with variation of extraction aperture width. The plot on the left shows the typical ripple pattern produced for an extraction aperture with a width of 4.5 pixels ( $1.8\sigma$  of the fibre width). The graph on the right shows the enclosed flux and measured systematic for various extraction widths, expressed as fractions of FWHM of the reference fibre spectra.

The effect can be seen in Figure 6-28 - and although the cross-talk is not removed, it is minimised considerably. The results of the two methods are summarised in Figure 6-29.

### 6.7.3 Tolerance of extraction to errors in tramline determination

The tramline fits to the actual spectra positions have an error associated with them, typically 0.10 pixels or less. The next simulation was to move the extraction window and spatial filter with respect to the data image (see Figure 6-30). The spatial filter was set to the same FWHM as the simulated fibre. The horizontal line represents the fibre separation as measured for COHSI, and the

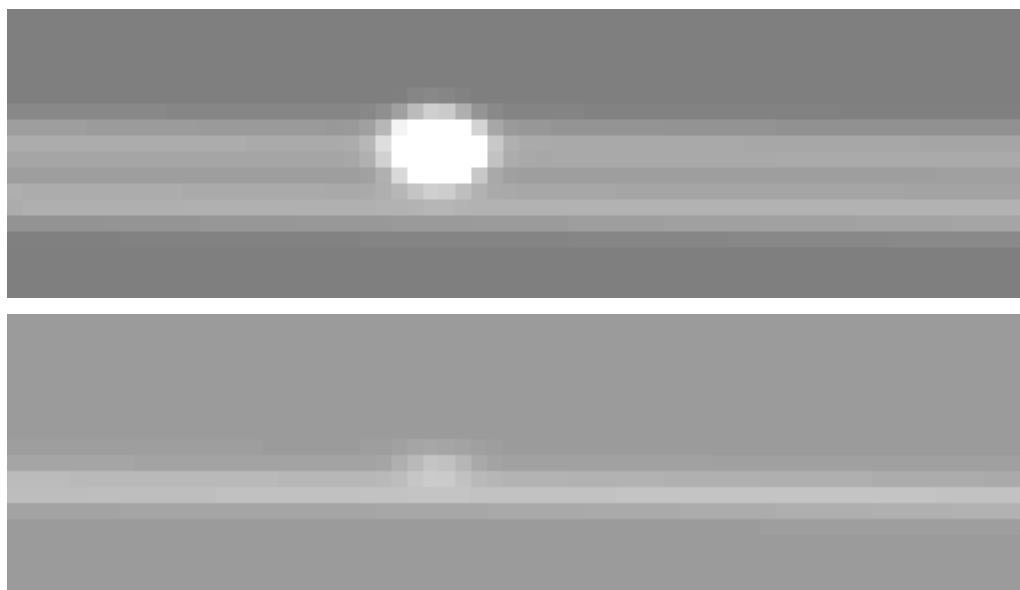


**Figure 6-28** Using a spatial filter to minimise the cross-talk. The emission line spectrum in the upper frame overlaps with the reference fibre. By multiplying the image with a spatial Gaussian filter the cross-talk is minimised as in the lower frame.

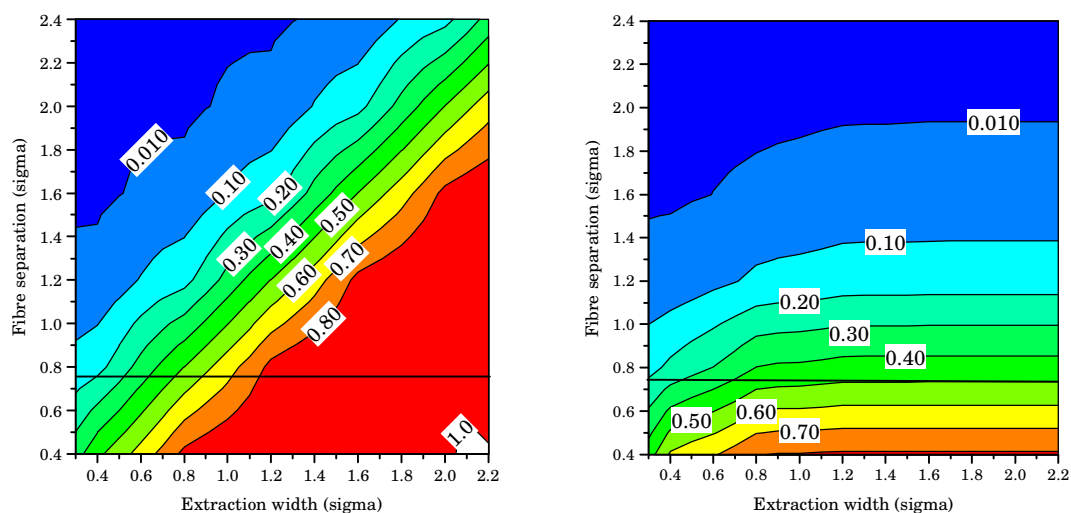


**Figure 6-29** The results of the cross-talk simulations. The lower left-hand contour graph is for the simple extraction technique, whilst the lower right-hand graph shows the reduction in cross-talk when the spatial filter is used. The numbers on the contour plots show the fraction of cross talk detected.

two vertical lines represent the extreme difference in tramline fit from actual fibre position (see Figure 6-22). In Figure 6-30 for an exact tramline fit the amount of cross-talk is 50%, and for 0.1 pixels error either side the change in cross talk is only 5% - a very small change.

The conclusion for interpolated tramline extraction is covered in the next section.

#### 6.7.4 Conclusions of the simulations

As can be seen in Figure 6-29, the COHSI fibre separations ( $0.75 \sigma$ ) leads to over 50% cross talk for an extraction width for  $0.75 \sigma$  extraction widths. Reducing the extraction width reduces the cross talk, but then the total flux from the fibre is 80% of the total flux (see Figure 6-27) so reducing the extraction width is a trade-off between minimising cross-talk and obtaining the maximum possible signal from the fibre. For 50% loss in signal the cross-talk is reduced to 17%.

Using the spatial filter considerably reduces the cross-talk, as seen by the right-hand graph in Figure 6-29. For a  $0.75 \sigma$  extraction width the cross-talk is only 40%.

In conclusion, the spatial filter technique leads to reduction in cross talk and is essential for minimising the possibility of mistaken identity of spectral lines. In many cases a simple examination of the raw data image can tell the astronomer whether an observed emission line is due to cross-talk.

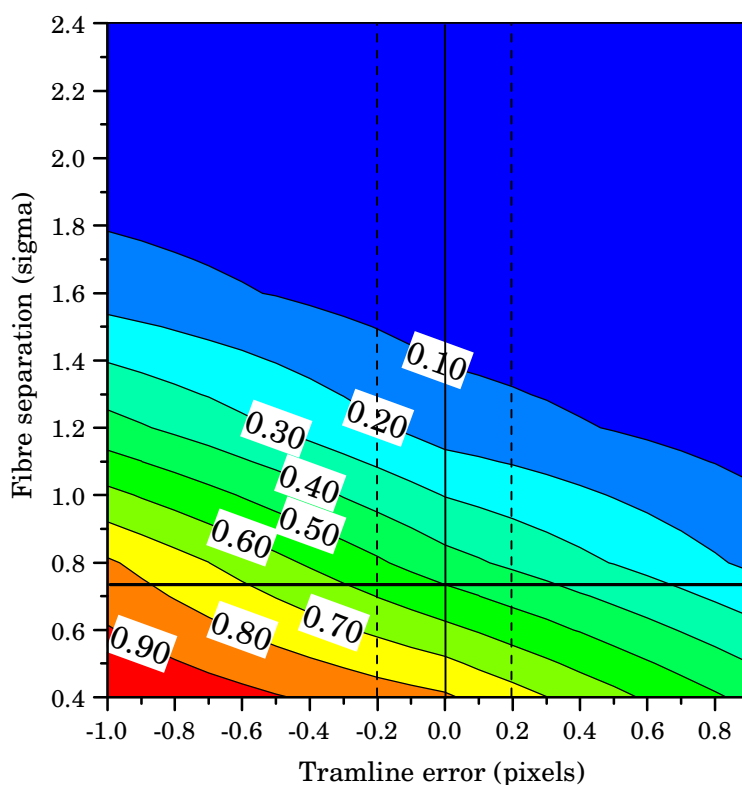


**Figure 6-30** The variation in cross-talk for fibre separation and error in tramline determination.

## 6.8 Displaying IFS data with LDISPLAY

New software is needed to display the hexagonal geometry of the lens array data and be able to manipulate it interactively and it is crucial to be able to look at a raw data frame at the telescope and immediately produce an image that helps orientation and alignment of the lens array. This means that two different modes are needed for the display software: a ‘quicklook’ mode that can reduce a raw data image and a ‘multispec’ mode that reads spectral data files in some generic format.

The first issue was what language to write the software in. The Image Reduction and Analysis Facility (IRAF) is a modular collection of software packages produced by the National Optical Astronomical Observatories (NOAO) which is used for all types of astronomical data reduction. Its advantages are:

- It is installed on every major telescope site
- There is a large infrastructure of tried and tested computer routines
- A large knowledge base of users who can be contacted via e-mail
- A machine-independent compilation language, simplifying transfer to other systems

Other languages and packages such as Figaro, IDL and Fortran were considered, but IRAF was concluded to be the most suitable environment for developing the display software.

The program needs these functions:

- A ‘quicklook’ mode
- Be able to read in either an IRAF ‘multispec’ file or a text list of numbers.
- Be able to flip and rotate the lens array image to give the right sky orientation
- Measure the distance between two lenslets on the lens array
- Measure the FWHM of a stellar profile to determine the best focus of the telescope.
- Be adaptable so that any lens array with hexagonal geometry can be drawn.

An additional capability needed is to examine the spectra of a selected lenslet from the displayed lens array. Once a lenslet has been selected, a new lens array image can be generated from different measured parameters common to all spectra. These include:

- Integrating over a selected wavelength region to form a continuum map
- Selecting an emission line and performing a simple background subtraction to produce a line intensity map
- Selecting two emission lines and producing a line ratio map.
- Selecting a single emission line, performing a Gaussian fit and producing a velocity map (from the measured Doppler shift), a velocity dispersion map (from the FWHM of the fitted curve) or an intensity map.

With these parameters defined, the program was then produced.

### 6.8.1 Introduction and use

The program is called 'LDISPLAY', named after the DISPLAY routine used in IRAF for putting images onto the screen. The parameter file for LDISPLAY is shown in Table 6-3.

When properly installed and running, the program is called with `LDISPLAY file.img`, where `file.img` is either a raw data frame to be looked at in 'quicklook' mode, a 'multispec' file or a text file containing a single column list of numbers. The typical output is shown in Figure 6-31. There are three windows used. The command line window from which LDISPLAY is launched, the output plotting device which displays the spectra of a lenslet when relevant, and the output graphics device which displays the lens array image. The parameters for the package are now explained.

`input` the name of the data file to be displayed. Either a raw data frame, a multispec file or a text list of numbers.

`band` specifies the band of the multispec image that contains spectral data. By default it is set to '1'.

`ldispdir` specifies the directory into which LDISPLAY puts all its temporary files and configure options. This directory is usually specified as `home$ldisplay/`.

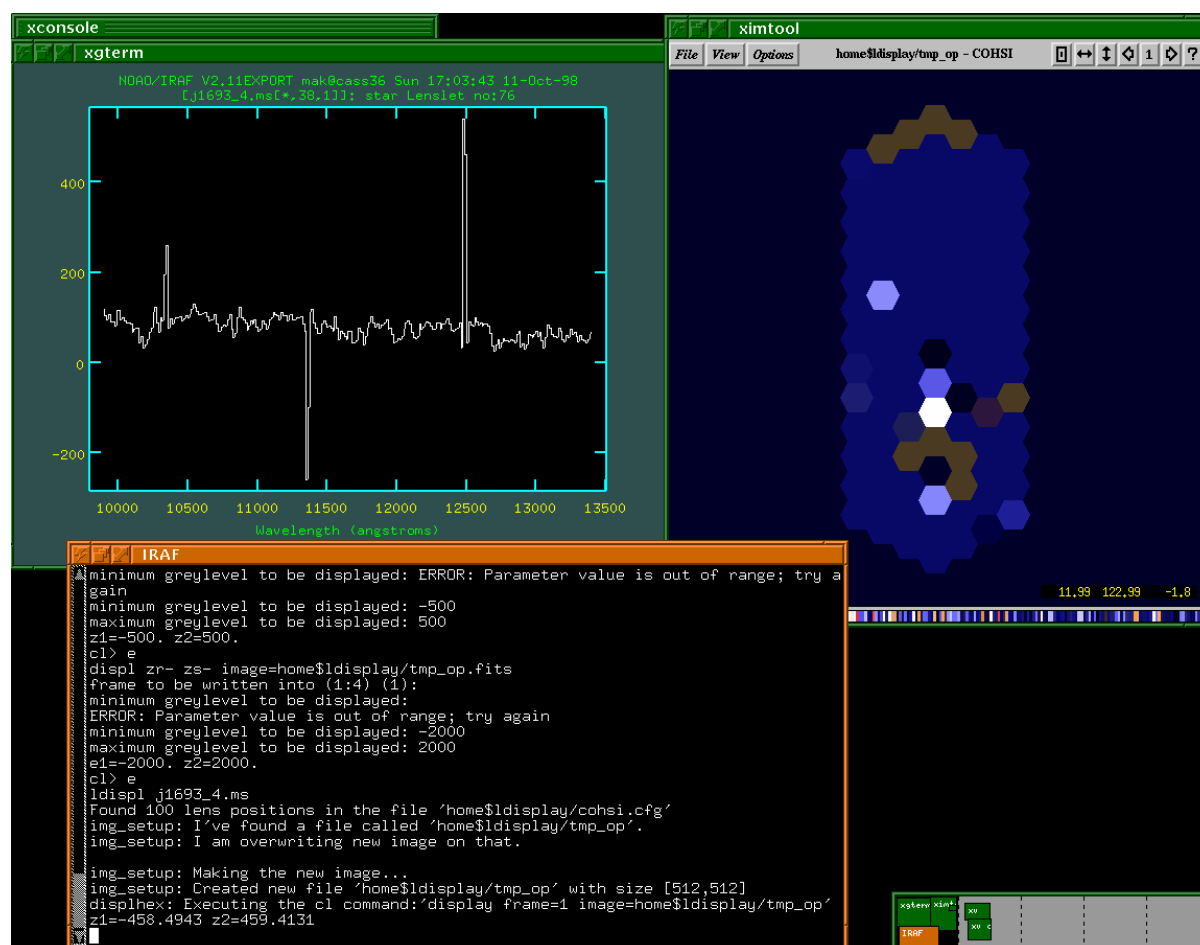


**Figure 6-31** LDISPLAY running in an X server. The two main windows of LDISPLAY are shown - the PLOT window displaying the spectrum of a selected lenslet and the GRAPH window showing the interactive lens array.

`output` is the name of the generated lens display image. By default it is placed in the `ldispdir` directory, but if a permanent output image is needed then this name is changed.

`title` specifies the title to be given to the output image

The `ARRAY GEOMETRY` parameters alter the display of the lens array on the graphical output (usually via `SAOIMAGE` or `XIMTOOL`). `xflip`, `yflip` and `axisflip` are used in combination to reflect and flip the lens array so that East is to the left and North is to the top of the display. As yet, there is no capability for displaying the lens array rotated at an arbitrary angle. `disqu` is for whether the image should be regenerated when the program is run - this is usually set to 'yes'.

The `DISPLAY SETTINGS` are the configuration options for a given lens array.

`lconf` The lens configuration file. This is a text list of pairs of space separated numbers that define the relation between the spectra and the lenslet on the lens array. The details of

```
PACKAGE = clpackage
TASK = ldisplay

input = Input fibre file
(band = 1) Band number
(ldispdi= home$ldisplay/) Directory for config files
(output = tmp_op) Lens array image
(title = Lens array output) Title of the lens array image

QUICK LOOK OPTIONS
(quick = no) Quick reduction of input fibre file?
(flatfie= ) Raw flat-field fibre file (not necessary)
(qfibres= 100) Number of fibres in flat field
(wfibres= 3) Width in pixels of single fibre
(firfib = 33) Row number of first fibre image
(lasfib = 251) Row number of last fibre image
(dispaxi= 1) Dispersion axis of image

ARRAY GEOMETRY
(xflip = no) Flip lens array image about the x-axis?
(yflip = no) Flip lens array image about the y-axis?
(axisfli= no) Flip the lens array image about the x=y axis?
(disqu = yes) Automatically display the lens array image?

DISPLAY SETTINGS
(lconf = cohsi.cfg) File containing lens array geometry
(deadfib= dead_cohsi.cfg) File with locations of dead fibres
(lscale = 0.7) Centre to centre (arcsec) lenslet distance
(siz = 512) Size of lens array image
(device = stdgraph) Graphics device (usually STDGRAPH)
(graphcu= gcur) graphics cursor input (usually gcur)
(imagecu= imcur) image cursor input (usually imcur)
(display= display frame=1 image=) command to run 'display'
(mode = ql)
```

**Table 6-3** *Parameter file for LDISPLAY.*

how the numbers are used is discussed in §6.8.4.

<code>deadfib</code>	A text file with a single column of numbers, each number relating to a lenslet in the array. The first number in the file corresponds to lenslet 1, the second to lenslet 2, and so on. The number is 1 for a working lenslet, or 0 for a low throughput/broken lenslet, although in principle the value can be anywhere between 0 and 1. This file is used in the ‘quicklook’ mode only.
<code>lscale</code>	This is the distance in arcseconds between the centres of two adjacent lenses, and represents the lens scale of the array.
<code>siz</code>	The size of the output graphical image as specified in output. The square output image is restricted to side lengths of powers of two, with the minimum value being 256 pixels. If the image is not big enough to display the array, the program stops and requests the user to increase the image size.
<code>device</code>	The output device to which the lens array images go to. This is usually left unchanged.
<code>graphcu</code>	Graphics cursor input. Usually left unchanged.
<code>imagecu</code>	Image cursor input. Usually left unchanged.
<code>display</code>	Parameters to be added to the command that puts the output image on the graphics terminal.

### 6.8.2 The ‘multispec’ mode

For the first lens array image the flux across the whole spectral range of each fibre is summed and an intensity map generated. The user can then choose to display the spectrum of a given lenslet by placing the cursor over the lenslet and pressing the space bar. The spectrum is then displayed on the plot device.

The user can then select a region of the spectrum and a particular operation can be performed on the same region for all the fibres to produce a new lens array image. The options are:

‘c’	Two wavelengths on the spectrum are selected with the cursor and the flux between the two points is summed to produce an intensity map.
‘l’	Two wavelengths either side of an emission line or absorption line are selected and the flux between the two points is integrated. A simple continuum subtraction is then performed with the flux at the endpoints defining the average continuum level.
‘r’	Two spectral lines are measured as in the ‘l’ operation and a ratio of the first line flux to the second line flux is performed.
‘d’	Two lenslets are selected from the lens array and their separation in arcseconds is printed to the screen.
‘q’	Exits the program and returns control to the command mode of IRAF.

### 6.8.3 The 'quicklook' mode

When the program is run with `quicklook=yes`, the parameters in the `QUICK LOOK OPTIONS` are used to determine the approximate positions of the fibre spectra on the data image.

- `flatfield` This is an optional raw image that is used to correct for the variation in throughput of the fibres. It is usually a dome flat field.
- `qfibres` The number of fibres in the input image
- `wfibres` The width (in pixels) of each fibre spectra. Whatever the input number, it is rounded off to the nearest odd integer.
- `firfib` The row number of the first fibre spectrum in the raw frame.
- `lasfib` The row number of the last fibre spectrum in the raw frame.
- `dispaxis` The dispersion axis of the raw data image. 1=Rows, 2=Columns.

A diagram of a raw data frame is shown in Figure 6-32. To generate each fibre spectrum, the centre of the fibre spectrum is calculated by interpolating between the first and last fibre rows. `wfibres` then defines an integer aperture width for the fibre spectrum and the rows of pixels within the aperture are added together to give a single fibre spectrum. This is repeated for all the fibre apertures down the frame.

If a flat field image is specified then all the pixels in a given flat field fibre spectra are added together to produce a single number representing the throughput of that fibre. The extracted fibre spectra are then normalised using the values calculated from the flat field. The raw multispec data can then be manipulated in the same way as normal reduced multispec file.

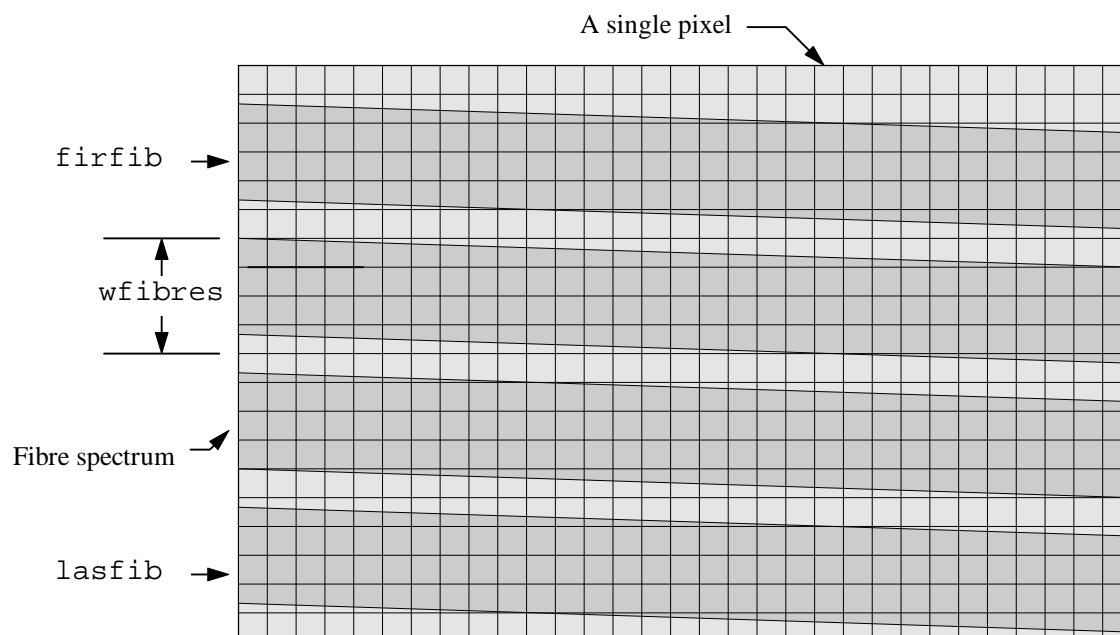


**Figure 6-32** The parameters of 'quicklook' for a raw data frame. The number of fibres in the whole image is `qfibres`.

### 6.8.4 The hexagonal array routine

The data reduction process assigns an aperture number to each extracted fibre spectrum. The fibres are numbered sequentially from the top to the bottom of the data frame, and the aperture number then relates a fibre spectrum to a lenslet position on the array.

Each line of the `lconf` file contains the co-ordinates for a lenslet in the lens array. The first line corresponds to the position of aperture number 1, the second line to aperture number 2, and so on for all the lenslets in the array. The relation of aperture number to fibre spectra position is shown in Figure 6-33. By defining a new configuration file, any hexagonal lens array can be displayed with the program.

### 6.8.5 Current status and conclusions

The code has been successfully compiled at two different telescope sites with no error reports. Not all options have been coded in, but the `quicklook` routine provides very good results - with this mode the COHSI lens array was aligned and orientated in less than ten minutes on UKIRT.

The one option that has not been written is a centroid fitting and profile measuring routine, but an alternative method has been found. By using the `IMPLOT` program to look at the output image, the profile of the image can be measured with the 'p' key. A version of this will be built into future versions of `LDISPLAY`.

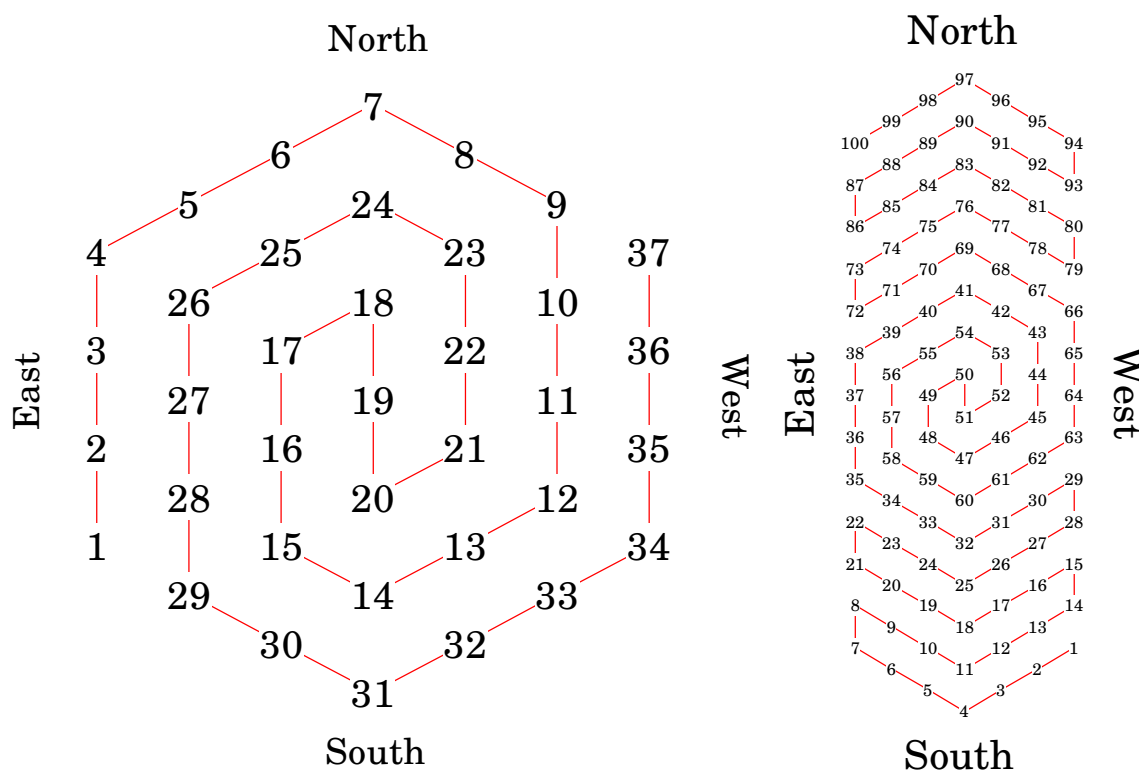


**Figure 6-33** The *SPIRAL* and *COHSI* fibre slit maps used in *LDISPLAY*.

## 6.9 Summary of data reduction

To help keep identification of the data reduction steps, the data frames are referred to with three letter acronyms (TLA):

- **Object frame (OBJ)** - this is the science object frame and is assumed to be clean of all cosmic ray events. These events are removed either by median combining three or more frames, or by using a  $\sigma$  clipping algorithm as supplied in the IRAF CCDRED package.
- **Standard star frame (STD)** - This is a spectrophotometric star located near the objects field in the sky. and is used to remove absorption bands from the atmosphere. Typically it is a white dwarf or star that has a featureless continuum.
- **Twilight flat field (TFF)** - this gives the relative fibre throughput for the instrument. This can also be used as the pixel-to-pixel flat field, but the low number counts per pixel that are usually found in twilight flats mean that these flats introduce extra shot noise into the data. The twilight sky also has a large scale colour variation and absorption features present which make obtaining a pixel-to-pixel flat field difficult.
- **Dome flat field (DFF)** - A tungsten lamp is shone onto the inside of the dome producing a dome flat field. The relative throughputs of the fibres are different than those obtained from the TFF because the optical fibres are illuminated with rays that would otherwise be vignetted for objects located at infinity. The large number count per pixel and the featureless continuum from the tungsten lamp mean that the DFF is suitable for removing the pixel-to-pixel QE variation in the detector and is also used to define the tramlines for the fibre spectra extraction.
- **Arc lamp frame (ALF)** - An arc lamp illuminates the lens array and the resultant data frame has a distribution of emission lines along each fibre track. Ideally an ALF should have known bright emission lines whose wavelengths are evenly distributed across the frame, allowing a well defined dispersion solution to be found.
- **Zero level frame (ZLF)** - A data frame taken after an exposure of 'zero' seconds with no

Frame	Scattered light removal	Fibre (tramline) extraction	Flat fielding	Wavelength calibration	Atmospheric transmission
<b>ALF</b>	not needed	YES ( .ms )	not needed	Note 2: see text	
<b>DFF</b>	NO	YES ( .ms )	Note 1: see text		
<b>TFF</b>	YES ( _s1 )	YES ( _s1.ms )	Note 1: see text		
<b>STD</b>	YES ( _s1 )	YES ( _s1.ms )	YES ( _s1f.ms )	YES ( _s1fc.ms )	Note 3: see text
<b>OBJ</b>	YES ( _s1 )	YES ( _s1.ms )	YES ( _s1f.ms )	YES ( _s1fc.ms )	OBJ_final.ms

**Table 6-4** Table of IFS data reduction steps. The text in brackets shows the filename extension used to keep track of the data files during data reduction. The notes refer to extra data reduction procedures described in the text.

illumination. This frame is used to correct for the DC bias applied to CCDs and arrays to prevent the analogue to digital converter misinterpreting a negative input voltages from the CCD readout amplifier.

- **Dark current frame (DCF)** - A frame that has an integration time equal to that of the science frame, but the camera shutter is closed. This is a correction for pixel to pixel dark current accumulation, but is usually unnecessary for the MIT/Lincoln Laboratory CCD. For COHSI a dark current frame is not necessary if beam switching is being performed.

All data reduction uses the `noao.twodspec.apextract` routines and the `onedspec` routines, and 1-D extracted fibre spectra are stored as multispec files with the extension `.ms` in the IRAF package.

### 6.9.1 SPIRAL integral field spectroscopy mode

The ZLF is subtracted from all data frames and the overscan region used to correct for the pixel-to-pixel DC offset using `CCDPROC`. Table 6-4 shows the sequence of steps needed for IFS data reduction. Starting with the left-hand column (scattered light removal) each column is followed from top to bottom, with the relevant routines being used.

The DFF is used to define the tramlines used in the spectral extraction. These apertures are also used in the `APSCATTER` routine to define regions of the image that contain scattered light. The second stage is to extract all the images with the defined apertures, as shown in Column 2.

**Note 1:** Detector pixel-to-pixel variations are now divided out of the extracted spectra. Ideally the TFF should be used as its optical path is identical to that used by the science observations. However, the large number of absorption features in the twilight spectra and low number counts in an individual spectral channels can introduce extra noise into the object spectra. The routine `MSRESP1D` uses the DFF to generate the pixel-to-pixel flat field. All the fibre spectra in the DFF are added together and a low order function is fit to this spectrum. This fit is then used to normalise each individual spectra in the `DFF.ms` image. Each fibre in the image is then normalised by its relative throughput as determined from the TFF image. In this way a response image is produced that can be divided into the other spectra frames to simultaneously perform flat fielding and fibre throughput corrections.

The response image is used to correct the `STD` frame and the `OBJ` frame.

**Note 2:** Arc lines are identified in one fibre spectrum in `ARC.ms` image using `IDENTIFY` and the remaining fibres have their dispersion solutions found by using `REIDENTIFY`. `ARC.ms` is then used to dispersion correct (with `DISPCOR`) the individual spectra in `STD` and `OBJ` frames.

**Note 3:** With the spectra in `STD` wavelength calibrated all the fibres are added together with `SCOMBINE` to produce a high signal to noise standard star spectra. Normalising the spectrum with a linear fit then produces a spectrum which is then divided into the `OBJ` spectra to produce the final spectra `OBJ_final.ms`.

Sky background subtraction is performed by taking a sky observation before and after the OBJ exposure. This is peculiar to SPIRAL A because the field of view of the IFU is very small. If a star is centred in the lens array then the lenses on the edge of the array will still receive light from the star due to typical seeing conditions at the AAT. Instead an equivalent sky exposure is performed on the sky near the object and is reduced in the same way that the OBJ is reduced. A simple subtraction of the sky then completes the data reduction.

If needed the spectra can then be flux calibrated by using the known flux of a standard star. By summing up all the spectra in the STD image and assuming that all the flux from the standard star falls into the lens array, a conversion factor can be calculated and applied.

### 6.9.2 SPIRAL pupil imaging mode

A data frame for the pupil mode is shown in Figure 6-34, with the CREs removed by median combining consecutive exposures. The sky fibres are close packed together in the slit, and are extracted with a single aperture since they all contain the same signal. The two groups of sky fibres are kept separate because they sample different areas of sky - if a star happens to fall in one set of sky fibres then the others can be used for background estimation. As the apertures for the sky fibres are wide (over 50 pixels wide) it is important to ensure that the dispersion axis is as parallel to the pixel rows as possible. If the fibre slit is strongly tilted with respect to the dispersion axis on the CCD, then the effective spectral resolution decreases as shown in Figure 6-35. By rotating the CCD dewar the fibre tracks are aligned to be as parallel as possible with the dispersion axis.

The ZLF is subtracted from all data frames and the overscan region used to correct for the pixel-to-pixel DC offset.

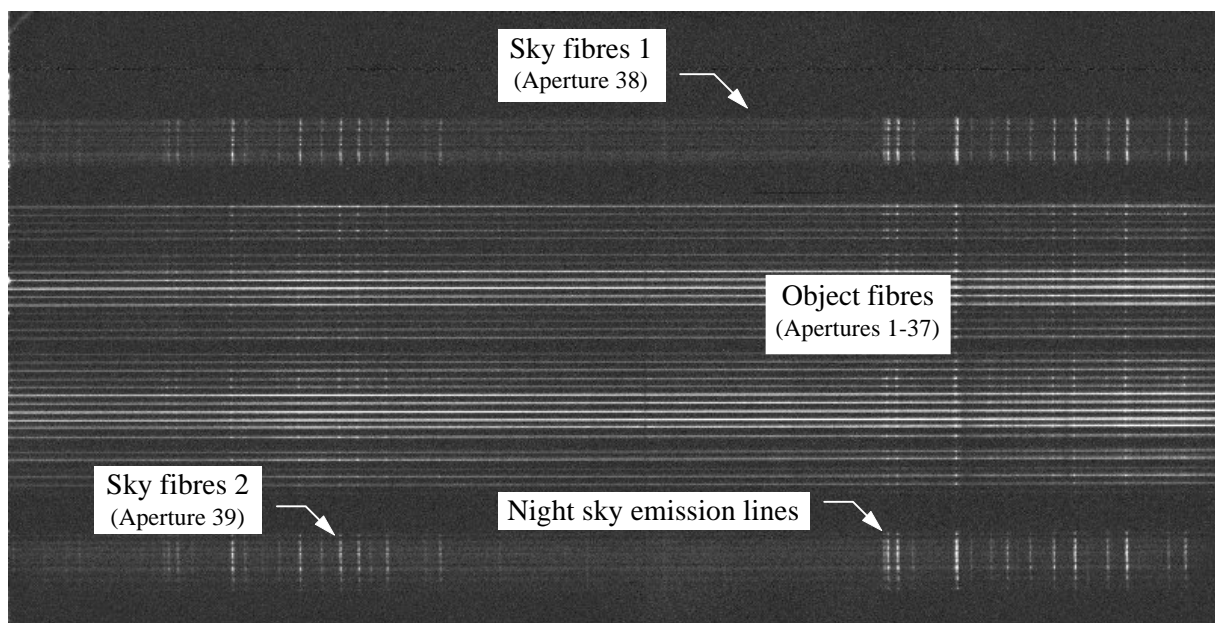


**Figure 6-34** A pupil imaging data frame. This frame is a median of eight half-hour exposures of the brown dwarf BRI 0337-3535. The night sky emission lines can be clearly seen in both the sky fibres and the object fibres.

The pupil data is more complicated in its format due to the separate background fibres, and that the twilight image TFF does not have an even illumination of the fibres - the pupil image of the telescope is on the fibre array and the central fibre of the array does not receive any flux either from the object or the twilight image.

The aim is to correct the OBJ image for the pixel-to-pixel flat field whilst the spectra are in pixel co-ordinates and then perform the sky background subtraction after wavelength calibration. The object fibre spectra are then all combined, weighted by their relative throughput as determined by the TFF throughput. This method is complicated by the fact that fibres with small levels of flux contribute more noise to the final reduced spectrum if not weighted correctly in the final combining step.

The first two steps in the data reduction are identical to those in Table 6-4. The subsequent pupil image data reduction steps are then followed below. Only the OBJ frame is discussed here: the method is repeated on the standard star data to produce the atmospheric correction.

The apertures defined in the DFF field now have the object fibre spectra (in apertures 1-37) and the two close-packed fibre bundle of sky fibres (apertures 38 and 39).

- Form the response spectrum from DFF and TFF for all 39 apertures using `msresp1d` → `TD_resp.ms`.

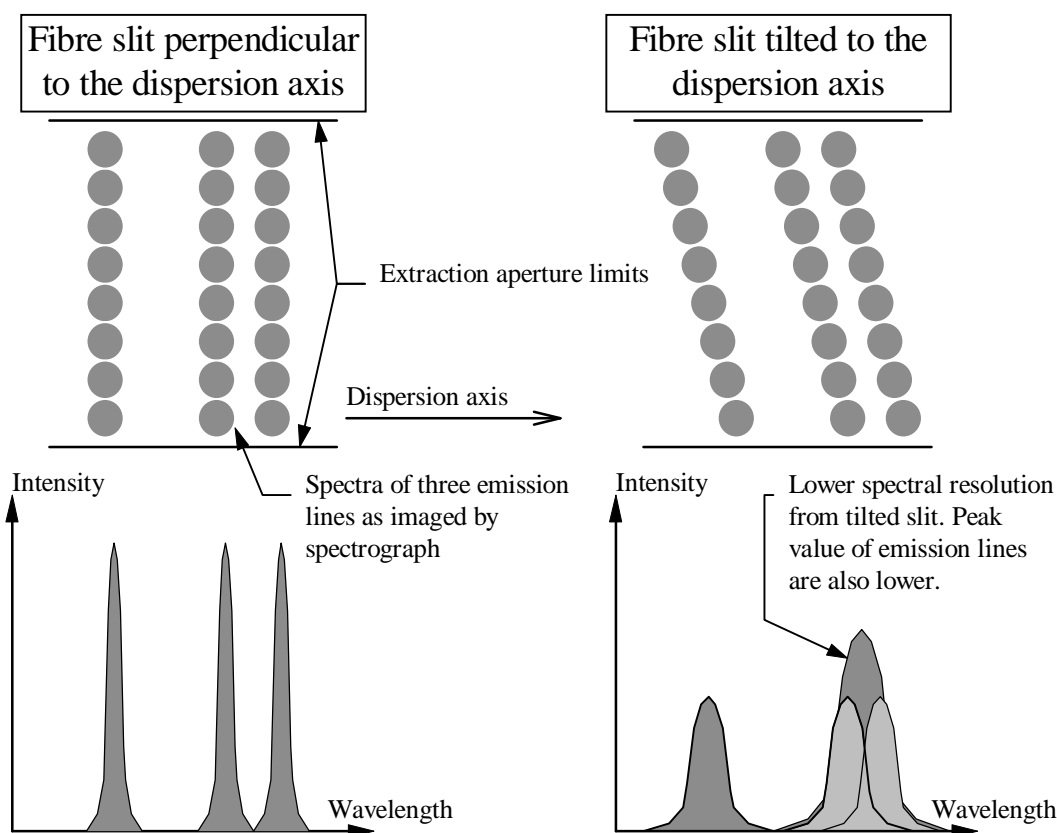


**Figure 6-35** The effect of a tilted fibre slit on pupil imaging extraction. A slit perpendicular to the local dispersion axis produces extracted spectra with the expected resolution. If the slit is tilted, the extracted spectra have a lower spectral resolution, degrading the performance of the spectrograph.

- Create a response spectrum that has just the relative throughputs of the fibres → `T_resp.ms`
- Divide `TD_resp.ms` into the object file `OBJ_sl.ms` / `TD_resp.ms` → `OBJ_slf.ms`
- All the spectra in `OBJ_slf.ms` are now normalised and corrected for pixel-to-pixel flat field.
- Wavelength calibrate and dispersion correct `OBJ_slf.ms` → `OBJ_slfc.ms`
- Average the two sky background spectra and subtract the resultant spectrum off all the other fibres. `OBJ_slfc.ms` - [average of apertures 38, 39 from `OBJ_slfc.ms`] → `OBJ_slfcs.ms`
- Now all the object fibres have had the sky background subtracted and are normalised with respect to each other. The fibres which have a low throughput have been multiplied by a large factor, so if the fibres are added together now then the noise of the low throughput fibres will decrease the signal to noise of the final spectrum.

The solution is to divide out the relative throughput introduced by `TD_resp.ms` before adding the fibres together, so the sky subtracted fibres are now multiplied by the fibre response function, `T_resp.ms`. However, the fibres have been dispersion corrected since the first normalisation, so `T_resp.ms` needs to be wavelength calibrated to produce `T_resp_c.ms`.

- `OBJ_slfc.ms` / `T_resp_c.ms` → `OBJ_slfcf.ms`
- The final step is to add up all the object fibres in `OBJ_slfcf.ms`, ignoring any spectra which have a low throughput. The result is `OBJ_sum`. When the STD spectrum is processed in the same manner, it is normalised and divided into the OBJ spectrum to correct for atmospheric absorption: `OBJ_sum` / `STD_sum` → `OBJ_final`.

### 6.9.3 COHSI integral field spectroscopy mode

The COHSI IFS mode data is reduced in almost the same way as the SPIRAL IFS data. One important difference is that it is difficult for an estimate of the scattered light in the cryogenic spectrograph to be made as the fibre slit image fills the whole detector. However, due to the fibre-fed design of the cryogenic spectrograph and the earlier removal of OH night sky emission lines, the amount of scattered light is expected to be minimal.

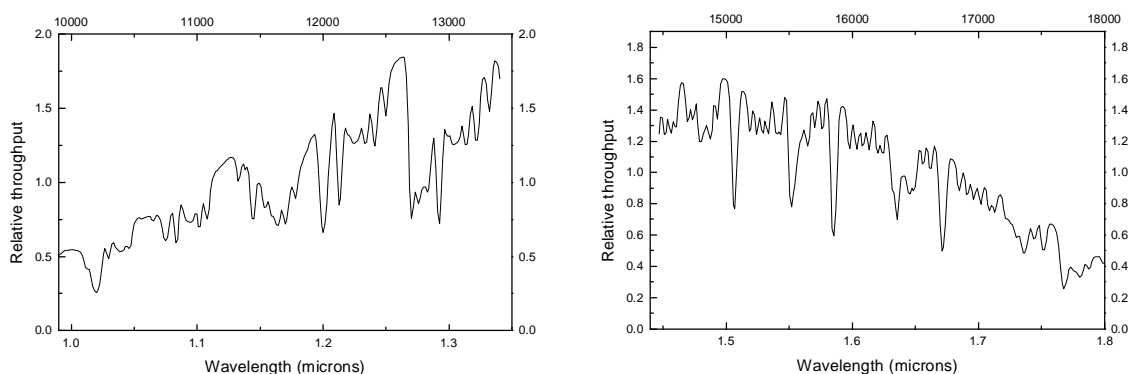


**Figure 6-36** *The COHSI flat fields.* The left-hand image is the J band flat field and the right-hand image is for the H band.

The original science driver for COHSI is the detection of emission lines from high redshift galaxies, and in this case the flat-fielding process is not necessary for line detection. Later work with COHSI may involve the colours of galaxies and hence the flat fielding is crucial. The problem is exaggerated due to the peculiar nature of the COHSI flat field, which contains ‘absorption lines’ due to the OH blocking mask features (see Figure 6-36).

The mask flat field is treated in a similar manner to a standard star - the features of the masks are treated as atmospheric absorption features and are divided out as the last step of the data reduction.

# 7. The Performance of SPIRAL Phase A

---

## 7.1 Introduction

From two observing runs on the AAT (see Table 7-1) the SPIRAL spectrograph and fibre feed were aligned, tested and used for scientific observations. The SPIRAL spectrograph performance is characterised in §7.2, with spectrographic parameters such as the measured spectral resolution and variation of point spread function (PSF) across the detector (§7.2.1) and an estimate of the scattered light fraction (§7.2.2). The relative throughputs of the fibres is shown (§7.2.3) along with the total throughput of the instrument (telescope, fibre feed and spectrograph) as a function of wavelength (§7.2.4).

Two different objects were used to test the scientific capability of SPIRAL ‘A’ (§7.3). For the pupil imaging mode, the search for a brown dwarf proved successful with the first candidate examined (§7.3.4) and the measurements agreed with data taken independently with the CASPEC echelle spectrograph three years earlier (Tinney 1998).

The integral field spectroscopy mode required good seeing at the AAT for spatially resolved observations to occur. Seeing better than 1 arcsecond was observed on the 23<sup>rd</sup> November 1997 and SPIRAL ‘A’ observed the 1987 supernova remnant in the Large Magellanic Cloud. Recent observations from the Hubble Space Telescope suggested that supernova ejecta had reached the slower moving HII region with resultant blue-shifted emission appearing in the H $\alpha$ [6563]. Besides looking for this blue emission, SPIRAL also demonstrated its IFS mode by generating velocity

Date	Detector used	Tests performed	Mode tested
14 <sup>th</sup> Feb 1997	Tek 1024 <sup>2</sup>	Alignment	IFS
15 <sup>th</sup> Feb 1997	Tek 1024 <sup>2</sup>	None (Cloudy)	IFS
16 <sup>th</sup> Feb 1997	Tek 1024 <sup>2</sup>	Alignment	Pupil imaging
20 <sup>th</sup> Nov 1997	MIT/LL 2Kx4K	Alignment	IFS
21 <sup>st</sup> Nov 1997	MIT/LL 2Kx4K	Throughput	IFS
22 <sup>nd</sup> Nov 1997	MIT/LL 2Kx4K	SN1987A	IFS
23 <sup>rd</sup> Nov 1997	MIT/LL 2Kx4K	Brown dwarf	Pupil imaging

**Table 7-1** The dates and CCD’s used on the SPIRAL observation runs.

dispersion maps showing the distribution of the gas in the nebula.

A discussion of the merits of the pupil imaging mode then concludes this chapter (§7.4).

## 7.2 The astronomical performance of the SPIRAL spectrograph

The SPIRAL spectrograph was initially designed to use the Tek  $1K^2$  array, where two of the  $24\mu\text{m}$  pixels matched well to the  $50\mu\text{m}$  fibre core from the fibre feed. The MIT/Lincoln Laboratory  $2K \times 4K$  CCD, which was used for all the science and throughput calculations, has  $15\mu\text{m}$  square pixels. To keep the sampling matched optimally and reduce the storage of excessively large data frames, the MIT/LL was set to on-chip bin 2 pixels by 2 pixels, forming an effective frame of  $1024$  by  $2048$   $30\mu\text{m}$  pixels.

Examination of the dome flat fields revealed vignetting at the edges of the data frame which was assumed to be due to the edges of the camera shutter in front of the dewar. One of the earlier test exposures had a significant amount of light leakage from outside of the spectrograph, and an image of the edges of the shutter could be clearly seen (see Figure 7-1). In addition to the vignetting by the shutters, scattered reflections can be seen on the left-hand side of the image, probably due to scattered light off the mechanism operating the shutter. Other observed effects include dust on the dewar window and regions of lower QE, appearing as darker spots across the CCD. Along the top of the image the overscan region can be seen. The white rectangle defines the region of the final processed CCD image after overscan and the zero level frame has been subtracted. This rectangle defines a region of unvignetted fibre spectra and is used to process all the frames as the first step of data reduction.

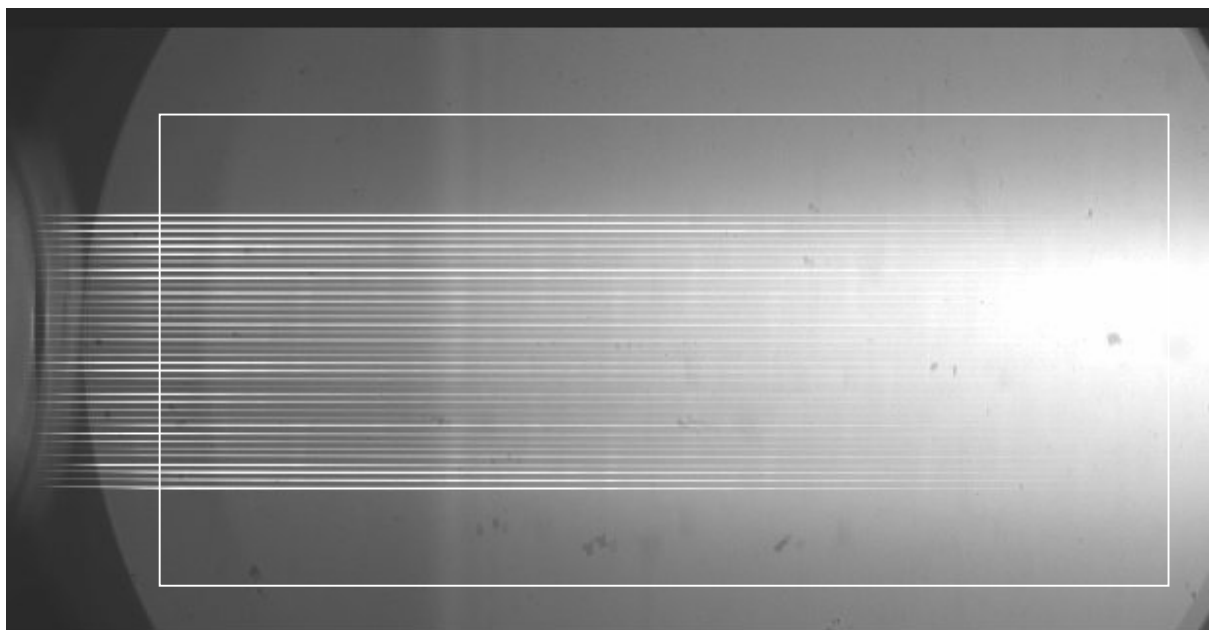


**Figure 7-1** *Vignetting and scattered light in the spectrograph.* An unprocessed data frame showing scattered light, vignetting and dust on the dewar window. The white box shows the approximate area of the clipped and processed data image.

### 7.2.1 Spectral resolution and PSF across the detector

The point spread function across the CCD was examined for a typical exposure. An arc emission data frame provided a set of evenly spaced emission lines with which to measure the PSF introduced by the spectrograph optics. The results are shown in Figure 7-2. The PSF was measured to be  $(2.31 \pm 0.11)$  pixels, corresponding to an image size of  $(69.3 \pm 3.3)$  microns, larger than the fibre core diameter of  $50 \mu\text{m}$  but in agreement with the PSF of the computer model. There was no significant variation in the measured PSF across the image, showing that the spectrograph optics were performing to specification.

Different gratings were inserted into the spectrograph and arc spectra images were taken for various wavelength ranges. By using a dome flat field to define the fibre tracks (as described in Chapter 6) the spectra were extracted and a dispersion solution identified for the arc lines. The best low-order fit for the dispersion was a 4<sup>th</sup> order polynomial (either Legendre or Chebyshev). The results for three configurations are shown in Table 7-2.

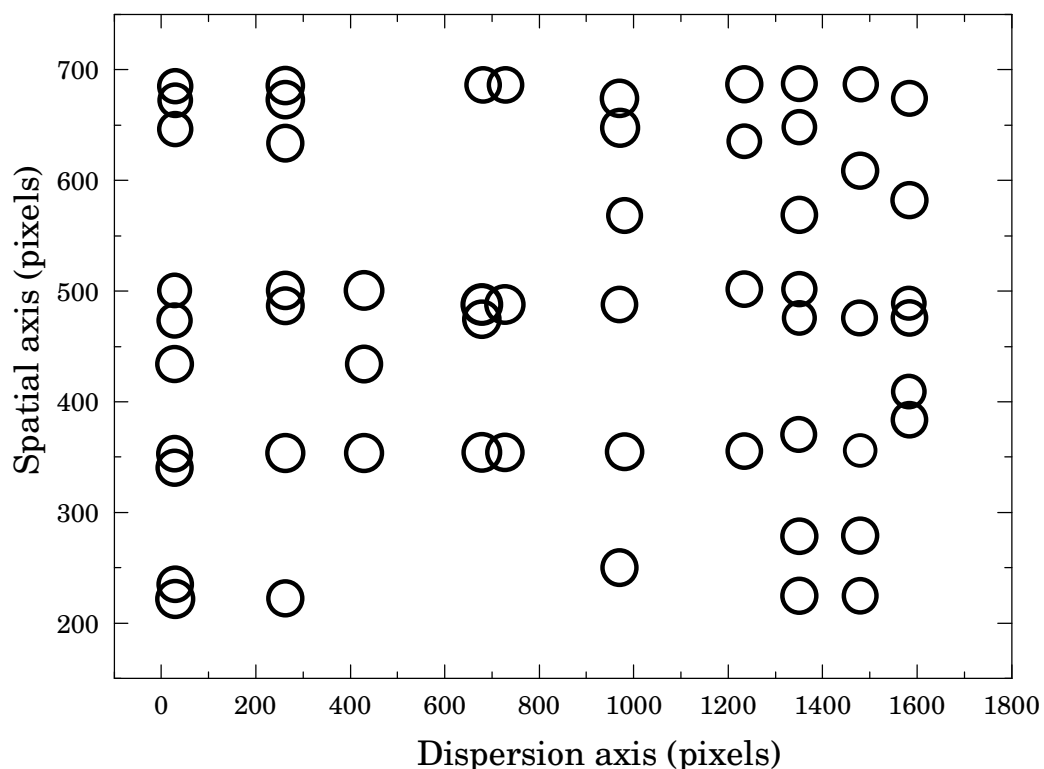


**Figure 7-2** Point spread function of arc emission lines across the MIT/LL CCD. The diameter of the circles are proportional to the width of the arc lines. The mean measured FWHM across the whole field is  $(2.31 \pm 0.11)$  pixels. The arc frame was used to calibrate the brown dwarf spectra in §7.3.2.

Grating	Wavelength range	Dispersion	Line FWHM	Resolution (middle of wavelength range)
270R 1 <sup>st</sup> order	6500-8900Å (2400Å)	1.525Å/pixel	1.85±0.12 pix (2.82±0.18)Å	2730
1200R 1 <sup>st</sup> order	6270-6770Å (500Å)	0.314Å/pixel	2.75 pix (0.864±0.036)Å	7550
1200R 2 <sup>nd</sup> order	6200-6450Å (250Å)	0.155Å/pixel	2.70 pix (0.419±0.017)Å	15000

**Table 7-2** Measured dispersions and resolutions of the SPIRAL spectrograph

### 7.2.2 Scattered light

A fraction of the light entering the spectrograph is scattered by the lenses and the reflection grating and appears on the CCD as a smoothly varying background (see Figure 7-1). This scattered light is dependent on the intensity of the fibre spectra themselves and is a non-trivial function of position on the CCD, but a simple estimate can be made. Low order functions are fitted to the scattered light across and along the dispersion axis and using interactive fitting a scattered light image can be generated. The number of counts in this image is then compared to the total number of counts from the fitted image, giving a lower bound on the fraction of scattered light present in the spectrograph.

Central observed wavelength (Å)	Grating used	Scattered light fraction
6450	1200R	24.7%
6700	1200R	19.1%
6520	1200B	19.6%
6520	1200B	19.4%
7600	270R	5.2%

**Table 7-3** Scattered light levels for different gratings.

From the results in Table 7-3 the fraction of scattered light is dependent on the grating used - the higher dispersion gratings have typically 15% or more scattered light than the lower dispersion gratings. One possible explanation for this variation is due to the manufacture of the gratings. Higher dispersion gratings require narrower and higher tolerances than low dispersion gratings and so they are more prone to manufacturing errors. This leads to the higher levels of scattered light for higher dispersion gratings.

### 7.2.3 Relative throughputs of the fibres

In the IFS mode it is necessary to know the relative throughput of each aperture in the image. The throughput of a given aperture is a function of the fibre throughput and the alignment of the pupil image of the telescope with the end of the fibre core (see §4.3.1).

Twilight flat fields give the most reliable method for determining the throughput of the SPIRAL spectrograph. Although dome flat fields are suitable for removing detector systematic errors, they are not reliable indicators of relative aperture throughput.

Ideally a telescope pupil image coincides exactly with a fibre face in the lens array. However due to the error in manufacturing, the telescope pupils are misaligned and a fraction of the telescope pupil light does not pass into the fibre. The position of the telescope pupil with respect to the fibres changes each time the IFS mode is realigned on the telescope, so the relative throughput of the fibres changes each time.

For calculating the throughput of the whole instrument it is only meaningful to use the relative throughput as defined by twilight sky exposures. Altogether six twilight flat fields were taken over three days when the IFS mode was aligned on the telescope. The throughput of each aperture was calculated and the whole set of fibre throughput normalised, and repeated for each of the six flat fields. Comparing the plots of throughput as a function of fibre number, all six frames were found to have relative aperture throughputs consistent to typically 3.5% (see Figure 7-3). This shows that the fore-optics remained in good alignment over three days on the telescope. This error of 3.5% stems predominantly from the scattered light subtraction process - slight errors in the estimation of the scattered light for a twilight image leads to a different calculated aperture throughput.

The second graph in Figure 7-3 shows the relative throughput of the fibres - this was calculated in a similar manner to the aperture relative throughput graph but by using flat frames with a torch bulb illuminating the lens array directly. By doing this the fibres have their faces evenly illuminated, removing the effect of the telescope pupil alignment error. This graph then gives a better estimate of the relative fibre throughput of the SPIRAL fibre feed.

The large variation in relative aperture throughput is consistent with the misalignments seen in the SPIRAL lens array. Four fibres have throughputs less than 0.4 of the mean. Of these, two fibres (33 and 37) were due to a cracked lens and fibre damage, and the other two (6 and 7) were due to

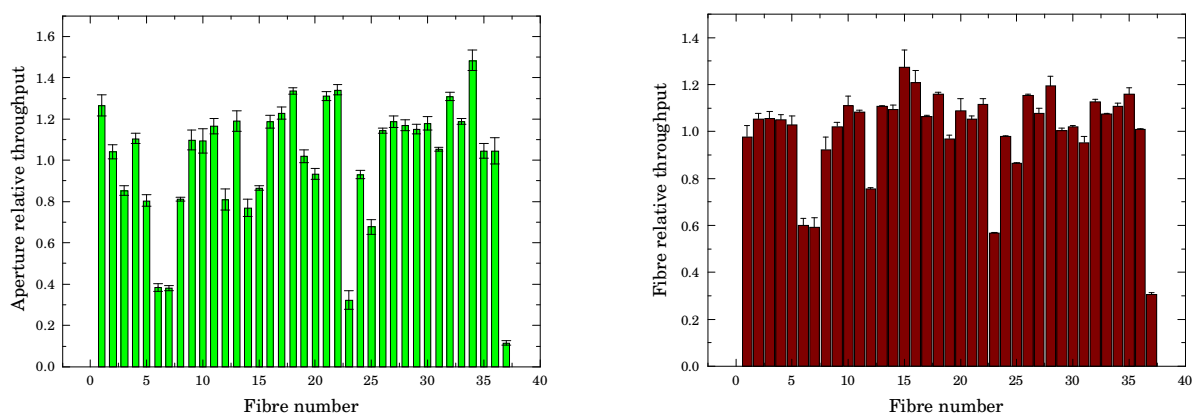


**Figure 7-3** Normalised SPIRAL aperture throughputs and fibre throughputs.

extreme misalignments with the telescope pupil image. For data reduction it is the aperture relative throughput image that is used for throughput correction.

A histogram of the remaining 33 apertures throughputs are fitted by a Gaussian distribution which shows the spread due to fibre throughput and misalignments along with a similar histogram for the fibre throughputs. The standard deviation for the aperture histogram is 0.28 and for the fibre histogram is 0.18, showing that the misalignments of the fibres have caused a reduction in throughput (Figure 7-4).

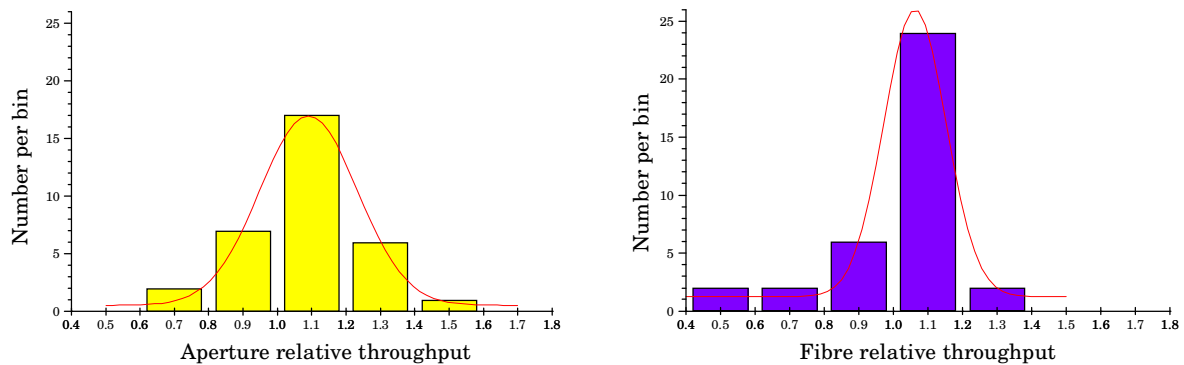


**Figure 7-4** Histograms of the aperture throughputs and fibre throughputs of the SPIRAL lens array.

#### 7.2.4 Total transmission as a function of wavelength

Spectrophotometric standard stars were selected and observed in both modes. By knowing the gain of the CCD a direct conversion into detected photon flux could be calculated and graphs of transmission versus wavelength produced. The data reduction procedure was kept deliberately simple to avoid introducing systematic errors.

A data frame of a standard star was taken and the scattered light subtracted off. A rectangular region that enclosed all the fibre spectra was then selected and all the dispersion rows were summed together to form a single output flux spectrum. An arc image was similarly reduced to produce an arc spectrum with the same dimensions as the standard star spectrum. The arc spectrum was then used to find a dispersion solution and this was applied to the standard star spectrum to form a wavelength calibrated spectrum.

By knowing the flux per wavelength interval for the standard star and the exposure time the efficiency as a function of wavelength can be produced (see Figure 7-5). The pupil imaging mode was measured with the highest efficiency, with 14% in the first measurement. A second standard star gave a lower measurement of 11% and the IFS mode was measured with an efficiency of 9.8%.

The differences in calculated transmission for the pupil mode can be caused by:

**Variation of seeing.** On the nights that the pupil mode was tested the seeing was between 1.5 - 2.0 arcseconds. The second curve was obtained later on in the evening in worse conditions.

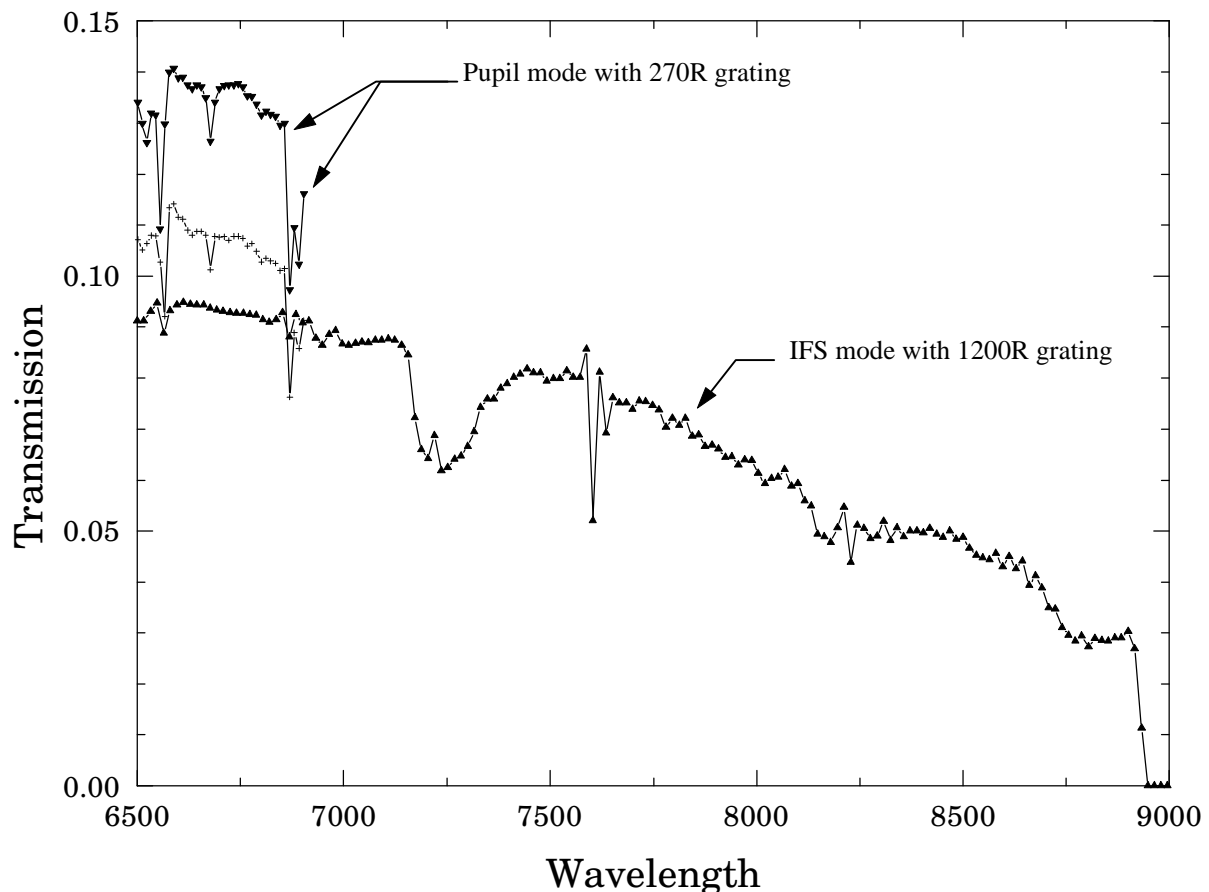


**Figure 7-5** *Transmission versus wavelength for SPIRAL.* The two higher curves are measured for standard stars with the pupil imaging mode and the lower curve was measured for the IFS mode.

**Misalignment of the object with the pupil imaging aperture.** Locating a star exactly in the centre of the pick-off mirror proved difficult. The hole in the POM was drilled with a diameter larger than the effective diameter of the fibre pupils. Unlike a long slit spectrograph where light not visible on the edge of the slit enters the collimator, there was a ‘dead region’ within the POM hole where light from the star would not enter the fibres in the lens array. Even taking these transmission variation into account, it became apparent that the pupil imaging mode gave a high throughput.

The integral field mode showed a lower overall transmission, but this could have been due to bad seeing during the observation. Another possible source of variation in transmission came from the position of the stellar image on the lens array. If the core of the stellar image passed through fibres with lower transmission than the average, then this would give a lower overall efficiency for the fibre feed.

Considering that the throughput for the pupil imaging mode was 15% for the 1200R grating, 25% of the light into the spectrograph was scattered by the grating and optics. Taken in conjunction with the fact that the fibre with the highest throughput was 1.5 times greater than the mean, this implies that given more careful construction the throughput can be as high as 20%.

The difference between the throughput of the IFS mode and pupil mode can also be explained in terms of the fibre misalignments (see Figure 7-6), and this leads to the conclusion that the IFS mode can be as efficient as the pupil imaging mode.

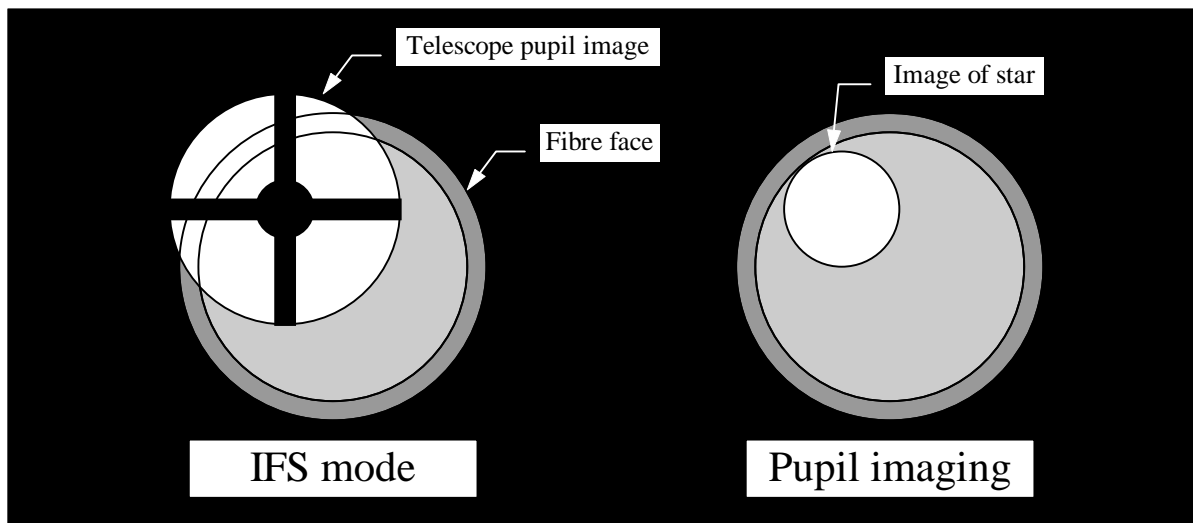


**Figure 7-6** *The effect of misalignment on throughput.* The two diagrams show the fibre face illumination in the two modes. The IFS mode loses more flux than the pupil mode for a given misalignment due to the distribution of flux in each fibre image.

### 7.2.5 Testing the dome flat fielding

Two pairs of dome flat fields were taken at the start (DFF1 and DFF2) and the end (DFF3 and DFF4) of one evening and were used to investigate the flat fielding properties of the fibres. For each frame the extraction apertures were separately identified for each frame and the fibre spectra extracted. Two typical fibre spectra (from DFF1) are shown in the top row of Figure 7-7. Both large scale and small scale variations in the pixel flat field can be seen, so it was seen if these were real pixel variations or not.

The first pair of flat fields were divided into each other, and the results are on the second row of the figure. As can be seen, all the features present in the first row disappear in the second row of images, demonstrating good flat fielding properties. To check this, fibre 18 was examined and the noise was measured in the individual frames (DFF3 and DFF4).

Aperture 18 in DFF3 had typically 22000 counts, giving a Poisson noise of 0.67%

Aperture 18 in DFF4 had typically 11000 counts, giving a Poisson noise of 0.95%

Looking at the measured noise in the resultant division of the two apertures gave 1.1% - in agreement with photon noise statistics. In all cases the read noise of the CCD ( $\sim 1.45e^-$ ) is negligible.

Comparing the pairs of frames taken a short period of time apart showed good flat fielding. However, performing a division of DFF1 by DFF3 showed some fibres with an extra sinusoidal component added to them (see the last row of Figure 7-7). This has been noted in the 2dF

spectrograph at the AAO and has been suggested that it is caused by thin film interference between the fibre end and the prism on one of the movable fibre buttons. This can be explained in SPIRAL as air bubbles moving around in the uncured UV adhesive. As can be seen looking down the right-hand column of Figure 7-7, this effect is time dependent, appearing over a period of hours in the flat field.

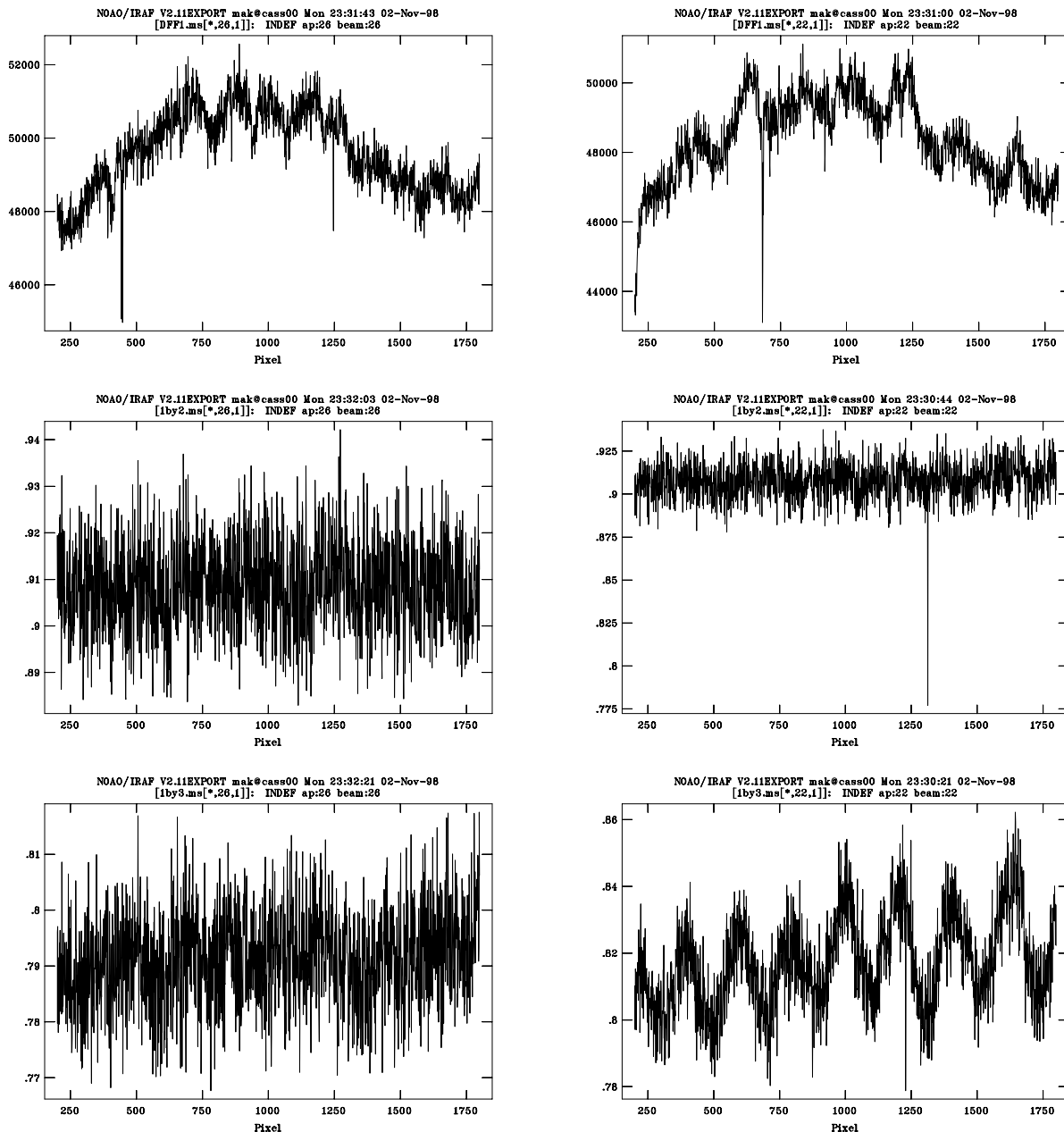


**Figure 7-7** Pixel to pixel flat fielding with SPIRAL. The top pair of fibre spectra are extracted from a flat field frame taken with SPIRAL. The middle pair of fibre spectra show the result when the top row of spectra are divided by the extracted spectra of another flat field taken immediately after the first one. The bottom pair of spectra show the division into a flat field taken many hours after the first flat field. The flat field spectra in the left hand column are typical of most SPIRAL fibres, but occasionally a large scale ripple is seen in the fibre flat fields (right hand column).

## 7.3 Science with the SPIRAL fibre feed

### 7.3.1 Introduction: big explosions and cool embers

Commissioning the SPIRAL feed also involved a test of its scientific capabilities in both modes. For the pupil imaging mode, a high resolution observation was needed of a faint star, and for the integral field mode a combination of good seeing and an object with small spatial extent was needed. After following various lines of enquiry, the two objects examined turned out to be two very different endpoints of stellar evolution. For the pupil imaging mode a list of candidate brown dwarfs was suggested by Mike Hugh-Jones and the IFS mode was tested by looking at the supernova remnant SN1987A in the Large Magellanic Cloud.

Both projects proved successful in testing the modes of SPIRAL and demonstrating the fibre feeds capability.

### 7.3.2 The pupil imaging mode: brown dwarf candidates

Brown dwarfs are scientifically interesting because they fill the mass gap in between Jupiter-like planets and low mass M stars. They potentially cover two orders of magnitude of mass, and were one of the original candidates for dark matter, although various searches have shown that the number density is not high enough (Chabrier 1998). However there is a large interest in discovering their number density, as no real idea of their numbers is known. The search for brown dwarfs has been approached in three different ways - a direct detection as part of a young cluster (Zapatero Osorio 1996, Festin 1998, Zapatero Osorio 1997, Zapatero Osorio 1998, Magazzu 1995, Wilking 1998), indirect detection as a companion to another star (Geballe 1996, Nakajima 1995, Oppenheimer 1998), or wide deep surveys for field objects (Hawkins 1988, Tinney 1993). All three methods are being used in brown dwarf searches and are listed in a recent conference proceeding (Rebolo et al 1998).

The definition of a brown dwarf is a star that is not able to sustain stable thermonuclear fusion of hydrogen at its core - they are balls of gas that fail to shine like normal stars. As a consequence brown dwarfs glow many magnitudes fainter than their slightly more massive nuclear burning counterparts. What radiation comes from them is due to their gravitational contraction, and their surface temperature is typically 2500K or less (Rebolo et al. 1998). The bulk of their emission is in the near infra-red ( $1\mu\text{m}$  -  $2\mu\text{m}$ ) and surveys have been carried out to put upper limits on their number density (Rebolo et al. 1998).

By the middle of 1997, the number of brown dwarfs was still in single figures, and the discovery of new brown dwarfs was crucial to determining their first order properties. Hugh-Jones at the Liverpool John Moores University produced a list of faint red candidate stars that could be examined by SPIRAL phase A. These candidates had been selected on the basis of their extremely red colour using R and I colours and their absolute magnitude determined by astrometry (for example, Tinney 1996).

The spectroscopic test for SPIRAL is to look for the Lithium resonance absorption line at 6708Å in the continuum. This Lithium test was proposed by Rebolo et al. (1992) as a test for brown dwarfs and has since proved to be an effective test for distinguishing them from late type stars (Nelson 1993, Rebolo 1996, Martin 1994). Primordial Lithium present in forming stars is destroyed rapidly in thermonuclear reactions with hydrogen. Lithium/hydrogen burning occurs at a much lower temperature than hydrogen/hydrogen burning, so if lithium is detected in cool, late type stellar objects it is assumed that the core temperature was never high enough to initiate stable lithium burning and therefore imply that stable hydrogen burning never occurred. The object is therefore a brown dwarf.

More recent tests have looked for methane absorption in the near infra-red (Rosenthal 1996) as indicators of cool brown dwarfs, while the Lithium test is more sensitive to brown dwarfs with an effective temperature greater than ~1600K (Rebolo 1998a).

### **7.3.3 The brown dwarf LP 944-20**

The first star observed on the candidate list was BRI 0337-3535, otherwise known as LP 944-20. Three 1800s exposures were taken on the night of the 23/24 November 1997 on the AAT in poor conditions (measured seeing was 2 arcseconds). After median combining the three frames it became apparent that there was Lithium absorption present in the stellar spectrum, thereby confirming that the star was indeed a brown dwarf.

This star has been discovered and catalogued as a very red faint star in the literature for over 15 years under various names. Astrometry has been performed on this star as part of a sample of low mass stars showing it to have  $m_k=(9.58 \pm 0.03)$ ,  $I-K=4.58$  and  $M_k=(11.10 \pm 0.06)$  making it to be at a distance of  $(20.1 \pm 0.7)$  parsecs (Tinney 1996). A spectrum of this star was taken in February 1994 at ESO as part of a study of the velocities of the lowest mass stars (Tinney and Reid 1998a). However, the authors did not check their spectra for Lithium absorption and it remained unidentified as a brown dwarf for over three years.

The spectra were re-examined in 1997, and the Lithium absorption in LP 944-20 was discovered and a paper was submitted a week before the SPIRAL observations were performed (Tinney 1998). Although this is an unfortunate coincidence, it allows SPIRAL to be compared to another spectrograph and to confirm the measured properties of the Lithium absorption line.

### **7.3.4 Results and conclusions**

The pupil imaging data was reduced with the method described in §6.10.2, and the reduced spectrum is shown in Figure 7-8. The absorption line profile was fitted using the IRAF routine FITPROFS and the results of a Monte Carlo fitting gave an estimate of the errors on the measurement.

	Equivalent width of LiI line	Heliocentric velocity as measured by LiI line
Tinney 1998	$(0.53 \pm 0.05) \text{ \AA}$	$(+12.6 \pm 4) \text{ km/s}$ - cross correlation
SPIRAL Phase 'A'	$(0.54 \pm 0.06) \text{ \AA}$	$(-22 \pm 12) \text{ km/s}$

**Table 7-4** Comparison of LP 944-20 properties.

	$m_R$	$m_I$	$m_K$	R-I	R-K
Magnitude	$17.19 \pm 0.10$	$14.16 \pm 0.03$	$9.58 \pm 0.04$	3.03	7.61

**Table 7-5** Magnitudes and colours of LP 944-20.

The position of the LiI line was measured to be  $(6707.854 \pm 0.16) \text{ \AA}$ , with the RMS of the wavelength fitting as  $0.03 \text{ \AA}$ . The equivalent width of the Lithium absorption was measured to be  $(0.54 \pm 0.06) \text{ \AA}$ .

Knowing the rest wavelength of the Atomic Lithium resonance line ( $6707.8120 \text{ \AA}$ ) the velocity of the star with respect to the Earth could be calculated. The resultant velocity is  $(1.9 \pm 11.7) \text{ km/s}$  with respect to the Earth. This velocity is then corrected to a heliocentric velocity with the result shown in Table 7-4.

The R magnitude of the brown dwarf was also calculated. By using the standard photometric star HD49798 a calculation of the AB magnitude at  $6710 \text{ \AA}$  was made. The dominant source of error on the determined magnitude is due to the uncertainty in the throughput of the pupil imaging mode between the brown dwarf observations and the standard star observations. A nominal variation of

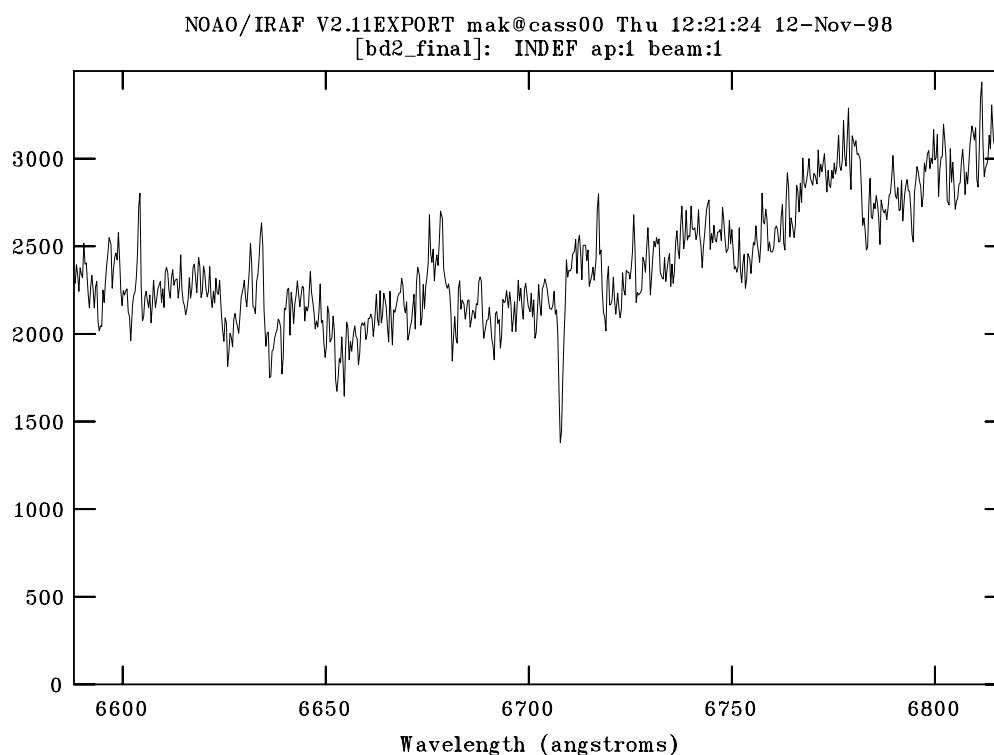


**Figure 7-8** The spectrum of BRI 0337-3535. The Lithium I absorption feature can be clearly seen at  $6708 \text{ \AA}$ .

10% in throughput has been estimated leading to an uncertainty in the magnitude of 0.1. The result along with the other magnitudes from Tinney 1998 are shown in Table 7-5.

The equivalent widths agree within the measured errors but there is a discrepancy between the heliocentric velocities. The velocity obtained by Tinney was by cross-correlation with the spectrum of a standard star, whilst the SPIRAL observation was made with the centroid of the Lithium line only. Tinney states that the radial velocity obtained with the Lithium line centroid is coincident with the radial velocity obtained from the cross correlation technique. However, by fitting the centroid of the H $\alpha$  line Tinney gets a result of  $0 \pm 10$  km/s from the same spectra as the Lithium line. Clearly there is some activity on the brown dwarf that means that reliable radial velocity measurements are dubious by fitting to one line. Cross correlation seems to be the most robust technique.

The conclusions drawn in Tinney (1998) are that LP 944-20 is an intermediate age brown dwarf with age in the range 475-650 Myr, the mass lies in the range  $0.057-0.063 M_{\text{solar}}$  and the models imply a luminosity  $\log(L/L_{\text{solar}}) = -3.84 \pm 0.03$  and  $T_{\text{eff}} = 2000\text{K}$ .

### 7.3.5 Observations of SN 1987A

To test the integral field mode of SPIRAL, an object with detail on a small scale was required for the 3.5 arcsecond field. Ralyee Stathakis and Russell Cannon suggested the supernova remnant in the Large Magellanic Cloud, SN1987A. This was observed during sub-arcsecond seeing on the night of the 23<sup>rd</sup> November 1997.

This object is arguably one of the most intensely studied objects in recent astronomy. Since the burst of neutrinos that arrived on February 23.316 UT, 1987, the results of the explosion has been monitored on many wavebands, and the rapid nature of the event had led to rapid changes in the small scale structure in the local environment, seen with the high spatial resolution of the Hubble Space Telescope.

The circumstellar environment of the supernova is still not well understood and is under continual examination (Crotts 1998). A picture of the supernova taken with HST has the field of view of the SPIRAL lens array superimposed on it in Figure 7-9. The three ring structure which is visible in the image lies on the surface of an hourglass shape tilted partially towards us (Crotts et al. 1989). The inner ring marks the waist of the hourglass (Crott & Heathcote 1991) whilst the two larger rings mark a circumference further up the lobes, delineating the extent of a double-lobe nebula (Crotts 1995).

The aim of the SPIRAL observations were simple - demonstrate the integral field capabilities of the IFU. The data consisted of two sets of data frames. Three 1800 second exposures were taken of the supernova, and three 1200 second exposures of the adjacent sky were taken for sky background

subtraction. This was especially important as the supernova is within an HII region, with the associated nebular emission from various lines such as [OIII] and [NII].

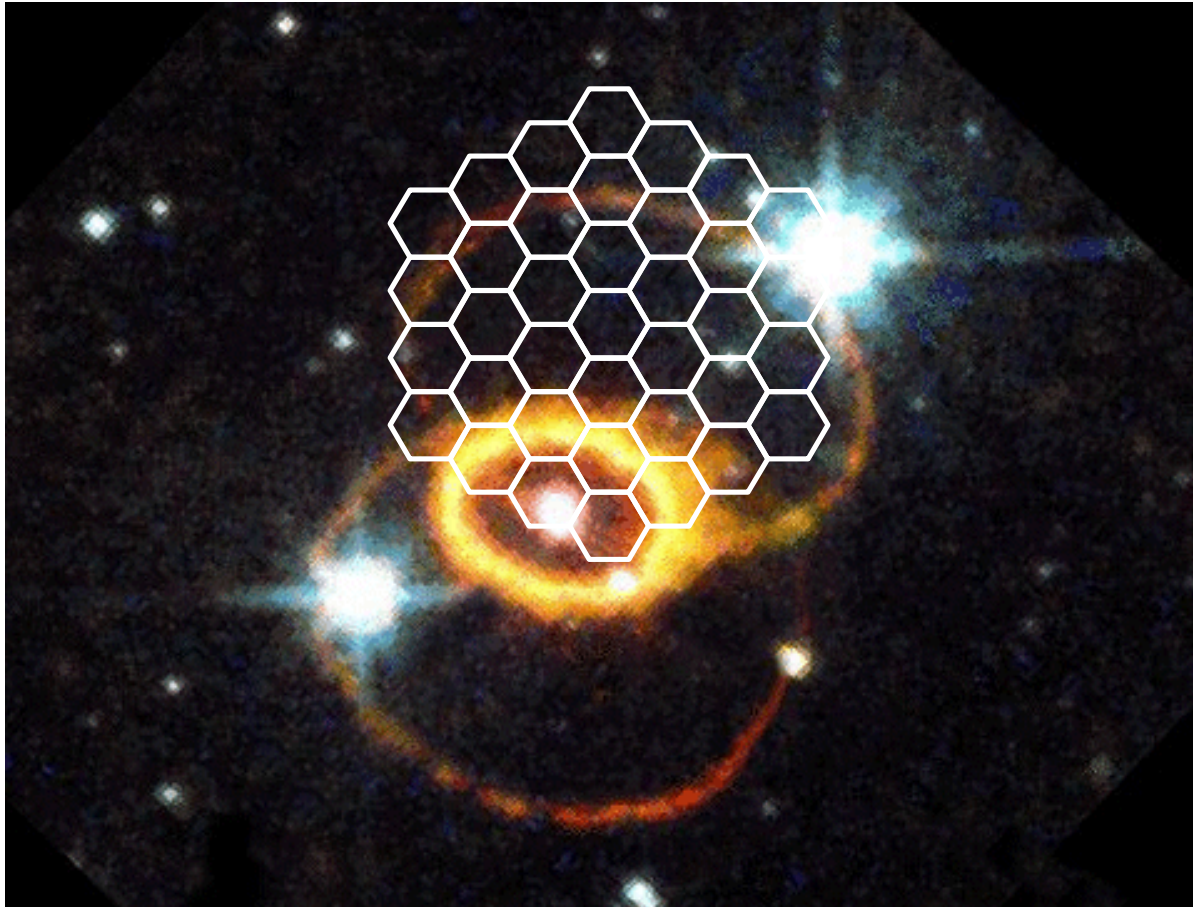


**Figure 7-9** *HST WFPC image of 1987A.* The estimated position of the SPIRAL lens array is shown superimposed on the image. North is to the top and East to the left. (Photo: Chun Shing Jason Pun (NASA/GSFC), Robert P. Kirshner, taken on March 5 1995 in NII[6584]).

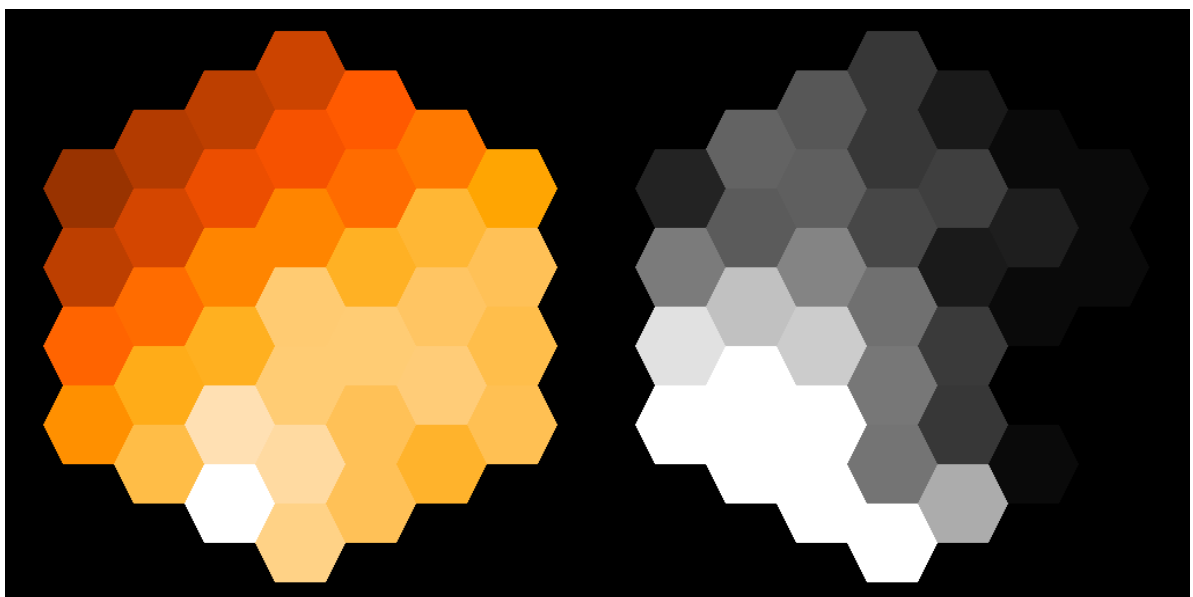


**Figure 7-10** *SPIRAL maps of hydrogen in SN 1987A.* The left hand diagram shows the intensity of  $H_{\alpha}[6563]$  and the right hand map shows the measured FWHM of  $H_{\alpha}[6563]$ . The largest width is 123km/s with the resolution of the spectrograph at 45km/s. North is top and East is left.

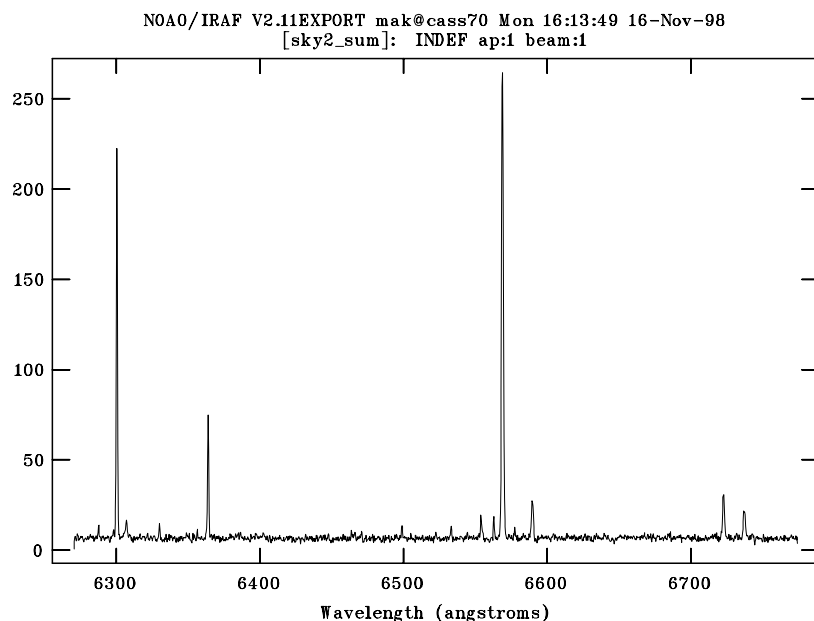


**Figure 7-11** Sky background spectra for SN 1987A. The emission lines characteristic of nebular emission regions can be seen. These lines originate from the vicinity of our Galaxy.

The data was reduced as described in §6.9.1. It is interesting to compare the sky spectra and supernova spectra together. Figure 7-11 shows emission lines due to [OI] $\lambda\lambda$ 6300, [OI] $\lambda\lambda$ 6364, [NII] $\lambda\lambda$ 6548, [H $\alpha$ ] $\lambda\lambda$ 6563, [NII] $\lambda\lambda$ 6583, [SII] $\lambda\lambda$ 6716 and [SII] $\lambda\lambda$ 6731. The supernova spectra have had the sky background spectra subtracted from them. Adding all the spectra together gives a supernova spectra with greater signal to noise, and some sky emission lines still remain due to incorrect sky subtraction.

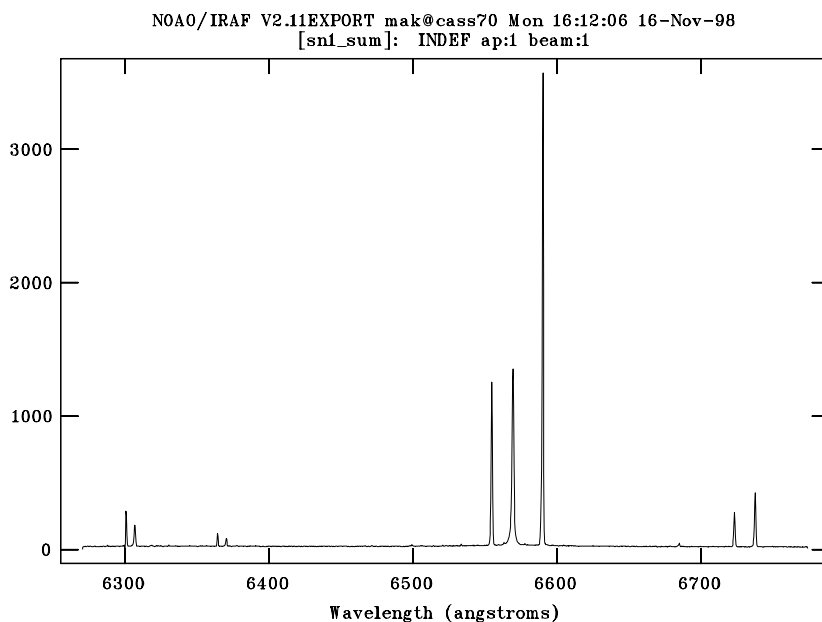


**Figure 7-12** The combined fibre spectra of SN 1987A. Here, the nebular emission lines in the LMC are red shifted by its velocity of 300km/s (6Å shift at 6500Å).

The nebular emission lines in the LMC are red shifted by its velocity of recession (typically 300 km/s) and are visible in the spectra. The bright narrow  $H_{\alpha}$  line is predominantly from the supernova and this line width is mapped in Figure 7-10.

A magnified version of the spectrum in Figure 7-12 is given in Figure 7-13. A lower intensity broad profile can now be seen in the spectrum. Its measured velocity profile is  $\sim 2,600$  km/s and this is identified as the first signs of the fast moving supernova ejecta hitting and shocking slow moving

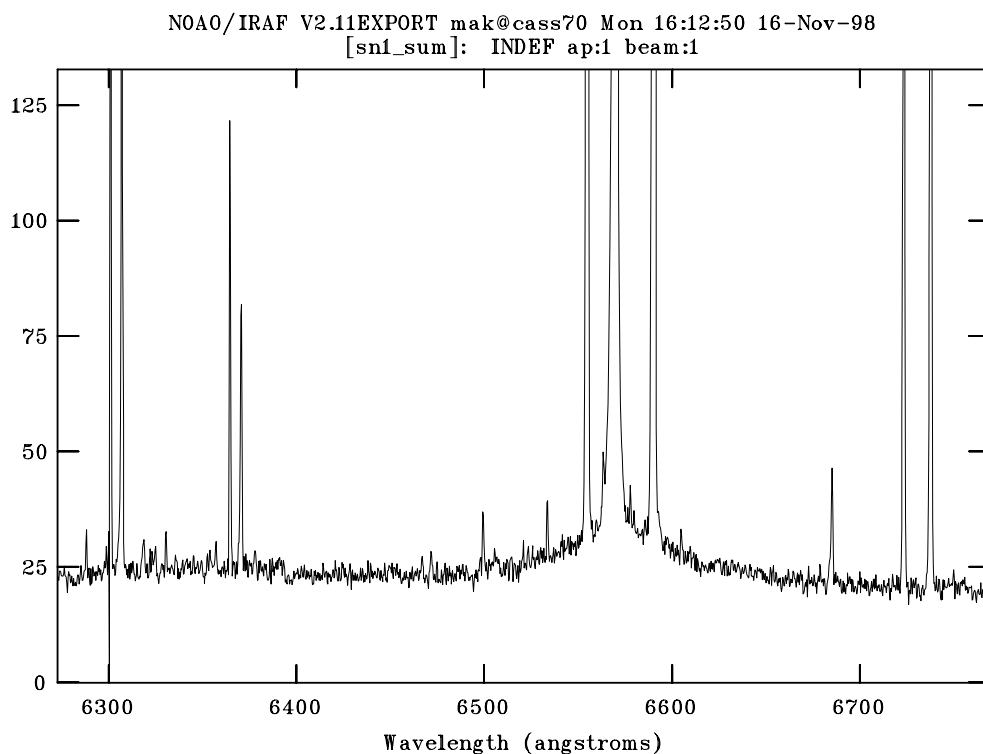


**Figure 7-13** *The SN 1987A spectrum.* Superimposed on the bright narrow hydrogen line is a broad line contribution from fast moving ejecta.

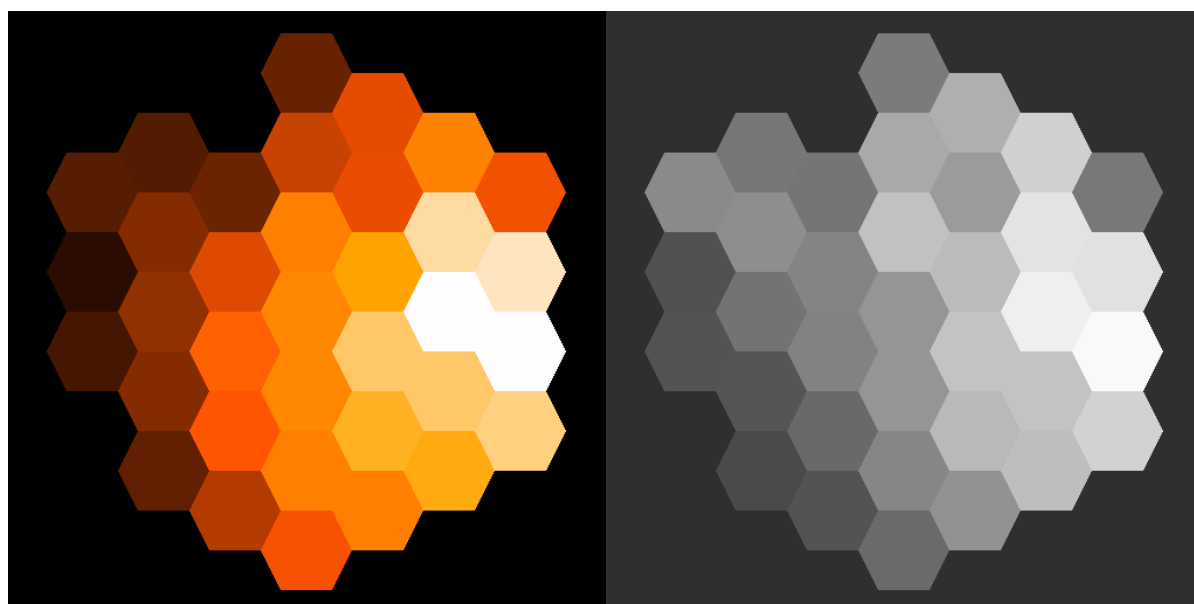


**Figure 7-14** *Maps of [OI] $\lambda\lambda$ 6364 and its ratio with  $H_{\alpha}$ .*

circumstellar gas released during the progenitors giant star phase (Chevalier 1982 and Sonneburn 1997).

The high signal to noise ratios achieved with the supernova observations allow maps of line ratios with good signal to noise (see Figure 7-14). The seeing at the telescope makes it difficult for this prototype to show significant spatial variations over a limited field of view, but the maps of  $H_{\alpha}$  and [OI] clearly show large variations, demonstrating the versatility of integral field spectroscopy.

## **7.4 SPIRAL and the pupil imaging mode**

### **7.4.1 Rationale**

The pupil imaging mode is a novel method of using the lens array more efficiently to match a spectrograph to seeing conditions at a given telescope whilst keeping a high spectral resolution. The pupil mode is intended for high resolution spectroscopy of faint objects. By imaging the telescope pupil on the lens array, the sky is imaged in the plane of the fibres and the sky background is simultaneously sampled with dedicated fibres. Many fibres can be packed into the plane of the fibres, increasing the sky background sampling and improving the sky background subtraction.

The technique is intended to use on-chip binning of the CCD to reduce the contribution of read-out noise when faint sky subtraction is needed. To see whether the mode is worth further investigation the brown dwarf observations were used as an evaluation of the technique.

### **7.4.2 The sky background in the pupil imaging mode**

In an 1800 second image, the integrated number of sky counts in one extracted aperture was 75 photons per wavelength bin for the sky continuum, with the peak night sky emission lines coming in at 360 photons per wavelength bin per 1800 seconds. The two sky fibre slits each consisted of 37 fibres close-packed into a straight line, and their extent on the CCD was 120 pixels. The CCD had been previously set to on-chip bin 2 pixels by 2 pixels to optimally match to the fibre images.

The sky emission lines at  $7000\text{\AA}$  were being detected at a rate of 0.00167 electrons/pixel/second at a spectral resolution of  $\sim 8000$ . A similar rate of counts were noted in the other sky aperture. Ideally the object fibres should be close packed together like the sky fibres, but in SPIRAL they are separated so that individual fibre spectra can be extracted with no cross-talk from the adjacent fibres.

To collect all the flux in the object fibres, the aperture extraction width was 10.61 pixels per fibre for each of the 36 object fibres (the fibre in the middle of the lens array receives no flux - see Figure 4-5a for details). In a dedicated pupil imaging unit, these fibres would be close packed to form a continuous line of fibres, but in SPIRAL the separate fibres mean that extra read noise is added to the object.

The pupil imaging mode is designed to work in a sky-limited mode, where the dominant source of noise is due to the shot noise of the sky. As the pupil mode works at the moment, this is not the case - the pupil mode is read-noise limited in the case of the brown dwarf observations.

A mathematical condition can be derived for when the pupil imaging mode becomes read-noise limited.

The expression for the signal-to-noise for a total exposure time  $t$  can be re-written (from Ennico 1998) as:

$$\text{SignaltoNoise} = \frac{S \cdot \sqrt{t}}{\sqrt{S + \alpha \cdot \left( \sum_{i=1}^m \left( B + D + \frac{R^2}{t} \right) \right)}} \quad (7-1)$$

where :

- $S$  is the object signal (electrons/second/pixel) and includes the contributions of telescope throughput, slit width and telescope diameter.
- $B$  is the sky background contribution (electrons/second/pixel).
- $D$  is the detector dark current in electrons/second/pixel
- $R$  is the read-out noise in electrons per readout
- $t$  is the total exposure time
- $m$  is the number of binned pixels in a spectral resolution element.
- $\alpha$  is the sky background subtraction factor

The case for the when the noise in Equation 7-1 is dominated by the sky is when:

$$B \gg D + \frac{R^2}{t} \text{ and } B \gg S \quad (7-2)$$

In the case of the sky seen in the brown dwarf observation,  $D$  is negligible ( $<0.3$  electrons/4000 seconds/pixel), so  $Bt \gg R^2$  for the pupil imaging mode to be worthwhile. In this case, with  $B = 0.0067$  electrons/second/pixel and  $R=1.35$  electrons, this gives  $t \gg 1000$  seconds for objects fainter than the sky background.

This suggests that only exposures of a few hours make the pupil imaging mode worthwhile.

However, if the pixels are binned up such that  $m$  pixels form one binned pixel the readout noise is then only for the one binned pixel and the factor of 1000 seconds goes down by a factor of  $m$ . Even so, many pixels need to be binned up in order to win over the sky.

Another problem is to do with cosmic ray events (CRE). By binning up the pixels, the probability of having a CRE within a binned pixel increases by a factor of  $m$ . For long exposures the CRE rate is high, so multiple exposures need to be taken in order to remove the increased CRE

detection rate. In doing this the read noise contribution in the final summed image rises again and the advantages of binning are reduced.

### **7.4.3 The usability of the pupil imaging mode**

The pupil imaging mode was the easier of the two modes to set up on the telescope, but many problems were encountered during acquisition of objects. As there was no spatial resolution on the lens array, the telescope had to be scanned in a raster each time a new object was acquired and the telescope aligned with the pointing that gave the highest measured flux.

The alignment was time consuming to perform - the pick-off mirror and the pupil imaging aperture did not mutually cover the focal plane of the telescope. It was possible for the star to be on the edge of the pupil imaging aperture and not be seen on the inside edge of the pupil imaging aperture, resulting in a loss of light and efficiency. It is this effect which is believed to be the explanation for the variation in throughput of the pupil mode in Figure 7-5.

### **7.4.4 The future of the pupil imaging mode**

Although the measured throughput of the pupil imaging mode is greater than the integral field mode and it offers simultaneous sky background capabilities, the pupil imaging mode is not considered to be a useful scientific mode. The high dispersion means that the sky background sampled is very small, requiring many hours of integration before the read noise is no longer the dominant source of noise. The pupil segmentation also means that each fibre receives only a small fraction of light from the pupil aperture, effectively spreading what few photons pass through the system across a large set of pixels, diluting the signal even further.

With the modern large format integral field units a large fraction of the lenses now sample the sky background with considerably greater ease. The two dimensional format mean that a better estimate of the sky background can be made from the areas surrounding the objects of interest, and the sampling is not just restricted to a thin strip of sky from a slit based spectrograph.

The pupil imaging mode is an interesting concept but its difficulties are judged to outweigh its modest gains, and there are no provisions as yet for a pupil imaging mode on SPIRAL Phase 'B'.





## 8. SPIRAL Phase B - a design study

---

### 8.1 Introduction

The aim of SPIRAL 'A' was to build a small prototype integral field unit and fibre feed for the AAT, the experience gained whilst constructing SPIRAL A now giving insight into how a larger lens array and fibre feed can be successfully constructed. The name for this larger fibre feed and lens array is SPIRAL 'B'. A simple design study of the optics required to build a large IFU is presented, incorporating the techniques learned earlier. The emphasis of the SPIRAL project is on minimising the potential cost of the instrument in terms of man-hours and materials whilst building a scientifically useful; instrument.

The chapter begins with the initial parameters and constraints of the design. The spectrograph built for the SPIRAL 'A' project was designed with SPIRAL 'B' in mind, and using this spectrograph then defines some of the constraints in the design, such as the number of fibres that can be used and the range of input focal ratios for the beam entering the optical fibre.

Graphs showing the relationship between input focal ratio, fibre core diameter and the angular size sky seen by one fibre allow different options to be examined, along with the number of fibres possible to fit along the fibre slit.

Having chosen the dimension and number of fibres to be used, different lens array designs are presented and the relative merits of different manufacturers products. Using the fibre placement technique used in COHSI limits the individual lenslets to be no smaller than 3mm, and the dimensions of the arrays are listed.

The fore-optics are the final part of the design. Using paraxial lenses to calculate the approximate dimensions of the layout, the detailed calculations are performed on a computer. With the final design completed, estimates are made for the approximate cost of the system and the approximate assembly time.

#### 8.1.1 The fibre feed

A perpetual concern with instruments is their cost, and the SPIRAL project is no exception. The original spectrograph was designed with the Phase B fibre feed in mind - the brief included the provision for using a large format 2Kx4K array with good imaging quality over a slit length of 30mm. The dimensions of the 2Kx4K array is 30.7mm x 61.4mm, with 15 $\mu$ m square pixels, so there

are approximately 2000 pixels along which the fibres are spatially sampled. The spectrograph is designed to work optimally at  $f/4.8$ . If a beam is faster then it overfills the collimator and light is lost, and if the beam is too slow then the grating is not totally illuminated and there is a degradation of spectral resolution.

The input focal ratio into the fibres is crucial as the predominant loss in fibres is due to FRD. For an efficient fibre feed it is not recommended that the input ratio for the fibre not be faster than  $f/5.0$ , with slower beams being preferred. Using Equation 3-3 the relation between fibre diameter, input focal ratio and size of fibre on the sky for the AAT and Gemini telescopes is plotted (see Figure 8-1). Any focal ratio between  $f/5$ - $f/6$  would be considered suitable for the SPIRAL B fibre feed, and after the experience with the SPIRAL A and COHSI fibres it is worthwhile allowing for a reasonable amount of FRD.

Any optical fibre has to have a cladding glass surrounding the core to ensure proper total internal reflection along the fibre length, and most fibre optic companies recommend a minimum core/cladding ratio of 1:1.2. This must be taken into account the packing of fibres along the fibre slit. Taking  $f/5.25$  for the input focal ratio then fixes a relationship between angular size of the fibre on the sky and the diameter of the fibre. Table 8-1 shows how the diameter of the fibres fixes the other optical and physical properties of the fibre feed.

### 8.1.2 The fibre slit

A  $60\mu\text{m}$  fibre leads to a cladding diameter of  $72\mu\text{m}$ . An extra buffer layer made of plastic can then be used to surround the fibre so that there is extra environmental protection. This outer layer is then removed for assembly into the fibre slit.

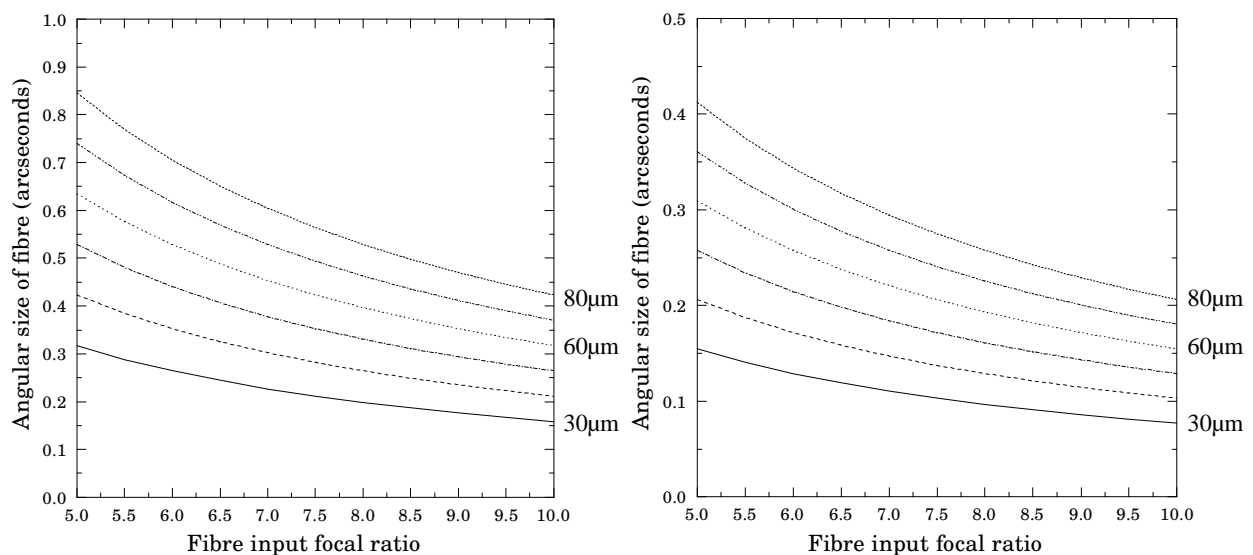


**Figure 8-1** Angular size of fibres for the AAT and Gemini telescopes. The left hand graph shows the relation between input focal ratio and the angular size of the fibre on the sky for different fibre diameters (shown on the right of each graph). The left hand diagram is for the AAT and the right hand diagram for the Gemini telescopes.

Fibre core diameter ( $\mu\text{m}$ )	Fibre buffer diameter ( $\mu\text{m}$ )	Fibre pitch in fibre slit ( $\mu\text{m}$ )	Number of fibres possible in the slit	Angular size for $f/5.25$
30	36	40	750	0.30''
40	48	55	540	0.40''
50	60	65	460	0.50''
60	72	75	400	0.60''
70	84	90	333	0.70''
80	96	100	300	0.80''

**Table 8-1** *Combinations of fibre diameter and number of fibres in the fibre slit. The chosen fibre diameter is highlighted.*

400 fibres can be packed along the fibre slit for a 60 $\mu\text{m}$  core diameter fibre, and this gives each fibre an angular diameter on the sky of 0.60 arcseconds. With the success of the COHSI curved slit assembly, a similar construction method is suggested for the SPIRAL B fibre slit. A single metal block with 75 $\mu\text{m}$  pitch machined grooves holds the fibres in position against a flat metal surface.

### 8.1.3 The lens array

Both the SPIRAL and COHSI lens arrays were assembled out of individual lenses placed onto a glass substrate and fixed in place with an UV curing epoxy. The small numbers of lenses in both arrays made this a convenient method of building a custom lens array. However, the cost of 400 lenses is large - the SPIRAL A lenslets were approximately £25 each, leading to a cost of £10,000 for a similar lens array for SPIRAL B.

Constructing such a lens array is a time consuming and would require stringent procedures to avoid the trapping of dirt and dust between the lenslets and substrate. Small tolerance errors in the sides of the hexagonal lenses also mean that they do not close-pack together exactly. The effect of many lenslets pushed together is for the sides formed by the outermost rows to 'bow' outwards. This was not noticeable with the SPIRAL array but was becoming noticeable with the COHSI lens array.

It is now worth considering buying a lens array from a manufacturer. Lee (1998) carried out extensive investigations into manufacturers of resin microlens arrays and found that Adaptive Optics Associates (AOA) produced the best arrays out of the sample of manufacturers he investigated. The AOA quote for a similar lens array of 500 hexagonal lenslets with a pitch of 2mm was \$12,600 (March 1997 price). This quote included a 10mm thick BK7 glass substrate with the lenses having a focal length of 10mm, complete with an anti-reflection coating.

This seems to be a good solution for the lens array design. However, the measured scattered light fraction in the AOA microlens arrays was found to be 20-40%, and further investigation into their macrolens array process would be needed. Tests on a sample would help resolve these issues.

A recent development is the design of crossed cylindrical lens arrays. Produced by the German company LIMO, these lens arrays are composed of two sets of cylindrical lenses (see Figure 8-2) at right angles to each other, forming a lens array with square lenslets. Two sets of cylindrical lenses need to be manufactured, the main cost of which is the fabrication of the metal dye used in drawing the lenses. The curvature of the lenses can be specified as non-cylindrical, so by designing a crossed lens array with two identical sets of cylindrical lenses, the cost of the array can be reduced.



**Figure 8-2** A set of cylindrical lenses. This picture was taken from the LIMO web site catalogue. <http://www.limo.de/>

Having demonstrated the accuracy and repeatability of placing fibres onto the back of a lens array with the COHSI fibres, the same method is suggested for this design. The minimum size of each lenslet therefore needs to be 3mm, so that the fibres can be manoeuvred into position and the UV curing epoxy does not run over into an adjacent fibre space. The only limit to the size of the

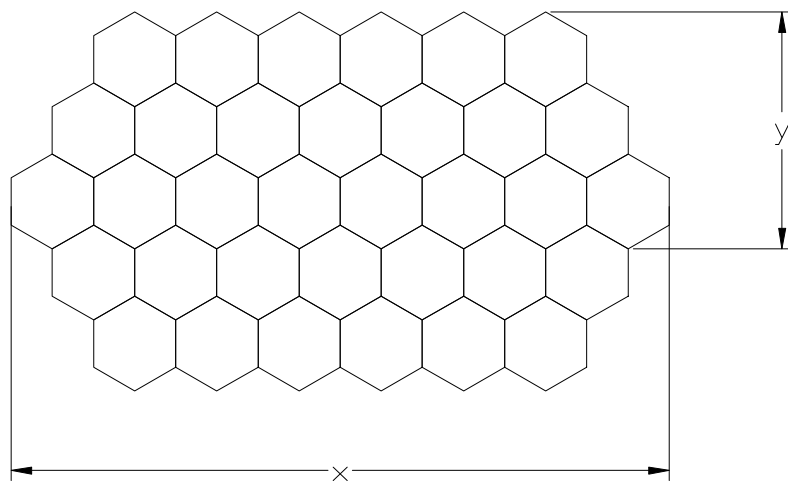


**Figure 8-3** Simple hexagonal array.  $x$  is the number of lenslets along the long axis and  $y$  the number of rows (including the middle row) from the middle to one edge. In the picture above,  $x=8$  and  $y=3$ .

lenslets is that imposed by the manufacturing process and the size of the field lens required to cover the extent of the lens array.

The geometry of the lens array is loosely based on the type of science required from the instrument, either in the form of a 'fat slit' or a circular aperture. It is difficult to build a symmetric array with exactly 400 lenses, so hexagonal designs have been produced which have lenslets in the range of 390-405 lenslets (see Figure 8-4). A useful formula relating the number of lenslets  $L$  to the geometry of the 'long hexagon' shape (see Figure 8-3 for definitions of  $x$  and  $y$ ) is:

$$L = x^2 - (x - y)(x - y + 1) \quad (8-1)$$

The dimensions of the hexagonal lens arrays are shown with lens pitch of 3mm. Table 8-2 shows the physical dimensions for the hexagonal arrays and the area they subtend on the sky. Some figures for crossed lens arrays with rectangular areas are shown in Table 8-3.

The lens array chosen is the hexagonal lens array (c). The focal ratio of the array is  $f/5.25$ , giving a focal length of 15.75mm for 394 lenses. This array requires a field lens with a diameter of at least 90mm.

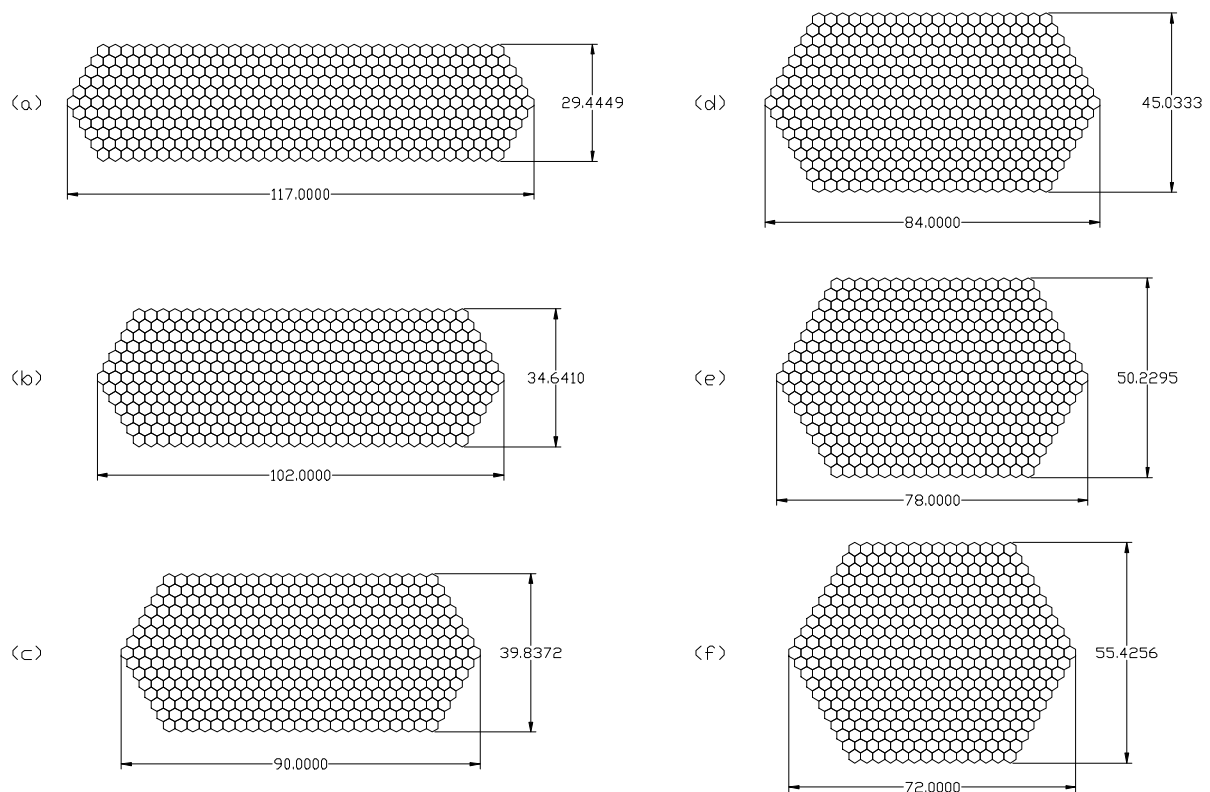


**Figure 8-4** Drawings of possible hexagonal lens arrays for SPIRAL B. The dimensions refer to the size of the array in millimetres.

Hex array	Lenses on long axis	Number of rows of lenses	lenslets in the array	Physical size of the array
(a)	39	11	399	117x29.4mm (23.4x5.8")
(b)	34	13	400	102x34.64mm (20.4x6.9")
(c)	30	15	394	90x39.8mm (18.0x8.0")
(d)	28	17	404	84x45.03mm (16.8x9.0")
(e)	26	19	404	78x50.23mm (15.6x10.0")
(f)	24	21	394	72x55.42mm (14.4x11.1")

**Table 8-2** Different possible hexagonal lens arrays for SPIRAL Phase B.

#### 8.1.4 The fore-optics

The two lenses of the fore-optics enlarge the image scale of the telescope to match the scale defined by the lens array. The schematic of the fore optics is shown in Figure 8-5, copied from a figure in Chapter 4. The magnifying lens (ML) has a focal length  $F_{ML}$  and diameter  $D_{ML}$  with a focal ratio  $f_{ML}$  and the field lens (FL) has a focal length  $F_{FL}$  and diameter  $D_{FL}$  with a focal ratio  $f_{FL}$ .

The diameter of the field lens is fixed by the size of the lens array - to make allowance for the clearance of the lens holder  $D_{ML}$  is set at 100mm. The ratio of the focal lengths of the two lenses give a first order approximation for the magnification of the fore-optics. The plate scale of the AAT is 6.67"/mm and the plate scale of the lens array is 0.6"/3mm. This means that the magnification required is 33.35, although the exact focal lengths and lens separations are determined in the detailed calculation.

Square array	Lenses on long axis	Number of rows of lenses	Lenslets in the array	Physical size of the array	Minimum diameter of the field lens
(a)	20	20	400	60x60mm (12x12")	85mm
(b)	25	16	400	75x48mm (15x9.6")	90mm
(c)	40	10	400	120x30mm (24x6")	124mm
(d)	22	18	396	66x56mm (12.2x10.8")	87mm
(e)	28	14	392	84x42mm (16.8x8.4")	94mm
(f)	33	12	396	99x36mm (19.8x7.2")	106mm

**Table 8-3** Different possible crossed lens arrays for SPIRAL Phase B.

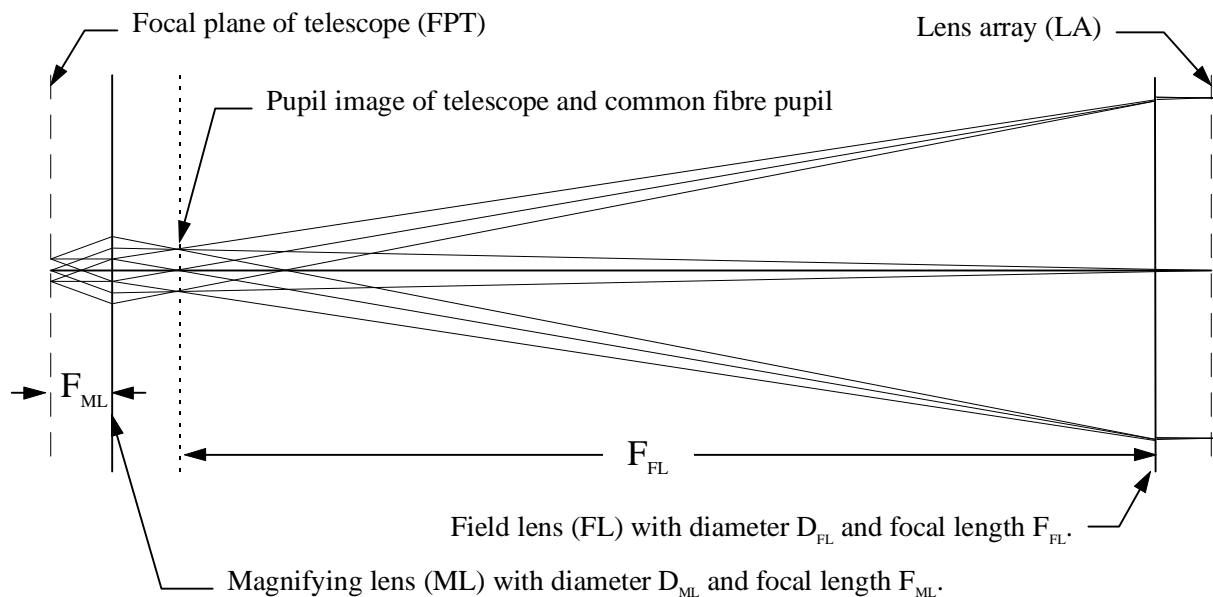


**Figure 8-5** Schematic of the SPIRAL Phase B fore-optics.

$F_{FL}$  is chosen so that the fore-optics will fit on the optics table mounted at the Cassegrain focus. This table is over a metre in length, so the slowest focal ratio the field lens can have is approximately  $(1000/100) = f/10$ . Any faster focal ratio can be chosen, such as  $f/4$ ,  $f/6$  or  $f/8$ . The design is performed with  $f/5$  in mind, giving a focal length of 500mm.

This now gives an approximate focal length for the magnifying lens of  $F_{ML} = F_{FL} / 33.35 = (500 / 33.35) = 15.0\text{mm}$ . The minimum diameter for the magnifying lens is the sum of  $F_{ML} / f_{\text{telescope}}$  and the diameter of the lens array's field of view in the plane of the telescope. Hence, the minimum diameter for  $D_{ML}$  is  $(15/8) + (18/6.67) = 4.57\text{mm}$  and preferably larger.

With the fore-optics parameters determined, the detailed lens calculation are performed with an optical design program. It is also possible to search the lens catalogues that are kept as part of the computer program and look for suitable stock lenses.

### 8.1.5 The final design

The fore optics was designed using paraxial lenses on the ZEMAX program. The lens catalogues were then examined for suitable lenses and two suitable lenses were found from a wide selection of combinations. The magnifying lens is an Edmund 45209 ( $F=15.00\text{mm}$ ,  $D=12.50\text{mm}$ ) and the field lens is a Spindler and Hoyer 322316 ( $F=499.49$ ,  $D=100\text{mm}$ ) lens. The final f-ratio of the field lens was  $f/5.0$  as expected. Note that the lens array was kept as a paraxial lens, as it was the optical performance of the fore-optics that was under investigation.

To check the optical performance, spot diagrams were produced for the resultant optical system. Figure 8-6 shows the spot diagrams in the plane of the optical fibres at the edge of the array. The two different fields shown are for a ray entering the middle of the lenslet and another ray entering at the edge of the lenslet. Figure 8-7 shows similar plots for a lenslet in the middle of the array. It is

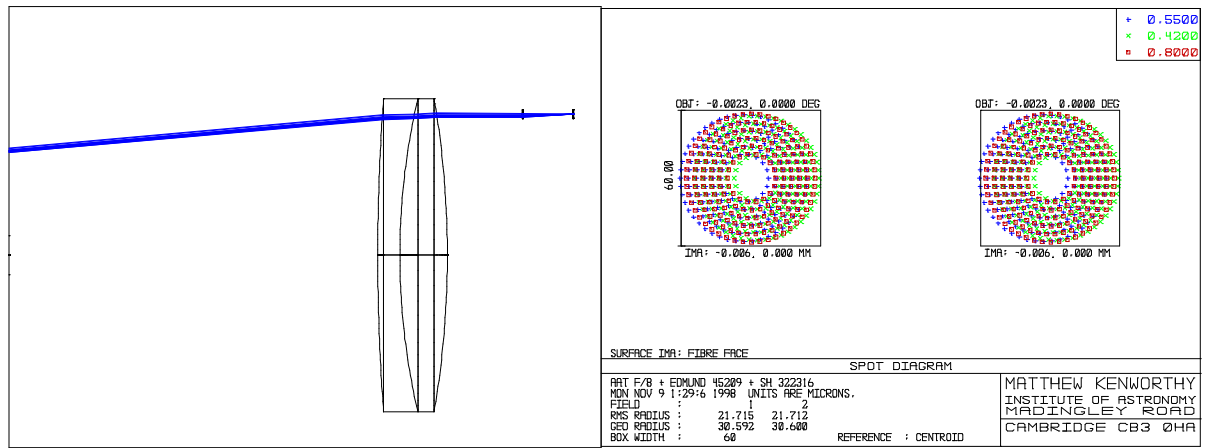


Figure 8-6 Spot diagrams for a fibre at the edge of the array.

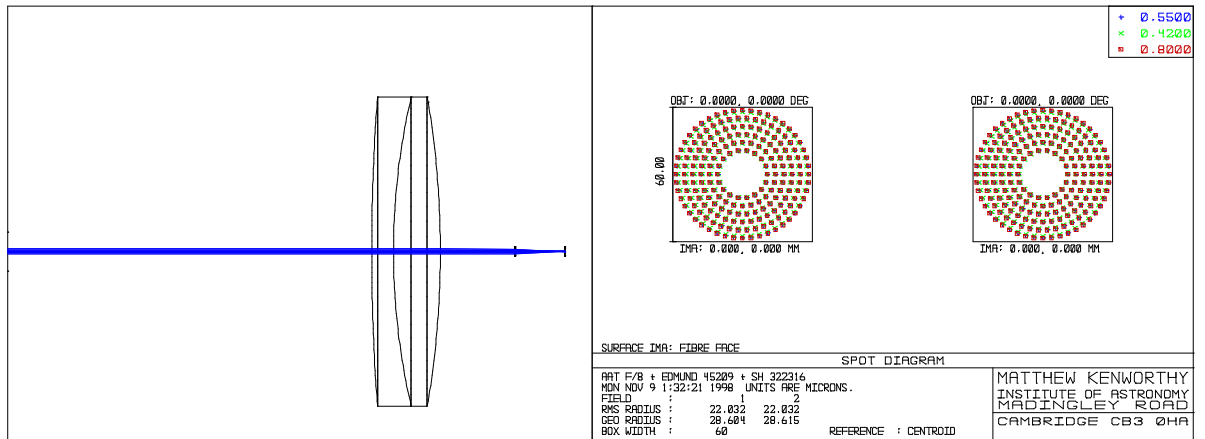


Figure 8-7 Spot diagrams for a lenslet in the middle of the array.

clear from both sets of plots that the fore-optics produce good achromatic images of the telescope pupil on the fibres from all across the array, and that the images are 60 microns in diameter as expected from the initial calculations.

The transmission curves for the glasses used in the lenses were checked - the glasses for the field lens are shown in Figure 8-8 and those in the magnifying lens have no noticeable internal absorption from 380µm to 900µm. The final layout of the fore-optics is shown in Figure 8-9.

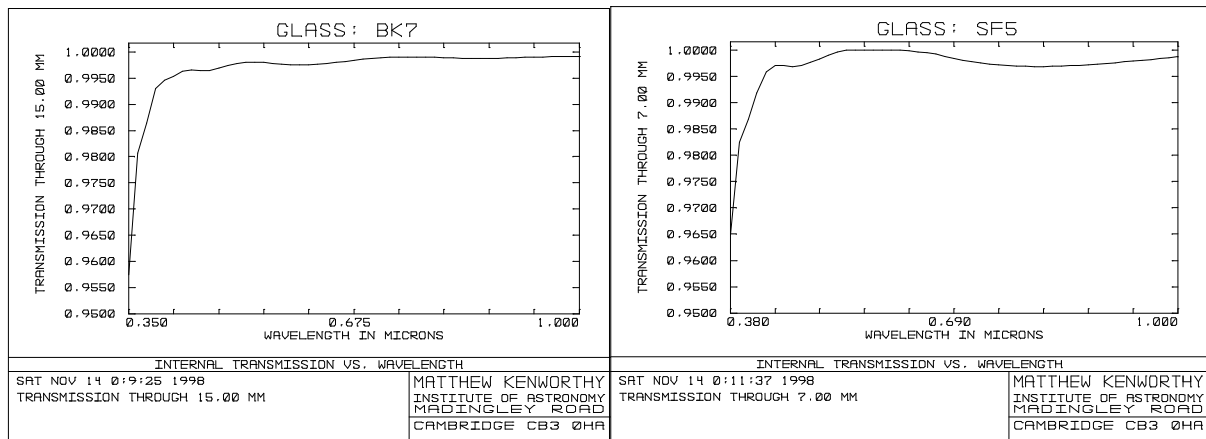
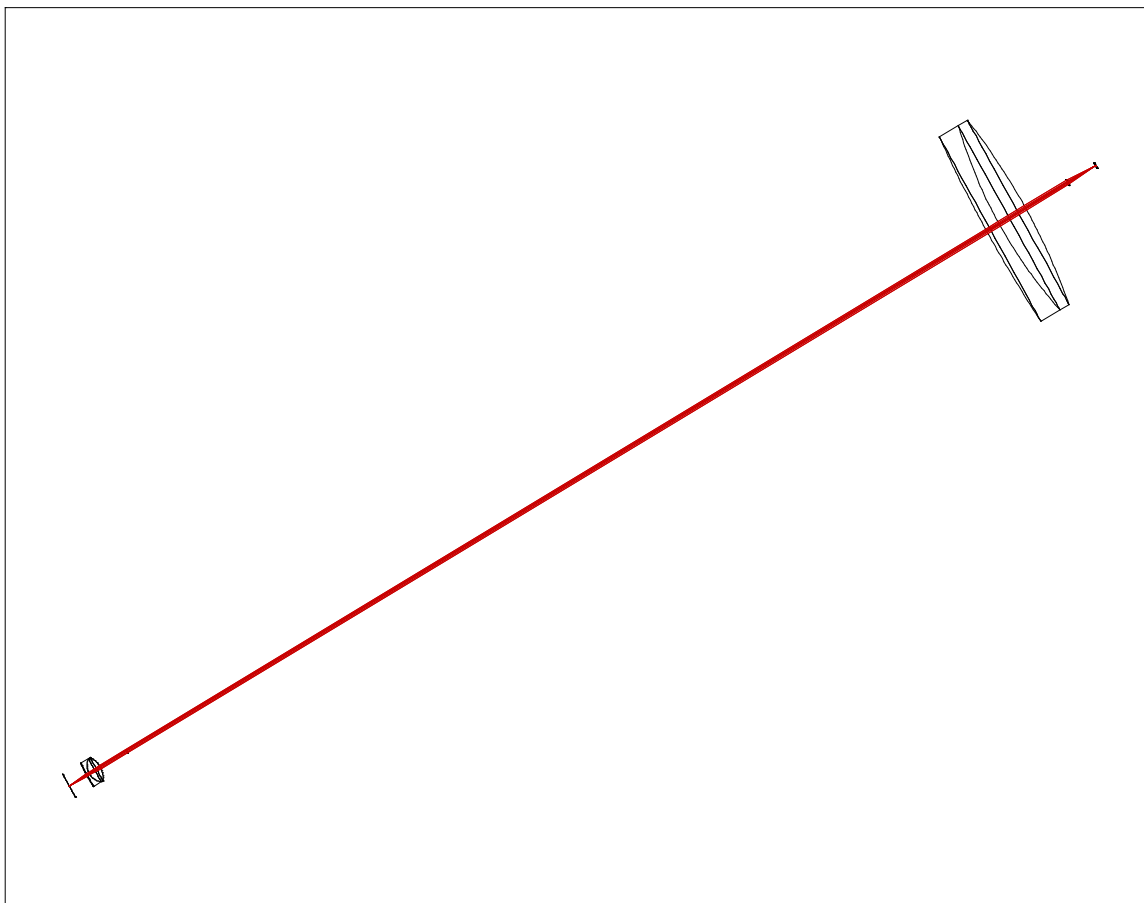


Figure 8-8 Transmission curves for the field lens. The two graphs show the transmission for the glasses used in the field lens from Spindler and Hoyer.

The fore-optics then feed a hexagonal lens array as shown in Figure 8-4c, which then are arranged into a fibre slit 30mm long. The physical parameters of the final design are shown in Table 8-4. This completes the design study of the SPIRAL Phase B fore-optics.



**Figure 8-9** The layout of the SPIRAL Phase B fore-optics. The telescope focal plane is at the lower left, passing to the magnifying lens and field lens before forming the image of the telescope focal plane on the lens array.

<b>Fore optics lenses</b>	<i>Magnifying lens</i> - Edmund 45209 (F=15.00mm, D=12.50mm) <i>Field lens</i> - Spindler and Hoyer 322316 (F=499.49, D=100mm)
<b>Image scale at lens array</b>	0.20"/mm
<b>Type of lens array</b>	Hexagonal lenslets, 3mm pitch. Mounted on BK7 substrate. $f/5.25$
<b>Geometry of lens array</b>	30 lenslets on the long axis, 15 in width, 394 in total. 102 x 34.64mm
<b>Area on sky</b>	With 0.60"/lenslet, 20.4x6.9 arcseconds.
<b>Diameter of fibre optic</b>	60 $\mu$ m core, 72 $\mu$ m cladding, 100 $\mu$ m outer plastic
<b>Length and pitch of fibre slit</b>	30mm long, 394 grooves with pitch of 76.1 $\mu$ m
<b>FRD allowance</b>	$f/5.25$ into $f/4.80$ spectrograph collimator

**Table 8-4** Results of SPIRAL Phase B study.

## 8.2 Conclusions

This design study has shown how fore-optics for a large scale lens array suitable for integral field spectroscopy can be produced. The large selection of ‘off the shelf’ lenses mean that a suitable combination can be found easily, negating the requirement for specially made lenses.

The fore-optics principle is powerful because the lens array and fibre feed can be transferred to other telescopes by a simple change of the magnifying lens. The example shown earlier in Figure 8-1 is for the Gemini telescopes, where for SPIRAL Phase ‘B’ the size of each fibre on the sky would be 0.30 arcseconds across. This would be a good match to the expected seeing at the Gemini telescopes with their adaptive optics systems, and would only require the changing of the magnifying lens to match the scale. A calculation shows that the magnification needed for Gemini ( $D=8$ metres, Cassegrain focus  $f/16$ ) is 16.11, so if a longer focal length field lens is used (say 1000mm) the focal length of the magnifying lens is 62mm, with a minimum diameter of 15mm.

One issue that has not been discussed is the length of the fibre feed. The internal transmission of the optical fibre available today is >99% for tens of metres, with only one or two narrow absorption features in the red end of the spectrum visible in transmission plots. The length of the optical fibres does not manifest itself in any part of the optical design, but the cost of the fibre is critical where the budget is concerned.

A custom draw of optical fibre costs approximately £1.50 a metre, so for the design that is £600 per metre of conduit. For the SPIRAL ‘A’ prototype there was 16 metres of fibre running from the base of the Cassegrain cage to the floor of the observatory, making for a cost of £9600. By placing the spectrograph on a raised platform the length can be made shorter, or placing it on a platform nearby. If cost is paramount, the spectrograph may have to be considered to go on the

<b>Cost of fore optics</b>	£1000
<b>Cost of lens array</b>	£15,000 for cylindrical lenses £9,000 for AOA lens array
<b>Cost of optical fibre</b>	£1,800 for Cassegrain spectrograph (3 m) £9,000 for platform mounted (15m)
<b>Time taken to polish fibres for lens array</b>	1 week
<b>Time taken for fibre alignment on lens array</b>	~ 6 weeks
<b>Time for building the fibre slit</b>	~ 2 weeks
<b>Miscellaneous construction</b>	~ 1 week
<b>Total estimated cost of optical components</b>	~ £25,000
<b>Total estimated cost for man-hours</b>	~ 3 months → £10,000
<b>Total estimated cost</b>	£45,000

**Table 8-5** *Estimated cost of the SPIRAL B project*

Cassegrain focus along with the IFU. Obviously this is a bad situation as the spectrograph is prone to flexure, but it should be noted that due to the simple Littrow design the spectrograph could be made rigid with very little effort.

A simple costing of the whole lens array is shown in Table 8-5.

A medium resolution integral field spectrograph for £45,000 is cheap when compared to the million pound projects that are the domain of other 8 metre projects, and SPIRAL Phase B is currently being built at the Anglo Australian Observatory.



# 9. Conclusions

---

## 9.1 SPIRAL Phase A and the COHSI fibre feeds

SPIRAL Phase A showed that the techniques for positioning fibres on the back of macro lens arrays was feasible, but that a proper design for the lens array mount was needed to allow direct ultraviolet illumination of the fibre faces. The SPIRAL lens array was a permanently bonded achromatic flat that did not allow easy illumination of the fibres, and combined with the very low UV transmission of the lens array substrate this led to the misalignment of the fibres on the SPIRAL fibre feed.

Even with the large alignment errors, the method of alignment was believed to have a positional accuracy of 2 microns, and this method was used for the assembly of the larger COHSI lens array. Here, the lens array was composed of two detachable substrates which allowed UV light transmission to the fibre faces, ensuring a strong mechanical joint.

The COHSI lens array fibre alignment was measured eight months after the fibre feeds were built, and the results showed an RMS positioning error of  $3.0\mu\text{m}$ , with 95% of the fibres being aligned within  $6\mu\text{m}$ . This confirmed the accuracy of the fibre alignment method.

Three different types of fibre slits were constructed and tested. The first type was a straight fibre slit with the fibres perpendicular to the plane polished surface (the SPIRAL fibre slit). The fibres were held in position underneath a metal block with grooves holding the fibres in position. The second type was a staggered fibre slit, the fibres orientated in a similar fashion to the SPIRAL fibre slit but with the optical fibres supported by the two adjacent fibres in the slit. This configuration ensured that the fibres were imaged continuously in the along the spatial axis of the spectrograph detector, and was necessary in order to fit all the fibres onto the  $256^2$  array. Both of these slits met specifications and performance required.

The third fibre slit was the curved double fibre slit, with a spherical fibre slit surface, the fibres all at a range of angles to the normal of the surface and with tight alignment tolerances. This slit combined many of the techniques practised in building the other fibre slits, and the final measured performance was slightly less than optimal. The error in the measured vector for the fibre slit (see §2.5.2) was dominated by a systematic effect implying that either one or both of the fibre plates was

distorted. With a fit to the systematic error, the residuals showed that the CNC machining that manufactured the plates allowed the fibres to be aligned with RMS errors of  $6.6\mu\text{m}$ .

The fibre alignment techniques developed have been shown to be successful and fulfil the requirements asked of them. They also present themselves as useful methods for future fibre fed instruments and will hopefully complement the large number of optical fibre techniques that the IFS instrumentation builder uses.

By using fore-optics to enlarge the scale of the telescope, a macrolens array is used to feed optical fibres instead of a microlens array sitting directly in the focus of the telescope. The technical problems of aligning the optical fibres with the telescope and lens array is transformed and the methods developed in this thesis show that the required accuracy in fibre placement can be achieved. This fore-optics and macrolens idea is developed in the SPIRAL Phase B design study and it is shown that the lens array and fibre can be matched to larger telescopes by changing the fore-optics. The simplicity and low cost of the fore-optics system change allows the fibre feed to be used at many different telescopes, increasing the versatility of the instrument.

## 9.2 Data reduction techniques

The SPIRAL spectrograph produced data frames with fibre spectra that were spatially well separated and well defined on the data frame. Data reduction was performed with a combination of IRAF packaged and a developed methodology to reduce the contributions of systematic errors that can occur with fibre-fed spectrographs, notably the time-varying flat field of some of the SPIRAL fibres. This was attributed to the problems with the lens array alignment problem, and the other fibres showed no such variations.

The COHSI data contained overlapping fibre spectra that had adjacent fibres with different zero points to their dispersion solutions, resulting in spectral cross-talk between fibres. A simulation was performed to investigate the problems associated with the cross-talk. By using a spatial filter the fraction of cross talk present in the fibres was successfully reduced and the improvements given with the filter were presented

Tracing of close packed fibre spectra was also discussed, with a hardware mask being used to help determine the position of fibre spectra on the detector. Using the work from the cross talk simulations and measurement of fibre positions an interpolation could be implemented for close packed fibre slits such as the COHSI cryogenic fibre slit.

Finally, computer routines were written to help aid visualisation of the data cubes produced by the two IFS built in Cambridge. A routine was also developed to allow display of the hexagonal lens arrays used in the fibre feeds and to perform a rough and quick data reduction for target acquisition (see Figure 9-1). With the change of a simple configuration file the software can be used by any other hexagonal lens array IFS.

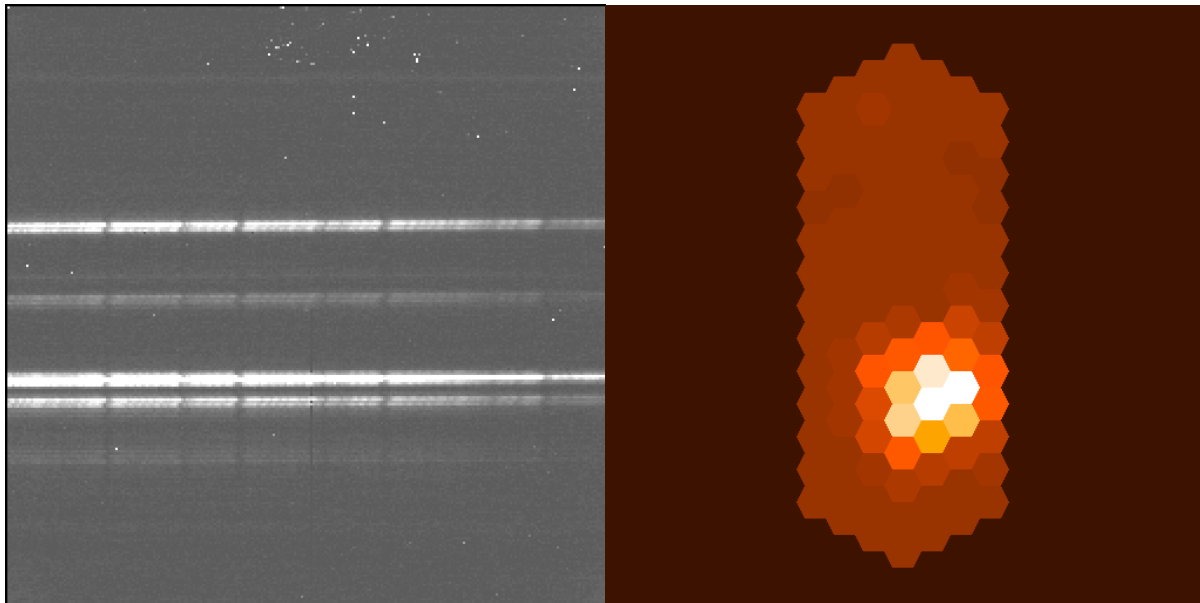


**Figure 9-1** Image reconstruction using the *LDISPLAY* software. The image of the left is a raw image from the COHSI spectrograph. By knowing the relation between fibres on the sky and fibres in the slit an image can be reconstructed (right-hand panel).

### 9.3 To the future

It is an exciting time to be in instrumentation. Many of the international eight metre telescopes are coming on-line in the next few years, and the instrumentation being developed for them is being built on a similarly large scale, with many possible combinations of operational modes to ensure optimum use of the telescope apertures.

The advent of the large telescopes and the increase of aperture is bringing about a change in the science that can be performed. Red shifts have been measured for many thousands of galaxies with four metre telescopes but with the larger telescopes, individual galaxy dynamics for low to intermediate redshift objects are being considered, and integral field spectroscopy is well suited to these types of objects.

The Gemini telescopes have the GMOS spectrographs and amongst their modules is an IFS being built by the Durham Instrumentation Group (Allington-Smith 1997) which uses 1600 hexagonal lenslets and an optical fibre feed to reformat the focal plane into a slit for the spectrograph. The same group is also building a thousand element IFU (Haynes 1998) and fibre feed for the William Herschel Telescope which feeds the WYFFOS fibre spectrograph (coverage 0.5-1.0 $\mu\text{m}$ ). With the use of adaptive optics the spatial sampling of this array is matched to 0.25 arcseconds. Both use microlens arrays placed in the focal plane of the telescope to do the image slicing.

Image slicers are being investigated and elegant solutions to the slit length problem of large image slicers has been investigated by Content (1998a and b). The mirror optics require high tolerance machining, and it remains to be seen if the optical components can be manufactured and

aligned. If these image slicers turn out to be feasible, then the possibilities for high spatial imaging using cooled mirrors opens up new scientific possibilities as demonstrated by the 3D spectrometer (Krabbe 1996).

Indeed, the Garching group are now building a 1000 element imaging spectrometer (SPIFFI) using a cryogenically cooled hexagonal lens array and fibre feed (Tecza 1998). Because of the thermal cycling inherent in the cryogenic design of their spectrograph, they are using a novel hybrid lens array and optical fibre design whereby the end of a fibre tip is formed into a lenslet so that the lens array and fibre are formed from one continuous piece of silica.

With the beginning of the large telescope era the demand for new instruments is large and the drive imposed by deeper and fainter science targets requires that telescopes are used with the greatest possible efficiency. Integral field spectrographs offer the ability to record vast quantities of data within a single nights observing, potentially requiring many months to interpret fully. After an initial reluctance to part with the tried and trusted slit based spectrograph, astronomers are slowly turning to IFS and the advantages they give. The next challenge will be how to cope with the giga-bytes of data that will flow from these instruments, and the development of suitable programs that can help produce the required information from them.

Whatever the case, the next few years in astronomy will surely be marked with discoveries made with integral field spectrographs and the field will continue to develop rapidly - watch this space!

## 10. References

---

- Afanasiev V.L., Vlasiouk V.V., Dodonov S.N., Sil'chenko O.K. (1990). "Multi pupil fiber spectrophotometer of the 6m telescope", *Preprint Special Astrophysical Observatory*, No.54, 1990.
- Allington-Smith J.R., Content R.C., Haynes R., Lewis, I.J. (1997). "Integral Field Spectroscopy with the Gemini Multi-object Spectrographs," in *Optical Telescopes of Today and Tomorrow*, A.L. Ardeberg, ed., Proc. *SPIE* **2871**, 1099-1106, 1997.
- Angel J.R.P. (1980). "*Optical and infrared telescopes for the 1990's*", ed. Hewitt:263 (1980).
- Arnett W.D. (1989). "Supernova 1987A", in *Annu. Rev. Astron. Astrophys.* **27**:629-700, 1989.
- Arribas S., Mediavilla E., Rasilla J.L. (1991). *Ap.J.* **369**:260, 1991.
- Arribas S.T., Mediavilla E., Rasilla J.L. (1993). "Bidimensional spectroscopy with a multi-bundle arrangement" in *Fiber Optics in Astronomy II, ASP Conf. Ser.* **37**:322-330, 1993.
- Atherton P.D., et al. (1982). *MNRAS* **201**:661, 1982.
- Barden S.C., Scott K. (1986). *BAAS* **18**:951, 1986.
- Barden S.C., Wade R.A. (1988). "Densepak and spectral imaging with fiber optics", in *Fiber Optics in Astronomy, ASP Conf. Ser.* **3**:113-124, 1988.
- Bates D.R., Nicolet M., (1950). "The photochemistry of atmospheric water vapor", *J. Geophys. Res.* **55**:301-327, 1950.
- Bland J., Tully R.B., Cecil G.N. (1990). "The Hawaii Imaging Fabry-Perot interferometers (HIFIs)" in *Instrumentation in astronomy VII, SPIE* **1235**:590-600, 1990.
- Boulesteix J., Georgelin Y., Marcelin M., Monnet G. (1984). "First results from CIGALE scanning Perot-Fabry interferometer", in "*Instrumentation in Astronomy V*" *SPIE* **445**:37-41, 1984.
- Boyd R.W. (1983). "Radiometry and the Detection of Optical Radiation", P.75 John Wiley and Sons, 1983.

- Chabrier G., Mera D. (1998). "Brown Dwarfs and Extrasolar Planets", *ASP Conf. Ser.* **134**, 1998.
- Chevalier R. (1992). *Ap.J.* **258**:790, 1992.
- Clark D., Wallace P. (1984). "ASPECT: a technique for Area Spectroscopy" in *Q. Jl. R. Astr Soc* **25**:114-121, 1984.
- Clayton C.A. (1989). "The implications of image scrambling and focal ratio degradation in fibre optics on the design of astronomical instrumentation", *A&A* **213**:502-515, 1989.
- Content R. (1998a). "Advance image slicer for integral field spectroscopy with UKIRT and GEMINI", *SPIE* **3354**:187-200, 1998.
- Content R. (1998b). "A new design for integral field spectroscopy with eight metre telscopes", *SPIE* **3354**, 1998.
- Crotts A.P.S., Kunkel W.E., McCarthy P.J. (1989). *Ap.J.* **347**:L61, 1989.
- Crotts A.P.S., Kunkel W.E., Heathcote S.R. (1995). *Ap.J.* **438**:724, 1995.
- Crotts A.P.S., Heathcote S.R. (1991). *Nature* **350**:683, 1991.
- Crotts A.P.S. (1997). "Rings and echoes: an overview", in "*SN 1987A: Ten Years After*" M. Phillips and N. Suntzeff (eds.), 1997.
- Ennico K.A. (1998). "Near Infrared Faint Object Spectroscopy", PhD Thesis, Cambridge University 1998
- Epps H.W., Vogt S.S. (1993). *Applied Optics*, **32**(31), 6270-6279, 1993.
- Festin L. (1998). "Brown dwarfs in the Pleiades", *A&A* in press, 1998.
- Fransson C., et al. (1989). *Ap.J.* **336**:429, 1989.
- Franx M., Illingworth G.D., Kelson D.D., Dokkum G.V., Tran K.V. (1997). "Pair of Lensed Galaxies at  $z = 4.92$  in the Field of CL 1358+62", *ApJ* **486**:L75-78, 1997.
- Geballe T., Kulkarni S.R., Woodward C.E. Sloan G.C. (1996). *Astrophys. J.* **467**:L101-104, 1996.
- Gray P.M., Philips M.M., Turtle A.J., Ellis R.S. (1992). "Fibre Optic Development at the AAO", *Proc. ASA* **4** (4):477-478, 1982.

- Haynes R., Content R., Turner J., Allington-Smith J., Lee D. (1998). "SMIRFS-II: Multi-object and integral field near-IR spectroscopy at UKIRT", *SPIE* **3354**:419-430, 1998.
- Haynes R., Doel A.P., Content R., Allington-Smith, Lee D. (1998). "TEIFU: a thousand element integral field unit for the WHT fed by the ELECTRA AO system", *SPIE* **3354**, 1998.
- Hawkins M.R.S., Bessell M.S. (1988). *MNRAS* **234**:177-191, 1988.
- Heacox W.D., Connes P. (1992). "Optical fibers in astronomical instruments" *A&A Rev.* **3**:169-199, 1992.
- Heel A.C.S. (1954). *Nature* **173**:39, 1954.
- Krabbe A., Thatte N., Kroker H., Tacconi-Garman L.E., Tecza M. (1996). "3D - A new generation imaging spectrometer", *SPIE* **2871**:1179-1186, 1996.
- Krabbe A., et al. (1995). *SPIE* **2457**:172-178, 1995.
- Lee D. (1998). "New Techniques in Astronomical Spectroscopy for 8 metre Telescopes", PhD Thesis, Durham University, 1998.
- Lundqvist P. (1997). "The structure of the circumstellar gas of SN 1987A", in "*SN1987A: Ten years on*", 1997.
- Magazzu A., Rebolo R., Zapatero Osorio M.R., Martin E.L. (1995). "A brown dwarf candidate in the Praesepe open cluster", *AJ* **110**:3014, 1995.
- Maillard J.P. (1995). "3-D spectroscopy with a Fourier Transform Spectrometer", in "*3D Optical Spectroscopic Methods in Astronomy*", *ASP Conf. Ser.* **71**:316-327, 1995.
- Maillard J.P., Michel G. (1982). "A high resolution Fourier transform spectrograph for the Cassegrain focus at the CFH telescope", in "*Instrumentation for Astronomy with Large Optical Telescopes*" C.M. Humphries (ed.), 213-222, 1982.
- Martin E.L., Rebolo R., Magazzu A. (1994). "Constraints to the masses of brown dwarf candidates from the Lithium test", *ApJ.* **436**:262-269, 1994.
- McClellan I. (1997). "CCD Imaging Techniques in Astronomy", J. Wiley, 1997.
- Nakajima T., et al. *Nature* **378**, 463-495, 1995.

- Nelson L.A., Rappaport S., Chiang E. (1993). "On the Li and Be tests for brown dwarfs", *ApJ* **413**:364-367, 1993.
- Oppenheimer B.R., Kulkarni S.R., Matthews K. (1998). *Astro-ph/9802299*, 1998.
- Pain H.J. (1993) "The physics of vibrations and waves", pub. J. Wiley, 1993.
- Ramsay S.K., Mountain C.M., Geballe T.R. (1992). "Non-thermal emission in the atmosphere above Mauna Kea", *MNRAS* **259**:751-760, 1992.
- Ramsay Howat S., Hecht J. (1996). "UKIRT observations during ALOHA93", *Spectrum* **9**:22-24, 1996.
- Ramsey L.W. (1988). "Focal Ratio Degradation in Optical Fibers of Astronomical Interest" *Fiber Optics in Astronomy*, ed. S. Barden, *PASP Conf. Ser.* **3**, 1998.
- Rasilla J.L., Arribas E., Mediavilla E., Sebastian J.L. (1990). *Astrophys. Sp. Sc.* **171**:301, 1990.
- Rebolo R., Martin E.L., Magazzu A. (1992). *ApJ* **389**, 93.
- Rebolo R., Martin E.L., Basri G., Marcy G.W., Zapatero-Osorio M.R. (1996). "Brown dwarfs in the Pleiades cluster confirmed by the Lithium test", *ApJ*. **469**:L53-56, 1996.
- Rebolo R., Martin E.L., Zapatero Osorio M.R. (eds) (1998). "Brown Dwarfs and Extrasolar Planets", *ASP Conf. Ser.* **134**, 1998.
- Rosenthal E.D., Gurwell M.A., Ho P.T.P. (1996). "Efficient detection of brown dwarfs using methane band imaging", *Nature* **384**:243-244, 1996.
- Sonneborn G., et al. (1997). "Spatially resolved STIS spectroscopy of SN 1987A: Evidence for shock interaction with circumstellar gas", *Ap.J.Lett. HST Second Servicing Mission Special*, 1997.
- Taylor K., Atherton P.D. (1980). *MNRAS* **191**:675, 1980.
- Taylor M.J., Hill M.J., (1991). "Near infrared imaging of hydroxyl wave structure over an ocean site at low altitude", *Geophys. Res. Lett.* **18**:1333-1336, 1991.
- Tecza M., Thatte N., Krabbe A., Tacconi-Garman L.E. (1998). "SPIFFI: A high resolution near-infrared imaging spectrometer", *SPIE* **3354**:394-403, 1998.
- Tinney C.G. (1993). *Astrophys. J.* **414**:279-301, 1993.

- Tinney C.G., (1996). “CCD Astrometry of Southern Very Low-Mass Stars”, *MNRAS* **281**:644-658, 1996.
- Tinney C.G., (1998). “The Intermediate Age Brown Dwarf LP 944-20”, *MNRAS*, in press.
- Turnbull D.N., Lowe R.P. (1983). “Vibrational population distribution in the hydroxyl night airglow”, *Can. J. Phys.* **61**:244-250, 1983.
- Tyndall J. (1854). *Proc. R. Inst.* **1**:446 1854.
- Vanderriest C. (1993). “Integral field spectrography with optical fibres at the C.F.H telescope”, in *Fiber Optics in Astronomy II* **37**:338-346, 1993.
- Vanderriest C., Lemonnier J.P. (1988). “Instrumentation for ground-based optical telescopes” *Conf. Proc. IX<sup>th</sup> Santa Cruz Workshop, Robinson (ed.):304*,.1988.
- Vogt S.S. (1994). “HIRES Users Manual”, *UCO/Lick Observatory Technical Report* **67**, 1994.
- Wilkling B.A., Greene T.P., Meyer M.R. (1998). “ Spectroscopy of brown dwarf candidates in the rho Ophiuchi molecular core”, *astro-ph/9810508*, 1998.
- Wilkinson A., Sharples R.H., Fosbury R.A.E., Wallace P.T. (1986). *MNRAS* **218**, 1997.
- Weitzel L., et al. (1996). *A&ASupp.* November 1996.
- Zapatero Osorio M.R., Rebolo R., Martin E.L. (1996). “Brown dwarfs in the Pleiades cluster I”, *A&A*, 1996.
- Zapatero Osorio M.R., Martin E.L., Rebolo R. (1997). “Brown dwarfs in the Pleiades cluster II”, *A&A* **323**:105-112, 1997.
- Zapatero Osorio, et al. (1998). “New brown dwarfs in the Pleiades cluster”, *ApJ* in press, 1998.

